Investigation of interface stability during the filling of liquid into a tank under reduced gravity

Vom Fachbereich Produktionstechnik

der

UNIVERSITÄT BREMEN

zur Erlangung des Grades
Doktor der Ingenieurwissenschaften (Dr.-Ing.)
genehmigte

Dissertation

von

M.Sc. Sesha Narayanan Chithathurveeravalli Govindan

Gutachter:
Prof. Dr.-Ing. habil. Michael E. Dreyer, Universtität Bremen
Prof. Mohammad Kassemi, PhD,
Case Western Reserve University & NASA Glenn Research Center, USA

Tag der mündlichen Prüfung: 24.06.2024

Eidesstattliche Erklärung

Hiermit erkläre ich durch meine Unterschrift, dass ich die vorliegende Arbeit selbstständig und ohne unerlaubte fremde Hilfe angefertigt habe, keine anderen als die von mir angegebenen Quellen und Hilfsmittel benutzt habe und die den benutzten Werken wörtlich oder inhaltlich entnommenen Stellen als solche kenntlich gemacht habe.

Sesha Narayanan Chithathurveeravalli Govindan	Ort, Datum

Abstract

Long-range and long-term space exploration missions can be accomplished in the future with the help of in-space propellant depots. An orbiting propellant depot is comparable to a gas station on Earth, that stores and delivers propellant to spacecraft tanks. Before flying to their destination, the spacecraft can dock at the propellant depot and refill their tanks. However, to effectively develop and operate propellant depots in space, the fluid mechanics coupled with thermodynamics under reduced gravity conditions has to be clearly understood. The multiphase flow phenomena related to the storage, transfer and filling of liquids under reduced gravity conditions have to be also separately investigated. The liquid-gas interface in normal gravity has a flat shape, as it is mainly influenced by the body forces. Whereas, in reduced gravity, the capillary forces are dominant and this leads to a change in the shape and position of the liquid-gas interface. There are two methods to fill tanks under reduced gravity: vented and no-vent filling. In the vented filling, the gas is vented as the liquid is filled into the tank. While in the no-vent filling, the gas is not vented as the tank is filled. The liquid jet that enters the tank interacts with the liquid-gas interface and forms different flow patterns. Different flow patterns may be required to tackle different challenges. Therefore, the stability criterion of the liquid-gas interface during the filling of a tank under reduced gravity has to be determined, so that the corresponding flow regimes can be categorized and chosen according to the requirements.

This thesis work investigates the interface stability during the vented filling of a tank under reduced gravity conditions. The investigation of interface stability during the vented filling was carried out by performing experiments and 2D numerical simulations under isothermal conditions. A multi-species multiphase system of the storable test liquid HFE-7500 and air was used in the experiments and simulations. The vented filling experiments were conducted on the ground, in the Bremen Drop Tower and on a parabolic flight. The 2D numerical simulations were performed using the multiphase volume of fluid (VOF) model of ANSYS Fluent. A cylindrical tank with an inner radius of $R_T = 30\,\mathrm{mm}$, a height of $H_T = 94\,\mathrm{mm}$, inlet and outlet radii of $R_I = R_O = 2\,\mathrm{mm}$ was used for the ground and drop tower experiments. A pipe of length $L_I = 220\,\mathrm{mm}$ was attached to the tank inlet to obtain a fully developed parabolic velocity profile of the liquid jet at the tank inlet. The experimental setup that was assembled in the drop capsule was tested on the ground under normal gravity conditions. In the ground experiments, the interaction of the incoming liquid jet with the liquid interface was investigated for different volumetric flow rates in the range of $0.8\,\mathrm{mL\,s^{-1}} \leq Q_L \leq 4.8\,\mathrm{mL\,s^{-1}}$, and for different initial liquid fill heights in the range of $9.6\,\mathrm{mm} \leq H_L \leq 45.6\,\mathrm{mm}$. Different fill patterns were noticed and the interface was found to be unstable for $Q_L > 2.8\,\mathrm{mL\,s^{-1}}$ for all H_L.

Abstract

The drop tower experiments were performed with the same experimental setup, that was used for the ground experiments, in the Bremen Drop Tower with the catapult mode, such that a longer microgravity time of about 9 s can be achieved. All the drop tower experiments were carried out with an initial liquid fill height of $H_L = (30 \pm 0.1)$ mm. The shape of the liquid interface changed from flat under normal gravity to hemispherical under microgravity conditions. The oscillation of the centre point of the liquid interface during the reorientation of the liquid inside the tank was studied. The liquid filling was initiated after 3.5 s in microgravity and continued until the end of microgravity time at 9 s. The volumetric flow rates were varied in the range of $1.00\,\mathrm{mL\,s^{-1}} \leq Q_L \leq 1.50\,\mathrm{mL\,s^{-1}}$. Based on the interaction of the liquid jet with the interface under microgravity, the volumetric flow rates were classified as subcritical, critical and supercritical regimes, which in turn helped to identify the stable and unstable liquid interfaces. The perturbation of the interface by the liquid jet and the formation of a geyser were the attributes of a stable liquid interface. The growth of the geyser and its subsequent disintegration into liquid droplets were observed for an unstable liquid interface. The critical volumetric flow rate from the drop tower experiments was found to be $Q_L = 1.30\,\mathrm{mL\,s^{-1}}$ and the corresponding critical Weber number was $\mathrm{We}_{1cr} = 1.04 \pm 0.03$.

The gas-free liquid filling into a rectangular experiment tank under variable accelerations was demonstrated by performing parabolic flight experiments on the Airbus A310 Zero-G aircraft. The experiments were part of the 39$^{\text{th}}$ DLR parabolic flight campaign. Each parabolic maneuver provided a reduced gravity time of 22 s. The parabolic flight experiment setup consisted of hydraulic, electrical and laptop racks. The internal components like a screen channel liquid acquisition device (SC-LAD), a velocity control plate (VCP), ring baffles and a gas port (GP) were fitted into the experiment tank. The inner dimensions of the experiment tank were 100 mm in length, 100 mm in breadth and 130 mm in height. The filling of liquid into an initially empty tank was predominantly tested during the parabolic flight experiments for different volumetric flow rates in the range of $0.2\,\mathrm{mL\,s^{-1}} \leq Q_L \leq 0.8\,\mathrm{mL\,s^{-1}}$. A convex liquid meniscus that is pinned to the inlet orifice and exhibits intermittent fluctuating movements due to the disturbances in the accelerations was observed for $Q_L \leq 0.6\,\mathrm{mL\,s^{-1}}$. With an increase in flow rate, the curvature shape of the liquid jet at the inlet orifice changed and the liquid covered the surfaces of the velocity control plate (VCP). A complete wetting of the solid surfaces inside the tank by the liquid could be noticed. For tests with a pre-filled tank, a violent sloshing of the bulk liquid caused by variable accelerations obstructed the optical observation. Faster filling of the liquid into the experiment tank with a higher volumetric flow rate Q_L was demonstrated with the help of VCP and the liquid-free gas was vented through the gas port.

2D numerical simulations were carried out using ANSYS Fluent with an axisymmetric model of the experiment tank used for the drop tower experiments. The numerical simulations investigated the interface stability under reduced gravity for different volumetric flow rates in the range of $1.00\,\mathrm{mL\,s^{-1}} \leq Q_L \leq 1.50\,\mathrm{mL\,s^{-1}}$ and different initial liquid fill heights in the range of $0\,\mathrm{mm} \leq H_L \leq 60\,\mathrm{mm}$. After a mesh sensitivity study, a mesh with an element size of 125 µm was chosen for the simulations. The final equilibrium position of the centre point of the interface under reduced gravity detected from the numerical simulations matched well with the drop tower experiments and the theoretical prediction for $H_L = 30$ mm. For $H_L = 30$ mm, the simulations over-predicted the geyser height and did not capture the unsteady movements of the geyser.

Moreover, the critical Weber number determined by the numerical simulations for $H_L = 30\,\text{mm}$ was $\text{We}_{1cr} = 1.15$, which was higher than the drop tower experiments ($\text{We}_{1cr} = 1.04$). Furthermore, a parametric study of different initial liquid fill heights H_L and refined volumetric flow rates Q_L was performed using the numerical simulations and the corresponding critical Weber numbers were found.

The critical Weber numbers from the simulations and drop tower experiment were compared with the existing literature. It was found that the centreline velocity, which is dependent on the velocity profile of the incoming liquid jet that enters the tank, directly affects the stability of the interface. Some more dimensionless numbers that describe the filling problem were defined and their influence on the interface stability was also discussed. A linear curve fitting of the data from the numerical simulations was performed and correlations between the dimensionless numbers were developed. All these results lead to the design of an international space station (ISS) experiment to demonstrate the filling and transfer of a storable liquid under microgravity conditions.

Zusammenfassung

Zukünftige Missionen zur Erkundung des Weltraums können mit Hilfe von Treibstoffdepots im Weltraum erfolgreich durchgeführt werden. Ein in der Umlaufbahn befindliches Treibstoffdepot ist mit einer Tankstelle auf der Erde vergleichbar, die den Treibstoff lagert und an die Tanks von Raumfahrzeugen liefert. Vor dem Flug zu ihrem Zielort können die Raumfahrzeuge an das Treibstoffdepot andocken und dort betankt werden. Um Treibstoffdepots im Weltraum effektiv entwickeln und betreiben zu können, muss die Strömungsmechanik in Verbindung mit der Thermodynamik unter Schwerelosigkeit deutlich verstanden werden. Die Phänomene von Mehrphasenströmungen im Zusammenhang mit der Lagerung, dem Transfer und der Befüllung von Flüssigkeiten unter Schwerelosigkeit müssen im Detail untersucht werden. Die freie Oberfläche unter Erdbeschleunigung ist flach, weil sie hauptsächlich von den Körperkräften beeinflusst wird. Bei Schwerelosigkeit hingegen dominieren die Kapillarkräfte, was zu einer Veränderung der Form und Lage der freien Oberfläche führt. Die Tanks können mit oder ohne Druckentlastung unter Schwerelosigkeit befüllt werden. Bei der entlüfteten Befüllung (Druckentlastung) wird das Gas entlüftet, während die Flüssigkeit in den Tank befüllt wird. Bei der entlüftungsfreien Befüllung (ohne Druckentlastung) bleibt das Gas im Tank, während die Flüssigkeit befüllt wird. Der Flüssigkeitsstrahl, der in den Tank eintritt, interagiert mit der freien Oberfläche und bildet unterschiedliche Strömungsmuster. Je nach Zuständen und Voraussetzungen können unterschiedliche Strömungsmuster benötigt werden. Daher muss das Stabilitätskriterium der freien Oberfläche während der Befüllung eines Tanks unter Schwerelosigkeit bestimmt werden. Mithilfe des Stabilitätskriterium können die Strömungsregime eingeordnet und nach den Anforderungen ausgewählt werden.

In dieser Arbeit wird die Stabilität der freien Oberfläche während der entlüfteten Befüllung eines Tanks unter Schwerelosigkeit untersucht. Die Untersuchung der Oberflächenstabilität während der Befüllung wurde durch Experimente und 2D numerische Simulationen unter isothermen Bedingungen durchgeführt. In den Experimenten und Simulationen wurde ein Mehrphasensystem verwendet, das aus der lagerfähigen Testflüssigkeit HFE-7500 und Luft besteht. Die Experimente der Befüllung wurden am Boden, im Bremer Fallturm und an Bord des Parabelfluges durchgeführt. Die 2D numerische Simulationen wurden mit dem mehrphasigen VOF (volume of fluid) Modell von ANSYS Fluent durchgeführt. Für die Boden- und Fallturmexperimente wurde ein zylindrischer Tank mit dem Innenradius $R_T = 30\,\text{mm}$, der Höhe $H_T = 94\,\text{mm}$ und den Ein- und Auslassradien $R_I = R_O = 2\,\text{mm}$ verwendet. Ein Einlassrohr mit der Länge $L_I = 220\,\text{mm}$ wurde mit dem Tankeinlass verbunden, um ein voll entwickeltes Geschwindigkeitsprofil des Flüssigkeitsstrahls am Tankeinlass zu erhalten. Der in der Fallkapsel montierte Versuchsaufbau wurde am Boden unter Erdschwerkraft getestet.

In den Bodenexperimenten wurde die Wechselwirkung des eintretenden Flüssigkeitsstrahls mit der freien Oberfläche für verschiedene Volumenströme im Bereich von $0{,}8\,\mathrm{mL\,s^{-1}} \leq Q_L \leq 4{,}8\,\mathrm{mL\,s^{-1}}$ und für verschiedene anfängliche Flüssigkeitsfüllhöhen im Bereich von $9{,}6\,\mathrm{mm} \leq H_L \leq 45{,}6\,\mathrm{mm}$ untersucht. Es wurden unterschiedliche Strömungsmuster festgestellt und die Oberfläche wurde instabil für $Q_L > 2{,}8\,\mathrm{mL\,s^{-1}}$ für alle anfänglichen Füllhöhen H_L.

Die Fallturmexperimente wurden mit demselben Versuchsaufbau von Bodenexperimente im Bremer Fallturm mit Katapultmodus durchgeführt, so dass eine längere Schwerelosigkeitszeit von etwa 9 s erreicht werden kann. Alle Fallturmexperimente wurden mit einer anfänglichen Flüssigkeitsfüllhöhe von $H_L = (30 \pm 0{,}1)\,\mathrm{mm}$ durchgeführt. Die Form der freien Oberfläche änderte sich von flach unter Erdschwerkraft zu halbkugelförmig unter Schwerelosigkeit. Die Oszillation des Mittelpunkts der freien Oberfläche während der Reorientierung der Flüssigkeit im Tank wurde beobachtet. Die Einströmung und Befüllung des Tanks wurde nach 3,5 s gestartet und bis zum Ende der Schwerelosigkeitszeit bei 9 s fortgesetzt. Es wurden unterkritische, kritische und überkritische Regime der Volumenströme im Bereich von $1{,}00\,\mathrm{mL\,s^{-1}} \leq Q_L \leq 1{,}50\,\mathrm{mL\,s^{-1}}$ identifiziert, um stabile und instabile Oberflächen aufgrund der Wechselwirkung des Flüssigkeitsstrahls mit der Oberfläche unter Mikrogravitation einzuordnen. Eine stabile Oberfläche war durch eine Verformung aufgrund des ankommenden Flüssigkeitsstrahls und die Bildung einer Ausbuchtung (Geysir) gekennzeichnet. Das Wachstum des Geysirs und der anschließende Zerfall in Flüssigkeitströpfchen führen zu einer instabilen Oberfläche. Die kritische Weber-Zahl wurde mit $\mathrm{We}_{1cr} = 1{,}04 \pm 0{,}03$ ermittelt, was einem kritischen Volumenstrom von $Q_L = 1{,}30\,\mathrm{mL\,s^{-1}}$ entspricht.

Die Befüllung der gasfreien Flüssigkeit in einen rechteckigen Experimenttank unter variablen Beschleunigungen wurde an Bord des Airbus A310 Zero-G während der 39. DLR-Parabelflugkampagne durchgeführt. Jedes Parabelmanöver ermöglichte eine Schwerelosigkeitszeit von 22 s. Der Aufbau des Parabelflugexperiments bestand aus hydraulischen, elektrischen und Laptop-Racks. Der Experimenttank war mit internen Komponenten wie einem siebbedeckten Flüssigkeitsentnahmekanal (SC-LAD), einer Prallplatte (VCP), Ringblechen und einem Gasauslass (GP) ausgestattet. Der Innenraum des Experimenttanks hatte eine Länge von 100 mm, eine Breite von 100 mm und eine Höhe von 130 mm. Die Befüllung der Flüssigkeit in einen anfänglich leeren Tank wurde während der Parabelflugkampagne für verschiedene Volumenströme im Bereich von $0{,}2\,\mathrm{mL\,s^{-1}} \leq Q_L \leq 0{,}8\,\mathrm{mL\,s^{-1}}$ getestet. Für $Q_L \leq 0{,}6\,\mathrm{mL\,s^{-1}}$ wurde ein konvexer Flüssigkeitsmeniskus beobachtet, der an der Einlassöffnung anhaftet und aufgrund der Störungen in den Beschleunigungen intermittierende schwankende Bewegungen aufweist. Mit zunehmender Strömungsgeschwindigkeit änderte sich die Krümmungsform des Flüssigkeitsstrahls an der Einlassöffnung und die Flüssigkeit bedeckte die Oberflächen der Prallplatte (VCP). Es konnte eine vollständige Benetzung der festen Oberflächen im Inneren des Tanks durch die Flüssigkeit festgestellt werden. Die optische Beobachtung wurde bei Versuchen mit vorgefülltem Tank stark beeinträchtigt. Der Grund dafür war das heftige Schwappen der vorhandenen Flüssigkeit im Tank, welches durch variable Beschleunigungen des Flugzeugs verursacht wurde. Mit Hilfe der Prallplatte wurde eine schnellere Befüllung der Flüssigkeit in den Experimenttank mit höherem Volumenstrom Q_L bewiesen und das flüssigkeitsfreie Gas durch den Gasauslass entlüftet.

2D numerische Simulationen wurden mit ANSYS Fluent mit einem achsensymmetrischen Modell des für die Fallturmexperimente verwendeten Experimenttanks durchgeführt. Im Rahmen der numerischen Simulationen wurde die Stabilität der freien Oberfläche unter reduzierter Schwerkraft für verschiedene Volumenströme im Bereich von $1{,}00\,\mathrm{mL\,s^{-1}} \leq Q_L \leq 1{,}50\,\mathrm{mL\,s^{-1}}$ und unterschiedliche anfängliche Flüssigkeitsfüllhöhen im Bereich von $0\,\mathrm{mm} \leq H_L \leq 60\,\mathrm{mm}$ untersucht. Es wurde für die Simulationen ein Gitter mit einer Elementgröße von 125 µm anhand einer Gitterstudie ausgewählt. Es wurde die finale Gleichgewichtsposition des Mittelpunkts der Oberfläche unter Schwerelosigkeit ermittelt und es wurde eine gute Übereinstimmung mit den Fallturmexperimenten und den theoretischen Vorhersagen für $H_L = 30\,\mathrm{mm}$ beobachtet. In den Simulationen wurden für $H_L = 30\,\mathrm{mm}$ die Geysirhöhe überschätzt und die instationären Bewegungen des Geysirs konnten nicht erfasst werden. Die kritische Weber-Zahl für $H_L = 30\,\mathrm{mm}$ von den Simulationen wurde als $\mathrm{We}_{1cr} = 1{,}15$ berechnet. Die von den Simulationen ermittelte kritische Weber-Zahl war höher als von den Fallturmexperimenten für $H_L = 30\,\mathrm{mm}$ ($\mathrm{We}_{1cr} = 1{,}04$). Weiterhin wurde in den numerischen Simulationen eine Parameterstudie für unterschiedliche anfängliche Flüssigkeitsfüllhöhen H_L und feiner aufgelöste Volumenströme Q_L durchgeführt und die entsprechenden kritischen Weber-Zahlen ermittelt.

Die kritischen Weber-Zahlen aus den Simulationen und dem Fallturmexperiment wurden mit der vorhandenen Literatur verglichen. Es wurde festgestellt, dass die Geschwindigkeit auf der Mittellinie, die vom Geschwindigkeitsprofil des in den Tank einströmenden Flüssigkeitsstrahls abhängt, einen direkten Einfluss auf die Stabilität der Oberfläche hat. Einige weitere dimensionslose Zahlen, die den Befüllvorgang beschreiben, wurden definiert und deren Einfluss auf die Stabilität der Oberfläche wurde ebenfalls diskutiert. Eine lineare Kurvenanpassung der Daten aus den numerischen Simulationen wurde durchgeführt und es wurden Korrelationen zwischen den dimensionslosen Zahlen entwickelt. All diese Ergebnisse führen zum Entwurf eines Experiments auf der internationalen Raumstation (ISS), mit dem die Befüllung und der Transfer einer lagerfähigen Flüssigkeit unter Mikrogravitationsbedingungen durchgeführt werden soll.

Acknowledgements

First and foremost, I would like to thank my PhD supervisor and the first reviewer of my PhD thesis, Prof. Dr.-Ing. habil. Michael Dreyer for giving me the opportunity to come to Bremen and work in a world-class facility at ZARM. I would also like to thank him for all the guidance, motivation, teachings and discussions during the course of my PhD at ZARM. He created a comfortable and positive work atmosphere in his working group, which enabled me to easily get accustomed to the field of microgravity fluid mechanics. I would also like to thank Prof. Dr. Marc Avila, the director of ZARM, for approving my employment at ZARM and continuously supporting the project ZBOT-FT.

This PhD thesis work was carried out at ZARM during the phase of the project ZBOT-FT, which was funded by the German Federal Ministry for Economic Affairs and Climate Action through the German Aerospace Center (DLR e.V.) under the grant numbers 50WM1968 and 50WM2248. Therefore, I would like to thank Dr. Thomas Driebe, Dr. Rainer Forke and Dr. Alexander Kreplin of DLR Bonn for granting the funding for our project.

I am extremely grateful to Prof. Dr. Mohammad Kassemi of Case Western Reserve University and NASA Glenn Research Center, USA for agreeing to be the second reviewer of my PhD thesis.

I would also like to extend my thanks to all my colleagues at NASA and DLR Bonn, who were part of our international collaboration, for their constructive review of my work and fruitful discussions during the teleconferences.

I would like to express my deepest gratitude to my colleagues at ZARM, namely Dipl.-Ing. Holger Faust, Dipl.-Ing. Frank Ciecior and Dipl.-Ing. Peter Prengel for their technical assistance and valuable suggestions in preparing and performing the experiments. A special thanks is extended to the technical team of ZARM FAB mbH, who supported the building of the drop tower experiment capsule and the performance of the drop tower experiments. Furthermore, I am extremely grateful to my peers M.Sc. Prithvi Shukla, M.Sc. Niklas Weber and my colleague Dr.-Ing. André Pingel for motivating and supporting me generously throughout the duration of my PhD. I would also like to thank Dr.-Ing. Sebastian Schmitt, a former PhD candidate at ZARM, for clarifying my questions on ray tracing.

I would like to acknowledge Dr. Katrin Stang of DLR Bonn for giving me the opportunity to take part in the 39$^{\text{th}}$ DLR parabolic flight campaign in Bordeaux, France. My sincere

thanks to the Novespace team, who supported us in conducting the parabolic flight experiments smoothly. Special thanks to Dipl.-Ing. Ronald Mairose of ZARM for agreeing to come with us to Bordeaux and be part of our experiment campaign. I am also thankful to the student assistants Vishal Joshi, Vishwas Kulkarni, Julian Lützen, Sudhir Kumar, David Jaramillo Restrepo and Srinath Chanda, who assisted me in various capacities during my PhD time. I would like to acknowledge M.Sc. Johannes Kind, whose master thesis work paved the way for carrying forward the project.

I would like to extend my sincere thanks to the secretaries at ZARM, namely Stephanie Dackow, Maria Petrogiannis, Andrea Fischer and Annette Leonhardt for their support in taking care of all the administrative work. I would also like to thank Birgit Kinkeldey and Dr. Lucie-Patrizia Arndt of the ZARM communication team for offering me the chance to demonstrate our project to the public during the ZARM events.

Finally, I am deeply indebted to my parents for motivating me to pursue my dreams and backing me to complete the PhD work. This would not have been possible without the support of my wife Dr. Deepanjalee Dutta, who supported me throughout the ups and downs and oriented me towards the completion of my thesis. I dedicate this thesis to my parents and wife.

Contents

List of Figures

List of Tables

List of Symbols

Latin symbols

$0g_E$	Reduced gravity, $\mathrm{m\,s^{-2}}$
$1g_E$	Normal gravity, $\mathrm{m\,s^{-2}}$
A	Area, $\mathrm{m^2}$
A_I	Cross-sectional area of the inlet pipe, $\mathrm{m^2}$
a_c	Characteristic acceleration, $\mathrm{m\,s^{-2}}$
a_P	Acceleration in the parabolic flight experiment, $\mathrm{m\,s^{-2}}$
a_{Px}	x-axis acceleration in the parabolic flight experiment, $\mathrm{m\,s^{-2}}$
a_{Py}	y-axis acceleration in the parabolic flight experiment, $\mathrm{m\,s^{-2}}$
a_{Pz}	z-axis acceleration in the parabolic flight experiment, $\mathrm{m\,s^{-2}}$
a_z	z-axis acceleration of the drop capsule, $\mathrm{m\,s^{-2}}$
B	Extensive property in governing equations
$\boldsymbol{B}$	Vectorial extensive property in governing equations
Bo	Bond number
C	Courant number
c_p	Specific heat capacity at constant pressure, $\mathrm{J\,kg^{-1}\,K^{-1}}$
D_{ju}	Diameter of the unperturbed liquid jet, mm
E	Energy, J
e	Specific energy, $\mathrm{J\,kg^{-1}}$
$\boldsymbol{F}$	Force vector, N
$\vec{F}$	Force vector in ANSYS Fluent, N
F_r	Force term in the radial direction in ANSYS Fluent, N
F_v	Volume force, $\mathrm{N\,m^{-3}}$
F_x	Force term in the axial direction in ANSYS Fluent, N
f	Face of the computational cell in ANSYS Fluent
f	Frequency, Hz
$\mathbf{g}$	Gravitational acceleration vector, $\mathrm{m\,s^{-2}}$
$\vec{g}$	Gravitational acceleration vector in ANSYS Fluent, $\mathrm{m\,s^{-2}}$
g_E	Acceleration due to gravity, $\mathrm{m\,s^{-2}}$
H_{c1}	Camera 1 height from the origin, mm
H_{c2}	Camera 2 height from the origin, mm
H_{cur}	Mean curvature of the interface, m
H_I	Liquid interface height in microgravity at the start of filling, mm

H_J	Height of the liquid jet above the inlet orifice, mm
H_L	Initial liquid fill height in normal gravity, mm
H_T	Height of the tank, mm
h	Meniscus rising height in normal gravity, m
h_e	Elevation above a reference plane, m
h_{e1}	Elevation above a reference plane in point 1 of Bernoulli equation, m
h_{e2}	Elevation above a reference plane in point 2 of Bernoulli equation, m
I	Unit tensor in ANSYS Fluent, Pa
k	Wave number, mm^{-1}
L	Length, m
L_c	Capillary length, m
L_{c1}	Camera 1 distance from the tank wall, mm
L_{c2}	Camera 2 distance from the tank wall, mm
L_{cr}	Critical length of Rayleigh-Plateau instability, mm
L_e	Entrance length for laminar flow, m
L_I	Length of the inlet pipe, mm
l_c	Characteristic length, m
M	Liquid jet momentum, $\mathrm{kg\,m\,s}^{-1}$
m	Mass, kg
$\dot{m}_{pq}$	Volumetric mass transfer rate from primary to secondary phase, $\mathrm{kg\,m}^{-3}\,\mathrm{s}^{-1}$
$\dot{m}_{qp}$	Volumetric mass transfer rate from secondary to primary phase, $\mathrm{kg\,m}^{-3}\,\mathrm{s}^{-1}$
$\dot{m}_\Gamma$	Mass flux across the interface, $\mathrm{kg\,m}^{-2}\,\mathrm{s}^{-1}$
n	Time step index in ANSYS Fluent
$\boldsymbol{n}$	Unit normal vector to the control surface
$\boldsymbol{n}_\Gamma$	Unit normal vector pointing towards first phase
n_a	Refractive index of air
n_d	Number of droplets formed from the liquid jet
n_l	Refractive index of liquid
n_s	Refractive index of solid
$\hat{n}$	Unit normal to the interface
$\hat{n}_w$	Unit vector normal to the wall
Oh	Ohnesorge number
p	Primary phase in ANSYS Fluent
p	Pressure, Pa
p_1	Pressure in point 1 of Bernoulli equation, Pa
p_2	Pressure in point 2 of Bernoulli equation, Pa
p_c	Capillary pressure, Pa
p_G	Gas pressure, Pa
p_L	Liquid pressure, Pa
Q	Thermal energy, J
Q_L	Mean volumetric flow rate, $\mathrm{mL\,s}^{-1}$
q	Secondary phase in ANSYS Fluent
$\mathbf{q}$	Heat flux vector, $\mathrm{J\,m}^{-2}\,\mathrm{s}^{-1}$
R_1	Radius of curvature in the first dimension, m
R_2	Radius of curvature in the second dimension, m
R_c	Radius of curvature of the interface, mm

R_I	Radius of the tank inlet, mm
R_J	Radius of the liquid jet at the liquid interface, mm
R_{ju}	Radius of the unperturbed liquid jet, mm
R_O	Radius of the outlet port, mm
R_T	Radius of the experiment tank, mm
R_{VP}	Radius of the velocity control plate, mm
r	Radial coordinate, mm
Re	Reynolds number
Re_1	Inlet Reynolds number
S_{α_q}	Mass source term in volume fraction equation of ANSYS Fluent, $\mathrm{kg\,m^{-3}\,s^{-1}}$
s	Length of a streamline, m
T	Temperature, K
T_{ET}	Experiment tank wall temperature, °C
T_L	Temperature of the liquid, °C
T_w	Period of oscillation, s
t	Time, s
t_b	Droplet breakup time after the start of filling in reduced gravity, s
t_{cr}	Liquid jet breakup time of Rayleigh-Plateau instability, s
t_{fs}	Filling start time in microgravity, s
t_l	Liquid layer thickness, mm
t_s	Equilibrium time in microgravity, s
t_w	Experiment tank wall thickness, mm
$\hat{t}_w$	Unit vector tangential to the wall
U_f	Volume flux through the cell face in ANSYS Fluent, $\mathrm{m^3\,s^{-1}}$
u	Velocity component in x-direction, $\mathrm{m\,s^{-1}}$
$\hat{u}$	Specific internal energy, $\mathrm{J\,kg^{-1}}$
V	Volume, $\mathrm{m^3}$
v	Velocity component in y-direction, $\mathrm{m\,s^{-1}}$
$\mathbf{v}$	Velocity vector, $\mathrm{m\,s^{-1}}$
$\vec{v}$	Velocity vector, $\mathrm{m\,s^{-1}}$
$\mathbf{v}_1$	Velocity of first phase, $\mathrm{m\,s^{-1}}$
$\mathbf{v}_2$	Velocity of second phase, $\mathrm{m\,s^{-1}}$
$\mathbf{v}_{\mathrm{CS}}$	Velocity of the control surface, $\mathrm{m\,s^{-1}}$
$\mathbf{v}_{\mathrm{F}}$	Fluid velocity, $\mathrm{m\,s^{-1}}$
$\mathbf{v}_{\mathrm{G}}$	Gas velocity, $\mathrm{m\,s^{-1}}$
$\mathbf{v}_{\mathrm{L}}$	Liquid velocity, $\mathrm{m\,s^{-1}}$
$\mathbf{v}_{\mathrm{S}}$	Solid velocity, $\mathrm{m\,s^{-1}}$
$\mathbf{v}_\Gamma$	Interface velocity, $\mathrm{m\,s^{-1}}$
v_1	Velocity in point 1 of Bernoulli equation, $\mathrm{m\,s^{-1}}$
v_2	Velocity in point 2 of Bernoulli equation, $\mathrm{m\,s^{-1}}$
v_c	Characteristic velocity, $\mathrm{m\,s^{-1}}$
v_I	Mean inlet velocity of the liquid, $\mathrm{m\,s^{-1}}$
v_J	Mean velocity of the liquid jet at the interface, $\mathrm{m\,s^{-1}}$
v_{max}	Maximum or centreline velocity of the liquid jet, $\mathrm{m\,s^{-1}}$
v_r	Radial velocity, $\mathrm{m\,s^{-1}}$
v_z	Axial velocity, $\mathrm{m\,s^{-1}}$

W	Work, J
w	Velocity component in z-direction, $\mathrm{m\,s^{-1}}$
We	Weber number
We_1	Weber number at the tank inlet
We_2	Weber number for a pre-filled tank with a uniform velocity profile
We_3	Weber number for a pre-filled tank with a parabolic velocity profile
We_4	Weber number of the liquid jet at the interface
$\mathrm{We}_{1\,cr}$	Critical Weber number
x	x-coordinate, m
y	y-coordinate, m
z	z-coordinate, m
z_c	Centre point position of the liquid interface from the origin, mm
z_{cr}	Critical geyser height, mm
z_{cu}	Uncorrected centre point of the liquid interface, mm
$z_{c,0g}$	Final equilibrium position of the liquid interface centre point in microgravity, mm
z_{pix}	Pixel value of the centre point, pixel
z_s	Axial distance from point source, m

Greek symbols

α	Angle of refraction in air, $^\circ$
α_p	Volume fraction of the primary phase in ANSYS Fluent
α_q	Volume fraction of the secondary phase in ANSYS Fluent
β	Angle of refraction in solid, $^\circ$
β	Intensive property in governing equations
γ	Angle of refraction in liquid, $^\circ$
$\triangle p$	Pressure jump across the interface, Pa
$\triangle Q_L$	Step size of volumetric flow rate, $\mathrm{mL\,s^{-1}}$
$\triangle t$	Time step, s
$\triangle x$	Computational cell size, m
$\triangle z_1$	First correction factor, mm
$\triangle z_2$	Second correction factor, mm
δ	Angle of refraction in ullage, $^\circ$
ϵ	Exponential term in velocity profile equation
η	Variable in velocity profile equation
η_c	Centre point of the liquid interface, mm
θ_c	Contact angle, $^\circ$
θ_s	Spreading angle of the liquid jet, $^\circ$
κ	Curvature of the interface, $\mathrm{m^{-1}}$
λ	Function of axial coordinate z in velocity profile equation
λ	Thermal conductivity, $\mathrm{W\,m^{-1}\,K^{-1}}$
λ_{max}	Maximum wavelength of perturbation, mm
μ	Dynamic viscosity of liquid, $\mathrm{kg\,m^{-1}\,s^{-1}}$
μg_E	Microgravity, $\mathrm{m\,s^{-2}}$
ν	Kinematic viscosity, $\mathrm{m^2\,s^{-1}}$

ξ	Similarity variable in axial velocity component equation
Π_0	Weber number at the tank inlet
Π_1	Dimensionless initial liquid fill height in normal gravity
Π_2	Ratio of inlet radius to tank radius
Π_3	Ratio of maximum velocity to mean velocity
Π_4	Dimensionless liquid interface height in microgravity at the start of filling
Π_5	Inlet Reynolds number
Π_6	Centreline Weber number at the tank inlet
ρ	Density, $\mathrm{kg\,m^{-3}}$
ρ_G	Gas density, $\mathrm{kg\,m^{-3}}$
ρ_L	Liquid density, $\mathrm{kg\,m^{-3}}$
ρ_p	Density of the primary phase in ANSYS Fluent, $\mathrm{kg\,m^{-3}}$
ρ_q	Density of the secondary phase in ANSYS Fluent, $\mathrm{kg\,m^{-3}}$
σ	Surface tension of the liquid, $\mathrm{N\,m^{-1}}$
$\boldsymbol{\sigma}_\mathrm{G}$	Stress tensor for the gas phase, Pa
$\boldsymbol{\sigma}_\mathrm{L}$	Stress tensor for the liquid phase, Pa
σ_GL	Surface tension between gas and liquid, $\mathrm{N\,m^{-1}}$
σ_SG	Surface tension between solid and gas, $\mathrm{N\,m^{-1}}$
σ_SL	Surface tension between solid and liquid, $\mathrm{N\,m^{-1}}$
$\overline{\overline{\tau}}$	Stress tensor in ANSYS Fluent, Pa
$\boldsymbol{\tau}_{ij}$	Viscous stress tensor, Pa
ψ	Radial position at which velocity is zero, m

Operators

$\dfrac{\mathrm{D}}{\mathrm{D}t}$	Total derivative
$\dfrac{\mathrm{d}}{\mathrm{d}t}$	Ordinary derivative
$\dfrac{\partial}{\partial t}$	Partial derivative
∇	Differential operator
∇_surf	Surface gradient operator
$\sum$	Sum

Abbreviations

2D	Two Dimensional
3D	Three Dimensional
ACES	Advanced Common Evolved Stage
AFTG	ANSYS Fluent Theory Guide
AFUG	ANSYS Fluent User's Guide
ASUS	Advanced Shuttle Upper Stage
ATM	Analogue Pressure Transmitter
BT	Bladder Tank
C_5F_{12}	Perfluoro-n-pentane
CAM1	Camera 1
CAM2	Camera 2
CAM3	Camera 3
CCl_4	Carbon tetrachloride
CCS	Capsule Control System
CEV	Crew Exploration Vehicle
CFD	Computational Fluid Dynamics
CFM	Cryogenic Fluid Management
COLD-SAT	Cryogenic On-orbit Liquid Depot Storage, Acquisition and Transfer satellite
CPST-TDM	Cryogenic Propellant Storage and Transfer - Technology Demonstration Mission
CRYOTE	Cryogenic Orbital Test
CS	Control Surface
CSAM	Cryogenic Systems Analysis Program
CSF	Continuum Surface Force
CSS	Continuum Surface Stress
CV	Control Volume
DLR	Deutsches Zentrum für Luft- und Raumfahrt (German Aerospace Center)
DTE	Drop Tower Experiment
DTW	Dutch Twilled Weave
eCryo	Evolvable Cryogenics
EDS	Earth Departure Stage
EELV	Evolved Expendable Launch Vehicle
ELV	Expendable Launch Vehicle

ET	Experiment Tank
FARE	Fluid Acquisition and Resupply Experiment
FROST	Future-oriented Research platform for Orbital cryogenic Storage Technologies
FM	Flow Meter
FP	Fluid Pump
GDNVF	General Dynamics No-Vent Fill program
GEO	Geosynchronous Orbit
GFSSP	Generalized Fluid System Simulation Program
GP	Gas Port
GRC	Glenn Research Center
GT	Ground Test
GUI	Graphical User Interface
HFE	Hydrofluoroether
ICES	Integrated Common Evolved Stage
IMU	Inertial Measurement Unit
ISCPD	In-Space Cryogenic Propellant Depots
ISS	International Space Station
L1	Earth-Moon Lagrange point 1
L2	Earth-Moon Lagrange point 2
LED	Light-Emitting Diode
LEO	Low-Earth Orbit
LES	Large Eddy Simulation
LPR	Low-Pressure Reservoir
LR	Liquid Reservoir
MLI	Multi-Layer Insulation
N/A	Not Applicable or Not Available
NASA	National Aeronautics and Space Administration
NC	Normally Closed valve
NO	Normally Open valve
NRC	National Research Council
NS	Numerical Simulations
NVFILL	No-Vent Fill
P1	Pressure sensor in the drop tower experiment
P1, P2, P3, P4	Pressure sensors in the parabolic flight experiment
PI	Primary Inlet
PISO	Pressure-Implicit with Splitting of Operators
PMD	Propellant Management Device
PMMA	Polymethyl methacrylate
PRESTO	Pressure Staggering Option
PS	Phase Separator
RANS	Reynolds-Averaged Navier-Stokes
RRM	Robotic Refueling Mission
SC-LAD	Screen Channel Liquid Acquisition Device
SI	Secondary Inlet
SRD	Science Requirement Document

ST	Storage Tank in the drop tower experiment
ST1, ST2	Storage Tanks in the parabolic flight experiment
STS	Space Transportation System
T1, T2, T3	Temperature sensors in the drop tower experiment
T1, T2, T3, T4	Temperature sensors in the parabolic flight experiment
TCS	Thermodynamic Cryogen Subcooler
TCTFE	Trichlorotrifluoroethane
TPCE	Tank Pressure Control Experiment
TV1, TV2	Throttle Valves in the parabolic flight experiment
V1	Gas valve in drop tower experiment
V2, V3, V4, V5, V6	Liquid valves in the drop tower experiment
V1, V2, V7, V8 V9, V10, V11	Liquid valves in the parabolic flight experiment
V12	Check valve in the parabolic flight experiment
V3, V4, V5, V6	Gas valves in the parabolic flight experiment
VCP	Velocity Control Plate
VOF	Volume Of Fluid
VP	Vacuum Pump
VTRE	Vented Tank Resupply Experiment
ZARM	Zentrum für angewandte Raumfahrttechnologie und Mikrogravitation (Center of Applied Space Technology and Microgravity)
ZBO	Zero Boil-Off
ZBOT	Zero Boil-Off Tank
ZBOT-DP	Zero Boil-Off Tank - Droplet Phase change
ZBOT-FT	Zero Boil-Off Tank - Filling and Transfer
ZBOT-NC	Zero Boil-Off Tank - Non-Condensable

Chapter 1

Introduction

This chapter introduces the topic of this thesis and gives a brief motivation behind it. Then, the objectives of this thesis work are listed followed by the structure of this thesis.

1.1 Motivation

After many decades humans have planned to set foot on the Moon again and yearn to explore our solar system further. NRC decadal survey report of 2011 [23] has prioritized the research areas like two-phase flow, thermal management and cryogenic fluid management for space exploration. It will not be economical to launch rockets with sufficient propellants for long-range and long-term space exploration missions from Earth. However, this challenge can be overcome by storing the propellants on-orbit and performing the orbital refuelling of spacecraft tanks. For accomplishing the orbital storage and refuelling, the expertise to handle cryogenic fluids under different acceleration conditions should be acquired. The propellants can be stored on-orbit in a propellant depot and the spacecraft tanks can be refilled from the propellant depot. The propellant depot can be envisioned as a supply tank that supplies the propellant to the spacecraft tank through a transfer line. The spacecraft tank acts as a receiver tank. However, in the beginning, the propellant depot may itself be a receiver tank, which is filled from a cargo spacecraft. Therefore, the microgravity fluid mechanics coupled with thermodynamics of the supply tank, receiver tank and transfer line have to be fully understood to carry out on-orbit refuelling of spacecraft.

Cryogenic liquids like liquid hydrogen and liquid methane may be preferred for storage in the propellant depots on-orbit. Under compensated or reduced gravity conditions, the capillary forces dominate over the body forces, which causes the shape of the liquid-gas interface (free surface) inside a tank to change. The position of the free surface inside the tank should be known to effectively perform filling and draining of liquid under reduced gravity conditions. Propellant management devices (PMD) help to separate the gas and liquid phases as well as to control the position of liquid inside the tank. Propellant tanks can be filled with liquid under reduced gravity conditions with or without venting the gas. The propellant tanks will get self-pressurized

due to the heat transfer into the tank from the ambient and other supporting components. Venting the gas relieves the pressure of propellant tanks. However, the liquid may also be vented if the free surface is not positioned properly under reduced gravity (Kassemi et al. 2018 [48]). Additionally, a liquid jet that is injected into a tank can also depressurize the tank by inducing a mixing of the bulk liquid, as reported by Hochstein et al. 1984 [43]. Therefore, the interaction of the liquid jet with the free surface during the tank filling has to be studied and the stability criterion of the free surface should be determined.

According to Chato and Kassemi 2012 [21], NASA Glenn Research Center has been working on an experiment series called ZBOT (Zero Boil-Off Tank) to study the methods to control tank pressurization for storing cryogenic liquids long-term in orbit. The ZBOT experiments are conducted on board the international space station (ISS) with a similitude fluid perfluoro-n-pentane C_5F_{12}. The ZBOT experiments are classified into four types as follows.

1. ZBOT-1 - This experiment was completed in 2017. It investigated the self-pressurization and jet mixing.
2. ZBOT-NC - This experiment is planned for 2024 to investigate the effects of non-condensable gases on self-pressurization and mixing.
3. ZBOT-DP - This experiment will study the effects of droplet transport and phase change on tank depressurization.
4. ZBOT-FT - This experiment will demonstrate the removal, transfer and filling of liquid between the supply tank and receiver tank through a transfer line.

This thesis work is part of the ZBOT-FT (Zero Boil-Off Tank - Filling and Transfer) experiment, that is carried out by ZARM, University of Bremen in collaboration with NASA and DLR. The overall goal of ZBOT-FT is to conduct an ISS experiment to demonstrate the removal, transfer and filling of liquid under non-isothermal conditions using the test fluid C_5F_{12}. However, in the first phase of the project ZBOT-FT, thermodynamics was decoupled and more emphasis was given to the multiphase fluid mechanics aspects of the experiment. Therefore, all the experiments and numerical simulations were performed under isothermal conditions using the storable test liquid hydrofluoroether HFE-7500. Furthermore, the project ZBOT-FT was subdivided into supply tank and receiver tank to independently investigate the phenomena associated with draining and filling tanks under normal gravity and reduced gravity conditions. This thesis only comprises of the work related to the liquid filling into a tank under normal gravity and reduced gravity conditions.

1.2 Objectives of the thesis

This thesis work was carried out to accomplish the following objectives.

1. to investigate the liquid interface stability during the vented filling of a tank and identify the different flow regimes by performing ground, drop tower and parabolic flight experiments

2. to describe the interface stability using the dimensionless Weber number and determine the critical Weber number
3. to model the liquid filling process in reduced gravity using ANSYS Fluent and carry out 2D numerical simulations
4. to compare and validate the numerical simulations with the drop tower experimental data
5. to predict the criterion of interface stability during the liquid filling with different initial liquid fill heights using numerical simulations
6. to compare the results of drop tower experiments and numerical simulations with the existing literature using dimensionless numbers

1.3 Overview of the thesis

The thesis is structured into 7 chapters. The governing equations and boundary conditions of fluid mechanics and the theoretical concepts of liquid-gas interfaces, fully developed flow, submerged laminar jet, geyser patterns and Rayleigh-Plateau instability are discussed in chapter 2. Furthermore, the physical problem of liquid filling into a tank is described and the associated dimensionless numbers are also discussed in chapter 2. An extensive review of the literature related to propellant depots, liquid filling, interface stability and liquid reorientation is carried out in chapter 3. The tank geometries and test liquids used in the experimental studies in the literature are summarized in a table in chapter 3. Chapter 4 describes the experiments performed under normal gravity conditions on the ground and under reduced gravity conditions in the Bremen Drop Tower and on the parabolic flight. The experimental data are evaluated and presented in chapter 4.

Chapter 5 is dedicated to the 2D numerical simulations carried out using ANSYS Fluent. The theory and settings of the numerical solver are elaborated in detail in this chapter. Furthermore, the mesh sensitivity study performed is also included in chapter 5. The results of ground, drop tower and parabolic flight experiments as well as the numerical simulations are discussed in chapter 6. The experimental results are also compared with the numerical results for some of the test cases. Then, a parametric study performed using numerical simulations with different initial liquid fill heights and refined volumetric flow rates is presented and finally, the results of the drop tower experiment and numerical simulations are compared with the existing literature. Based on the numerical simulation results, correlations between the dimensionless numbers are derived in chapter 6. This thesis is summarized in chapter 7 and some outlook for future work is recommended based on the obtained results.

The contents related to the drop tower experiments in this thesis have been published in Govindan and Dreyer 2023 [40]. Some parts of the contents related to the numerical simulations in this thesis have been published in Govindan and Dreyer 2023 [41].

Chapter 2

Theoretical Background

The governing equations of fluid mechanics along with the boundary conditions for multiphase flows are reported in this chapter. Additionally, the theoretical concepts of liquid-gas interfaces, fully developed flow and submerged laminar jet are discussed. Furthermore, different geyser patterns and Rayleigh-Plateau instability are explained and the liquid filling problem is described using a generic drawing. Finally, an analysis of the dimensionless numbers that characterize the liquid filling problem is also performed.

The contents in sections 2.6, 2.8 and 2.9 of this chapter have been published in Govindan and Dreyer 2023 [40] and reused here with permission.

2.1 Governing equations

A problem in fluid mechanics can be analysed using three methods, as mentioned in White 2011 [99]. They are the control volume method, differential method and experimental or dimensional analysis method. A specific region with boundaries in the flow field is called a control volume. The laws of mechanics are applied to the control volume. According to White 2011 [99], the Reynolds transport theorem states that the derivative of an arbitrary property is equal to the rate of change of the property within the control volume and the inflow and outflow fluxes across the boundaries (control surfaces).

Based on White 2011 [99], if B is an arbitrary extensive property of the fluid (mass, momentum and energy) and $\beta = \mathrm{d}B/\mathrm{d}m$ is an intensive property, the general integral form of the Reynolds transport theorem can be expressed as in equation 2.1. The change within the control volume is described in the first term on the right side of equation 2.1. The second term on the right side of equation 2.1 is the convective term that corresponds to the inflow and outflow fluxes across the control surfaces. $\mathbf{v}_{\mathrm{CS}}$ is the velocity of the control surface and $\boldsymbol{n}$ is the unit normal vector to the control surface. Based on this general form, the conservation equations can be derived.

$$\frac{\mathrm{d}B}{\mathrm{d}t} = \frac{\mathrm{d}}{\mathrm{d}t}\left(\iiint_{\mathrm{CV}} \beta\,\rho\,\mathrm{d}V\right) + \iint_{\mathrm{CS}} \beta\,\rho\,(\mathbf{v}-\mathbf{v}_{\mathrm{CS}})\cdot\boldsymbol{n}\,\mathrm{d}A \tag{2.1}$$

2.1.1 Mass conservation

The mass of fluid in a control volume is always conserved. The mass m is used as the property B in the conservation of mass equation. Then, the intensive property is $\beta = \mathrm{d}B/\mathrm{d}m = \mathrm{d}m/\mathrm{d}m = 1$. The integral form of the mass conservation equation is derived from the general form of the Reynolds transport theorem and is given in equation 2.2. The temporal change of mass in a control volume is equal to the mass flux across the control surfaces.

$$\frac{\mathrm{d}m}{\mathrm{d}t} = 0 = \frac{\mathrm{d}}{\mathrm{d}t}\left(\iiint_{\mathrm{CV}} \rho\,\mathrm{d}V\right) + \iint_{\mathrm{CS}} \rho\,(\mathbf{v}-\mathbf{v}_{\mathrm{CS}})\cdot\boldsymbol{n}\,\mathrm{d}A \tag{2.2}$$

For a fixed control volume (Eulerian approach), the mass conservation equation can be written in a differential form, as shown in equation 2.3. This is also called the continuity equation.

$$\frac{\partial\rho}{\partial t} + \nabla\cdot(\rho\,\mathbf{v}) = 0 \tag{2.3}$$

For an incompressible flow, the density variation can be neglected. Therefore, the first term of the continuity equation is $\partial\rho/\partial t \approx 0$. Hence, the continuity equation for an incompressible flow is given in equation 2.4.

$$\nabla\cdot\mathbf{v} = 0 \tag{2.4}$$

2.1.2 Momentum conservation

The conservation of momentum is based on Newton's second law of motion, which states that the net force acting on a body is equal to the rate of change of momentum. The extensive property is $\boldsymbol{B} = m\mathbf{v}$ and the intensive property is $\beta = \mathrm{d}\boldsymbol{B}/\mathrm{d}m = \mathbf{v}$. The momentum conservation equation can be written in an integral form as shown in equation 2.5. The temporal change of linear momentum inside a control volume and the sum of the momentum fluxes through the control surface are equal to the sum of forces acting on the control volume.

$$\frac{\mathrm{d}(m\mathbf{v})}{\mathrm{d}t} = \sum \boldsymbol{F} = \frac{\mathrm{d}}{\mathrm{d}t}\left(\iiint_{\mathrm{CV}} \mathbf{v}\,\rho\,\mathrm{d}V\right) + \iint_{\mathrm{CS}} \mathbf{v}\,\rho\,(\mathbf{v}-\mathbf{v}_{\mathrm{CS}})\cdot\boldsymbol{n}\,\mathrm{d}A \tag{2.5}$$

The reduced differential form of the momentum conservation equation for a fixed control volume derived by White 2011 [99] is given in equation 2.6. The term inside the brackets on the left side is the total acceleration of the fluid inside the control volume. The first two terms on the right side are the surface forces consisting of the pressure gradient and the divergence of the viscous stress tensor $\boldsymbol{\tau}_{ij}$. The last term on the right side is the body force (gravity) acting on the control volume.

$$\rho\left(\frac{\partial\mathbf{v}}{\partial t} + u\frac{\partial\mathbf{v}}{\partial x} + v\frac{\partial\mathbf{v}}{\partial y} + w\frac{\partial\mathbf{v}}{\partial z}\right) = -\nabla p + \nabla\cdot\boldsymbol{\tau}_{ij} + \rho\,\mathbf{g} \tag{2.6}$$

Following Bird et al. 2002 [7], the Navier-Stokes-equation for incompressible Newtonian fluids can be expressed as

$$\rho \frac{\mathrm{D}\mathbf{v}}{\mathrm{D}t} = \rho \left[\frac{\partial \mathbf{v}}{\partial t} + (\mathbf{v} \cdot \nabla \mathbf{v}) \right] = -\nabla p + \mu \nabla^2 \mathbf{v} + \rho \mathbf{g} \tag{2.7}$$

For inviscid flows, the Navier-Stokes equation is called the Euler equation.

$$\rho \frac{\mathrm{D}\mathbf{v}}{\mathrm{D}t} = \rho \left[\frac{\partial \mathbf{v}}{\partial t} + (\mathbf{v} \cdot \nabla \mathbf{v}) \right] = -\nabla p + \rho \mathbf{g} \tag{2.8}$$

The Euler equation can be used to derive the Bernoulli equation for a steady and inviscid flow. Based on Bird et al. 2002 [7], the velocity vector term in equation 2.8 can be rewritten as

$$(\mathbf{v} \cdot \nabla \mathbf{v}) = \frac{1}{2} \nabla (\mathbf{v} \cdot \mathbf{v}) - \left[\mathbf{v} \times (\nabla \times \mathbf{v}) \right] \tag{2.9}$$

Substituting the equation 2.9 in equation 2.8 yields equation 2.10, in which the elevation above a reference plane is denoted by h_e and g_E is the gravitational acceleration.

$$\frac{1}{2} \nabla (\mathbf{v} \cdot \mathbf{v}) - \left[\mathbf{v} \times (\nabla \times \mathbf{v}) \right] = -\frac{1}{\rho} \nabla p - g_E \nabla h_e \tag{2.10}$$

According to Bird et al. 2002 [7], the second term with cross product on the left side of equation 2.10 can be neglected by forming a dot product with the unit vector. The equation 2.10 can be expressed for a streamline with length s as

$$\frac{\mathrm{d}}{\mathrm{d}s} \left(\frac{1}{2} v^2 \right) = -\frac{1}{\rho} \frac{\mathrm{d}p}{\mathrm{d}s} - g_E \frac{\mathrm{d}h_e}{\mathrm{d}s} \tag{2.11}$$

The Bernoulli equation can be derived by integrating the equation 2.11 between two points along the streamline.

$$\frac{v_2^2 - v_1^2}{2} + \frac{p_2 - p_1}{\rho} + g_E (h_{e2} - h_{e1}) = 0 \tag{2.12}$$

2.1.3 Energy conservation

According to White 2011 [99], the first law of thermodynamics, as given in equation 2.13, states that the energy of a system changes when either heat is added to the system or work is done by the system.

$$\frac{\mathrm{d}Q}{\mathrm{d}t} - \frac{\mathrm{d}W}{\mathrm{d}t} = \frac{\mathrm{d}E}{\mathrm{d}t} \tag{2.13}$$

Using energy E as the extensive property B and $\beta = dB/dm = dE/dm = e$ in equation 2.1, the general form of the energy conservation equation can be written as given in equation 2.14.

$$\frac{\mathrm{d}Q}{\mathrm{d}t} - \frac{\mathrm{d}W}{\mathrm{d}t} = \frac{\mathrm{d}E}{\mathrm{d}t} = \frac{\mathrm{d}}{\mathrm{d}t} \left(\iiint_{\mathrm{CV}} e \, \rho \, \mathrm{d}V \right) + \iint_{\mathrm{CS}} e \, \rho \, (\mathbf{v} - \mathbf{v}_{\mathrm{CS}}) \cdot \boldsymbol{n} \, \mathrm{d}A \tag{2.14}$$

The energy per unit mass e is expressed in equation 2.15, where $\hat{u}$ is the internal energy, $\frac{1}{2}v^2$ is the kinetic energy and $g_E\, h_e$ is the potential energy.

$$e = \hat{u} + \frac{1}{2}v^2 + g_E\, h_e \tag{2.15}$$

Equation 2.16 shows the differential form of the energy conservation equation from Bird et al. 2002 [7]. The term on the left side represents the rate of change in internal energy. The first term on the right side is the change in internal energy caused by heat conduction followed by the second term, which is the work done by pressure forces. The last term on the right side is the work done by the viscous stresses.

$$\rho \frac{\mathrm{D}\hat{u}}{\mathrm{D}t} = -\left(\nabla \cdot \mathbf{q}\right) - p\left(\nabla \cdot \mathbf{v}\right) - \left(\boldsymbol{\tau} : \nabla \mathbf{v}\right) \tag{2.16}$$

If the viscous dissipation is neglected, the energy equation can be expressed with respect to temperature using Fourier's law as

$$\rho\, c_p \frac{\mathrm{D}T}{\mathrm{D}t} = \lambda \nabla^2 T \tag{2.17}$$

2.2 Boundary conditions

The boundary conditions of a flow problem should be well defined, in order to solve the governing equations. The information about the flow variables should be available at these boundaries. The two commonly used boundary conditions are the Dirichlet and Neumann boundary conditions. While the value of a flow variable is directly defined in the Dirichlet boundary condition, the Neumann boundary condition is defined as the derivative of the flow variable. The boundary conditions for a flow problem have to be defined at the inlet and outlet of the flow domain, fluid-solid interface (solid wall) and fluid-fluid interface. At the inlet and outlet boundaries, the flow variables pressure, velocity and temperature are generally known at all time instants (White 2011 [99]).

At the fluid-solid boundary, the tangential and normal components of the velocity of the fluid and the solid are equal. The no-slip boundary condition at the solid wall can be defined using equation 2.18, where $\mathbf{v}_\mathrm{F}$ is the velocity of the fluid and $\mathbf{v}_\mathrm{S}$ is the velocity of the solid.

$$\mathbf{v}_\mathrm{F} = \mathbf{v}_\mathrm{S} \tag{2.18}$$

A fluid-fluid interface is formed between two phases of liquid and gas, when they are in contact with each other. The gas phase that condenses is called a vapour and the gas phase that does not condense is called a non-condensable gas. The properties of the fluid change in a continuous manner across a fluid-fluid interface. According to the lecture notes of Shankar Subramanian 2015 [77], for a fixed interface with no mass transfer across it, the boundary condition at the fluid-fluid interface is defined in equation 2.19, where the normal components of the velocity of both phases are continuous across the interface. $\mathbf{v}_1$ is the velocity of phase 1 and $\mathbf{v}_2$ is the velocity of phase 2. $\boldsymbol{n}_\Gamma$ is the unit normal vector pointing towards the phase 1.

$$\mathbf{v}_1 \cdot \boldsymbol{n}_\Gamma = \mathbf{v}_2 \cdot \boldsymbol{n}_\Gamma = 0 \tag{2.19}$$

The fluid-fluid interface does not have any thickness and does not accumulate any mass. The mass is conserved across the fluid-fluid interface and the mass balance is given in equation 2.20, according to Burelbach et al. 1988 [13]. $\mathbf{v}_\mathrm{L}$ and $\mathbf{v}_\mathrm{G}$ are the liquid and gas velocities respectively. $\mathbf{v}_\Gamma$ is the velocity of the interface. The difference in the fluid and interface velocities leads to a mass transfer across the interface due to evaporation or condensation. The mass flux across the interface is indicated as $\dot{m}_\Gamma$ and has a unit of $\mathrm{kg\,m^{-2}\,s^{-1}}$.

$$\rho_\mathrm{L}\left(\mathbf{v}_\mathrm{L}-\mathbf{v}_\Gamma\right)\cdot\boldsymbol{n}_\Gamma=\rho_\mathrm{G}\left(\mathbf{v}_\mathrm{G}-\mathbf{v}_\Gamma\right)\cdot\boldsymbol{n}_\Gamma=\dot{m}_\Gamma \tag{2.20}$$

The mass conservation equation across the interface can be rewritten in terms of the normal components of the liquid and gas velocities as shown in equations 2.21 and 2.22 below.

$$\mathbf{v}_\mathrm{L}\cdot\boldsymbol{n}_\Gamma=\frac{\dot{m}_\Gamma}{\rho_\mathrm{L}}+\mathbf{v}_\Gamma\cdot\boldsymbol{n}_\Gamma \tag{2.21}$$

$$\mathbf{v}_\mathrm{G}\cdot\boldsymbol{n}_\Gamma=\frac{\dot{m}_\Gamma}{\rho_\mathrm{G}}+\mathbf{v}_\Gamma\cdot\boldsymbol{n}_\Gamma \tag{2.22}$$

Following Burelbach et al. 1988 [13], the stress boundary condition on the interface in its general form is given in equation 2.23.

$$\begin{aligned}\left[\rho_\mathrm{L}\left(\mathbf{v}_\mathrm{L}-\mathbf{v}_\Gamma\right)\cdot\boldsymbol{n}_\Gamma\left(\mathbf{v}_\mathrm{L}\cdot\boldsymbol{n}_\Gamma\right)-\rho_\mathrm{G}\left(\mathbf{v}_\mathrm{G}-\mathbf{v}_\Gamma\right)\cdot\boldsymbol{n}_\Gamma\left(\mathbf{v}_\mathrm{G}\cdot\boldsymbol{n}_\Gamma\right)\right]\boldsymbol{n}_\Gamma-\left(\boldsymbol{\sigma}_\mathrm{L}-\boldsymbol{\sigma}_\mathrm{G}\right)\cdot\boldsymbol{n}_\Gamma\\ -\sigma\left(\nabla\cdot\boldsymbol{n}_\Gamma\right)\boldsymbol{n}_\Gamma+\nabla_\mathrm{surf}\,\sigma=0\end{aligned} \tag{2.23}$$

Using equation 2.20 the first two terms inside the square brackets on the left side of equation 2.23 can be simplified as

$$\rho_\mathrm{L}\left(\mathbf{v}_\mathrm{L}-\mathbf{v}_\Gamma\right)\cdot\boldsymbol{n}_\Gamma\left(\mathbf{v}_\mathrm{L}\cdot\boldsymbol{n}_\Gamma\right)-\rho_\mathrm{G}\left(\mathbf{v}_\mathrm{G}-\mathbf{v}_\Gamma\right)\cdot\boldsymbol{n}_\Gamma\left(\mathbf{v}_\mathrm{G}\cdot\boldsymbol{n}_\Gamma\right)=\dot{m}_\Gamma\left(\mathbf{v}_\mathrm{L}-\mathbf{v}_\mathrm{G}\right)\cdot\boldsymbol{n}_\Gamma \tag{2.24}$$

The stress boundary condition equation 2.23 can be reduced and written as shown in equation 2.25, if the mass flux across the interface is neglected. The term on the left side is the stress tensor and the second term on the right side is the surface tension gradient.

$$-\left(\boldsymbol{\sigma}_\mathrm{L}-\boldsymbol{\sigma}_\mathrm{G}\right)\cdot\boldsymbol{n}_\Gamma=\sigma\left(\nabla\cdot\boldsymbol{n}_\Gamma\right)\boldsymbol{n}_\Gamma-\nabla_\mathrm{surf}\,\sigma \tag{2.25}$$

According to the lecture notes of Shankar Subramanian 2015 [77], the term inside the brackets on the right side represents the mean curvature of the interface, which is given in equation 2.26, where R_1 and R_2 are the principal radii of curvature of the interface.

$$\nabla\cdot\boldsymbol{n}_\Gamma=2H_\mathrm{cur}=\left(\frac{1}{R_1}+\frac{1}{R_2}\right) \tag{2.26}$$

The Young-Laplace-Gauss equation, as given in equation 2.27, can be derived by equating the left side and the first term on the right side of equation 2.25, when the viscous stress terms are neglected from the stress tensor.

$$\triangle p=p_\mathrm{L}-p_\mathrm{G}=\sigma\left(\frac{1}{R_1}+\frac{1}{R_2}\right) \tag{2.27}$$

2.3 Concepts of liquid-gas interfaces

In this section, the concepts that govern the behaviour of liquid-gas interfaces are discussed.

2.3.1 Surface tension

The molecules inside a liquid experience intermolecular forces in all directions between their neighbours and therefore the net force is zero. At the liquid-gas interface, as the liquid molecules are exposed to the gas molecules on one side, there is an imbalance in the intermolecular forces. Therefore, the liquid molecules on the interface experience a net downward force, which leads to a reduction in the surface area. A certain amount of work has to be done to increase the surface area of the interface, which is called the surface tension. It can also be defined as the force applied per unit length of the interface, as shown in equation 2.28. According to Dodge 2000 [26], as the liquid temperature increases, its surface tension decreases and it vanishes at the critical point.

$$\sigma = \frac{\mathrm{d}W}{\mathrm{d}A} = \frac{F\,\mathrm{d}x}{L\,\mathrm{d}x} = \frac{F}{L} \tag{2.28}$$

2.3.2 Pressure difference across an interface

There exists no pressure difference across a flat interface because the tangential forces balance each other. In the case of a curved interface, the resultant of the surface tension force, that acts perpendicular to the interface, causes the pressure to vary on both sides of the interface. The resultant force acts in the direction of the liquid for a convex-shaped interface and it leads to a higher pressure in the liquid than the gas. For a concave-shaped interface, the pressure on the liquid side is lower than the gas side, as the resultant force acts in the direction of the gas. White 2011 [99] states that the concave side of the interface will be at a higher pressure. The pressure jump across the interface is defined by the Young-Laplace equation in equation 2.29, where R_1 and R_2 are the principal radii of curvature.

$$\triangle p = \sigma \left(\frac{1}{R_1} + \frac{1}{R_2} \right) \tag{2.29}$$

2.3.3 Contact angle

When a liquid interface comes in contact with a solid or another liquid, an angle is formed. The angle between the solid surface and the tangent to the liquid-gas interface is called the contact angle. According to Dodge 2000 [26], the contact angle is dependent on the cohesive and adhesive forces. For a condition of three interfaces of solid-liquid, liquid-gas and solid-gas, the force balance in the horizontal direction on the contact lines of these interfaces is given in equation 2.30, as reported by Dodge 2000 [26]. This equation is also called the Young's equation. The contact angle θ_c can be determined from the equation 2.30.

$$\sigma_{\mathrm{SG}} = \sigma_{\mathrm{GL}} \cos\theta_c + \sigma_{\mathrm{SL}} \tag{2.30}$$

The wettability of a liquid with a solid surface is measured by its contact angle. The liquid's ability to wet the solid can be categorized into three conditions: perfectly wetting ($\theta_c = 0°$), wetting ($\theta_c < 90°$) and non-wetting ($\theta_c > 90°$).

2.3.4 Shape of the interface

The liquid interface shape is expressed using the Bond number, which is a ratio between the hydrostatic pressure and the capillary pressure, as shown in equation 2.31. a_c is the characteristic acceleration and l_c is the characteristic length in equation 2.31.

$$\mathrm{Bo} = \frac{\rho\, a_c\, l_c^2}{\sigma} \tag{2.31}$$

During the normal gravity and hypergravity phases, the hydrostatic pressure dominates over the capillary pressure, which leads to a higher Bond number $\mathrm{Bo} > 1$ and the liquid interface remains flat. The characteristic length at which the Bond number becomes unity is called the capillary length. At the capillary length, the hydrostatic and capillary pressures balance each other. The capillary length L_c under normal gravity conditions is expressed in equation 2.32, where the characteristic acceleration a_c is the acceleration due to gravity on Earth ($g_E = 9.81\,\mathrm{m\,s^{-2}}$).

$$L_c = \sqrt{\frac{\sigma}{\rho\, g_E}} \tag{2.32}$$

For a partly filled tank in normal gravity, a liquid meniscus is formed at the tank wall due to the adhesive force between the liquid and the wall. The height to which the meniscus rises in normal gravity is given by equation 2.33 from Landau and Lifshitz 1987 [56].

$$h = \sqrt{2}\, L_c \sqrt{(1 - \sin\theta_c)} \tag{2.33}$$

In reduced gravity, the hydrostatic pressure becomes negligible and the Bond number reduces to a lower value of $\mathrm{Bo} \ll 1$. The liquid interface changes from a gravity-dominated flat shape in normal gravity to a capillary-dominated hemispherical shape in reduced gravity. For a partly filled tank, as soon as the gravity is reduced, the liquid meniscus at the tank wall rises and a capillary wave travels from the tank wall to the centre, which makes the liquid interface to move downwards. This results in axial sloshing of the liquid interface in an axisymmetric tank and the liquid reorientation takes place inside the tank. The centre point of the interface oscillates during the reorientation and these oscillations dampen with time. The liquid interface reaches its final equilibrium configuration in reduced gravity after a certain period of time, which is called the formation time, as mentioned in Dodge 2000 [26].

The position of the centre point of the liquid interface after reaching its final equilibrium position in reduced gravity can be determined from equation 2.34. According to Friese et al. 2019 [34], for a cylindrical tank partly filled with a perfectly wetting liquid, the final equilibrium position of the centre point of the liquid interface in microgravity $z_{c,0g}$ reduces from its initial fill height H_L by a one-third factor of the tank radius R_T.

$$z_{c,0g} = H_L - \frac{R_T}{3} \tag{2.34}$$

According to Siegert et al. 1964 [78], the time when the centre point of the interface crosses the final equilibrium position for the first time in microgravity is called the equilibrium time t_s. The equilibrium time, which depends on the liquid properties and the tank radius, is defined for a cylindrical tank in equation 2.35. It is also called the characteristic time that describes the liquid reorientation inside the tank in reduced gravity.

$$t_s = 0.413 \sqrt{\frac{\rho\, R_T^3}{\sigma}} \tag{2.35}$$

2.4 Fully developed flow

The characteristic of the flow of liquid in a pipe can be described using the Reynolds number, which compares the inertial and viscous forces, as shown in equation 2.36, where R_I is the inner radius of the pipe. A smooth and steady flow in a pipe is called a laminar flow, while a fluctuating flow is called a turbulent flow. According to White 2011 [99], the region in which the flow changes from laminar to turbulent is called the transition region, which occurs at a Reynolds number of Re $\approx$ 2300 for the flow of liquid in a circular pipe.

$$\mathrm{Re} = \frac{2\,\rho\, v_I\, R_I}{\mu} \tag{2.36}$$

When a liquid flows inside a pipe, boundary layers are formed along the pipe walls. The velocity varies within the boundary layer and becomes zero at the wall of the pipe because of the no-slip condition. The region within the boundary layer is affected by viscosity, whereas the region outside the boundary layer is inviscid. The boundary layers from the pipe walls become thicker along the length of the pipe and they merge at a specific point on the centre axis of the pipe. Beyond this point, the flow is considered to be fully developed, as the flow velocity does not change in the axial direction but only in the radial direction. The length of the pipe from its entrance to the point where the flow is fully developed is called the entrance length. According to White 2011 [99], the entrance length L_e for a laminar flow can be defined as

$$L_e = 0.12\,\mathrm{Re}\,R_I \tag{2.37}$$

The reduced z-momentum equation for a fully developed laminar flow in cylindrical coordinates is given by White 2011 [99] as

$$\rho\, v_z \frac{\partial v_z}{\partial z} = -\frac{\mathrm{d}p}{\mathrm{d}z} + \frac{\mu}{r}\frac{\mathrm{d}}{\mathrm{d}r}\left(r\frac{\mathrm{d}v_z}{\mathrm{d}r}\right) \tag{2.38}$$

The left hand side term can be neglected because the axial velocity is only a function of the radial coordinate ($v_z = v_z(r)$). Applying the no-slip boundary condition at the pipe wall and assuming the centreline velocity to have a finite value, the solution to equation 2.38 leads to the Hagen-Poiseuille flow.

$$v_z = \left(-\frac{\mathrm{d}p}{\mathrm{d}z}\right)\frac{R_I^2}{4\mu}\left(1 - \frac{r^2}{R_I^2}\right) \tag{2.39}$$

For a fully developed flow, the shape of the velocity profile is parabolic. The axial velocity is maximum on the centreline of the pipe. The maximum or centreline velocity is given as

$$v_{max} = v_z(r=0) = \left(-\frac{\mathrm{d}p}{\mathrm{d}z}\right)\frac{R_I^2}{4\mu} \tag{2.40}$$

The mean velocity v_I of a pipe flow can be calculated from equation 2.41, where Q_L is the volumetric flow rate and A_I is the cross-sectional area of the pipe inlet. The cross-sectional area A_I for a circular pipe is given as $A_I = \pi R_I^2$.

$$v_I = \frac{Q_L}{A_I} \tag{2.41}$$

For a parabolic velocity profile, the mean velocity v_I is half of the centreline velocity v_{max}.

$$v_I = \frac{v_{max}}{2} \tag{2.42}$$

2.5 Submerged laminar jet

The liquid that flows out of a nozzle forms a jet. From Kneer et al. 2014 [49], a liquid jet that exits a nozzle and flows into a surrounding liquid is called a submerged jet. If the liquid jet flows into a gaseous environment, then it is called a free-surface jet. The submerged jets can be either laminar or turbulent depending on the Reynolds number at the nozzle exit. The geometry and length of the pipe through which the liquid flows out influence the velocity profile of the jet. A long inlet pipe and a low Reynolds number lead to a laminar jet flow with a fully developed parabolic velocity profile at the exit of the pipe. As reported in Viskanta 1993 [95], three regions are formed when a liquid jet flows into a surrounding liquid. They are called the potential core region, the region of flow development and the region of developed flow, as shown in figure 2.1. Within the potential core region, the centreline velocity remains the same as at the pipe exit. Although the potential core length can vary in the range of 6-7 times the nozzle diameter for an axisymmetric jet, for a parabolic velocity profile, the potential core is absent, as the centreline velocity begins to decay right at the pipe exit, as reported in Kneer et al. 2014 [49].

As the submerged liquid jet exits the pipe, it begins to spread and a shear layer is formed at the jet boundary by the surrounding liquid. This causes the liquid jet to decelerate and the velocity profile of the jet changes in the region of flow development. According to Kneer et al. 2014 [49], the velocity profile can be scaled using the non-dimensional parameter $z/(2\,R_I\,\mathrm{Re})$. After a certain distance from the exit of the pipe, the region of developed flow begins, where the velocity profile of the jet is fully developed again. The axial velocity component of a laminar jet according to Schlichting's boundary layer theory is given by Rankin and Sridhar 1981 [72] as

$$v_z = \frac{3M}{4\,\pi\,\mu}\,\frac{1}{z_s}\,\frac{1}{\left(1+\xi^2\right)^2} \tag{2.43}$$

with

$$\xi = \frac{1}{8\nu}\sqrt{\left(\frac{3M}{\pi\rho}\right)}\,\frac{r}{z_s} \tag{2.44}$$

The terms in equation 2.43 are described as: M is the liquid jet momentum, ξ is a similarity variable, z_s is the axial distance from the point source and r is the radial coordinate.

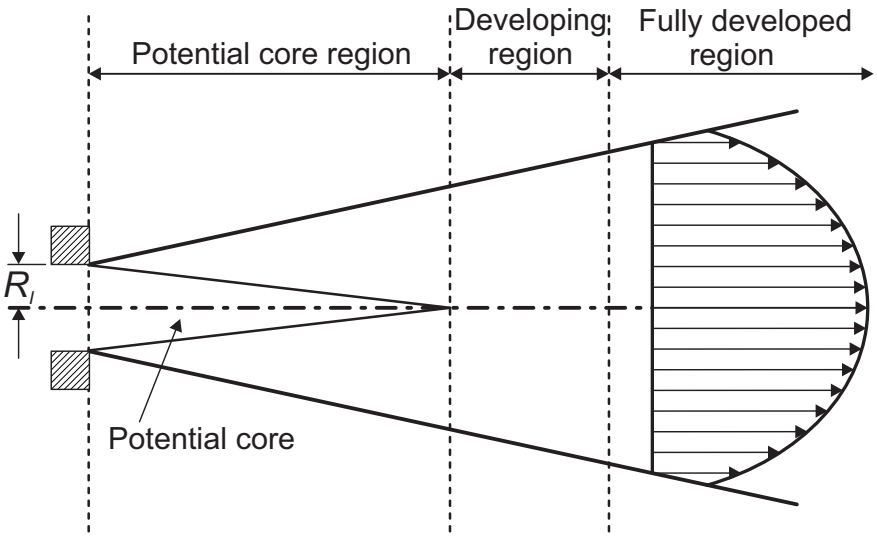

Figure 2.1: Profile of a liquid jet exiting an inlet pipe with radius R_I, as reported in Viskanta 1993 [95].

Rankin and Sridhar 1981 [72] simplified the general form of the parabolic velocity profile equation proposed by Thomas 1958 [91] as

$$\frac{v(z,r)}{v(z=0,r=0)} = \left(1-\eta^2\right)\left(1-\epsilon\, e^{(\eta/\lambda)}\right)^3 + \frac{3\,\epsilon\,\eta\,(1-\epsilon)^2\,(1-\eta)^3}{\lambda} \tag{2.45}$$

and presented an analytical solution of the velocity profile equation. In equation 2.45, $\eta = r/\psi$, where ψ denotes the radial position at which $v = 0\,\mathrm{m\,s^{-1}}$. The other term is $\epsilon = e^{-1/\lambda}$ and λ is a function of the axial coordinate z.

2.6 Geyser patterns

The reduction of gravitational acceleration causes the liquid to undergo a reorientation inside a pre-filled tank, and the interface shape changes from flat to hemispherical. Tanks can be filled with liquid under microgravity with or without venting the gas. During the vented filling of a tank under microgravity conditions, the gas-free liquid is filled into the tank and the gas is vented from the tank.

One of the common liquid injection techniques into a tank is to create a jet using an inlet pipe. The liquid jet that enters the tank interacts with the liquid interface and forms a geyser. The four different geyser flow patterns, as reported in Hochstein et al. 2008 [44], are shown in figure 2.2. Though they correspond to a no-vent filling of a tank, the patterns I, II and III are also relevant for the vented filling of a tank. As the liquid jet enters the tank, it exchanges momentum with the already present bulk liquid and travels towards the liquid interface. In pattern I, the liquid jet does not disturb the interface. The liquid jet penetrates the interface and creates a geyser in pattern II, if the momentum of the incoming jet is higher than the capillary pressure of the interface. In pattern III, this geyser moves towards the top part of the tank breaking the ullage bubble and circulates at the top of the tank.

In case of a vented filling, this geyser may reach the vent port and this may lead to a liquid propellant loss. In case of a no-vent filling, the liquid jet helps in cooling the tank down during the self-pressurization. Pattern IV occurs, when the liquid flows back along the tank wall and mixes with the bulk liquid. Pattern IV is possible in tanks pre-filled with a higher initial liquid fill heights. The spreading of the liquid jet inside a tank and the formation of a geyser is depicted in figure 2.3 for the pattern II of figure 2.2. The liquid jet enters the tank and begins to spread in the bulk liquid before it perturbs the interface and forms a geyser. The spreading of the liquid jet causes a decay in its mean and centreline velocities.

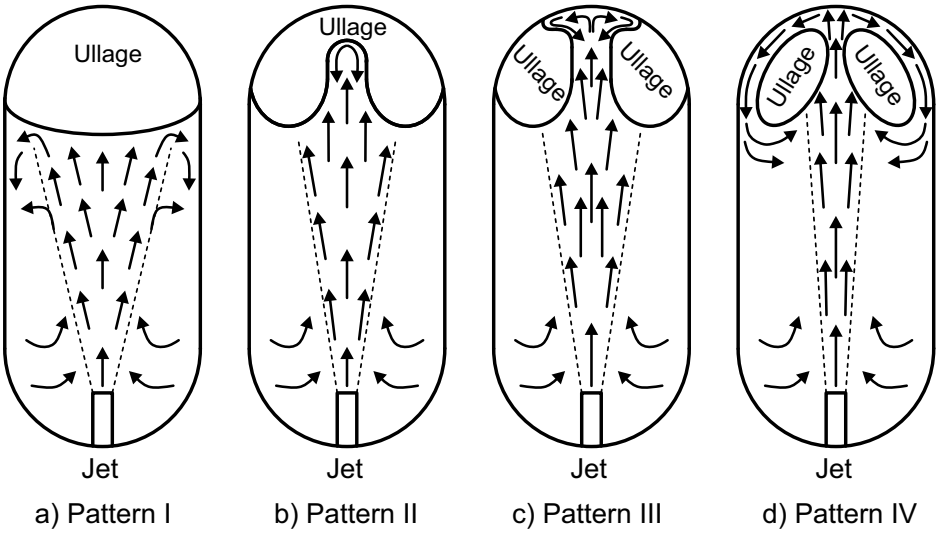

Figure 2.2: Geyser flow patterns in reduced gravity as reported in Hochstein et al. 2008 [44].

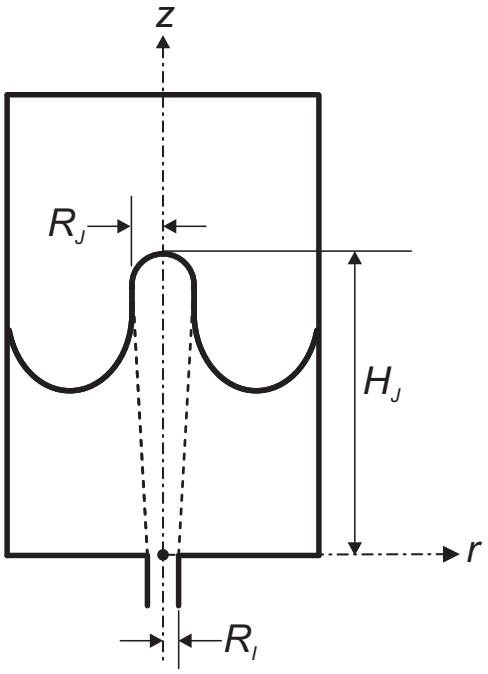

Figure 2.3: Spreading of the liquid jet and formation of a geyser in reduced gravity.

The force balance at the interface can be expressed as the ratio of stagnation pressure and capillary pressure. This ratio is called the Weber number, as given in equation 2.46. The numerator is the stagnation pressure and the denominator is the capillary pressure in equation 2.46, where v_c and l_c are the characteristic velocity and characteristic length respectively. The Weber number can be determined either with respect to the tank inlet or the interface.

$$\mathrm{We} = \frac{\rho\, v_c^2}{(\sigma/l_c)} \tag{2.46}$$

The Weber number with respect to the tank inlet We_1 from Symons et al. 1968 [86] is given in equation 2.47.

$$\mathrm{We}_1 = \frac{1}{2}\frac{\rho\, v_I^2\, R_I}{\sigma} \tag{2.47}$$

According to Symons and Staskus 1971 [87], two Weber numbers can be defined based on the velocity profile of the incoming liquid for the case of liquid filling into a partially filled tank. The Weber number for a uniform velocity profile is given as

$$\mathrm{We}_2 = \frac{1}{2}\frac{\rho\ v_I^2\ R_I}{\sigma}\frac{R_I}{R_J} \tag{2.48}$$

and the Weber number for a parabolic velocity profile is defined as

$$\mathrm{We}_3 = \frac{2}{3}\frac{\rho\ v_I^2\ R_I}{\sigma}\frac{R_I}{R_J} \tag{2.49}$$

For an initially empty tank, the radius of the liquid jet at the liquid interface R_J is equal to the inlet radius R_I, ($R_J = R_I$) and the term R_I/R_J in equations 2.48 and 2.49 becomes unity. According to Symons and Staskus 1971 [87], the radius of the liquid jet at the liquid interface R_J is dependent on the spreading angle θ_s of the liquid jet in the bulk liquid, as shown in equation 2.50, where H_J is the height of the liquid jet above the inlet orifice (see figure 2.3). The Reynolds number and the inlet velocity profile of the liquid jet affect the spreading angle of the jet. Symons and Labus 1971 [85] reported that a laminar jet with a parabolic velocity profile spreads with a half-angle of 2° - 3°. Furthermore, for a liquid jet with a uniform velocity profile and a higher Reynolds number (Re > 1500), the spreading angle in the potential core region varies between 6° - 8°, as mentioned in Symons and Staskus 1971 [87].

$$R_J = R_I + H_J\, \tan\theta_s \tag{2.50}$$

The Weber number of the liquid jet at the interface is given in equation 2.51. It can be determined by considering the mean velocity of the jet v_J and the radius of the jet R_J at the interface.

$$\mathrm{We}_4 = \frac{1}{2}\frac{\rho\, v_J^2\, R_J}{\sigma} \tag{2.51}$$

If the stagnation pressure is much lower than the capillary pressure, the liquid jet does not disturb the interface and its momentum is dissipated in the bulk liquid. This results in a nearly unperturbed and stable liquid interface. If the stagnation pressure is in the same order as the capillary pressure, the jet perturbs the interface and a geyser is formed. As long as the geyser remains intact and does not disintegrate into droplets, the liquid interface remains stable. If the stagnation pressure exceeds the capillary pressure, the geyser breaks into droplets, new surfaces are created and the liquid interface becomes unstable.

2.7 Rayleigh-Plateau instability

A liquid jet contains small perturbations as it exits the inlet pipe. These perturbations cause sinusoidal waves, which grow with time and create regions of positive and negative curvature in the liquid jet. These curvatures in the liquid jet lead to pinched and bulged segments, in which the liquid jet contracts and expands respectively. Smaller droplets are formed from the pinched segments, while the bulged segments give rise to larger droplets. Due to the instability called the Rayleigh-Plateau instability, the liquid jet becomes unstable and breaks up into droplets at its critical length, which is given by Kneer et al. 2014 [49] in equation 2.52. R_{ju} is the radius of the unperturbed liquid jet.

$$L_{cr} = 2\pi R_{ju} \tag{2.52}$$

The breakup time t_{cr} can be determined using the equation 2.53 from Eggers and Villermaux 2008 [31]. It can be noted that the liquid jet breaks up into droplets faster, as the surface tension of the liquid increases.

$$t_{cr} = \sqrt{\frac{\rho R_{ju}^3}{\sigma}} \tag{2.53}$$

According to Bush 2010 [14], the growth of perturbations depends on its wave number k by the relation $kR_{ju} < 1$. The fastest growth of perturbations occurs with the following conditions:

$$kR_{ju} = 0.697 \tag{2.54}$$

$$\lambda_{max} \approx 9.02 R_{ju} \tag{2.55}$$

where λ_{max} is the maximum wavelength of the perturbation. Eggers and Villermaux 2008 [31] reported that the decay of a jet can be scaled using the perturbation amplitude, wave number, Weber number and Ohnesorge number. The Ohnesorge number, as given in equation 2.56, describes the influence of viscosity, inertia and surface tension on the jet breakup.

$$\mathrm{Oh} = \sqrt{\frac{\rho\,\nu^2}{\sigma\,R_{ju}}} \tag{2.56}$$

2.8 Problem description

The generic drawing of an axisymmetric cylindrical tank considered for the interface stability study in the drop tower experiments of this thesis is shown in figure 2.4. The tank has an inner radius R_T and a height H_T. The tank has an outlet port of radius R_O. A circular plate (also called a velocity control plate (VCP)) of radius R_{VP} is fitted inside the tank. A hole of radius R_I is drilled on the circular plate and an inlet pipe of radius R_I is connected to it. Because of using the circular plate, two types of liquid injection into the tank are possible. The primary liquid inlet is the centre hole of the VCP. The secondary liquid inlet is the annular gap between the tank wall and the VCP. The length of the primary inlet pipe L_I is selected according to equation 2.37 for laminar flow from White 2011 [99], such that the velocity profile of the liquid jet at the exit of the inlet pipe is fully developed.

The tank coordinate system is at the centre of the primary inlet orifice, denoted by a dot in figure 2.4. The initial fill height of the liquid H_L and the height of the tank H_T are measured from the axis. H_I is the height of the liquid interface in microgravity at the start of liquid filling. η_c is the centre point of the liquid interface, whose location is marked in figure 2.4 by a solid square in normal gravity and by a solid triangle in microgravity. The mean velocity of the liquid at the inlet is v_I.

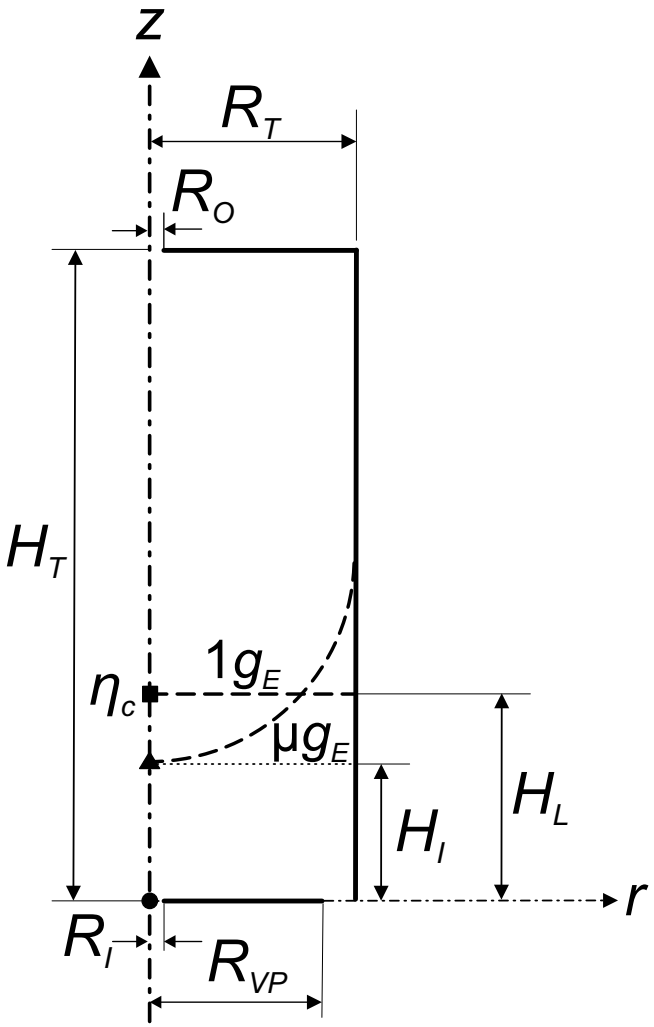

Figure 2.4: Generic drawing of the experiment tank. The length of the inlet pipe L_I is not shown.

2.9 Dimensional analysis

Dimensional analysis is carried out to scale the filling process of the tank shown in figure 2.4. The penetration of the liquid interface by an incoming liquid jet can be described using the Weber number. The liquid jet that enters the tank through the inlet spreads in the bulk liquid before reaching the liquid interface. As the spreading angle of the liquid jet in the bulk liquid could not be measured in the drop tower experiments, the Weber number definition according to equation 2.49 could not be considered for this study.

Therefore, the Weber number according to equation 2.47 is considered for this study. The liquid interface remains stable as long as the capillary pressure balances the stagnation pressure. It becomes unstable when the liquid jet momentum is notably higher than the capillary pressure. This results in the penetration of the interface, the formation of a geyser and the disintegration of the geyser into droplets. The Weber number at the tank inlet is repeated here and denoted as the first Π-parameter.

$$\mathrm{We}_1 = \Pi_0 = \frac{1}{2}\frac{\rho\, v_I^2\, R_I}{\sigma} \tag{2.57}$$

The initial fill height of the liquid inside the tank is expressed in dimensionless form as a ratio with the inlet radius in Π_1.

$$\Pi_1 = \frac{H_L}{R_I} \tag{2.58}$$

The ratio Π_2 is formed by relating the radius of the inlet R_I to the radius of the tank R_T.

$$\Pi_2 = \frac{R_I}{R_T} \tag{2.59}$$

The mean velocity at the inlet is defined as the ratio of the volumetric flow rate and the inlet cross-sectional area.

$$v_I = \frac{Q_L}{A_I} \tag{2.60}$$

The cross-sectional area of the inlet can be calculated using $A_I = \pi R_I^2$. The displacement of the centre point of the liquid interface due to the penetration of the liquid interface is governed by the maximum velocity (also called the centreline velocity) of the incoming liquid jet. This maximum velocity is determined by the shape of the velocity profile of the liquid jet at the exit of the inlet pipe. Therefore, another dimensionless number Π_3 is formed, which characterizes the velocity profile of the liquid jet.

$$\Pi_3 = \frac{v_{max}}{v_I} \tag{2.61}$$

In order to compare the critical Weber number from this study with the existing literature, another dimensionless number Π_4 is introduced in equation 2.62.

$$\Pi_4 = \frac{H_I}{R_I} \tag{2.62}$$

The initial height H_I is the height of the interface above the inlet at the beginning of the liquid filling in microgravity. This differs from H_L due to the reorientation of the liquid interface upon the step reduction of gravity. The Reynolds number predicts the flow pattern by comparing the inertial and viscous forces. The inlet Reynolds number is calculated using the radius of the inlet R_I and the mean velocity of the liquid at the inlet v_I.

$$\mathrm{Re}_1 = \Pi_5 = \frac{2\,\rho\, v_I\, R_I}{\mu} \tag{2.63}$$

The final Π_6-parameter is a combination of Π_0 and Π_3, which is the centreline Weber number at the exit of the inlet pipe (tank inlet).

$$\Pi_6 = \Pi_0\, \Pi_3^2 = \frac{1}{2}\frac{\rho\, v_{max}^2\, R_I}{\sigma} \tag{2.64}$$

With the help of the Π-numbers discussed above, the interface stability during the filling of a tank can be described and compared with the existing literature.

Chapter 3

State of the Art

This chapter presents the review of literature on the topics of propellant depots, liquid filling, interface stability and liquid reorientation under reduced gravity. A table summarizing the important parameters from the experimental studies of interface stability is also presented.

The contents in sections 3.3 and 3.4 of this chapter have been published in Govindan and Dreyer 2023 [40] and reused here with permission.

3.1 Propellant depots

To accomplish a long-range and long-term space exploration return mission from Earth, an enormous amount of propellant will be required. The propellant requirement poses a big challenge to the design of spacecraft for space exploration missions. The cryogenic propellants are considered to be best suited for space exploration missions because of their higher specific impulse and better performance than the other types of propellants. Building fuel depots in space to store propellants has been seen as a viable option to meet the propellant requirements for space exploration missions. The propellant depot may initially be empty during the launch from Earth and can be filled on-orbit. The cryogenic propellants such as liquid hydrogen, liquid oxygen and liquid methane may be stored in the propellant depot. Once the orbiting spacecraft docks to the propellant depot, the supply of gas-free cryogenic propellant can be enabled from the propellant depot to the spacecraft fuel tank using propellant management devices mounted inside the propellant depot. In this way, the spacecraft tanks can be refilled on-orbit and the spacecraft can fly to its destination. An extensive review of the literature on propellant depots is carried out below.

Bruns et al. 2020 [12] proposed an experiment called Future-oriented Research platform for Orbital cryogenic Storage Technologies (FROST), which was planned to be a payload on board the DLR satellite "CompSat". The experiment aimed to demonstrate the storage, transfer and behaviour of liquid nitrogen under microgravity using a storage tank, transfer line and an experiment tank. Both nitrogen and helium pressurization were intended to be tested

during the experiment. Perrin and Casler 2016 [71] conducted a study to assess different architectures for a propellant depot that will be supplied from the Moon. The locations in which the propellants will be processed, stored and transferred were considered along with the method of propellant transfer as factors for the study. It was reported that the ideal location for an orbiting propellant depot will be the Earth-Moon Lagrange point L1. Moreover, the operation of a propellant depot strongly depends upon the amount of propellant consumption and losses. Chai and Wilhite 2014 [15] developed a thermal model of an orbital propellant depot and studied how the overall system mass is affected by the active and passive thermal management systems. It was shown that lower boil-off rates can be achieved when active cryocoolers are used, as compared to multi-layer insulation (MLI). However, in order to have a propellant depot with a zero boil-off (ZBO), the power requirements for a cryocooler will be $80 - 100\,\mathrm{W}$ at $80\,\mathrm{K}$ for liquid oxygen and $100 - 120\,\mathrm{W}$ at $20\,\mathrm{K}$ for liquid hydrogen, which are higher by an order of magnitude than what is available currently. Therefore, there is a need for further development of cryogenic thermal management technology to accomplish space exploration missions.

DeLee et al. 2014 [25] discussed the concept of Cryogenic Propellant Storage and Transfer Technology Demonstration Mission (CPST-TDM) to demonstrate the technologies related to propellant storage, transfer and orbital servicing of satellites. The mission was later transformed from a technology demonstration under space conditions to a technology demonstration under normal gravity conditions. The new project was called Evolvable Cryogenics (eCryo). Schweickart 2014 [76] simulated the cryogenic propellant transfer, which was intended to be part of the CPST mission. Thermodynamic models developed in SINDA/FLUINT were used for the simulations and the models were verified with the ground experiment data of no-vent transfer of liquid hydrogen. McLean et al. 2011 [64] described a design of a propellant depot to store and transfer liquid hydrogen or liquid oxygen, which is conceptualized as the Cryogenic Orbital Test (CRYOTE). Cryogenic fluid management (CFM) under reduced gravity and storage of cryogenic propellants without any losses will support all manned and unmanned missions beyond low-earth orbit (LEO). The transport of cargo and fuel between propellant depots in LEO and geosynchronous orbit (GEO) or Lagrange points can be performed using the space resident transfer vehicles. Furthermore, the paper reported that the technology demonstration mission on propellant depots can be accomplished either by launching CRYOTE as a secondary payload or by launching a simple depot on a single Atlas flight.

Smitherman and Woodcock 2011 [80] discussed the infrastructure of propellant depots that could be developed to support future space missions to the Moon and Mars. Low-earth orbit (LEO), Earth-Moon Lagrange point (L1) and Mars orbital depot were highlighted as the three possible locations for the propellant depots. While the LEO depot will be primarily used for the missions to service the satellites, the L1 depot will be necessary for the missions to the Moon and Mars. All the missions to the Martian surface will be supported by the Mars orbital depot. The authors presented new design concepts for reusable vehicles and also recommended that 7 launches will be needed for a lunar mission and for a Mars mission, the number of launches required will be about $14 - 21$, when the Expendable Launch Vehicle (ELV) is used. The importance of developing technologies that help in building reusable in-space systems was also pointed out. Baine et al. 2010 [4] stated that the unrestricted access to the Moon and the possibility to generate solar power continuously make the Earth-Moon Lagrange point L1

the best position for having the propellant depot. The L1 depot can be operated along with a Crew Exploration Vehicle (CEV) and a lunar lander for a lunar surface mission. Although there are various choices of the propellant to be stored at the depot, liquid oxygen and liquid methane are preferred, due to the advancement in the technology. Mustafi et al. 2010 [69] proposed a technique to enhance the storage duration of cryogenic propellants in space. An isobaric subcooling can be performed at atmospheric pressure on the cryogenic propellant at the launchpad using the Thermodynamic Cryogen Subcooler (TCS). The subcooled propellant has an increased ability to absorb heat, due to its higher heat capacity. The TCS consists of a pump, heat exchanger, Joule-Thomson valve, compressor and an insulation system.

A plan to develop a propellant depot based on the Cryogenic Orbital Test (CRYOTE) and Advanced Common Evolved Stage (ACES) was proposed by Zegler and Kutter 2010 [100]. The authors also pointed out that the Earth-Moon Lagrange point L2 will be the gateway to the solar system and it is the best location for storing the propellants. Gaebler et al. 2009 [35] analysed different lunar transport architectures and proposed an architecture consisting of an orbital propellant depot, reusable transit vehicle and reusable lunar lander. This architecture will reduce the operating cost by 30 % for a lunar surface mission. Goff et al. 2009 [39] assessed the different concepts of the propellant depots from the industry and also the planned experiments to demonstrate the technologies associated with the depots. The authors pointed out that the technology is fairly mature and can be implemented for the propellant depots in the near-term. Chato 2008 [20] reviewed the issues related to cryogenic orbital transfer and emphasized the requirement for an on-orbit demonstration of technologies. Kutter et al. 2008 [55] proposed a propellant depot that need not be assembled on-orbit. Evolved Expendable Launch Vehicle (EELV) can be used to launch the depot. It was reported that the minimum requirement for a lunar mission is 77 t, but Ares V can only deliver 69 t to Earth escape velocity. 40 t of liquid oxygen can be refilled from a propellant depot at the Earth Departure Stage (EDS). The propellant depot could be filled with propellants in the quantity ranging from 1 t to 100 t at a time.

Chandler et al. 2007 [16] estimated the requirements for a propellant depot at the low-earth orbit or the Earth-Moon Lagrange point 1. They assessed the different operational concepts and configurations of depots and the technologies associated with them. It was reported that the propellant depots will help to increase the mass of the payload and to prolong the lifetime of a mission. A study was conducted on the development of an architecture for a propellant depot by Fikes et al. 2006 [32] to find out the requirements and concepts of propellant depots. Howell et al. 2006 [46] pointed out the importance of cryogenic fluid management in low gravity for developing in-space cryogenic propellant depots (ISCPD). Street 2006 [82] developed a scalable tool to design the propellant depots. The input parameters for the tool are the following: type of propellant, remaining propellant mass at the end of storage time, storage time, tank size and material, ratio of oxidizer and fuel and zero boil-off option. The tool provides the geometry and mass breakdown as output. Although the tool could be improved further, it primarily highlighted the benefits of having a propellant depot.

Kutter et al. 2005 [54] described the development of the Integrated Common Evolved Stage (ICES) by Lockheed Martin to fulfill the requirements of space exploration. The ICES, which is an advancement of the Centaur, also supports the in-space propellant depot and a Mars

propellant depot. According to Schuster et al. 1990 [75], NASA planned an orbital experiment in the late 1990s called the Cryogenic On-Orbit Liquid Depot Storage, Acquisition and Transfer Satellite (COLD-SAT) to demonstrate the orbital storage and transfer of liquid hydrogen under low gravity conditions. The experiment module was equipped with three tanks to test the fluid transfer. The aim was to gather in-space experimental data to advance the cryogenic fluid management technology. However, the mission was dropped.

The requirement for a space propellant depot has been clearly highlighted by several authors and it can be seen that a lot of work has been done in advancing the technology of propellant depots further. Although no propellant depot has been built in space so far, orbiting propellant depots can be realized using reusable space transport systems in possible locations like low-earth orbit or Earth-Moon Lagrange point L1.

3.2 Liquid filling

The vented and no-vent filling of tanks have been investigated experimentally, analytically and numerically in the past. They are discussed in this section.

Ma et al. 2017 [61] performed numerical simulations of no-vent filling of liquid hydrogen under microgravity conditions, which was based on the ground experiments of Moran et al. 1991 [67]. It was reported that better vapour-liquid mixing could be achieved in microgravity than in normal gravity and there was no influence of the inlet configuration on the no-vent filling in microgravity. Furthermore, the initial wall temperature was found to be significant only at the beginning of the filling process and the inlet liquid temperature should be sub-cooled to reduce the tank pressure. Flachbart et al. 2013 [33] conducted a feasibility study of the Advanced Shuttle Upper Stage (ASUS) concept by performing vented and no-vent fill experiments with liquid hydrogen under normal gravity conditions. The main objective of the experiment was to chilldown the tank wall while filling the tank within 5 min. The liquid was filled using a spray bar into a cylindrical tank with elliptical domes having a volume of $18\,m^3$. Film boiling occurred at the tank wall, which hindered the chilldown of the wall. A delayed chilldown led to a higher residual energy inside the tank, which affected the closure of the vent valve. The authors suggested that forced convection reduces the film boiling and the use of thin film coatings improves the tank chilldown. Majumdar 2013 [62] modelled the no-vent chill and fill process of a liquid hydrogen tank using the Generalized Fluid System Simulation Program (GFSSP) tool. Both the charge-hold-vent process and the chilldown of a transfer line were simulated using the node models. The node models were validated with the K-site test data and it was found that the model precisely predicts the propellant consumption and chilldown time.

Wang et al. 2011 [96] performed ground experiments to compare the results of no-vent and vented filling of a cryogenic cylinder with liquid nitrogen. Different inlet configurations comprising of top nozzle, bottom nozzle and top spray were tested for the no-vent filling. The vented filling tests were performed only with the bottom nozzle. The pressure variation was observed in two distinct regions during the vented filling, while the no-vent filling led to a pressure variation occurring in three distinct regions. It was reported that the

thermodynamic state of the receiver tank depends on the inlet configuration. Furthermore, the results and correlations could not be directly compared between no-vent and vented filling. The liquid-vapour interface area was calculated as a function of liquid height by Wang and Wang 2010 [97]. No-vent filling of liquid nitrogen into a tank with horizontal and vertical orientations was tested under normal gravity conditions. It was concluded that the horizontal orientation of the tank resulted in a higher fill volume than the vertical one. This was mainly because of the larger liquid-vapour interface area in the horizontal tank, which increases the condensation rate of the vapour and in turn helps in achieving better filling performance. Chato 1993 [19] conducted no-vent filling of liquid hydrogen with a bottom orifice and spray bar as inlet configurations under normal gravity conditions. Interaction of the liquid and vapour phases and ullage condensation could be achieved in both the inlet configurations. The ground test results showed good agreement with the results from a thermodynamic equilibrium model. The saturation temperature was the most influential parameter in the filling tests.

Moran and Nyland 1992 [66] performed ground experiments of no-vent filling of liquid hydrogen. A spray nozzle and a spray bar were used for injecting the liquid into the experiment tank. A final fill volume of more than 90 % could be achieved in most of the tests, independent of the liquid inlet configuration. However, the spray nozzle helped to reduce the tank pressure better than the spray bar. A combination of both spray nozzle and spray bar was recommended for low gravity applications. Taylor and Chato 1992 [90] developed a thermodynamic equilibrium model based on the test data of the no-vent filling of liquid hydrogen into a tank having a volume of 4.96 m^3. This model predicted the test results better than the droplet heat transfer model (NVFIL), which was developed earlier. No-vent filling of liquid hydrogen into a 4.96 m^3 tank was carried out under normal gravity conditions by Chato 1991 [18]. The liquid was sprayed into the tank from the top and bottom of the tank. The maximum final fill volume that was reached was more than 94 % and the maximum internal pressure of the tank was less than 0.18 MPa. The liquid could be filled into the tank even with an initial wall temperature of 126 K.

Honkonen et al. 1991 [45] developed the General Dynamics No-Vent Fill program (GDNVF) to model the chilldown and no-vent filling processes. The program was compared with the ground tests of no-vent filling of liquid hydrogen into a cylindrical tank. Although the initial pressure rise was over-predicted by the model, the overall trend of the tank pressure matched well with the test data. Moran et al. 1991 [67] also tested the no-vent filling of liquid hydrogen into a tank with three different liquid injection techniques (top spray, upward pipe discharge and bottom diffuser) under normal gravity conditions. The tank pressure, temperature and fill levels were measured continuously during the no-vent filling tests. The tank could be filled up to a level of 90 % with a maximum pressure of 2 bar. Spraying the liquid from the top of the tank was reported as the best liquid injection technique. It was observed that the tank pressure increases as the liquid inlet temperature and tank wall temperature increase and the inlet flow rate decreases. Furthermore, the final fill level exhibits a direct proportionality with the inlet liquid flow rate and an inverse proportionality with the tank wall temperature and inlet liquid temperature.

Schmidt et al. 1991 [73] conducted ground experiments of no-vent fill of the cryogenic simulant Freon-114. It was noticed that filling the liquid from the top of the tank has the highest filling

performance due to an agitated liquid interface. The test data matched well with the FILL model predictions of the transient behaviour. Vaughan and Schmidt 1991 [94] developed the FILL code to analytically model the no-vent fill process under normal gravity conditions. It was shown that the transient behaviour of the state properties predicted by the analytical model was in good agreement with the test data. Furthermore, the condensation rates calculated from the FILL model by applying the test data also matched well with the universal submerged jet theoretical prediction. No-vent filling was analysed experimentally and analytically by Vaughan et al. 1991 [93]. The test liquid Freon-114 was filled into the experiment tank, whose internal height was approximately twice its diameter. Different types of inlet configurations were tested and a better performance was observed with the top fill configuration. An existing thermodynamic model (FILL) was enhanced and an empirical relation for the condensation rate was derived.

The thermodynamics of a no-vent fill process was modelled analytically by Chato 1988 [17] in two parts. The first part was the liquid flashing and the second part was the vapour condensation and compression. The vapour condensation and compression were implemented into the model by considering a three-node system of liquid, gas and interface. The equations of two parts were solved using the NVFILL algorithm. This model was later improved by Taylor and Chato 1991 [89]. The liquid spray getting partially vaporized as it enters the tank and the bulk liquid heating up due to the parasitic heat were implemented in the new model. The results from the improved model were compared with the experiment data. Moran et al. 1990 [68] conducted no-vent fill tests of liquid nitrogen and liquid hydrogen at the Liquid Transfer Cryogenic Test Facility of the NASA Lewis Research Center. The liquid was sprayed from the top of the tank through a 120° cone nozzle. Although no-vent filling of liquid hydrogen was more challenging than liquid nitrogen, a final fill volume of more than 90 % was achieved in the tests. The inlet temperatures that led to the highest fill volume were 79.4 K for liquid nitrogen and 18.9 K for liquid hydrogen respectively. Three distinct regions of pressure variation were observed in the no-vent fill tests and the pressure variation was mostly influenced by the incoming liquid temperature. Gille 1986 [38] analysed the no-vent transfer of cryogenic liquids using the Cryogenic Systems Analysis Program (CSAM) and found that the no-vent transfer depends on the fluid properties and tank size. The transfer becomes more difficult with decreasing liquid temperature. Furthermore, Gille 1986 [37] reported that the liquid injection after the centrifugal positioning of the bulk liquid results in a better no-vent transfer, as it is independent of the tank size and gravity effects. Although the centrifugal positioning method is more complicated, it offers an advantage of faster transfer of cryogenic liquids.

The liquid filling experiments under normal gravity conditions have been carried out predominantly using the no-vent fill method and with liquid hydrogen as the test liquid. The influence of the type of the inlet configuration on the final fill volume is evident. While spraying the liquid from the top of the tank was recommended by Moran and Nyland 1992 [66], Moran et al. 1991 [67] and Chato 1991 [18], filling the tank from the top using a liquid jet was shown by Schmidt et al. 1991 [73] and Vaughan et al. 1991 [93] as the suitable technique to achieve best fill performance. The tank chilldown and the filling process have been studied analytically using the node models and compared with some ground test data.

3.3 Interface stability

The behaviour of the liquid jet entering a tank and its interaction with the liquid-gas interface under reduced gravity conditions should be studied to achieve a higher fill performance. Furthermore, the stability limit of the interface and different flow regimes should be identified, in order to choose the optimal filling condition based on the requirement. This section reviews the literature on interface stability during the filling of a tank, which includes both experimental and numerical studies.

The transfer of liquids under microgravity conditions has been investigated in various studies conducted at the Lewis Research Center. Symons et al. 1968 [86] investigated the interface stability during liquid inflow into an empty hemispherical-ended cylindrical tank under microgravity conditions. In this study, a non-dimensional number called the Weber number was defined, as shown in equation 3.1. The Weber number is defined as the ratio of stagnation pressure to capillary pressure. An approximation of the capillary pressure p_c is the ratio between the surface tension of the liquid and the characteristic length l_c: $p_c = \sigma / l_c$. The Weber number is the criterion that delineates the regions of interface stability. Symons et al. 1968 [86] determined the critical Weber number for the filling of an initially empty tank to be $\mathrm{We}_1 = 1.3$. The critical value of the Weber number was also confirmed in a study conducted with larger tanks and larger inlet radii by Symons 1970 [84].

$$\mathrm{We}_1 = \frac{1}{2} \frac{\rho \; v_I^2 \; R_I}{\sigma} \tag{3.1}$$

The study of Symons et al. 1968 [86] was then extended to a partially filled tank with different initial liquid fill heights and different liquids in Symons 1969 [83]. Stable and unstable regions of the interface were noticed and the critical inflow velocity was determined. Symons and Staskus 1971 [87] reported the effect of the velocity profile of the incoming liquid jet and initial liquid height on the critical inflow velocity. Weber numbers for different inlet velocity profiles of the liquid jet were defined for the filling into a partially filled tank, as shown in equation 3.2 for a uniform velocity profile

$$\mathrm{We}_2 = \frac{1}{2} \frac{\rho \; v_I^2 \; R_I}{\sigma} \frac{R_I}{R_J} \tag{3.2}$$

and equation 3.3 for a parabolic velocity profile

$$\mathrm{We}_3 = \frac{2}{3} \frac{\rho \; v_I^2 \; R_I}{\sigma} \frac{R_I}{R_J} \tag{3.3}$$

The radius of the liquid jet at the liquid interface R_J is equal to the inlet radius R_I for an initially empty tank, ($R_J = R_I$) and the term R_I / R_J in equations 3.2 and 3.3 becomes unity. The radius of the liquid jet at the liquid interface R_J is dependent on the spreading angle of the liquid jet in the bulk liquid, as given by equation 2.50 discussed in section 2.6.

Aydelott 1979 [3] conducted drop tower experiments on axial jet mixing of ethanol in a cylindrical tank and observed four different geyser flow patterns. Dominick and Tegart 1981 [28] demonstrated propellant transfer between supply and receiver tanks using vane devices

for different liquids under microgravity conditions. The critical Weber number for a bare tank was $We_1 = 7$, while the interface remained stable for the baffled tank even at $We_1 = 34$. Dominick and Driscoll 1993 [27] discussed the results of the three vented fill tests, which were conducted as part of the Fluid Acquisition and Resupply Experiment (FARE-I) on board the space shuttle STS 53. A spherical tank, that contained a screen channel propellant management device (PMD) and a perforated baffle near the inlet was used to study the stability regime of the liquid interface. A disturbed interface was observed for $We_1 = 5.2$. It was also reported that having the vent tube positioned at the centre of the tank would increase the final fill level of the tank. FARE-II experiments were conducted on board the space shuttle STS 57 and the results are reported in Dominick and Tegart 1994 [30]. In the FARE-II experiment, a standpipe was fitted into the receiver tank and 8 radial vanes were attached to the standpipe. An abrupt transition from stable to unstable flow was observed during the vented fill tests of FARE-II. It was demonstrated that for a stable liquid inflow, the gas can be vented without any loss of liquid, due to the presence of vanes.

Bentz et al. 1997 [6] demonstrated the pressure reduction of the tank with the help of an axial jet mixing of the refrigerant R-113. Several liquid filling tests were conducted with a cylindrical tank having a total volume of 13.7 L. The tests were part of the Tank Pressure Control Experiment (TPCE) performed during the three space shuttle flights. The tests showed that the liquid jet completely penetrates the ullage for $We_2 \geq 3$, when the tank is filled to an initial liquid volume of 39 % of the total volume. For an initial liquid fill volume of 83 % of the total volume, the complete ullage penetration occurred for $We_2 > 5$. Chato and Martin 2006 [22] illustrated the flight test results of the Vented Tank Resupply Experiment (VTRE), where refrigerant 113 was transferred between two tanks and liquid-free venting was accomplished for the tested flow rates. The results of the Zero Boil-Off Tank experiment (ZBOT-1) are reported in Kassemi et al. 2018 [48]. The results of tank ullage penetration by an axial jet at different inflow velocities and different fill levels under microgravity conditions to control the tank pressure were presented and compared with the numerical simulation results. Breon et al. 2020 [11] demonstrated new technologies to store and transfer cryogenic liquids on-orbit during the Robotic Refueling Mission-3 (RRM3). However, due to the malfunction of the cryocooler in the source dewar, the transfer of liquid methane to the receiver dewar could not be accomplished on-orbit. Lei et al. 2023 [57] discussed the design and development of the Tianzhou cargo spacecraft, which has demonstrated the orbital refuelling by providing a propellant supplement to the Chinese space station Tiangong. The test liquids and the tank geometries used in the experiments of interface stability are summarized in table 3.1.

Several numerical studies modelled the jet-induced geyser formation under microgravity, as observed in the experiments of Aydelott 1979 [3]. The mixing of cryogenic propellants induced by a jet in low-gravity was predicted numerically by Hochstein et al. 1984 [43]. Dominick and Tegart 1990 [29] used the FLOW-3D software to predict the liquid behaviour during the filling of tanks in low-gravity. The computational models were validated with the existing experimental data and were also extended to real-scale tanks. Wendl et al. 1991 [98] developed a computational model using the ECLIPSE code and simulated the four geyser patterns of Aydelott 1979 [3], in order to support the space shuttle experiment (TPCE). Thornton and Hochstein 2001 [92] improved the correlations from Aydelott 1979 [3] for the geyser height prediction of turbulent jets. However, these new correlations were

again amended by Simmons et al. 2005 [79] by performing numerical simulations. Marchetta and Benedetti 2010 [63] performed three-dimensional numerical simulations of the jet-induced geysers using ANSYS Fluent and compared the dimensionless geyser height with the experimental data of Aydelott 1979 [3]. Different turbulence models were tested and the jet spread rate was found to influence the geyser height prediction.

Breisacher and Moder 2015 [10] studied the dynamics of the liquid-vapour interface by carrying out numerical simulations using the FLOW-3D software. Ullage shape and movement caused by the jet penetration were qualitatively analysed and compared with the images from the TPCE. Kartuzova and Kassemi 2019 [47] validated the ANSYS Fluent CFD models with ZBOT-1 experiments for predicting the jet-induced mixing and ullage interaction. It was noticed that the jet tilt angle and orientation influence the jet-ullage interaction the most. It was also shown that the ullage shape and position during the jet mixing is predicted well by the LES model better than the RANS model.

Table 3.1: Summary of important parameters from the experimental studies of interface stability in the literature. N/A denotes not available or not applicable.

No.	Author	Test liquids	Tank shape	Tank dimensions/mm			
				R_T	H_T	R_I	R_O
1	Symons et al. 1968 [86]	Ethanol, TCTFE, Butanol	Cylinder	20	80	2	4
2				20	80	4	4
3				30	120	3	4
4				30	120	6	4
5				40	160	2	4
6				40	160	4	4
7				40	160	8	4
8	Symons 1970 [84]	Ethanol, TCTFE	Cylinder	75	300	7.5	N/A
9				150	600	15	N/A
10	Symons 1969 [83]	Ethanol, TCTFE	Cylinder	20	80	2	4
11				40	160	2	4
12	Symons and Staskus 1971 [87]	Ethanol, CCl_4, TCTFE	Cylinder	20	120	2	4
13				20	120	2	4
14				20	120	2	4
15	Aydelott 1979 [3]	Ethanol	Cylinder	50	200	2	N/A

Continued on next page

No.	Author	Test liquids	Tank shape	Tank dimensions/mm			
				R_T	H_T	R_I	R_O
16	Dominick and Tegart 1981 [28]	Isopropyl alcohol, Water, TCTFE	Sphere	63.5	N/A	N/A	N/A
17				50.8	N/A	3.2	N/A
18	Dominick and Driscoll 1993 [27]	Water	Sphere	158.8	N/A	4.8	N/A
19	Dominick and Tegart 1994 [30]	Water	Sphere	158.8	N/A	N/A	N/A
20	Bentz et al. 1997 [6]	TCTFE	Cylinder	127	355.6	5.1	N/A
21	Chato and Martin 2006 [22]	TCTFE	Sphere	177.8	N/A	N/A	N/A
22			Cylinder	158.8	406.4	N/A	N/A
23	Kassemi et al. 2018 [48]	C_5F_{12}	Cylinder	50.8	203.2	2.3	N/A

3.4 Liquid reorientation

Li et al. 2020 [58] performed numerical analyses of the liquid sloshing inside the storage tanks with different fill ratios by considering the dynamic contact angle. Friese et al. 2019 [34] described the theory of reorientation and axial sloshing of liquids inside cylindrical tanks under microgravity conditions. Some isothermal experiments were conducted to study the free surface behaviour under microgravity and the centre point and wall point progressions were plotted to understand the reorientation of liquid inside the tank. Li et al. 2018 [59] conducted drop tower experiments with two types of partially filled cylindrical tubes and compared the experiment results of the centre point evolution and the oscillation frequency of the liquid interface with the numerical simulation results. The liquid reorientation inside the tank under microgravity was also investigated by Li et al. 2013 [60] by carrying out drop tower experiments and numerical simulations.

Schmitt and Dreyer 2015 [74] and Kulev and Dreyer 2010 [53] investigated the liquid reorientation under non-isothermal conditions in microgravity with liquid hydrogen and liquid argon, respectively. Different temperature gradients were applied to the experiment tank wall and their influence on the liquid reorientation was analysed. Krahl and Gerstmann 2007 [51] highlighted the importance of refining the thermal boundary layers for numerically predicting

the reorientation behaviour of the test liquid HFE-7100 in an annular gap under non-isothermal conditions. Gerstmann and Dreyer 2006 [36] performed numerical simulations to predict the oscillations of the liquid interface inside a pre-filled tank under reduced gravity and analytically analysed the frequency and damping of the oscillations. Stief et al. 2005 [81] reported the drop tower experiments of the reorientation of liquid nitrogen and Michaelis et al. 2002 [65] studied the reorientation behaviour of the liquid interface with different test liquids and varying cylinder radii under microgravity conditions. Different timescales that govern the reorientation behaviour were discussed and it was reported that the velocity of the liquid that rises at the wall depends on the Morton number and the static contact angle. Siegert et al. 1964 [78] performed drop tower experiments with tanks of different shapes filled with different test liquids to estimate the time required for the liquid-vapour interface to reach its equilibrium configuration under microgravity conditions.

Although several studies have been carried out on liquid reorientation and interface stability in the past, this thesis work focuses on gathering experimental data on reorientation and filling of a storable liquid into a partly filled cylindrical tank under isothermal conditions. The advancements in the duration of microgravity, image resolution and measurement techniques make the experimental data in this thesis important. The experimental data has also been used to test the modelling capabilities of the flow solver ANSYS Fluent by comparing the 2D simulation results with the experimental data. Furthermore, the interface stability problem during the filling of liquid into a tank has been scaled using dimensionless numbers.

Chapter 4

Experiments

This chapter presents the experiments conducted to investigate the behaviour of the liquid interface and the interface stability during the filling of a tank under normal gravity and reduced gravity conditions. Ground experiments were performed in the laboratory, while reduced gravity experiments were carried out in the Bremen Drop Tower and on board the parabolic flight. The aim of all these experiments was to study the interaction of the liquid jet with the liquid interface and identify the stability criteria for the liquid interface during the filling of a tank.

The contents in section 4.1 of this chapter have been published in Govindan and Dreyer 2023 [40] and reused here with permission.

4.1 Drop tower experiments

The setup, procedure as well as the evaluation of the measured data of the drop tower experiments are described in this section.

4.1.1 Experimental setup

An experimental setup was built and assembled into a drop capsule, as used in the Bremen Drop Tower. The drop capsule consisted of five platforms, as shown in figure 4.1. The uppermost platform 1 housed the camera recorder for the acquisition of high-speed imagery. The second platform from the top was the experiment platform (platform 2), which consisted of the experiment tank and optical systems. The middle platform (platform 3) contained the fluid loop components. The experiment platform was placed at a height of 470 mm from the fluid loop platform, in order to accommodate the long primary inlet pipe for the experiment tank, such that the flow is fully developed and the velocity profile of the liquid jet is parabolic at the tank inlet. The components of the experimental setup assembled on platforms 2 and 3 are also shown in figure 4.1. The bottom two platforms (4 and 5) were allotted for the capsule control system (CCS) and power distribution unit.

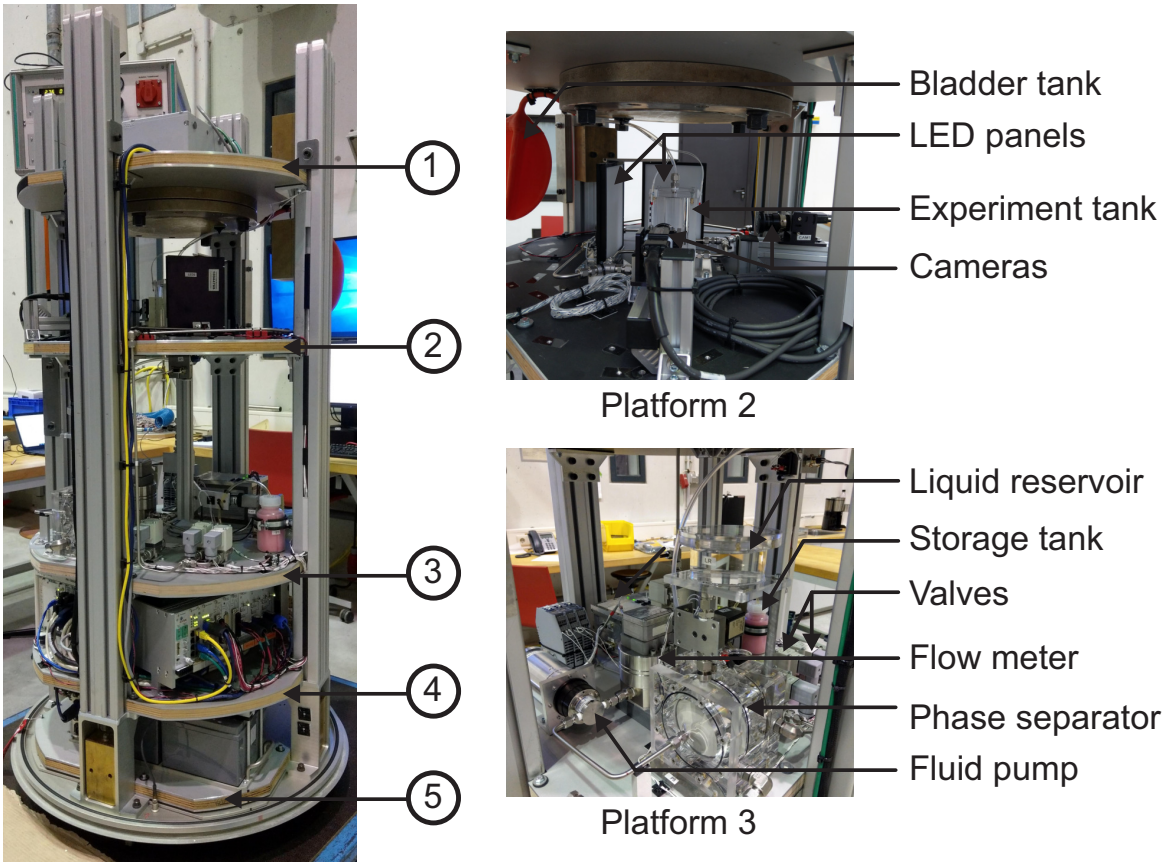

Figure 4.1: The drop capsule of the experimental setup with five platforms. The platforms are named as: 1 - camera recorder, 2 - experiment, 3 - fluid loop, 4 - capsule control system and 5 - power distribution unit. The components assembled on platforms 2 and 3 are also shown.

4.1.1.1 Experiment tank

The experiment tank is the main test article of the experimental setup. An axisymmetric drawing of the experiment tank is shown in figure 4.2. The drawing consists of 20 points and the corresponding r- and z-coordinates of these points are listed in table 4.1. There were two inlet lines to the experiment tank, which were the primary and the secondary inlet. The primary inlet is denoted by points 0, 1, 12 and 14 in figure 4.2. The experiment tank was made up of polymethyl methacrylate (PMMA) material and had a cylindrical cross-section with a height of $H_T = 94\,\text{mm}$ and an inner radius of $R_T = 30\,\text{mm}$. The total empty volume of the experiment tank was 265 mL. An outlet port was provided at the top of the tank to vent the gas. A circular velocity control plate (VCP) with a radius of $R_{VP} = 25\,\text{mm}$ and a thickness of 1 mm was mounted inside the experiment tank, so that two inlet configurations could be tested. The points 2–11 in figure 4.2 represent the secondary inlet, where the liquid enters the tank through an annular gap between the tank wall and VCP. However, in this thesis, only the primary inlet is considered to study the interface stability. The liquid entered the experiment tank directly from the bottom through the primary inlet. The inlet and outlet radii were $R_I = R_O = 2\,\text{mm}$. The length of the primary inlet pipe was $L_I = 220\,\text{mm}$, which was chosen based on equation 2.37 for laminar flow.

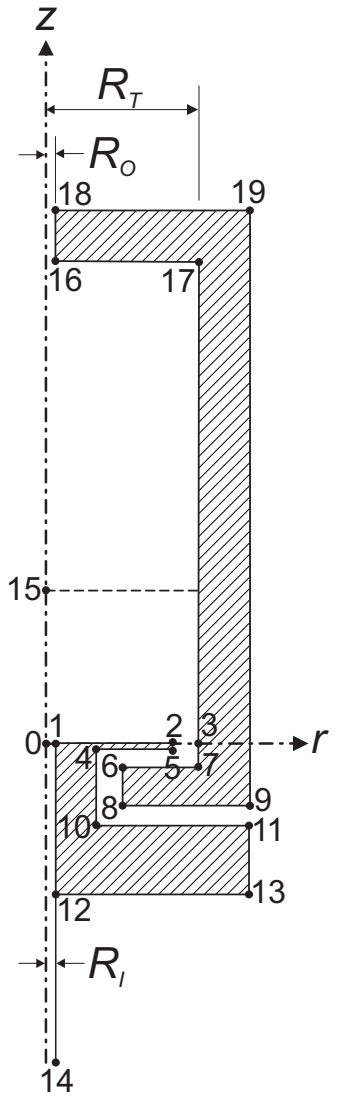

Figure 4.2: Axisymmetric drawing of the experiment tank. The inlet and outlet radii are $R_I = R_O = 2\,\text{mm}$ and the tank radius is $R_T = 30\,\text{mm}$.

4.1.1.2 Fluid loop

The fluid loop of the experimental setup is shown in figure 4.3. It consists of phase separator (PS), liquid reservoir (LR), experiment tank (ET), bladder tank (BT), storage tank (ST), fluid pump (FP) and flow meter (FM). A total of 6 solenoid valves V1 to V6 from the company SMC were used in the setup to control the flow. Valve V2 was normally open and all the other valves were normally closed. The in-house built PS, which was also made up of PMMA, contained two sections with a screen in between. The porous screen element Dutch twilled weave (DTW) 200×1400 was selected, which had an outer diameter of 90 mm. The screen blocks the gas and allows only liquid to pass through between the sections, as long as the bubble point pressure of the screen is not exceeded. The concept of phase separation using a screen element was demonstrated in the experiments conducted by Conrath and Dreyer 2012 [24] and Hartwig 2016 [42]. Bisht and Dreyer 2020 [8] also used the same PS in the parabolic flight experiments. Therefore, in the drop tower experiments, the gas-free liquid was withdrawn from the PS and filled into the experiment tank. The total volume of the PS was 445 mL.

Table 4.1: List of points and their position in radial (r) and axial (z) coordinates. These points describe the axisymmetric model of the experiment tank, as shown in figure 4.2.

Points	r/mm	z/mm
0	0	0
1	2	0
2	25	0
3	30	0
4	10	−1
5	25	−1
6	15	−6
7	30	−6
8	15	−12
9	40	−12
10	10	−16
11	40	−16
12	2	−31
13	40	−31
14	2	−220
15	0	30
16	2	94
17	30	94
18	2	104
19	40	104

The top section of the PS had a gas vent line, through which the gas collected in the gas side of the PS was vented manually before every drop tower experiment. The gas vent line is shown in figure 4.3. The liquid reservoir (LR) was pre-filled and the liquid side of the PS was connected to the LR through valve V6. Any gas bubbles trapped in the liquid side of the PS were removed by opening valve V6. The liquid from the PS was pumped in a closed loop, which consists of FP, FM and valve V2. The gear pump GA-T23 from the company Micropump Inc. was used to deliver the required flow rate. SIKA VZ 0.02 VA was the flow meter used to measure the volumetric flow rate of the liquid. The accuracy of the flow meter specified by the manufacturer was $\pm\,0.3\,\%$ of the measured value. However, the flow meter was calibrated in-house and the calibration measurements showed a maximum deviation of $\pm\,1\,\%$ to the measured mean value.

The Analogue Pressure Transmitter (ATM) pressure sensor (P1) from the company TetraTec Instruments GmbH was used to measure the absolute pressure in the fluid loop. The pressure sensor had an accuracy of $\pm\,2.5\,\mathrm{mbar}$ and measured the absolute pressure between 0 bar and 2.5 bar. PCA-type PT100 sensors from JUMO GmbH & Co. KG were used to measure the temperatures at three locations in the setup, which are marked as T1, T2 and T3 in figure 4.3. The temperature sensors had an accuracy of $\pm\,0.14\,^{\circ}\mathrm{C}$ at $25\,^{\circ}\mathrm{C}$. All the sensors recorded data at a sampling rate of 1000 Hz in the experiments. Both primary and secondary inlet lines consisted of a valve and a temperature sensor.

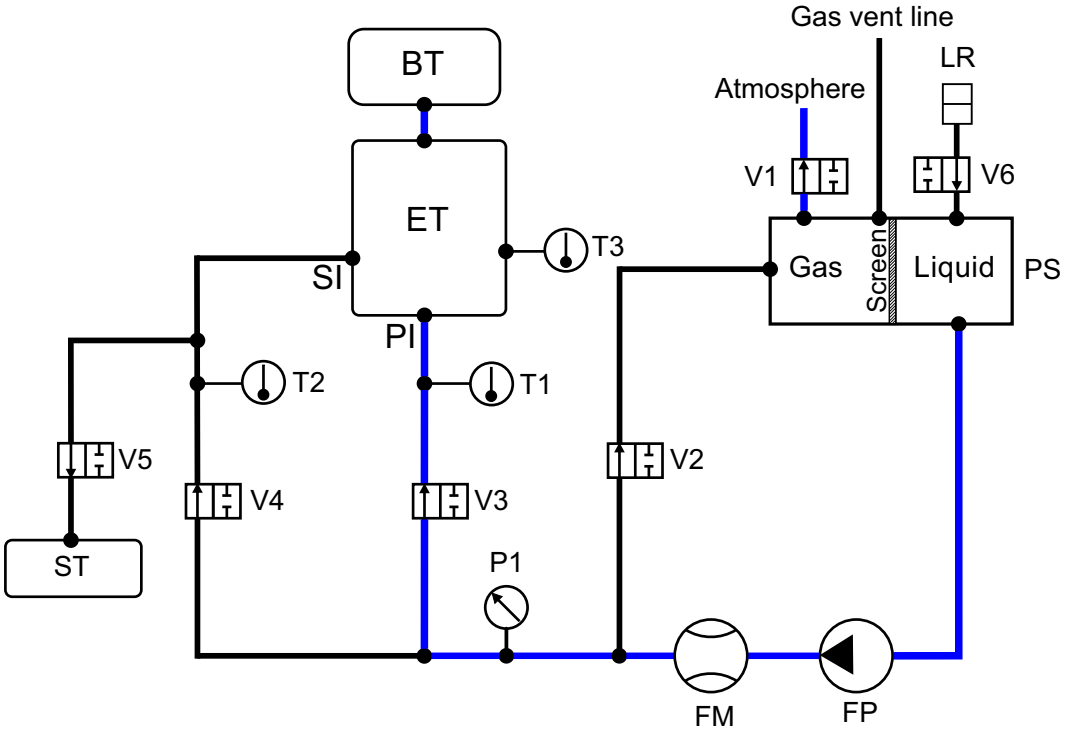

Figure 4.3: The fluid loop of the drop tower experimental setup. PI denotes the primary inlet and SI denotes the secondary inlet. The fluid loop consists of liquid reservoir (LR), phase separator (PS), fluid pump (FP), flow meter (FM), experiment tank (ET), bladder tank (BT), storage tank (ST), valves (V1, V2, V3, V4, V5, V6), temperature sensors (T1, T2, T3) and pressure sensor (P1). The lines activated during the liquid filling experiments are shown in blue colour.

The experiment tank was connected to the bladder tank (BT), which was used to collect any gas that escaped through the outlet port of the experiment tank. Moreover, during the landing of the drop capsule, the BT also helped to collect any liquid that entered the outlet port of the experiment tank. In case of an overfill of the initial liquid fill height, the excess liquid was drained from the experiment tank into the storage tank (ST).

4.1.1.3 Optics

Two high-speed camera heads CAM1 and CAM2 from Photron FASTCAM MC2 were used to record the images at a frame rate of 500 frames per second. The images had a resolution of 512×512 pixels and the recording time was 16.4 s. The recorded images were stored in the camera recorder, also from Photron, which was placed in the uppermost platform of the drop capsule.

CAM1 was equipped with a lens type 2.1/6 − 901 and CAM2 with a lens type 1.4/8 − 902. Both the lenses were from the company Schneider Kreuznach. The cameras CAM1 and CAM2 were placed perpendicular to each other. CAM1 focused on the total view of the experiment tank, while CAM2 captured the ullage region. Two LED panels from the company Stemmer Imaging AG were used as light sources and were placed at a distance of 5 mm behind the experiment tank. Both LED panels emitted red light with a wavelength of 635 nm.

For diffusing the light, a white sheet was attached to the walls of the experiment tank facing the LED panels. A black and white ruler was pasted on the two outer walls of the experiment tank, in order to measure the liquid fill height inside the tank. The experiment tank along with the LED panels, cameras and bladder tank were placed on the experiment platform (platform 2) of the drop capsule (see figure 4.1).

4.1.1.4 Test liquid

The test liquid chosen for the drop tower experiments was the storable liquid 3M Novec Engineering Fluid HFE-7500. It is a perfectly wetting liquid having a contact angle of 0° with the tank wall. Due to the experience and knowledge gained from using this liquid in the previous experiments conducted at ZARM, it was chosen for this set of experiments as well. The properties of the test liquid are listed in table 4.2.

Table 4.2: Properties of the test liquid HFE-7500, as reported in Bisht and Dreyer 2020 [8].

$T_L/°C$	$\rho/\mathrm{kg\,m^{-3}}$	$\mu/10^{-3}\,\mathrm{kg\,m^{-1}\,s^{-1}}$	$\sigma/\mathrm{N\,m^{-1}}$
15.0	1641	1.49	0.0176
20.0	1631	1.37	0.0172
25.0	1620	1.25	0.0167
30.0	1610	1.15	0.0162

4.1.2 Experimental procedure

15 drop tower experiments were conducted in three campaigns between December 2020 and August 2021 in the Bremen Drop Tower. According to Könemann 2022 [50], the drop tower offers two modes of operation: the drop mode with 4.7 s and the catapult mode with 9.3 s of microgravity time. The experiments were divided into two categories as reorientation and filling experiments. Three tests were used to observe the reorientation of the liquid interface under microgravity. The remaining 12 tests were performed to study the interface stability using the primary inlet of the experiment tank, in which each flow rate was tested twice. An overview of the drop tower test matrix of these 15 tests is shown in table 4.3. The drop mode was used only for one reorientation test F15. All the other tests were performed using the catapult mode. It can be noticed from table 4.3 that the measured liquid temperature T_L varies for each test. However, the mean of the liquid temperature from all the tests is $T_L = 25.1\,°C$ and the maximum deviation of the liquid temperatures from the mean temperature is $\pm 3\,°C$. Therefore, the liquid properties corresponding to $T_L = 25\,°C$ have been chosen from table 4.2 for calculating the dimensionless numbers $\mathrm{Re_1}$ and $\mathrm{We_1}$ in table 4.3. The variation of measured temperatures over time are discussed in section 4.1.3.5 for some of the drop tower tests.

As the first step, the liquid reservoir was filled manually by opening the lid. By opening valve V6, the PS was filled from the liquid reservoir. Then, the fluid pump was operated to establish the flow in the closed loop. The desired flow rate was obtained by setting the input set value of the gear pump between 0 V to 10 V. Then, valve V3 was operated to fill the experiment tank to a fill height of $H_L = 33\,\mathrm{mm}$.

Table 4.3: Test matrix of the drop tower experiments. Tests F15, F17 and F31 were reorientation tests without filling. The remaining 12 tests correspond to the study of interface stability during the filling of the experiment tank. The test F15 was a drop test. All the other tests were catapult tests. The flow regime for the filling experiments is also listed. The initial liquid fill height was $H_L = (30 \pm 0.1)\,\mathrm{mm}$.

Serial No.	Test ID	$Q_L/\mathrm{mL\,s^{-1}}$	$T_L/°\mathrm{C}$	Re_1	We_1	$v_I/10^{-3}\ \mathrm{m\,s^{-1}}$	Regime
1	F15	No flow	21.9	No flow	No flow	No flow	No flow
2	F17		24.2				
3	F31		25.5				
4	F08	1.00	24.1	412.53	0.61	79.58	Subcritical
5	F10	1.00	24.0	412.53	0.61	79.58	Subcritical
6	F26	1.09	26.9	449.66	0.73	86.74	Subcritical
7	F11	1.10	22.6	453.78	0.74	87.54	Subcritical
8	F12	1.20	24.8	495.04	0.88	95.49	Subcritical
9	F28	1.20	26.7	495.04	0.88	95.49	Subcritical
10	F24	1.30	24.8	536.29	1.04	103.45	Critical
11	F25	1.30	26.9	536.29	1.04	103.45	Critical
12	F19	1.38	26.0	569.29	1.17	109.82	Supercritical
13	F30	1.38	25.8	569.29	1.17	109.82	Supercritical
14	F22	1.50	25.0	618.79	1.38	119.37	Supercritical
15	F23	1.50	27.0	618.79	1.38	119.37	Supercritical

A higher fill level was required to account for any liquid loss due to evaporation inside the experiment tank, while the drop tower was being prepared for the catapult test. When valve V3 was opened, valve V1 was also opened and valve V2 was closed, such that PS does not get depressurized due to the removal of liquid from it. Valve V1 was exposed to ambient pressure inside the capsule. Any air bubbles in the loop were blocked by the screen and collected in the gas side of the PS, which was removed manually by opening the gas vent line. The liquid reservoir was refilled to a certain fill level and then the capsule was taken into the drop tower.

The fill level was adjusted to $H_L = 30\,\mathrm{mm}$ by operating valve V5 and removing the liquid from the experiment tank and purging it into the storage tank, shortly before the catapult launch or drop of the capsule. In all the experiments, the initial fill height of the liquid inside the tank was set to $H_L = (30 \pm 0.1)\,\mathrm{mm}$. An initial fill height of $H_L = 30\,\mathrm{mm}$ was chosen in such a way that it is equivalent to the tank radius R_T ($H_L/R_T = 1$). The desired flow rate was obtained by setting the corresponding input voltage value to the pump. The cameras were set to record ready. The operation of the experiment was programmed in LabVIEW. The catapult launch or drop of the capsule was triggered by pressing the drop sequence button on the LabVIEW program user interface. The beginning and end of the drop tower experiments were synchronized with the beginning and end of the microgravity time, although the experiment data were logged for a longer duration. In the filling experiments, from $t = 0\,\mathrm{s}$ to $t = 3.5\,\mathrm{s}$ in microgravity, the liquid was pumped in the closed loop, where valve V2 remained open.

During this time, the reorientation of the pre-filled liquid inside the experiment tank took place and the liquid interface approached its final equilibrium configuration in microgravity. At $t = 3.5\,\mathrm{s}$, the filling of the experiment tank commenced by opening valves V3 and V1 and closing valve V2. The filling continued until the end of the microgravity time. At the end of microgravity, valves V3 and V1 were closed and valve V2 was opened to pump the liquid again in the closed loop. The flow meter measured the volumetric flow rate for the whole duration of the experiment. For the reorientation experiments, the pump was stopped after the initial liquid fill height was set in the experiment tank. Therefore, there was no flow of liquid in the fluid loop during the reorientation experiments. The timeline of the drop tower experiments is presented in table 4.4.

Table 4.4: Timeline of the drop tower experiments.

t/s	Catapult test Filling	Catapult test Reorientation	Drop test Reorientation
0	Start of μg_E	Start of μg_E	Start of μg_E
3.5	Start of filling	-	-
4.6	-	-	End of μg_E
9.1	End of μg_E and End of filling	End of μg_E	-

4.1.3 Data evaluation

4.1.3.1 Image processing

Two images of the experiment tank in normal gravity before the catapult launch are shown in figure 4.4 for both cameras CAM1 and CAM2. CAM1 captured the total view of the experiment tank and CAM2 focused on the ullage view. An LED light present in the top left of the images indicated the beginning and end of microgravity time. The point of interest was the centre point of the liquid interface on the z-axis ($r = 0$). Its position was measured from the origin of the experiment tank, which was located at the centre of the inlet orifice, as shown on the left side of figure 4.4.

The images recorded from CAM1 were chosen for the image processing of the reorientation experiment, because the oscillation of the centre point of the liquid interface was completely captured in the total view. The images from CAM2 were used to detect the centre point position in the filling experiments. An image processing function was created in MATLAB, which read the image as a matrix and processed it. The images were cropped according to the regions of interest. The liquid interface was detected using the Sobel edge detection algorithm with an accuracy of ± 1 pixel.

The lowermost edge on the z-axis was detected in the liquid reorientation experiment, which corresponds to the centre point of the liquid interface, as shown in figure 4.5a. The uppermost edge on the z-axis was detected for the filling experiment. This is due to the penetration of the interface by the incoming liquid jet and the formation of a geyser. This can be noticed in figure 4.5b.

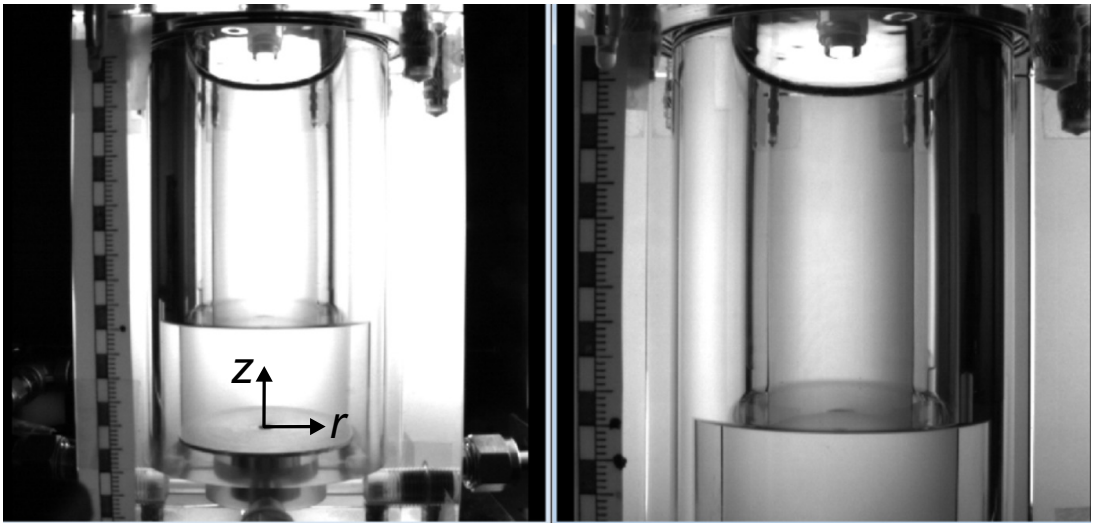

Figure 4.4: The camera views of the experiment tank in normal gravity with $H_L = (30 \pm 0.1)\,\text{mm}$. CAM1 captured the total view (left) and CAM2 captured the detailed view (right).

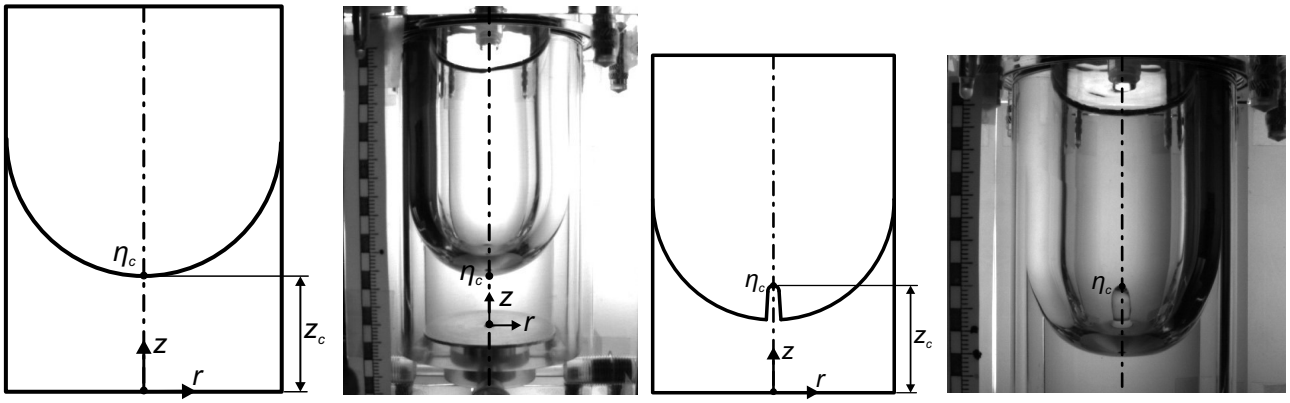

(a) Reorientation experiment (b) Filling experiment

Figure 4.5: Detection of the centre point of the liquid interface. A drawing depicting the centre point detection is on the left and the image from the experiment is on the right of each figure.

The raw pixel values corresponding to the detected edge were then converted to length scale using the transformation functions obtained from the calibration tests of the cameras. The calibration of images and transformation functions are elaborated in appendix sections A.1 and A.2 respectively. The image resolution on the z-axis was 4 pixels per millimetre for CAM1 and 5.5 pixels per millimetre for CAM2 respectively.

Due to the refraction of light, these transformed length scale values had to be corrected using two correction factors. An extensive ray tracing method, as described in Kulev 2020 [52], was carried out. The ray tracing method, that was applied to correct the measured centre point of the interface, is described in detail in appendix section A.3. The initial liquid fill height H_L inside the experiment tank in normal gravity was also obtained from the CAM1 images. The correction of the initial liquid fill height is explained in appendix section A.4. The measurement error of the centre point of the interface was $\pm\,0.3\,\text{mm}$ for CAM1 and $\pm\,0.2\,\text{mm}$ for CAM2 respectively.

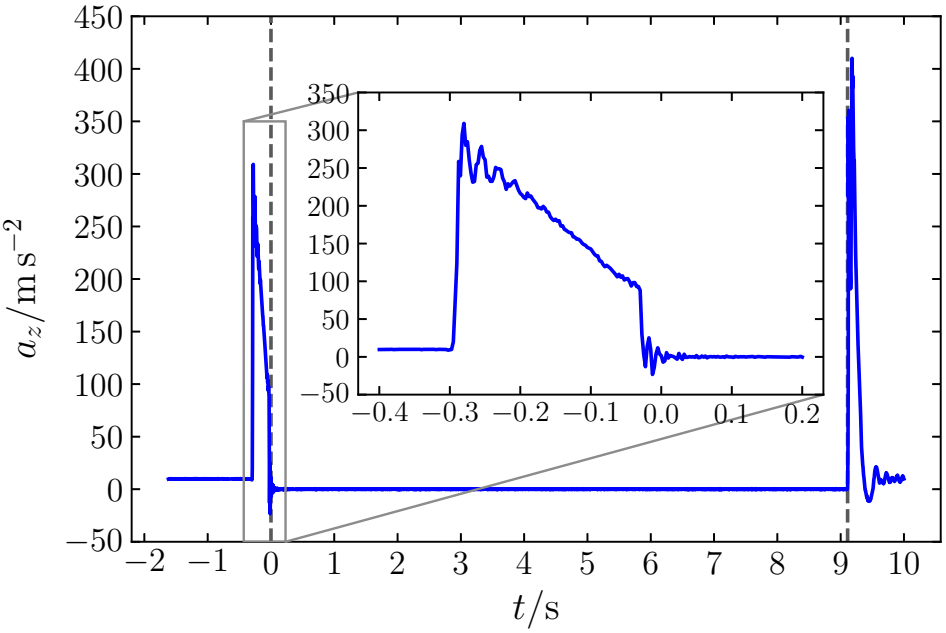

Figure 4.6: z-axis acceleration of the drop capsule for the catapult test F19. The first vertical dashed line denotes the beginning of microgravity and the second vertical dashed line denotes the end of microgravity. The z-axis acceleration profile before and after the beginning of microgravity is shown in the inset.

4.1.3.2 Acceleration measurement

An inertial measurement unit (IMU) from the company iMAR Navigation GmbH was mounted in the drop capsule, which measured the acceleration with a sampling rate of 400 Hz, as reported in Könemann 2022 [50]. Figure 4.6 shows the z-axis acceleration of the drop capsule for the test F19. The beginning and end of microgravity are marked by vertical dashed lines in figure 4.6. The capsule experiences a high acceleration of about $310\,\mathrm{m\,s^{-2}}$ during the catapult launch, which lasts for approximately 0.3 s. During the landing in the deceleration chamber at the end of microgravity, the capsule is again subjected to a high acceleration of about $410\,\mathrm{m\,s^{-2}}$.

4.1.3.3 Flow rate measurement

The flow meter was calibrated in-house and the volumetric flow rate as a function of the voltage output of the flow meter was obtained. This function was later used to convert the flow meter voltage output from the experiments to the volumetric flow rate. A moving average with an interval of 100 was performed on the original experiment data, which had a sampling rate of 1000 Hz. These moving averages of the volumetric flow rate are plotted over time in figure 4.7 for four different tests. The flow rates are plotted from $t = 0\,\mathrm{s}$ to $t = 9\,\mathrm{s}$ in microgravity. The vertical dashed line indicates the opening of valve V3 to fill the experiment tank. The valve operation causes fluctuations in the flow rate and these fluctuations dampen after $t = 5\,\mathrm{s}$. Therefore, the time-averaged volumetric flow rate is calculated between $t = 5\,\mathrm{s}$ and $t = 9\,\mathrm{s}$. This is the mean volumetric flow rate Q_L considered for the calculation of the dimensionless numbers. The mean volumetric flow rates obtained from the drop tower experiments helped to choose the range of volumetric flow rates for the numerical simulations.

The mean volumetric flow rates from the experiments were compared with the calibrated values and the deviation was found to be under 3 %.

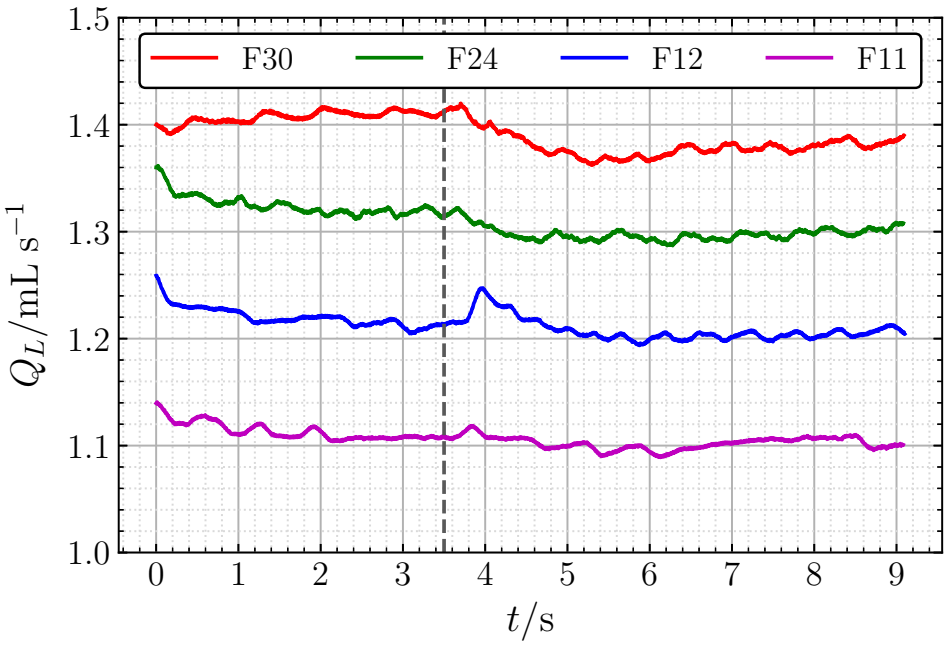

Figure 4.7: The progression of volumetric flow rate Q_L over time in microgravity. The vertical dashed line indicates the start of the liquid filling into the experiment tank.

4.1.3.4 Pressure measurement

The absolute pressure was measured in the filling line to the experiment tank using the pressure sensor P1. The absolute pressure values from the two tests F12 and F28 are plotted in figure 4.8. The first vertical dashed line from the left represents the start of microgravity at $t = 0\,\mathrm{s}$. The second and third vertical dashed lines represent the operation of valves V1 and V3, respectively. A sudden peak in the pressure before $t = 0\,\mathrm{s}$ is due to the catapult launch of the drop capsule, where the hypergravity causes an increase in pressure in the fluid loop. When the capsule enters microgravity, this high pressure relaxes and remains above 1 bar.

The penetration of the liquid interface by the incoming jet and the breakup into droplets immediately after valve V3 was operated at $t = 3.5\,\mathrm{s}$ were observed in tests F08, F10, F11 and F12. This rapid penetration of the liquid interface was caused by the high pressure in the fluid loop which remained above 1 bar and dropped to 1 bar only after the operation of valve V3, as shown in figure 4.8 for the test F12. This effect was later mitigated in all the other filling tests by operating valve V1 at $t = 3\,\mathrm{s}$, $0.5\,\mathrm{s}$ prior to the opening of valve V3. This relaxed the pressure to around 1 bar before the filling of the experiment tank began. This effect is compared between tests F12 and F28 in figure 4.9. Some liquid droplets can be seen moving towards the tank outlet in test F12, whereas in test F28, this was not observed. The mean volumetric flow rate was $Q_L = 1.20\,\mathrm{mL\,s^{-1}}$ in both tests F12 and F28. Some fluctuations in the pressure can be observed at $t = 3.5\,\mathrm{s}$, when the valve V3 is operated and the filling begins. A constant pressure value is maintained in the filling line to the experiment tank after $t = 4\,\mathrm{s}$.

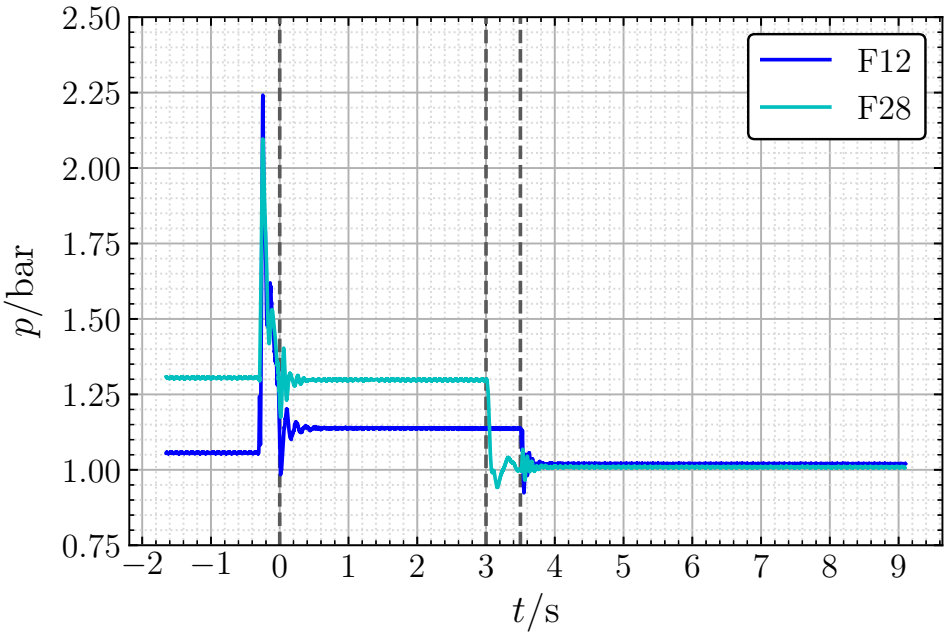

Figure 4.8: The measurement of the absolute pressure in the filling line. The first vertical dashed line indicates the start of microgravity. The second vertical dashed line indicates the operation of valve V1 to relax the pressure in test F28. The third vertical dashed line represents the start of the liquid filling into the experiment tank.

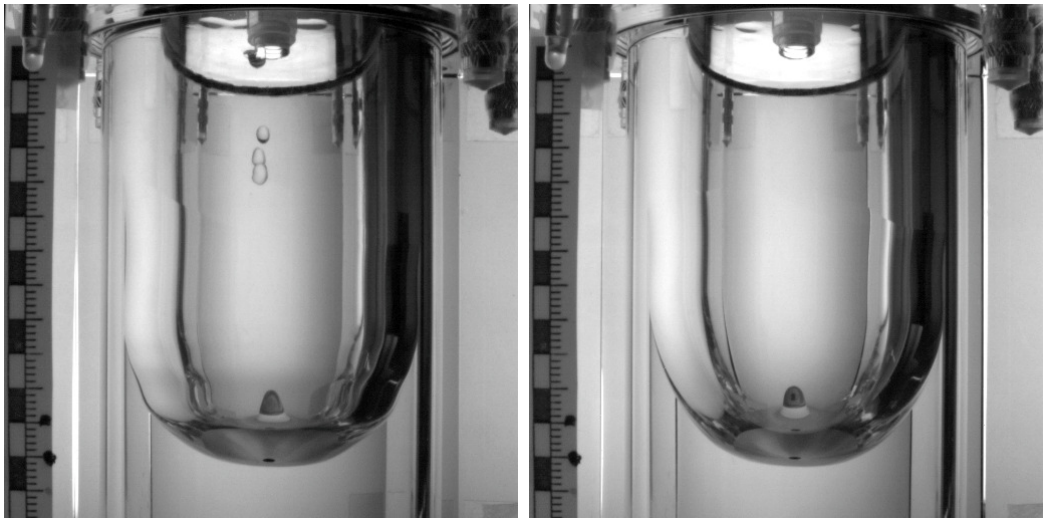

(a) F12 (b) F28

Figure 4.9: (a) The liquid jet penetrates the liquid interface and immediately breaks into droplets due to a higher pressure in the fluid loop in test F12. (b) The liquid jet penetrates the liquid interface but does not break into droplets in test F28. Both images correspond to the microgravity time of $t = 4\,\mathrm{s}$ and the volumetric flow rate was $Q_L = 1.20\,\mathrm{mL\,s^{-1}}$ in both tests.

4.1.3.5 Temperature measurement

The liquid temperature T_L measured in the primary inlet line by the temperature sensor T1 and the outer wall temperature of the experiment tank T_{ET} measured by the temperature sensor T3 are plotted in figures 4.10 and 4.11 respectively for the whole microgravity duration of 9 s. In both figures 4.10 and 4.11, the vertical dashed line indicates the start of liquid filling into the experiment tank. The temperatures are plotted for four different tests. The plots are created after a moving average with an interval of 100 is performed on the experiment data, which was originally sampled at 1000 Hz.

A smooth decline in the liquid temperature T_L is observed after $t = 5$ s for all the tests in figure 4.10. The temperature sensor T1 that measured the liquid temperature was located in the primary inlet line above the valve V3, as shown in figure 4.3. After the valve V3 opens, the liquid from the closed loop enters the inlet line, which causes a change in the measured value of T_L. Figure 4.10 shows that after $t = 8$ s, the liquid temperatures attain a constant value. Furthermore, the maximum deviation in the liquid temperature T_L before and after the start of filling is less than 1 °C in all the tests.

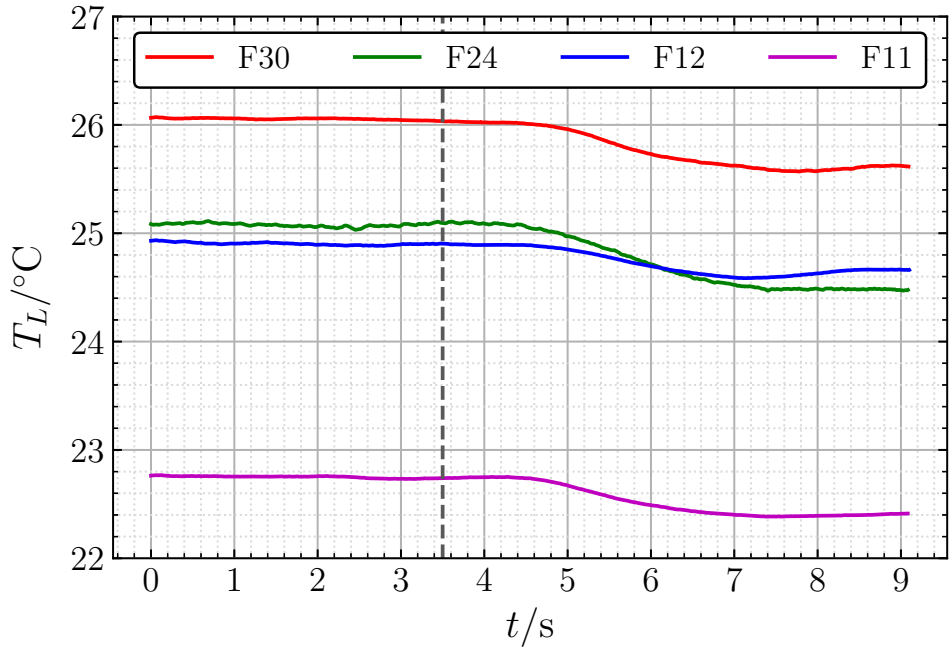

Figure 4.10: The liquid temperature T_L measured in the primary inlet line under microgravity for four different tests. The vertical dashed line indicates the start of the liquid filling into the experiment tank.

The temperature inside the drop capsule as well as the backlight from the LED panels influence the outer wall temperature of the experiment tank T_{ET}. However, in the drop tower experiments, the LED panels were operated only few seconds prior to the catapult launch or drop of the capsule. Moreover, the experiment tank was a solid block of PMMA material with a higher thermal inertia and the test duration was shorter to observe a significant change in the outer wall temperature of the experiment tank caused by the heat transfer from the LED panels. Therefore, the outer wall temperature of the experiment tank T_{ET} remained constant throughout the test duration, as can be seen in figure 4.11.

By comparing figures 4.10 and 4.11, it can also be noticed that the outer wall temperature T_{ET} is lower than the liquid temperature T_L in all the tests except F12. However, the difference between T_L and T_{ET} is less than 1.5 °C for the tests compared in figures 4.10 and 4.11. Therefore, it can be confirmed that the drop tower experiments were performed under isothermal conditions.

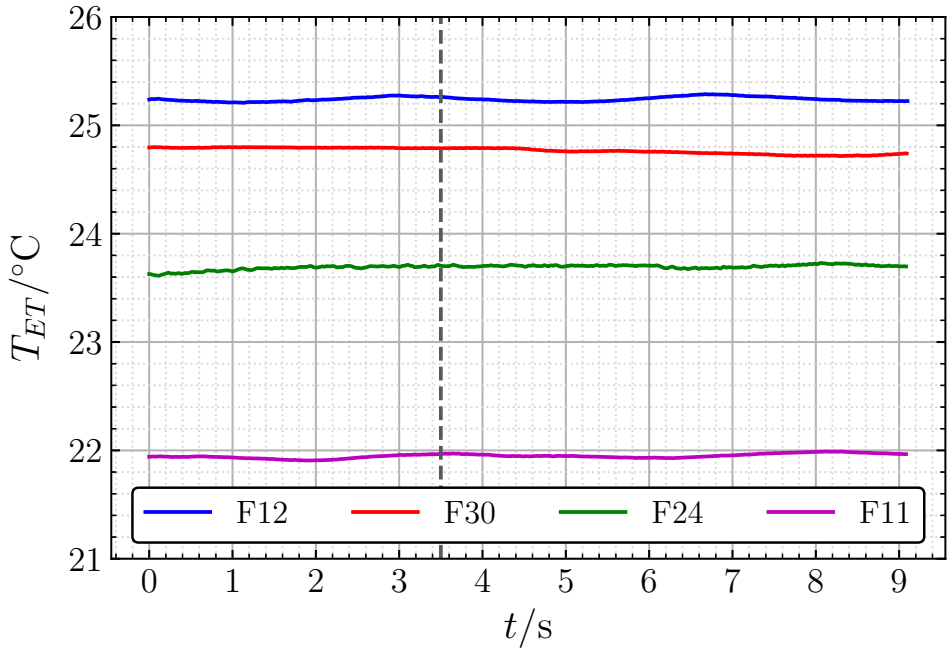

Figure 4.11: The outer wall temperature of the experiment tank T_{ET} measured under microgravity for four different tests. The vertical dashed line indicates the start of the liquid filling into the experiment tank.

4.2 Ground experiments

The ground experiments were conducted with the same experimental setup that was used for the drop tower experiments, as described in section 4.1.1. The following goals were envisioned for the ground experiments.

1. Test the experimental setup of the drop tower experiment under normal gravity conditions.
2. Formulate a procedure to evaluate the measurement data and to process the images.
3. Study the interaction of the liquid jet with the liquid interface for different initial liquid fill heights H_L and different volumetric flow rates Q_L.
4. Find the range of flow rates where the liquid interface becomes unstable for a given initial liquid fill height.

The fluid loop of the ground experiments can be referred to in figure 4.3. In all the ground experiments, the liquid was filled into the experiment tank using the primary inlet line only. Similar to the drop tower experiments, pressure, temperature and volumetric flow rate were measured in the fluid loop for all the experiments. Two cameras, as described in section 4.1.1.3, were used to capture the images of liquid filling under normal gravity conditions.

4.2.1 Experimental procedure

A series of experiments were carried out under normal gravity conditions with different initial liquid fill heights H_L and different volumetric flow rates Q_L. The ground experiments were performed for a test duration of 4.6 s. The same test liquid HFE-7500 was used for the ground experiments as well.

After establishing the closed loop, valve V3 was opened and valve V2 was closed to fill the experiment tank with an initial liquid fill height H_L. At this moment, valve V1 was also opened to balance the pressure in the phase separator. After setting the initial fill height, the valves were switched back to their original states. Then, the desired flow rate was set to the pump by providing the input voltage and the liquid was pumped in the closed loop. Then, the cameras were set to record ready. Finally, the drop sequence was pressed in the LabVIEW user interface of the computer, which started the filling experiments. As soon as the drop sequence was pressed, valves V3 and V1 were opened and valve V2 was closed, such that the liquid could be filled into the experiment tank through the primary inlet. The liquid filling continued until $t = 4.6\,\text{s}$ and the experiment data were also logged for the test duration of 4.6 s. At $t = 4.6\,\text{s}$, the liquid filling was stopped and the closed loop was activated again. At the end of the test, the liquid from the experiment tank was drained and a new initial fill height was set for the next test.

The test matrix of the ground experiments is shown in table 4.5. The ground experiments were performed for different initial liquid fill heights varying in the range of $9.6\,\text{mm} \leq H_L \leq 45.6\,\text{mm}$.

The accuracy of the initial liquid fill height was $\pm 0.1\,\mathrm{mm}$. For every initial liquid fill height H_L, the volumetric flow rates were varied in the range of $0.8\,\mathrm{mL\,s^{-1}} \leq Q_L \leq 4.8\,\mathrm{mL\,s^{-1}}$. The elevation of the liquid level and the deformation of the interface were observed, as the liquid is filled into the experiment tank under normal gravity conditions.

Table 4.5: Test matrix of the ground experiments. The filling experiments in microgravity were performed within the range of ground tests GT16 and GT17.

Serial No.	Test ID	H_L/mm	Q_L/mL s^{-1}	T_L/°C	Re_1	$v_I/10^{-3}$ m s^{-1}
1	GT1		0.8	21.8	165.01	63.66
2	GT2		1.8	21.9	371.28	143.24
3	GT3	9.6	2.8	22.0	577.54	222.82
4	GT4		3.8	22.1	783.81	302.39
5	GT5		4.8	22.3	990.07	381.97
6	GT6		0.8	22.5	165.01	63.66
7	GT7		1.8	22.7	371.28	143.24
8	GT8	19.5	2.8	22.7	577.54	222.82
9	GT9		3.8	22.6	783.81	302.39
10	GT10		4.8	22.5	990.07	381.97
11	GT11		0.8	22.2	165.01	63.66
12	GT12		1.8	22.3	371.28	143.24
13	GT13	24.0	2.8	22.4	577.54	222.82
14	GT14		3.8	22.6	783.81	302.39
15	GT15		4.8	22.8	990.07	381.97
16	GT16		0.8	23.1	165.01	63.66
17	GT17		1.8	23.4	371.28	143.24
18	GT18	30.1	2.8	23.4	577.54	222.82
19	GT19		3.8	23.3	783.81	302.39
20	GT20		4.8	23.2	990.07	381.97
21	GT21		0.8	22.0	165.01	63.66
22	GT22		1.8	22.2	371.28	143.24
23	GT23	45.6	2.8	22.2	577.54	222.82
24	GT24		3.8	22.8	783.81	302.39
25	GT25		4.8	22.8	990.07	381.97

4.2.2 Data evaluation

The experiment data were logged at a frequency of 1000 Hz. The sensor data for the measurement of volumetric flow rate, pressure and temperature are analysed and plotted for three ground tests GT1 ($H_L = 9.6\,\mathrm{mm}$, $Q_L = 0.8\,\mathrm{mL\,s^{-1}}$), GT8 ($H_L = 19.5\,\mathrm{mm}$, $Q_L = 2.8\,\mathrm{mL\,s^{-1}}$) and GT20 ($H_L = 30.1\,\mathrm{mm}$, $Q_L = 4.8\,\mathrm{mL\,s^{-1}}$).

4.2.2.1 Flow rate measurement

The volumetric flow rate Q_L measured by the flow meter is plotted against time in figure 4.12 for three ground tests GT1, GT8 and GT20. The flow rate remains constant before the start of liquid filling at $t = 0\,\mathrm{s}$. The volumetric flow rate declines marginally after the start of filling, due to the hydrostatic pressure and frictional loss in the primary inlet pipe. The maximum variation in the flow rate between the closed loop and filling loop is $\pm 0.1\,\mathrm{mL\,s^{-1}}$. The mean volumetric flow rate is calculated by taking the average of the flow rate between $t = 0\,\mathrm{s}$ and $t = 4.6\,\mathrm{s}$. A similar pattern in the flow rate was observed for all the initial liquid fill heights H_L.

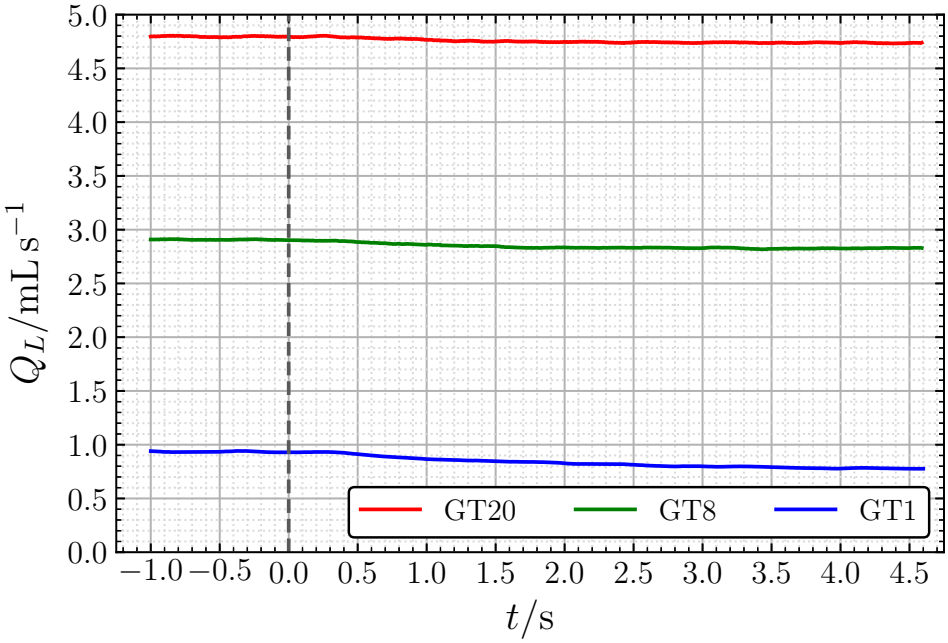

Figure 4.12: Volumetric flow rate Q_L measurement during the filling of the experiment tank in normal gravity for three different tests. The vertical dashed line represents the start of filling.

4.2.2.2 Pressure measurement

The absolute pressure measured by the pressure sensor P1 during the liquid filling experiments in normal gravity is shown in figure 4.13 for three tests GT1, GT8 and GT20. The liquid was first pumped in the closed loop and then the liquid filling into the experiment tank began at $t = 0\,\mathrm{s}$. An abrupt jump in the pressure can be noticed in all the tests after $t = 0\,\mathrm{s}$, when valve V3 is opened to start the liquid filling into the experiment tank. After some fluctuations, the pressures show a stable trend. A significant increase in pressure during the liquid filling can be observed, as compared to the phase where the liquid was pumped in the closed loop at $t < 0\,\mathrm{s}$. This increase in pressure mainly comes from the hydrostatic head under normal gravity conditions, which is caused by the height difference of 470 mm between the two platforms, where the fluid pump and experiment tank were assembled (see figure 4.1). Furthermore, the absolute pressure increases as the volumetric flow rate and the initial liquid fill height increase.

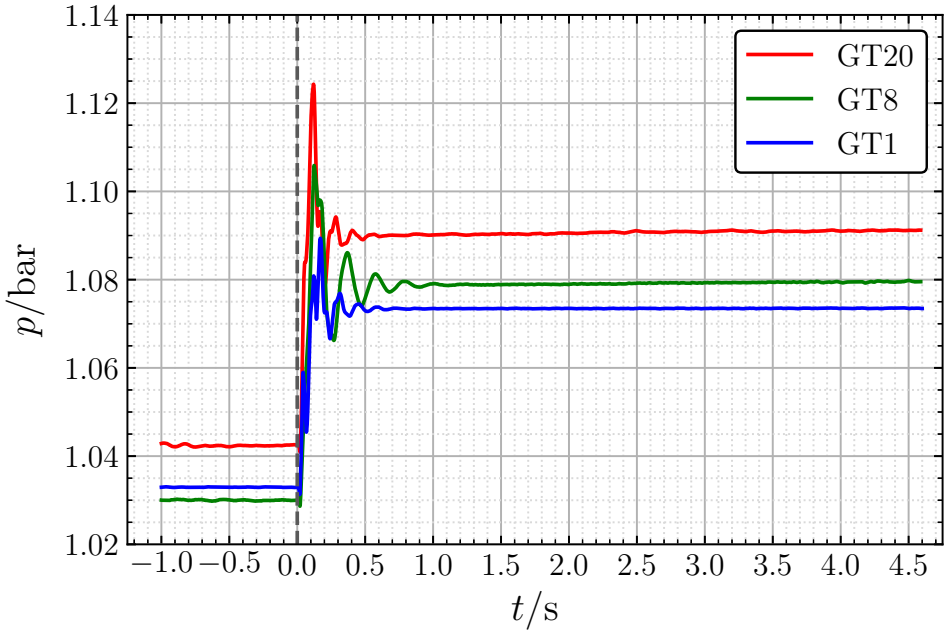

Figure 4.13: Pressure measurement during the filling of the experiment tank in normal gravity for three different tests. The vertical dashed line represents the start of filling.

4.2.2.3 Temperature measurement

The liquid temperature T_L measured in the primary inlet line is shown in figure 4.14 for three ground tests GT1, GT8 and GT20. After the liquid filling begins, the temperatures increase slightly and then tend towards a constant value. The change in measured value of T_L could again be attributed to the liquid from the closed loop flowing through the inlet line. However, the maximum increase in temperature for a test is less than 1 °C. The liquid temperature T_L measured in every test is listed in table 4.5. The average of liquid temperature from all the tests is $T_L = 22.6\,°C$ and the maximum deviation of the liquid temperature T_L from the average value is 0.8 °C. Therefore, it can be inferred that the ground tests were also performed under isothermal conditions.

The experiment tank wall temperature T_{ET} measured during the three ground tests GT1, GT8 and GT20 is plotted against time in figure 4.15. The outer wall temperatures of the experiment tank T_{ET} in all the tests are higher than the liquid temperatures T_L, which could be possibly due to the longer operation of the LED panels in the ground experiments. A constant value of the experiment tank wall temperature can be observed in all the tests in figure 4.15, which exhibits a similar trend like the drop tower experiments.

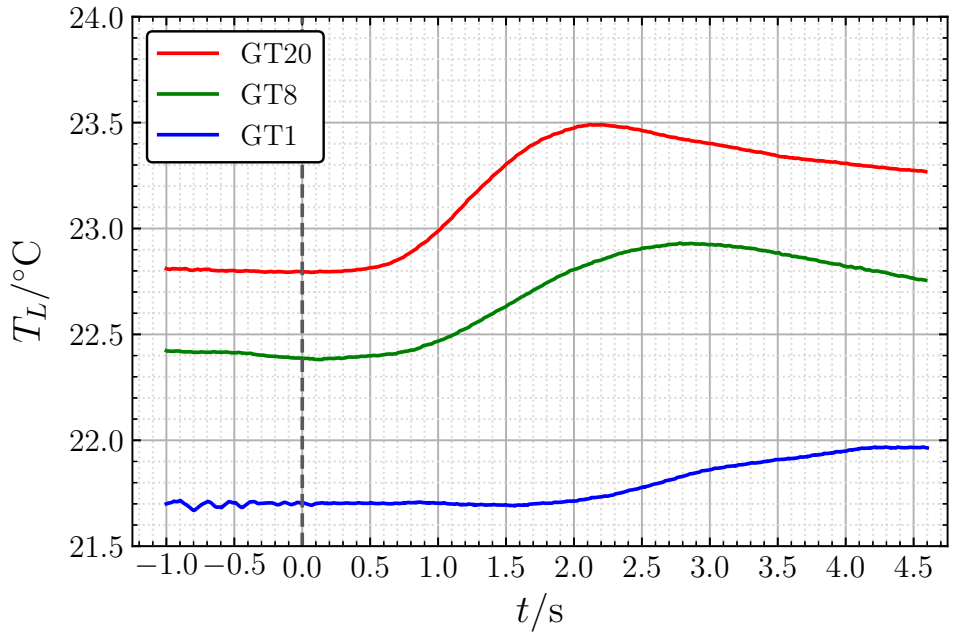

Figure 4.14: Liquid temperature T_L measurement during the filling of the experiment tank in normal gravity for three different tests. The vertical dashed line represents the start of filling.

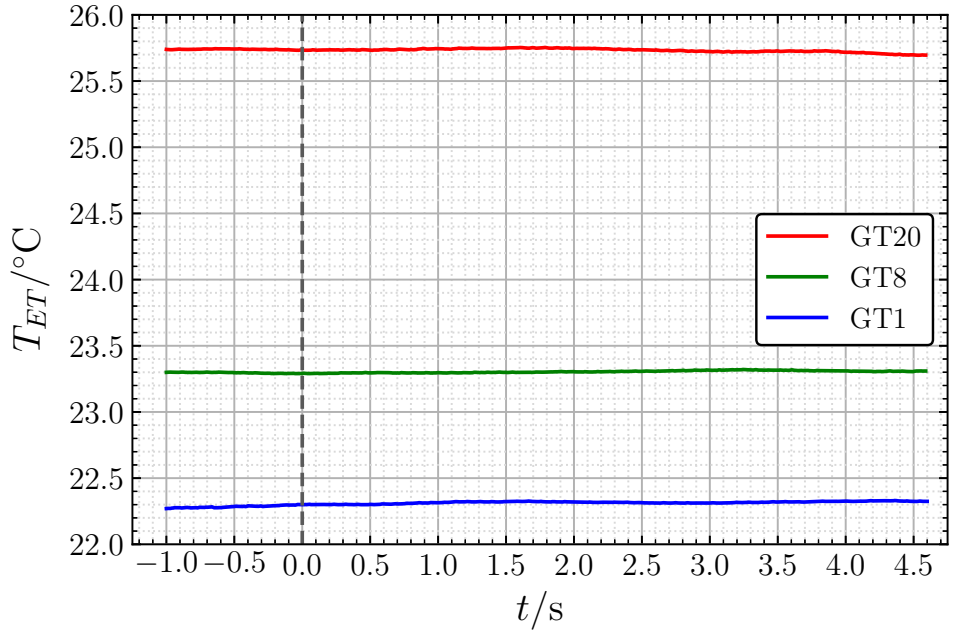

Figure 4.15: Experiment tank wall temperature T_{ET} measurement during the filling of the experiment tank in normal gravity for three different tests. The vertical dashed line represents the start of filling.

4.3 Parabolic flight experiments

A parabolic flight is an aircraft, that serves as a laboratory to perform experiments in reduced gravity with direct physical access and also to personally experience weightlessness. A state of weightlessness is created inside the aircraft, as three pilots fly the aircraft in a parabolic maneuver. These maneuvers (also called parabolas) are repeated 31 times a day. A parabolic maneuver consists of a reduced gravity phase of 22 s, in which the aircraft experiences a free fall. The reduced gravity phase is preceded and succeeded by hypergravity phases lasting for roughly 20–25 s each. In the hypergravity phase, the passengers experience a high acceleration of $1.8g_E$. Between two parabolas there is a phase of steady flight for a duration of about 100 s to prepare the experiment for the next parabola. The parabolic flight experiments were carried out during the 39^{th} DLR parabolic flight campaign in Bordeaux, France over the course of three days between 6^{th} and 8^{th} September 2022. The parabolic flight experiments were conducted on board the Airbus A310 Zero-G aircraft operated by Novespace.

The concept of filling and removing liquid under reduced gravity conditions was tested in the parabolic flight experiments. The experiment was designed in such a way to test the phase separation and gas-free liquid removal from the experiment tank with the help of a screen channel liquid acquisition device (SC-LAD) and the vented filling of the experiment tank using a velocity control plate (VCP) in a reduced gravity environment. Therefore, an experiment tank consisting of components like a screen channel liquid acquisition device (SC-LAD), ring baffles, a velocity control plate (VCP) and a gas port (GP) was built. During the liquid filling process, the gas inside the tank was vented through the GP and the behaviour of the liquid jet, as it entered the experiment tank was examined for different volumetric inflow rates.

The following goals and objectives were envisioned for the parabolic flight experiment.

1. To test the procedures of filling and removal of liquid using one experiment tank.
2. To demonstrate the performance of a screen channel liquid acquisition device (SC-LAD) during liquid removal.
3. To fill gas-free liquid into the experiment tank and observe the free surface behaviour.
4. To demonstrate liquid-free venting of the gas during the filling.

4.3.1 Experimental setup

The experimental setup comprised of three racks. They were the hydraulic rack, the electrical rack and the laptop rack. The hydraulic rack and the electrical racks were enclosed in a Zarges box each. The hydraulic rack consisted of two platforms. The lower platform housed all the hydraulic loop components. The experiment tank and the optical systems were placed on the upper platform. The hydraulic rack is shown in figure 4.16. The electrical and laptop racks are shown in figure 4.17. The electrical rack provided power to all the components in the hydraulic rack and the laptop rack. The laptop rack functioned as an operating table for mounting the two

laptops on the top plate and the experimenters used these laptops to operate the experimental setup. One laptop was used for the LabVIEW program to run the experiment and the other laptop was used to have a live feed of the cameras and store the recorded images.

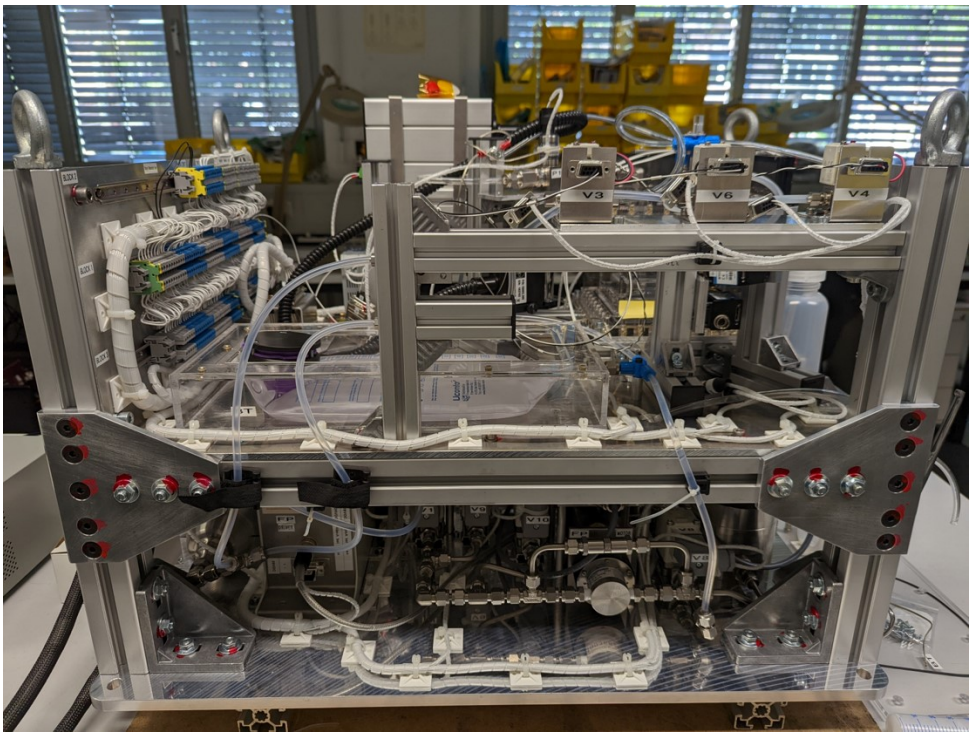

Figure 4.16: Hydraulic rack of the parabolic flight experiment.

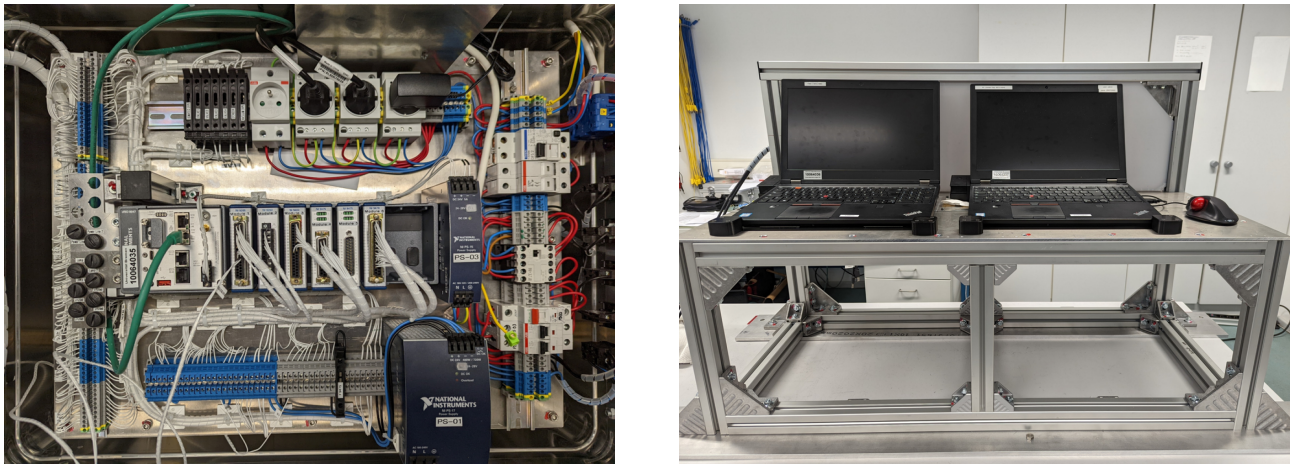

Figure 4.17: Electrical rack (left) and laptop rack (right) of the parabolic flight experiment.

4.3.1.1 Hydraulic loop

The hydraulic loop of the experiment is shown in figure 4.18. The hydraulic loop consists of one common inner loop and one outer loop for liquid removal and liquid filling each. The valves V10 and V11 were normally open valves and all the other valves were normally closed. The components phase separator (PS), valve V10, fluid pump (FP) and valve V11 formed the inner

loop for both liquid removal and liquid filling. The inner loop was connected to a bladder tank (BT), which stored the required liquid for the experiment. The bladder tank was a commercial product called the 'HydroBag' from the company Fresenius Kabi Deutschland GmbH and it had a maximum volume of 1.5 L. The in-house manufactured phase separator PS had a screen element inside to separate the gas and liquid phases. The gas collected in the gas side of the phase separator was removed through line 3, which was connected to a low-pressure reservoir (LPR). The LPR was set to a pressure lower than the cabin pressure of 855 mbar by operating the vacuum pump (VP) at the beginning of the experiment. The throttle valves TV1 and TV2 were mounted in the vent lines connected to the LPR. Four temperature sensors and four pressure sensors were used to measure the temperature and pressure inside the loop. The sampling rate of the sensors was 100 Hz. The liquid was filled into the experiment tank through line 2, which consisted of valve V2, pressure sensor P2 and temperature sensor T2, as marked in blue colour in figure 4.18. In order to avoid over-pressurization of the experiment tank during the liquid filling, a check valve V12 was assembled in parallel to the fluid pump. This check valve V12 was designed to open when the absolute pressure on the pressure side of the fluid pump exceeded the pre-set cracking pressure of about 1.2 bar.

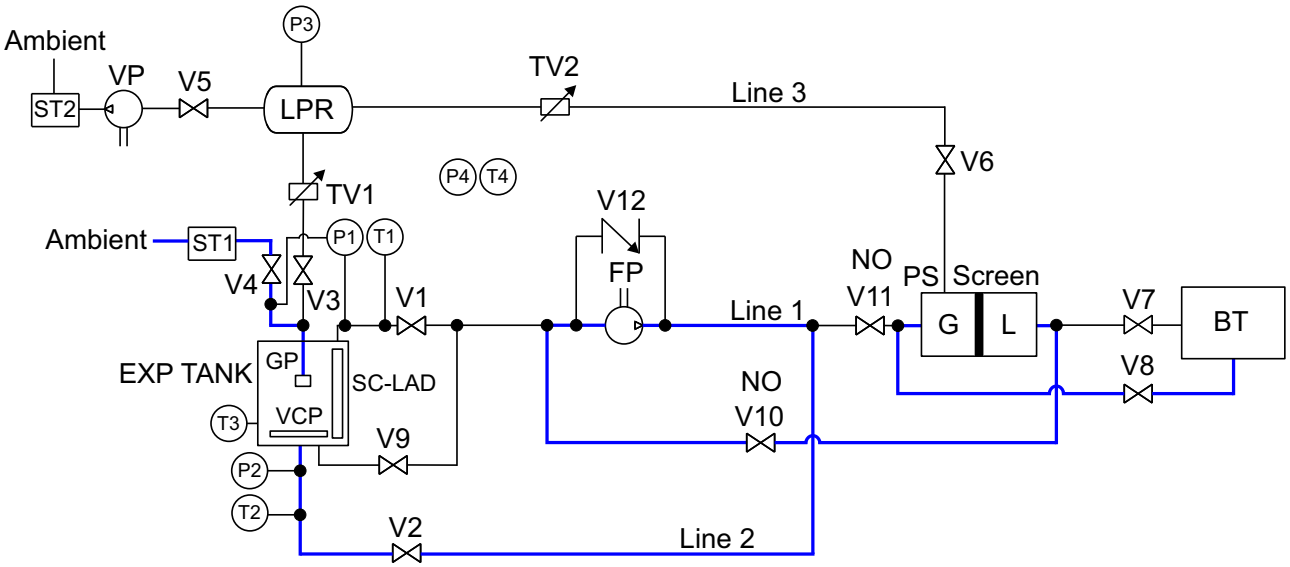

Figure 4.18: Hydraulic loop of the parabolic flight experiment. The liquid filling loop is marked in blue colour.

4.3.1.2 Experiment tank

The experiment tank shown in figure 4.19 was made up of polymethyl methacrylate (PMMA) and had inner dimensions of 100 mm length, 100 mm breadth and 130 mm height. The technical drawing of the experiment tank is given in figure A.8. The experiment tank consisted of components like a screen channel liquid acquisition device (SC-LAD), ring baffles, a velocity control plate (VCP) and a gas port (GP). The screen channel liquid acquisition device (SC-LAD) mounted inside the tank enabled gas-free removal of liquid. The SC-LAD was a rectangular channel, which had three sides made up of acrylic and one side where the DTW 200×1400 screen was glued. This screen element helped in blocking the gas and letting the liquid pass through, as long as the bubble point pressure was not exceeded. Additionally, the

ring baffles were attached to the walls of the tank to delay the liquid movement towards the top part and to control the position of liquid during variable accelerations.

The tank was filled from the bottom through an inlet pipe. The inlet pipe protruded into the experiment tank by 10 mm. A velocity control plate (VCP) was fitted above the inlet pipe at a height of 30 mm from the tank bottom surface, to diffuse the momentum of the incoming flow, such that the tank can be filled with higher flow rates. This was done to avoid the creation of any geyser, which might eventually touch the gas port of the tank. The liquid entering the tank through the inlet pipe was retarded by the VCP and its momentum was dissipated in the bulk liquid. Moreover, the provision of ring baffles helped in retaining the incoming liquid in the bottom part of the tank. Faster and quiescent filling of the tank could be achieved by using the VCP. As the liquid was filled inside the tank, the gas in the ullage region was vented through the gas port (GP). The inlet of the gas port protruded to the middle of the experiment tank, in order to keep the gas port liquid-free under reduced gravity conditions. The gas port was connected to a storage tank ST1. During the liquid filling into the experiment tank, the pressure inside the tank was balanced by opening valve V4, which was exposed to the cabin pressure. In case the liquid entered the gas port line, the absorbent materials inside the storage tank were equipped to absorb the escaped liquid. The gas port was also connected to LPR through valves V3 and TV1, in order to remove any liquid that remained inside the gas port. HFE-7500 was used as the test liquid and the experiments were performed under ambient conditions prevailing inside the aircraft cabin. The interface stability studies could not be planned for the parabolic flight experiments due to the design constraints of the experiment tank and the residual accelerations.

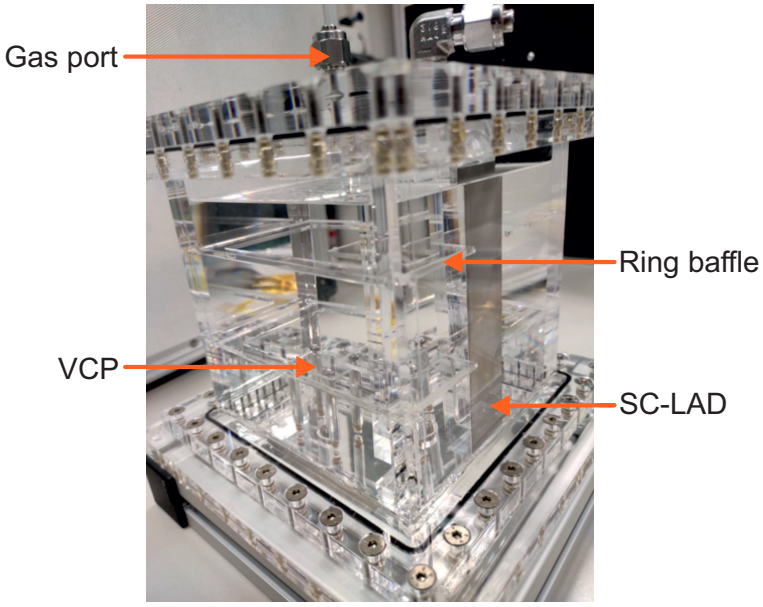

Figure 4.19: Experiment tank used in the parabolic flight experiment.

4.3.1.3 Optics

Three cameras from the company Imaging Source Europe GmbH were used to capture the images at a frame rate of 42 frames per second for a duration of 24 s. Two cameras CAM1

and CAM2 were used for the liquid removal experiments, while CAM3 was used to capture the liquid filling into the experiment tank. The resolution of the images from CAM3 was 1080×1920 pixels. The recorded images were stored in the camera laptop after each parabola. Cinegon lens 2.1/6-0901 from the company Schneider Kreuznach was used in CAM3 to capture the liquid filling. The inlet pipe, VCP, ring baffles and the gas port were in the field of view of CAM3, as shown in figure 4.20. An LED light at the top right of the image indicated the opening and closing of the filling valve V2. The liquid fill height inside the experiment tank was measured using a black and white ruler pasted on the outer wall of the experiment tank. The background lighting of the experiment tank was enabled by the LED panels emitting red light at a wavelength of 635 nm. The LED panels were purchased from the company Stemmer Imaging AG.

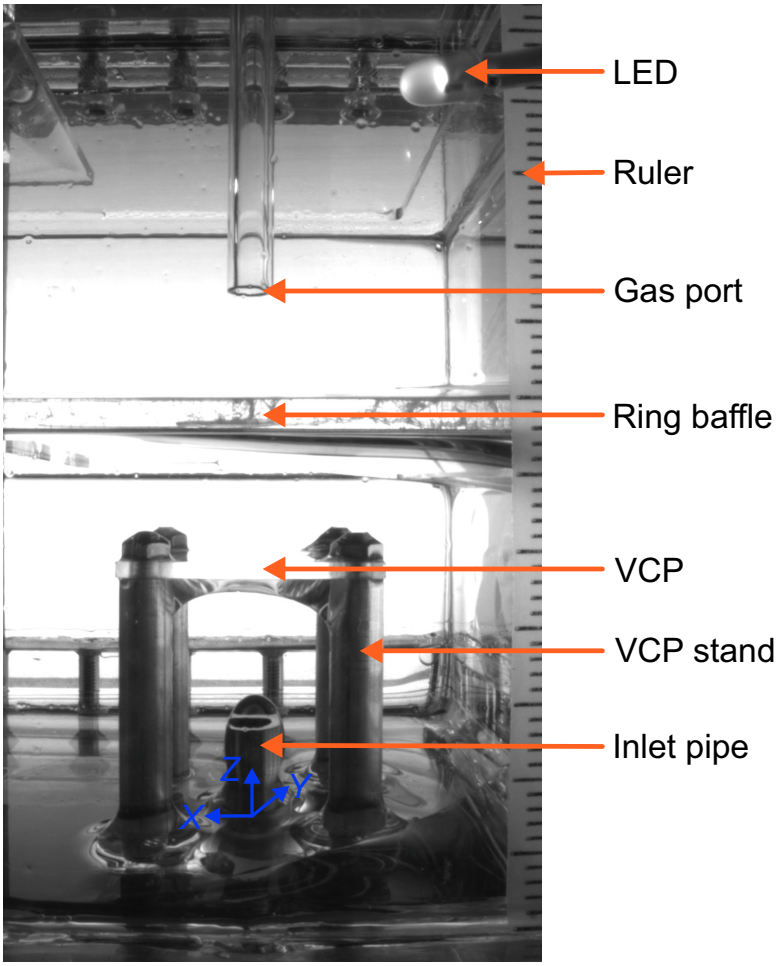

Figure 4.20: View from the camera CAM3 focusing on the liquid filling into the experiment tank. The origin of the coordinate system is located inside the inlet pipe at the tank bottom.

4.3.2 Experimental procedure

A total of 45 liquid filling experiments were performed during the three days of the parabolic flight experiment campaign. In this thesis, only the liquid filling experiments are discussed.

Preparation

The experimental setup was prepared in the $1g_E$ phase for the liquid filling experiments. Firstly, the liquid was pumped in the inner loop. Then, the required initial liquid fill height H_L was set in the experiment tank by opening the valves V2, V8 and V4 and closing the valve V11. The liquid fill height H_L was measured from the origin of the coordinate system located inside the inlet pipe at the tank bottom. It was ensured that the gas port line was void of any liquid. In case any liquid was present in the gas port line, the vacuum pump (VP) was started to create a low pressure of 400 mbar in the LPR. Then, the valve V3 was opened shortly to suck the liquid out from the gas port line and purge it into the LPR. As the final step for the preparation, based on the test matrix the desired flow rate was set as the input set value for the fluid pump (FP). During the hypergravity phase, the liquid was pumped in the inner loop with the desired flow rate.

Filling of liquid

The filling loop was programmed to run automatically in LabVIEW and was initiated by pressing the function key F12 on the LabVIEW laptop after the cabin announcement of '*injection*', which corresponds to the start of the reduced gravity phase. The camera recording was also triggered by this key. However, in all the experiments the liquid filling was initiated 3 s after the press of the function key F12. This was done to avoid the initial negative acceleration in the z-axis during the transition from hypergravity to reduced gravity. After 3 s in weightlessness, the valves V2, V8 and V4 opened and valve V11 closed. This enabled the liquid to flow from the bladder tank (BT) through valve V8, phase separator (PS), valve V10, fluid pump (FP) and valve V2 to enter the experiment tank. The PS allowed only liquid to pass through and blocked the gas, as long as the bubble point pressure of the screen inside the PS was not exceeded. In this way, a gas-free supply of liquid was ensured. The incoming liquid inside the experiment tank hit the VCP and its momentum was dissipated into the bulk liquid. The gas inside the tank was vented through the gas port (GP). The liquid filling stopped automatically at $t = 22$ s and the setup switched back to the inner loop for the pull-out (hypergravity) phase of the parabola.

The test matrix of the parabolic flight experiment is given in table 4.6. The liquid filling into an initially empty tank was predominantly tested for different volumetric flow rates in the range of $0.2\,\mathrm{mL\,s^{-1}} \leq Q_L \leq 9.5\,\mathrm{mL\,s^{-1}}$. Moreover, in the tests with a pre-filled tank, the initial liquid fill height H_L could only be set approximately due to the continuous vibrations in the aircraft.

4.3.3 Data evaluation

4.3.3.1 Acceleration measurement

The accelerations in all the three axes of the aircraft were measured by an acceleration sensor on board the aircraft and the acceleration data was provided to the experimenters by Novespace after the experiment campaign. The acceleration data was sampled at a rate of 10 Hz. The three-axes accelerations are shown for the whole parabolic maneuver (P17) from the flight day 3 (08.09.2022) in figure 4.21a. The green curve corresponds to the longitudinal acceleration in

Table 4.6: Test matrix for the liquid filling experiments on board the parabolic flight from three flight days D1, D2 and D3. The parabolic maneuver number is prefixed with 'P'.

Test ID	H_L/mm	Q_L/mL s^{-1}	Test ID	H_L/mm	Q_L/mL s^{-1}	Test ID	H_L/mm	Q_L/mL s^{-1}
P16D1	0	0.9	P16D2	0	0.6	P16D3	0	0.4
P17D1	0	0.5	P17D2	0	0.7	P17D3	0	0.5
P18D1	0	0.3	P18D2	0	0.8	P18D3	0	0.6
P19D1	0	0.4	P19D2	0	0.5	P19D3	0	0.7
P20D1	0	0.2	P20D2	0	0.4	P20D3	0	0.8
P21D1	25	0.5	P21D2	0	0.6	P21D3	0	0.8
P22D1	25	1.0	P22D2	0	0.7	P22D3	0	0.3
P23D1	25	0.7	P23D2	15	0.5	P23D3	0	0.3
P24D1	30	0.7	P24D2	15	0.6	P24D3	0	0.2
P25D1	15	0.7	P25D2	15	0.7	P25D3	0	5.0
P26D1	15	0.5	P26D2	25	0.5	P26D3	0	5.0
P27D1	35	5.0	P27D2	25	0.6	P27D3	0	9.5
P28D1	35	7.5	P28D2	25	0.7	P28D3	0	9.5
P29D1	35	9.5	P29D2	35	5.0	P29D3	15	0.6
P30D1	40	9.5	P30D2	35	7.5	P30D3	25	0.6

the x-axis, which is from the rear to the cockpit of the aircraft. The red curve represents the transverse acceleration in the y-axis, extending from the left to the right wing of the aircraft. The vertical acceleration in the z-axis is indicated by the blue curve.

The plot is shown for the entry, injection and exit phases of the parabola. The first vertical dashed line marks the start of the reduced gravity phase and the second vertical dashed line indicates the end of the reduced gravity phase. In the injection phase, the aircraft is in the state of a free fall for 22 s. The entry and exit phases last for approximately 25 s. During the entry and exit phases, the experimenters and the experiments experience a maximum vertical acceleration of about 18 m s^{-2}, which corresponds to a hypergravity of about $1.8 g_E$. This can be seen in the trend of the blue curve in figure 4.21a. In comparison to the vertical acceleration, the longitudinal and transverse accelerations remain at a lower scale during the parabolic maneuver.

The three-axes accelerations are shown for the reduced gravity phase in figure 4.21b, where the acceleration values are plotted against time. The vertical acceleration represented in blue colour fluctuates between positive and negative acceleration during the reduced gravity phase of the parabola. The progressions of the longitudinal and transverse accelerations are smoother, compared to the vertical acceleration. According to the A310 Zero-G user guide 2019 [70], the residual accelerations vary in the range of $\pm 0.02 g_E$ in the vertical axis and in the range of $\pm 0.01 g_E$ in the longitudinal and transverse axes of the aircraft. However, it has to be noted that every parabola has a different acceleration profile, which depends on the parabolic trajectory of the aircraft.

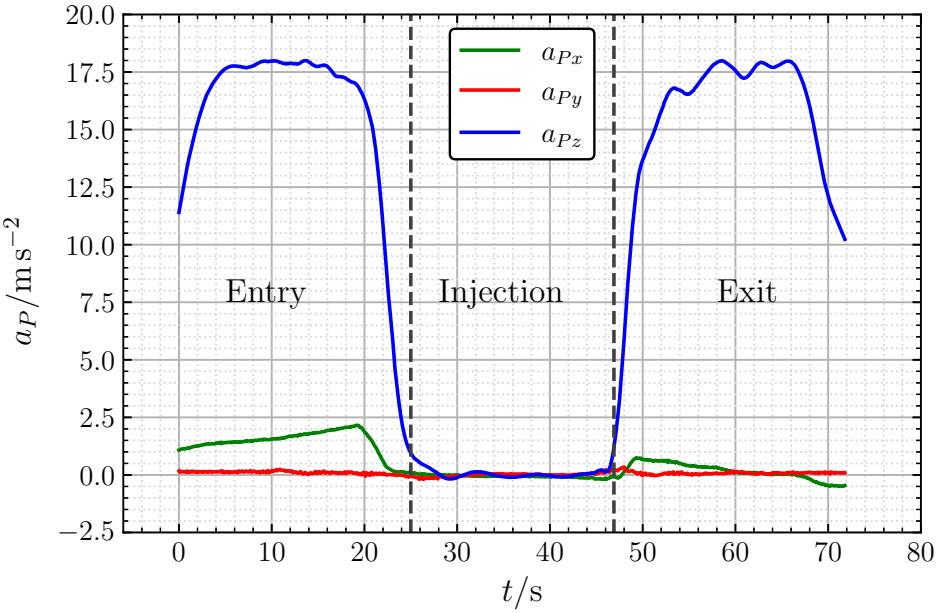

(a) Whole parabolic maneuver

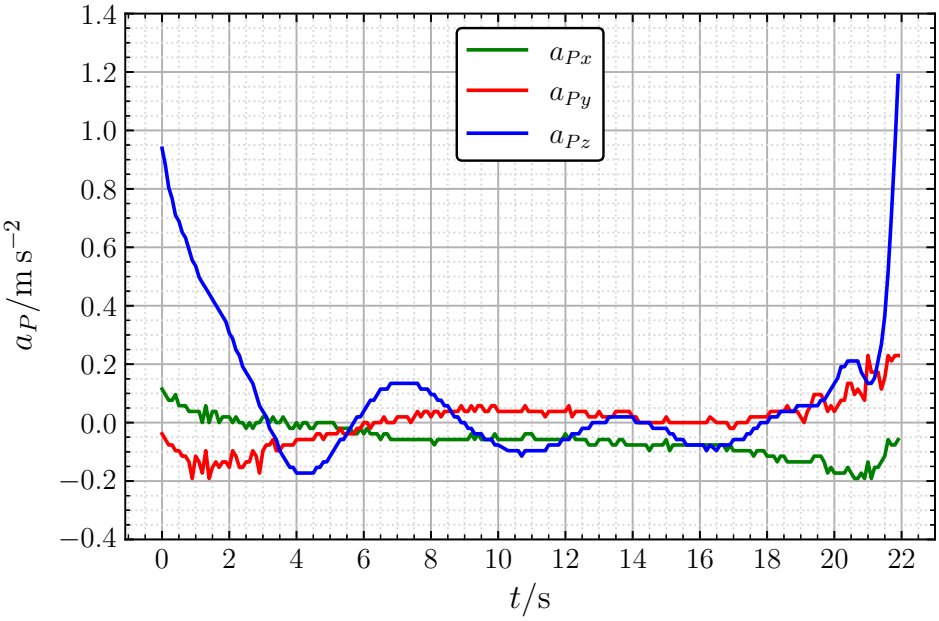

(b) Reduced gravity phase

Figure 4.21: Acceleration profiles for the parabola P17 on day 3.

4.3.3.2 Flow rate measurement

The volumetric flow rate was not directly measured in the experiments, due to the failure of the flow meter days before the experiment campaign. However, the input set values given to the fluid pump during the experiments were noted down. After the experiment campaign, calibration tests were conducted in the ZARM laboratory to measure the volumetric flow rates corresponding to these input set values. The calibration tests were carried out three times for each data set and the mean volumetric flow rates were determined.

4.3.3.3 Pressure measurement

The analogue pressure transmitter from the company TetraTec Instruments GmbH was used as the pressure sensor P2 to measure the absolute pressure in the filling line 2. The measurement range of the pressure sensor P2 was from 0 bar to 2.5 bar and the measurement accuracy was ± 2.5 mbar. The sampling rate of the pressure sensor was 100 Hz. The absolute pressure measured in the filling line 2 is shown in figure 4.22 for three parabolas from day 3. For better readability, the absolute pressures are presented in the scale of mbar. The start of filling into the experiment tank is indicated by the vertical dashed line. At $t = 3$ s, a sudden peak in the pressure can be observed, which results from the switching of valves in the experiment loop and the start of filling. The pressure relaxes after $t = 4$ s and except for some fluctuations in between, it remains almost constant for the duration of reduced gravity. The absolute pressures of tests P19D3 and P18D3 coincide with each other because their flow rates are similar. For P26D3, the absolute pressure is higher because of the higher volumetric flow rate of the liquid ($Q_L = 5.0\,\mathrm{mL\,s^{-1}}$). The ambient pressure inside the Zarges box of the hydraulic rack was measured by the pressure sensor P4 in the experimental setup. During the liquid filling experiments on the third day of the parabolic flight experiment campaign, the ambient pressure was measured to be about 850 mbar.

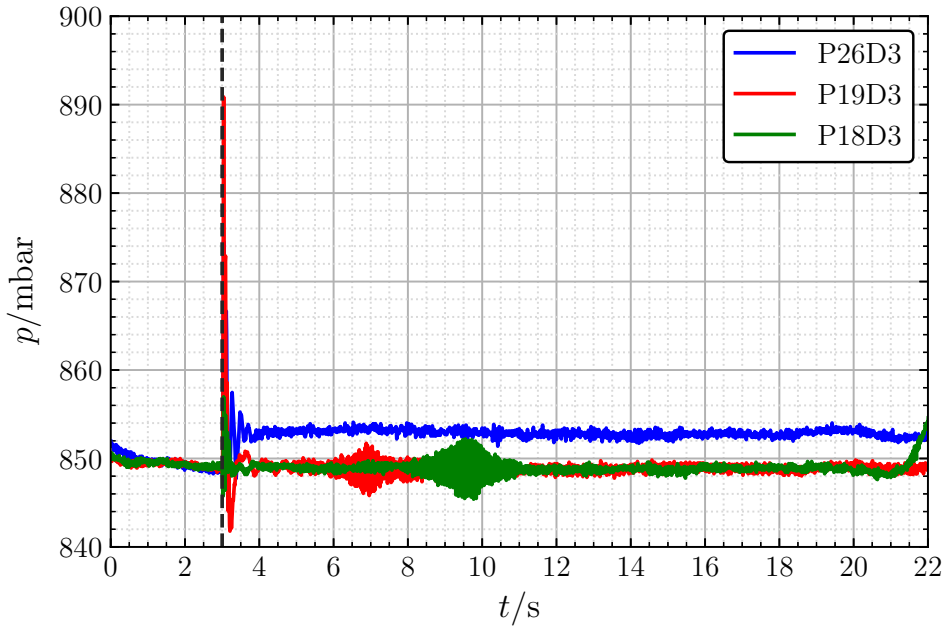

Figure 4.22: Absolute pressure measured in the filling line for different parabolas on day 3. The vertical dashed line indicates the start of the liquid filling.

4.3.3.4 Temperature measurement

The temperatures in the hydraulic loop were measured using PT100 temperature sensors with a measurement frequency of 100 Hz. The accuracy of the temperature sensors was $\pm 0.14\,°C$ at 25 °C. The liquid temperature T_L measured by the temperature sensor T2 in the filling line is plotted in figure 4.23a and the outer wall temperature of the experiment tank T_{ET} measured by the temperature sensor T3 is plotted in figure 4.23b. The ambient temperature T_A was measured on the upper platform of the hydraulic rack by the temperature sensor T4 and is shown in figure 4.23c. The temperature data corresponds to the reduced gravity phase of three parabolas from day 3 of the parabolic flight experiment campaign. The vertical dashed line specifies the start of liquid filling.

The liquid temperature T_L in the filling line has a maximum variation of $\leq 0.5\,°C$ over time in the parabolas shown in figure 4.23a. Furthermore, it can be noticed from figure 4.23a that, after the start of liquid filling, the liquid temperature increases initially and then approaches a constant value. The outer wall temperature of the experiment tank T_{ET} is higher than the liquid temperature by approximately 4 °C. This is mainly caused by the background illumination from the LED panels, which were placed right behind the experiment tank. However, the outer wall temperature of the experiment tank T_{ET} can be considered as constant, as the maximum variation over time is $\leq 0.2\,°C$. Compared to the drop tower and ground experiments, the difference between the outer wall temperature of the experiment tank T_{ET} and the liquid temperature T_L in the parabolic flight experiments was higher because of the larger emitting surface area and the longer operation time of the LED panels.

The ambient temperature T_A is slightly lower than the outer wall temperature of the experiment tank T_{ET} and remains constant over time, as can be seen in figure 4.23c. Although differences in temperatures exist within the range of $\pm 5\,°C$ approximately, it was assumed that the parabolic flight experiments were carried out under isothermal conditions.

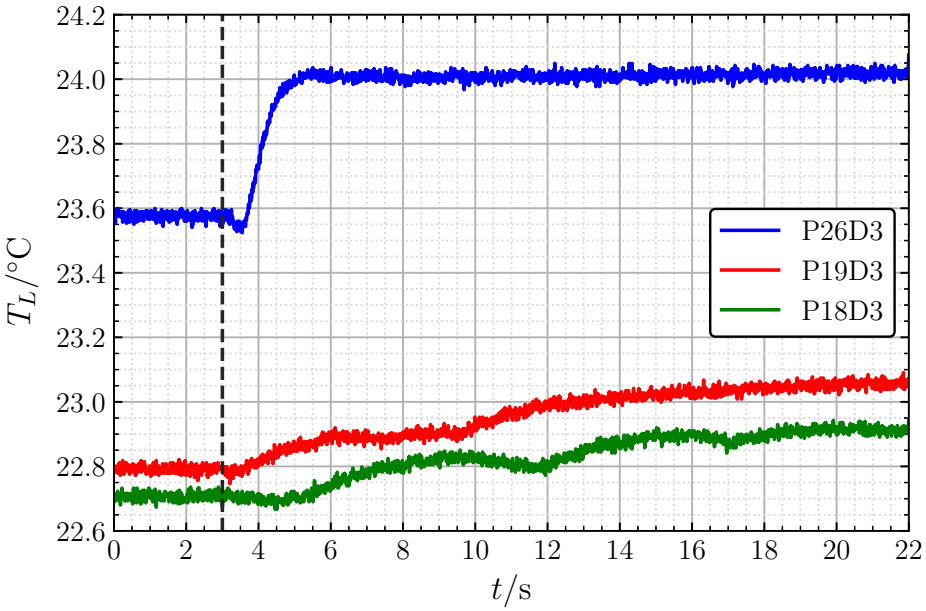

(a) Liquid temperature

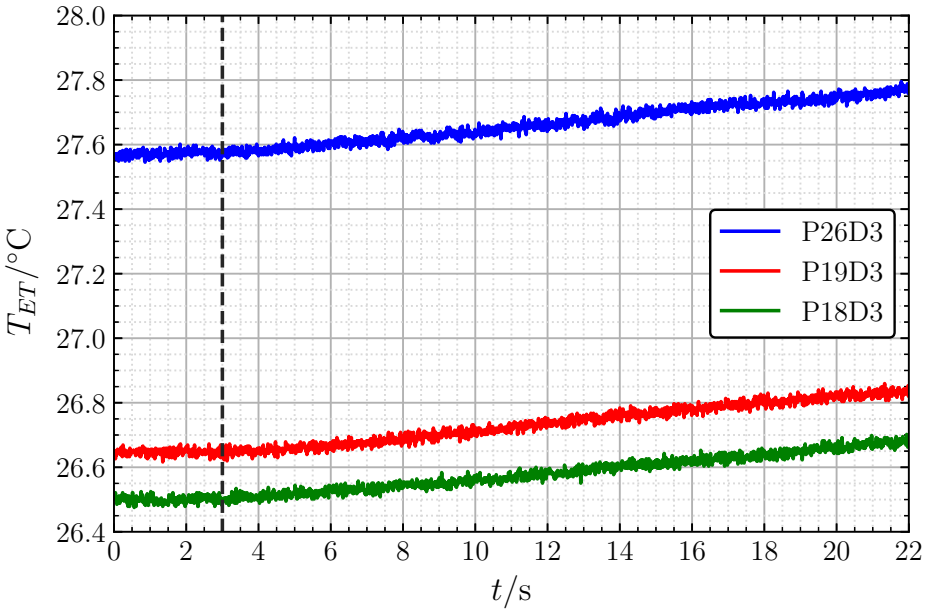

(b) Tank wall temperature

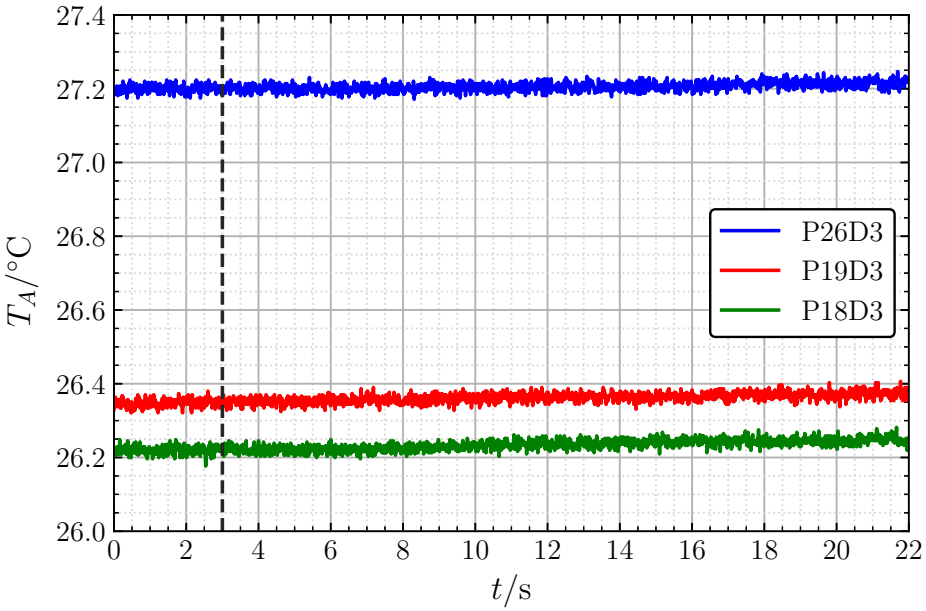

(c) Ambient temperature

Figure 4.23: Temperatures measured during the reduced gravity phase of different parabolas on day 3. The start of the liquid filling is indicated by the vertical dashed line.

Chapter 5

Numerical Simulations

The liquid filling into a tank under reduced gravity conditions has been investigated numerically by performing 2D axisymmetric numerical simulations using ANSYS Fluent 19.2. This chapter contains the theory and settings of the flow solver ANSYS Fluent. The simulation setup, post-processing of the numerical simulation results and the criterion for defining an unstable interface are also included in this chapter. Furthermore, the influence of the mesh element size on the simulation results is also discussed.

Some of the contents in section 5.3 of this chapter have been published in Govindan and Dreyer 2023 [41] and reused here with permission.

5.1 Governing equations in ANSYS Fluent

ANSYS Fluent follows a different nomenclature to describe the governing equations discussed in section 2.1. The equations are taken from the ANSYS Fluent theory guide AFTG 2019 [1].

Conservation of mass

The mass conservation equation without involving any mass transfer between the phases is given as

$$\frac{\partial \rho}{\partial t} + \nabla \cdot (\rho \, \vec{v}) = 0 \tag{5.1}$$

The mass conservation equation in the axial (z) and radial (r) coordinates for a 2D axisymmetric geometry is given in equation 5.2, where v_z and v_r are the axial and radial velocities respectively.

$$\frac{\partial \rho}{\partial t} + \frac{\partial}{\partial z}(\rho \, v_z) + \frac{\partial}{\partial r}(\rho \, v_r) + \frac{\rho \, v_r}{r} = 0 \tag{5.2}$$

Conservation of momentum

Following AFTG 2019 [1], the general form of the momentum conservation equation for an inertial frame of reference is expressed in equation 5.3.

$$\frac{\partial}{\partial t}\left(\rho\,\vec{v}\right) + \nabla\cdot\left(\rho\,\vec{v}\,\vec{v}\right) = -\nabla p + \nabla\cdot\left(\overline{\overline{\tau}}\right) + \rho\,\vec{g} + \vec{F} \tag{5.3}$$

The right hand side terms of the equation are: static pressure p, the body force due to gravity $\rho\,\vec{g}$ and other external body forces $\vec{F}$. The stress tensor $\overline{\overline{\tau}}$ is given by equation 5.4, where I is the unit tensor.

$$\overline{\overline{\tau}} = \mu\left[\left(\nabla\,\vec{v} + \nabla\,\vec{v}^{\,T}\right) - \frac{2}{3}\,\nabla\cdot\vec{v}\,I\right] \tag{5.4}$$

Considering no swirl or rotation for a 2D axisymmetric geometry, the axial momentum conservation equation is written as

$$\begin{aligned}\frac{\partial}{\partial t}\left(\rho\,v_z\right) + \frac{1}{r}\frac{\partial}{\partial z}\left(r\,\rho\,v_z\,v_z\right) + \frac{1}{r}\frac{\partial}{\partial r}\left(r\,\rho\,v_r\,v_z\right) = &-\frac{\partial p}{\partial z} + \frac{1}{r}\frac{\partial}{\partial z}\left\{r\,\mu\left[2\,\frac{\partial v_z}{\partial z} - \frac{2}{3}\left(\nabla\cdot\vec{v}\right)\right]\right\} \\ &+ \frac{1}{r}\frac{\partial}{\partial r}\left\{r\,\mu\left[\frac{\partial v_z}{\partial r} + \frac{\partial v_r}{\partial z}\right]\right\} + F_z\end{aligned} \tag{5.5}$$

and the radial momentum conservation equation is written as

$$\begin{aligned}\frac{\partial}{\partial t}\left(\rho\,v_r\right) + \frac{1}{r}\frac{\partial}{\partial z}\left(r\,\rho\,v_z\,v_r\right) + \frac{1}{r}\frac{\partial}{\partial r}\left(r\,\rho\,v_r\,v_r\right) = &-\frac{\partial p}{\partial r} + \frac{1}{r}\frac{\partial}{\partial z}\left\{r\,\mu\left[\frac{\partial v_r}{\partial z} + \frac{\partial v_z}{\partial r}\right]\right\} \\ &+ \frac{1}{r}\frac{\partial}{\partial r}\left\{r\,\mu\left[2\,\frac{\partial v_r}{\partial r} - \frac{2}{3}\left(\nabla\cdot\vec{v}\right)\right]\right\} \\ &- 2\,\mu\frac{v_r}{r^2} + \frac{2}{3}\frac{\mu}{r}\left(\nabla\cdot\vec{v}\right) + F_r\end{aligned} \tag{5.6}$$

The divergence of the velocity vector is given as

$$\nabla\cdot\vec{v} = \frac{\partial v_z}{\partial z} + \frac{\partial v_r}{\partial r} + \frac{v_r}{r} \tag{5.7}$$

5.2 Multiphase flow in ANSYS Fluent

A flow problem in which more than one phase of a fluid exists is called a multiphase flow. Multiphase flows occur in all flow problems involving free surfaces. According to AFTG 2019 [1], the multiphase flows are modelled using two approaches in ANSYS Fluent, namely the Euler-Lagrange approach and the Euler-Euler approach. In the Euler-Lagrange approach, the Navier-Stokes equations are solved for the fluid phase, which is treated as a continuous phase. The particles, bubbles or droplets are tracked and the equations are solved for the dispersed phase. The Euler-Lagrange approach is not applicable for flows where the second phase has a larger volume fraction, as described in AFTG 2019 [1].

According to AFTG 2019 [1], in the Euler-Euler approach, a property called the volume fraction is defined for each phase, whose value sums up to unity. The conservation equations are solved for each phase. As the Euler-Euler approach can be applied to flow problems, where the volume fraction is larger, it is used for the numerical simulations in this thesis work. As stated in AFTG 2019 [1], the Euler-Euler approach is implemented in ANSYS Fluent in the form of three models: the volume of fluid (VOF) model, the mixture model and the Eulerian model. As reported in AFTG 2019 [1], the VOF model is used in the modelling of free surface flows, liquid filling and sloshing problems, breakup of a jet and liquid-gas interface behaviour. The mixture model is applied for the particle-laden flows, bubbly flows and sedimentation. For modelling the bubble columns, risers, particle suspension and fluidized beds, the Eulerian model is used. Therefore, the VOF model was chosen for the simulations in this thesis work.

5.2.1 VOF model

According to AFTG 2019 [1], for each control volume in the computational domain, the volume fraction of the phases is determined by solving a single set of momentum equations for the phases in the VOF model. The VOF model focuses on tracking the interface between the phases. The VOF model is formulated in such a way that the phases do not interpenetrate each other. Every phase is described by its own volume fraction value and adding the volume fractions of all the phases inside a control volume results in the value of 1. The field variables and properties of the phases inside a control volume are described based on their respective volume fractions.

If a computational domain contains two phases: the primary phase p and the secondary phase q, the amount of a control volume occupied by the secondary phase can be described in terms of its volume fraction α_q as follows:

1. $\alpha_q = 0$: the control volume does not contain the secondary phase.

2. $\alpha_q = 1$: the control volume is filled completely with the secondary phase.

3. $0 < \alpha_q < 1$: the control volume contains both the primary and secondary phases. Hence, the interface between the phases is located inside this volume.

In addition to the mass conservation equation 5.1, a continuity equation is written with volume fraction as the variable in equation 5.8. It is also called the volume fraction equation, as given in equation 18.8 in page 545 of AFTG 2019 [1]. ANSYS Fluent solves equation 5.8 and tracks the interface between the phases. In equation 5.8, S_{α_q} is the additional mass source term, $\dot{m}_{pq}$ is the volumetric mass transfer rate from the primary phase p to the secondary phase q and $\dot{m}_{qp}$ is the reverse volumetric mass transfer rate from the secondary phase to the primary phase.

$$\frac{1}{\rho_q}\left[\frac{\partial}{\partial t}\left(\alpha_q \rho_q\right) + \nabla \cdot \left(\alpha_q \rho_q \vec{v_q}\right) = S_{\alpha_q} + \sum_{p=1}^{n}\left(\dot{m}_{pq} - \dot{m}_{qp}\right)\right] \tag{5.8}$$

ANSYS Fluent solves the volume fraction equation only for the secondary phase q and calculates the volume fraction of the primary phase p from the condition:

$$\alpha_p + \alpha_q = 1 \tag{5.9}$$

Implicit and explicit time formulations can be used to solve the volume fraction equation. In the implicit formulation, the volume fraction of the secondary phase is calculated by solving the transport equation for every time step because the volume fraction depends on other quantities at the current time step. On the other hand, the explicit formulation is a direct method, where the quantities known from the previous time step are used to calculate the volume fraction at the current time step, as explained in AFTG 2019 [1]. The explicit formulation was chosen for the numerical simulations in this thesis because of its better accuracy and ability to solve transient flow problems. According to equation 18.11 in page 546 of AFTG 2019 [1], the volume fraction is discretized using the explicit formulation as

$$\frac{\alpha_q^{n+1}\,\rho_q^{n+1} - \alpha_q^n\,\rho_q^n}{\triangle t} V + \sum_f \left(\rho_q\, U_f^n\, \alpha_{q,f}^n\right) = \left[\sum_{p=1}^{n} \left(\dot{m}_{pq} - \dot{m}_{qp}\right) + S_{\alpha_q}\right] V \tag{5.10}$$

The terms of the equation are:
$n+1$ - index for the current time step
n - index for the previous time step
$\alpha_{q,f}$ - volume fraction value of the secondary phase at the face of the computational cell
V - computational cell volume
U_f - volume flux through the face of the cell, which depends on the normal velocity

The density inside a computational cell is calculated from the volume fractions of the phases as

$$\rho = \alpha_q\,\rho_q + \left(1 - \alpha_q\right)\rho_p \tag{5.11}$$

and the volume-fraction-averaged density is given as

$$\rho = \sum \alpha_q\,\rho_q \tag{5.12}$$

ANSYS Fluent solves only one momentum equation, as given in equation 5.3. The fluid properties density and viscosity contain the volume fractions of the phases. Both phases share the velocity field that is obtained by solving the momentum equation.

5.2.2 Capillary pressure

The capillary pressure can be modelled in ANSYS Fluent using the continuum surface force (CSF) or continuum surface stress (CSS) methods. According to AFTG 2019 [1], if the surface tension is not constant, then the CSS model could be used. The CSF model in ANSYS Fluent is implemented from Brackbill et al. 1992 [9]. In the CSF model, the surface tension is added as a source term to the momentum equations. The surface tension and radii of curvature cause a pressure jump across an interface, as seen in the Young-Laplace equation (equation 2.29). AFTG 2019 [1] states that the divergence of the unit normal results in the curvature of the interface, as given in equation 5.13.

$$\kappa = \nabla \cdot \hat{n} \tag{5.13}$$

The unit normal $\hat{n}$ is calculated from the gradient of the volume fraction of the secondary phase as

$$\hat{n} = \frac{\nabla \alpha_q}{|\nabla \alpha_q|} \tag{5.14}$$

As reported in AFTG 2019 [1], ANSYS Fluent includes the volume force given in equation 5.15 as a source term in the momentum equation for depicting the surface tension in the CSF model.

$$F_v = \sigma \frac{\rho \kappa \nabla \alpha_p}{\frac{1}{2}\left(\rho_p + \rho_q\right)} \tag{5.15}$$

5.2.3 Wall adhesion

The wall adhesion in the CSF model is treated using the contact angle of the fluid with the wall. As shown in equation 5.16, the contact angle along with the normal and tangential unit vectors at the wall are used to calculate the unit normal to the surface of the cell adjacent to the wall. The local surface curvature depends on the contact angle and the unit normal to the cell surface adjacent to the wall (AFTG 2019 [1]).

$$\hat{n} = \hat{n}_w \cos\theta_c + \hat{t}_w \sin\theta_c \tag{5.16}$$

5.3 Simulation setup

In this section, the setup of 2D numerical simulations in ANSYS Fluent is elaborated.

5.3.1 Geometry

A 2D sketch of the tank geometry considered for the numerical simulations is shown in figure 5.1 and its dimensions are given in table 5.1. The tank has a cylindrical cross-section with a height of $H_T = 94\,\text{mm}$ and a radius of $R_T = 30\,\text{mm}$. It has a total empty volume of 265 mL. A vent port of radius $R_O = 2\,\text{mm}$ is provided at the top of the tank. An inlet pipe of length $L_I = 200\,\text{mm}$ and radius $R_I = 2\,\text{mm}$ is attached to the tank inlet port, to have a fully developed flow with a parabolic velocity profile of the incoming liquid at the inlet of the tank. The origin of the coordinate system is in the centre of the tank inlet. This tank geometry corresponds to the one that was used in the drop tower experiments, as discussed in section 4.1.1.1. The initial fill height of liquid inside the tank is denoted by H_L. In this thesis, different initial liquid fill heights in the range of $0\,\text{mm} \leq H_L \leq 60\,\text{mm}$ have been chosen to study the stability of the liquid interface by performing numerical simulations under reduced gravity conditions. The initial liquid fill heights H_L were chosen in such a way that the ratio H_L/R_T varies in the range of $0 \leq H_L/R_T \leq 2$.

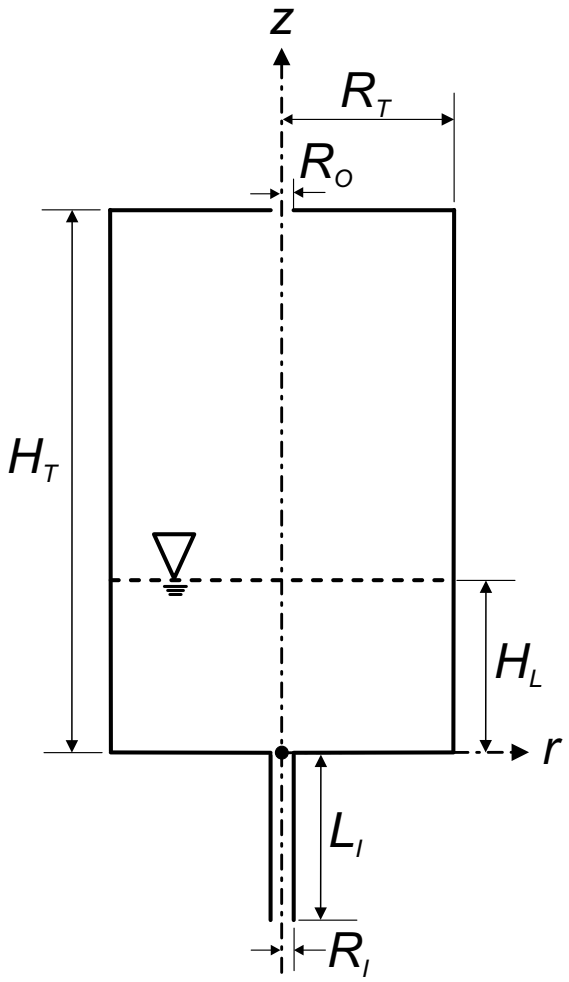

Figure 5.1: Tank geometry considered for numerical simulations.

Table 5.1: Dimensions of the tank considered for 2D numerical simulations. The total volume is 265 mL. The initial liquid fill height H_L was varied in the range of 0 mm $\leq H_L \leq$ 60 mm.

No.	Parameters	Dimensions/mm
1	H_T	94
2	R_T	30
3	R_I	2
4	R_O	2
5	L_I	200
6	H_L	0
		15
		30
		45
		60

The stability of the liquid interface in reduced gravity is characterized by the non-dimensional Weber number, which compares the stagnation pressure to the capillary pressure. Although various Weber numbers have been reported in the literature, the inlet Weber number as defined in equation 2.47 has been considered for the numerical simulations. The other dimensionless numbers, that are important for this problem, have already been discussed in section 2.9.

The tank geometry is simplified to a 2D axisymmetric model for the numerical simulations, as shown in figure 5.2. The flow direction is in the positive z-axis. The boundary conditions used for the numerical model are also shown in figure 5.2. The origin is located at the inlet of the tank. The z-axis is the symmetry axis. The inlet boundary is at the top left corner and the outlet boundary is at the top right corner in figure 5.2. All the other boundaries were chosen as a wall with a no-slip boundary condition.

It has to be noted that the default coordinate system for the 2D simulations in ANSYS Fluent is $x - y$ with x-axis chosen as the symmetry axis. Therefore, the z-axis of the model shown in figure 5.2 corresponds to the x-axis in ANSYS Fluent.

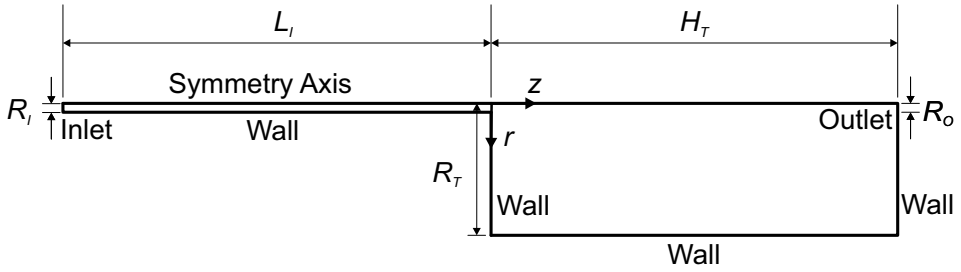

Figure 5.2: 2D axisymmetric model for numerical simulations.

The numerical simulations were carried out with the multiphase VOF model in ANSYS Fluent, where HFE-7500 was used as the liquid phase and air was chosen as the gas phase. The liquid mass flow rate was set as the inlet boundary condition and the outlet boundary condition was set to atmospheric pressure. The flow condition at the outlet boundary was not analysed in this study and it is assumed that the gas phase does not affect the interface, as no phase change has been considered.

The test matrix of the numerical simulations in reduced gravity is given in table 5.2. For every initial liquid fill height H_L, the numerical simulations were carried out with several inlet volumetric flow rates of HFE-7500 in the range of $1.00\,\mathrm{mL\,s^{-1}} \leq Q_L \leq 1.50\,\mathrm{mL\,s^{-1}}$. The corresponding mean inlet velocity v_I, inlet Weber number We_1, and inlet Reynolds number Re_1 are listed in table 5.2. From the Reynolds number range, it can be deduced that in all the simulations the flow is laminar.

Table 5.2: Test matrix of the numerical simulations.

No.	H_L/mm	Q_L/mL s^{-1}	$\dot{m}_L/10^{-3}$ kg s^{-1}	$v_I/10^{-3}$ m s^{-1}	We_1	Re_1
1	0	1.00	1.62	79.58	0.61	412.53
2		1.10	1.78	87.54	0.74	453.78
3		1.20	1.94	95.49	0.88	495.04
4		1.30	2.11	103.45	1.04	536.29
5		1.40	2.27	111.41	1.20	577.54
6		1.50	2.43	119.37	1.38	618.79
7	15	1.00	1.62	79.58	0.61	412.53
8		1.10	1.78	87.54	0.74	453.78
9		1.20	1.94	95.49	0.88	495.04
10		1.30	2.11	103.45	1.04	536.29
11		1.40	2.27	111.41	1.20	577.54
12		1.50	2.43	119.37	1.38	618.79
13	30	1.00	1.62	79.58	0.61	412.53
14		1.10	1.78	87.54	0.74	453.78
15		1.20	1.94	95.49	0.88	495.04
16		1.30	2.11	103.45	1.04	536.29
17		1.40	2.27	111.41	1.20	577.54
18		1.50	2.43	119.37	1.38	618.79
19	45	1.00	1.62	79.58	0.61	412.53
20		1.10	1.78	87.54	0.74	453.78
21		1.20	1.94	95.49	0.88	495.04
22		1.30	2.11	103.45	1.04	536.29
23		1.40	2.27	111.41	1.20	577.54
24		1.50	2.43	119.37	1.38	618.79
25	60	1.00	1.62	79.58	0.61	412.53
26		1.10	1.78	87.54	0.74	453.78
27		1.20	1.94	95.49	0.88	495.04
28		1.30	2.11	103.45	1.04	536.29
29		1.40	2.27	111.41	1.20	577.54
30		1.50	2.43	119.37	1.38	618.79

5.3.2 Meshing

The 2D mesh created using ANSYS Meshing is shown in figure 5.3. The `MultiZone Quad/Tri Method` was used to create 2D quadratic elements. To investigate the influence of mesh element size on the numerical simulation results, a mesh sensitivity study was carried out by creating four meshes with varying order of refinement in terms of element sizes in the range of 62.5 µm - 500 µm. The boundary layer at the tank wall opposite to the symmetry axis at $r = 30$ mm was resolved with 20 layers with a first layer height of 1×10^{-5} m to capture the rise of the liquid meniscus at the wall due to the complete wetting behaviour of the liquid with the wall. The resolved boundary layer at the wall is also shown in figure 5.3.

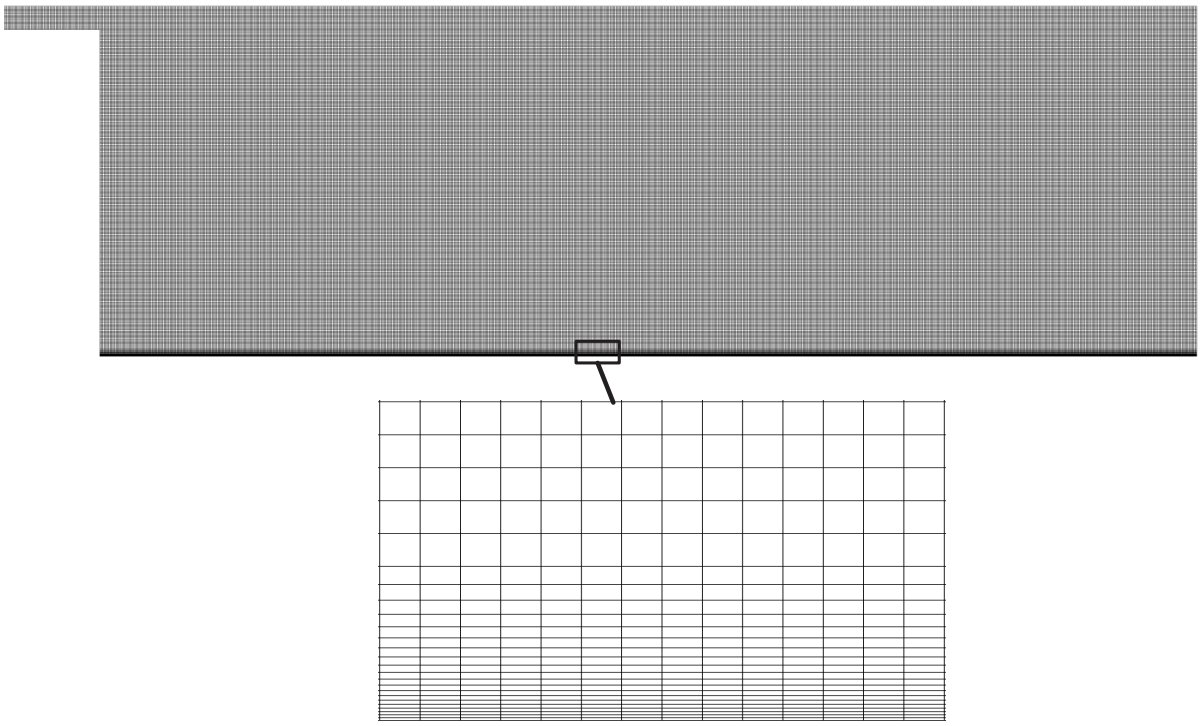

Figure 5.3: 2D mesh of the tank model used for the numerical simulations with a magnified portion of the boundary layer resolution at the wall. The inlet pipe is not shown fully.

5.3.3 Solver settings

ANSYS Fluent 19.2 was used as the flow solver for the numerical simulations. The solver settings that were selected are discussed in this section in the order in which they appear in the outline view of the ANSYS Fluent graphical user interface (GUI). The description of each setting is taken from AFUG 2019 [2]. Some of the important settings are summarized in table 5.5.

General

The solver type was chosen as `Pressure-Based` because it supports the multiphase flow problems with the VOF model. The `Pressure-Based` solver is also the default setting of ANSYS Fluent. In this method, the momentum equations are solved for the velocity field and

the pressure-based continuity equation is solved for obtaining the pressure field. `Absolute Velocity Formulation` was selected for the simulations, as the fluid velocity is small in the majority of the fluid domain. The liquid filling process is a time-dependent process and therefore the simulations were run with the `Transient` setting. The geometry of the tank was modelled as axisymmetric. Therefore, `Axisymmetric` was chosen. ANSYS Fluent by default sets the $x-y$ coordinate system for the 2D simulations. Therefore, the x-axis was chosen as the axial coordinate and the y-axis as the radial coordinate for the 2D simulations. For simulations in normal gravity, the gravitational acceleration was set to $-9.81\,\mathrm{m\,s^{-2}}$ in the x-axis and for simulations in reduced gravity, the gravity was turned off.

Models

The `Multiphase Model` was activated by choosing the `Volume of Fluid` model. The liquid filling simulations consist of liquid and gas phases. Therefore, the `Number of Eulerian Phases` was specified as 2. The `Explicit Formulation` was chosen for the volume fraction, as it is more accurate than the implicit formulation. The limiting factor for the explicit formulation is the Courant number, which relates the distance travelled by the flow at a given time step to the size of one computational cell. The Courant number is given by equation 5.17, where u is the flow velocity, $\triangle t$ is the time step and $\triangle x$ is the size of the computational cell.

$$\mathrm{C} = \frac{u \triangle t}{\triangle x} \tag{5.17}$$

The `Volume Fraction Cutoff` value was set to the default value of 1×10^{-6}. The value of volume fraction in the flow domain is considered to be zero, if it drops below the cut-off value. ANSYS Fluent uses a different time step for the calculation of volume fraction, than the time step which is typically used for the transport equations. The time step used for the VOF calculation is called the `Sub-Time Step` in ANSYS Fluent and is calculated using the maximum value of the Courant number near the interface. The default method for the calculation of the sub-time step is the `Hybrid` method, which is a combination of velocity and flux averaged methods. The maximum `Courant Number` was set to the default value of 0.25. In order to make the computations more robust and improve the convergence, the `Implicit Body Force` was selected in the `Body Force Formulation`. The type of `Interface Modeling` was selected as `Sharp` because the interface can be clearly noticed between the liquid and gas phases. All the other options remained unselected.

According to AFUG 2019 [2], the stability of a computation can be improved by specifying a phase as the primary phase if it is a compressible gas. Although in this thesis, the numerical simulations did not involve any compressible gas, air was defined as the primary phase and HFE-7500 as the secondary phase. The simulations were performed under isothermal conditions and did not include any phase change between the phases. Therefore, the `Number of Mass Transfer Mechanisms` was set to 0 in the `Phase Interactions` setting. The `Continuum Surface Force` (CSF) method was used to model the surface tension. In this method, the surface tension property is considered to be continuous across the interface and added as a source term to the momentum equation, as reported in AFTG 2019 [1]. In the numerical simulations, the surface tension coefficient was set to a constant value of $0.0167\,\mathrm{N\,m^{-1}}$ between the phases HFE-7500 and air and henceforth, the CSF method was used appropriately.

By choosing the `Wall Adhesion` option, the curvature of the interface near the solid wall is calculated from the contact angle of the fluid with the wall. All the numerical simulations in this thesis were carried out in the laminar regime and therefore, the `Laminar Viscous Model` was enabled.

Materials

The `Material Type` was `fluid` for both air and HFE-7500. The properties of the test liquid HFE-7500 at 25 °C are given in table 5.3. The properties of air were the default properties from the ANSYS Fluent database. The properties density and viscosity were defined as constants for both fluids in the ANSYS Fluent setup.

Table 5.3: Fluid properties used in the simulations.

Phase	Fluid	ρ/kg m^{-3}	μ/kg m^{-1} s^{-1}	σ/N m^{-1}
Primary	Air	1.225	1.7894×10^{-5}	-
Secondary	HFE-7500	1620	0.00125	0.0167

Cell Zone Conditions

In the `Cell Zone Conditions` setting, the `Operating Conditions` for the simulations were specified. The `Operating Pressure` was defined as atmospheric pressure with a value of 101 325 Pa, which is the default setting in ANSYS Fluent. The `Reference Pressure Location` was set to $x = 0.094$ m and $y = 0$ m, which signifies the outlet of the tank. For the simulations in normal gravity, the gravitational acceleration was automatically set in the `Operating Conditions` dialog box, as defined in the `General` setting. Additionally, the `Specified Operating Density` was selected and the density of air was set as `Operating Density` by default.

Boundary Conditions

Five different types of boundary conditions were set to the different zones of the computational domain. The zones were named during the mesh generation in ANSYS Meshing. The zones and their corresponding type of boundary condition are listed below. ANSYS Fluent chooses the zone name and type `interior` by itself.

1. central-inlet: `mass-flow-inlet`
2. outlet: `pressure-outlet`
3. symmetry-axis: `axis`
4. wall: `wall`
5. interior-sys-8_surface, sys-8_surface: `interior`

The boundary conditions can be set separately for the two phases air and HFE-7500. Along with that, ANSYS Fluent combines the two phases and offers the `mixture` phase, with which some boundary conditions can be defined as well. The inlet mass flow rate was defined as the inlet boundary condition for the central-inlet zone. For the `mixture` phase, the direction of the inlet boundary condition was set as `Normal to Boundary`. The `Mass Flow Rate` was set to $0\,\mathrm{kg\,s^{-1}}$ for the `air` phase, as only the liquid HFE-7500 was injected into the tank. The numerical simulations were carried out for several inlet volumetric flow rates of HFE-7500. The corresponding mass flow rates, as given in table 5.2, were prescribed as the inlet boundary condition for the phase HFE-7500.

The outlet boundary condition was set to `pressure-outlet` for the `mixture` phase. A constant value of 0 Pa was specified for the `Gauge Pressure`, which is equivalent to the atmospheric pressure of 101 325 Pa set in the `Operating Conditions`. Additionally, the `Backflow Volume Fraction` was set to 0 for the liquid phase HFE-7500. The boundary condition type `axis` was assigned to the symmetry-axis zone of the computational domain, as it represents the symmetry axis of the numerical model. The outer walls of the inlet pipe and the tank were defined as `wall` boundary condition. For the `mixture` phase, only the `Momentum` tab was active, in which `Stationary Wall` with `No Slip` shear condition was enabled by default. Furthermore, under `Wall Adhesion`, the contact angle between HFE-7500 and air was specified as 0°.

Methods

The default `SIMPLE` scheme was used for the `Pressure-Velocity Coupling`. SIMPLE is a segregated type of algorithm in ANSYS Fluent, in which the pressure and velocity are solved in a sequence. The pressure is first corrected using the under-relaxation factor and then the face flux is corrected. ANSYS Fluent recommends the Pressure-Implicit with Splitting of Operators (`PISO`) algorithm for transient flow problems. However, no significant difference was observed between SIMPLE and PISO methods for the numerical simulations performed in this thesis work. Therefore, the default `SIMPLE` scheme was used in all the simulations. The convective and diffusive terms in the governing equations are discretized by gradients. The computationally less expensive `Least Squares Cell Based` method is used by ANSYS Fluent to calculate the gradients at the centre of a cell. Therefore, this method was also used for the simulations in this thesis. The pressure values at the cell faces were calculated using the Pressure Staggering Option (`PRESTO!`) scheme, which is the default method for the VOF multiphase flow problems. The momentum equation was discretized using the `Second Order Upwind` method, which is more accurate than the first order upwind method and leads to better results. The volume fraction was discretized using the `Geo-Reconstruct` scheme, which tracks the interface accurately by assuming the slope of the interface to be piecewise-linear in a cell. The conservation equations were temporally discretized using the `First Order Implicit` formulation. The implicit method is unconditionally stable and an accuracy of first order was sufficient for the numerical simulations.

The `Under-Relaxation Factors` were set to the default values under the `Solution Controls` setting. For the convergence of the numerical simulations in every time step, the `Absolute Criteria` of the residuals from the conservation equations were unchanged from their default values of 1×10^{-3} under the `Monitors` setting.

Initialization

The numerical simulations with initial liquid fill heights ($H_L > 0\,\text{mm}$) were initialized by marking the region and patching it with a value of 1 for the liquid volume fraction. This was done by choosing `Region Adaption` from the `Mark/Adapt Cells` option in the `Adapt` tab of the Fluent ribbon at the top of the user interface. Then, the input coordinate corresponding to the required initial liquid fill height was specified in the `X Max (m)` box. The other coordinates were fixed for all the simulations with the values `X Min` $= -0.2\,\text{m}$, `Y Min` $= 0\,\text{m}$ and `Y Max` $= 0.03\,\text{m}$. After specifying the values, the button `Mark` was pressed to mark the cells within the given coordinates. The solution was then initialized using the `Hybrid Initialization` method. Furthermore, the `Patch` button was clicked, the liquid HFE-7500 was selected from the drop-down menu `Phase` and the variable `Volume Fraction` was clicked. Then, `hexahedron-r0` was selected from the `Registers to Patch` and the value of 1 was entered for the liquid volume fraction. In this way, the initial liquid fill height was set in the domain that was marked in the previous step.

Run Calculation

The timeline of the simulations is shown in table 5.4. The simulations of a pre-filled tank were carried out in three stages. In order to establish an initial condition for the simulations in reduced gravity, the simulations were first started in normal gravity with an initial liquid fill height and run until $t = 3\,\text{s}$, such that the liquid meniscus rises at the wall to a height corresponding to the Laplace length from its initial level, as given in equation 2.33. During this stage, all the boundaries were defined as a wall and the gravitational acceleration was set to $-9.81\,\text{m}\,\text{s}^{-2}$ for the x-axis under the `General` settings of the ANSYS Fluent solver. In the second stage, after $t = 3\,\text{s}$ of simulation time, the gravity was turned off with the gravitational acceleration set to $g_E = 0\,\text{m}\,\text{s}^{-2}$ and the pre-filled tank simulations were run until $t = 6.5\,\text{s}$ further without any inlet and outlet boundary conditions. This was performed to let the liquid inside the tank reorient, as expected in the drop tower experiments. In the third stage, at $t = 6.5\,\text{s}$, the inlet and outlet boundary conditions were defined and the simulations of liquid filling were continued under reduced gravity conditions until $t = 12\,\text{s}$, such that the total time in reduced gravity is 9 s, which corresponds approximately to the maximum microgravity time achievable in the Bremen Drop Tower. For the vented filling of an initially empty tank ($H_L = 0\,\text{mm}$), the computational domain was initialized completely with the primary phase (air) and the numerical simulations of liquid filling into an initially empty tank were started directly under reduced gravity conditions at $t = 0\,\text{s}$ and run until $t = 9\,\text{s}$, as shown in table 5.4.

The transient numerical simulations were carried out with a fixed time step size of $1 \times 10^{-4}\,\text{s}$. The time step sizes higher than $1 \times 10^{-4}\,\text{s}$ did not lead to a proper convergence of the solution. The time step size was reduced to $5 \times 10^{-5}\,\text{s}$ only for some of the simulation cases of an initially empty tank, in which convergence problems occurred. The number of time steps was varied for the different stages of the pre-filled simulations. For the simulations of an initially empty tank, the `Number of Time Steps` was set to 90 000, which corresponds to a reduced gravity time of 9 s. The `Max Iterations/Time Step` was set to 100, such that the residuals of the conservation equations are converged for every time step. The output data was saved for every 1000 time steps.

The important solver settings are summarized in table 5.5. The simulations were run on a cluster with 16 processors. The total time duration of the pre-filled tank simulations was in the range of 15 h - 20 h and the simulations of an initially empty tank ran for about 40 h - 45 h.

Table 5.4: Timeline of the numerical simulations.

t/s	Pre-filled	Empty
0	Start of $1g_E$	Start of $0g_E$ and start of filling
3.0	End of $1g_E$ and start of $0g_E$	-
6.5	Start of filling	-
9.0	-	End of $0g_E$ and end of filling
12.0	End of $0g_E$ and end of filling	-

Table 5.5: ANSYS Fluent solver settings.

Solver type	Pressure-based
Simulation type	Transient
Multiphase model	VOF
Volume fraction formulation	Explicit
Interface modelling	Sharp
Surface tension model	Continuum surface force
Adhesion options	Wall adhesion
Viscous model	Laminar
Operating pressure	101 325 Pa
Scheme	SIMPLE
Pressure discretization	PRESTO!
Momentum discretization	Second-order upwind
Transient formulation	First-order implicit
Time step size	1×10^{-4} s
Maximum iterations per step	100

5.3.4 Post-processing

The centre point detection method followed in the numerical simulations is shown in figure 5.4 for the three simulation cases considered in this thesis. The centre point η_c is defined as the point on the interface on the z-axis ($r = 0$ mm). For the reorientation simulation, the lowermost point of the liquid interface is detected as the centre point, whereas for simulations of filling

into a pre-filled and an initially empty tank, the uppermost point of the liquid interface is the centre point. z_c is the height measured from the origin of the tank to the centre point of the interface, as shown in figure 5.4. This height is called the geyser height when a geyser is formed, as shown in figures 5.4b and 5.4c.

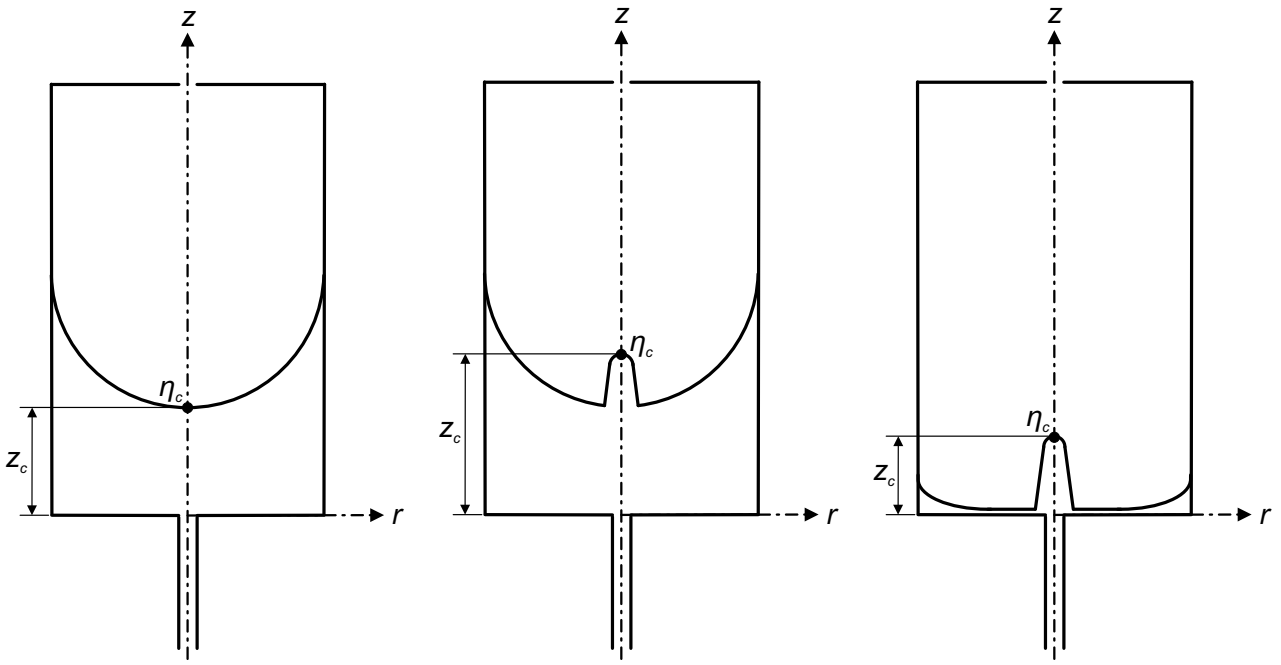

(a) Reorientation (b) Pre-filled (c) Empty

Figure 5.4: Centre point detection method followed in the numerical simulations.

The numerical simulation results were visualized and analysed using the post-processing tool ANSYS CFD-Post 19.2. The centre point of the liquid interface was determined from the simulation results in the following manner.

1. An `Isosurface` was created with the variable `Hfe.Volume Fraction` and value 0.5. This displayed the liquid interface boundary in the computational domain.

2. The isosurface was clipped by creating an `Iso Clip` with the visibility parameter `Y` $\leq 0.25\,\mathrm{mm}$. This made the isosurface to be visible only in the given region. This step was exclusively performed to detect the centre point of the liquid interface in the vicinity of the symmetry axis.

3. The centre point of the interface on the symmetry axis was found using the new expression `maxVal(X)@Iso Clip 1`. This expression was later used in the `XY-Transient or Sequence` chart in ANSYS CFD-Post to plot the centre point positions over time. The data was then exported by pressing the `Export` button.

5.3.4.1 Criterion for an unstable interface

The liquid jet that penetrates the interface forms a geyser, as explained in section 2.6. According to Symons et al. 1968 [86], during the liquid filling into a tank, the liquid interface is stable, if the geyser height does not vary with time. The interface becomes unstable, either if the geyser height increases continuously with time forming a long column of liquid or if the geyser disintegrates into liquid droplets.

The 2D numerical simulations were carried out for a total reduced gravity time of 9 s, which corresponds approximately to the maximum microgravity time achievable in the Bremen Drop Tower. A criterion for an unstable interface could not be defined based on the growth of the geyser height for this timescale. Therefore, in this thesis work, the disintegration of the geyser into liquid droplets was considered as the criterion for defining the interface to be unstable. The lowest inlet volumetric flow rate Q_L at which the geyser breaks into droplets is the critical flow rate and the interface is considered to be unstable for this critical flow rate. The corresponding critical Weber number is calculated using equation 2.47. The maximum height reached by the geyser before it disintegrates into droplets is called the critical geyser height z_{cr} and the time at which the first droplet disintegrates from the geyser after the start of liquid filling is called the droplet breakup time t_b. The interface is considered to be stable for all the flow rates, where the geyser does not disintegrate into droplets.

5.4 Mesh sensitivity study

Before beginning with the numerical investigation of interface stability during the liquid filling, the sensitivity of the mesh element size on the numerical simulation results was studied as the first step. The meshes of different sizes, as listed in table 5.6, were used for the mesh sensitivity study.

Table 5.6: Meshes created for the mesh sensitivity study.

Mesh parameter	Mesh 1	Mesh 2	Mesh 3	Mesh 4
Element size / µm	62.5	125	250	500
No. of elements	854400	221120	59040	16640

The mesh sensitivity study was conducted only for the pre-filled tank simulations with $H_L = 30\,\text{mm}$. Figure 5.5 shows the velocity profiles of the liquid jet at the exit of the inlet pipe ($z = 0$ mm) for different meshes. This is plotted from the simulations carried out with an inlet volumetric flow rate of $Q_L = 1.30\,\text{mL}\,\text{s}^{-1}$. The plot corresponds to a simulation time of $t = 12\,\text{s}$. It can be seen from figure 5.5 that the finer the mesh, the closer it matches the theoretical value of the parabolic velocity profile of the fully developed flow. The theoretical values, which are shown as black dots in figure 5.5, were calculated using equations 2.39 and 2.40 for the Hagen-Poiseuille flow. The liquid jet velocity reaches its maximum value at the pipe centre and it is depicted well by mesh 1 and mesh 2.

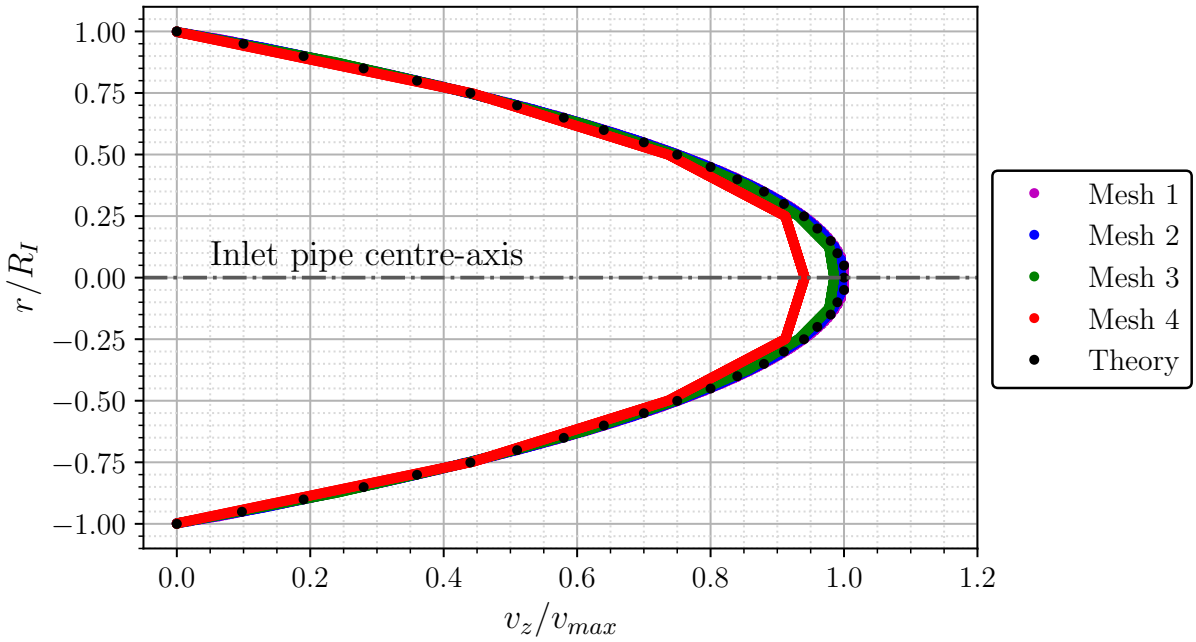

Figure 5.5: Velocity profiles of the liquid jet at the exit of the inlet pipe for different meshes with $Q_L = 1.30\,\mathrm{mL\,s^{-1}}$ and $H_L = 30\,\mathrm{mm}$ at $t = 12\,\mathrm{s}$.

The position of the centre point of the liquid interface is plotted over time in figure 5.6 for $Q_L = 1.30\,\mathrm{mL\,s^{-1}}$ and for four different mesh sizes considered. From $t = 0\,\mathrm{s}$ to $t = 3\,\mathrm{s}$, the simulations were run in $1g_E$ condition, where the liquid meniscus develops at the tank wall. As the centre point of the liquid interface does not move during this period, the results of all the meshes are superimposed. Liquid reorientation from a gravity-dominated configuration into a capillary-dominated configuration takes place between $t = 3\,\mathrm{s}$ and $t = 6.5\,\mathrm{s}$, where gravity is turned off. It can be seen from figure 5.6 that the mesh refinement affects the amplitude and frequency of oscillation of the centre point. Mesh 1 and mesh 2 capture the centre point oscillation well. The filling of the tank was started at $t = 6.5\,\mathrm{s}$. In this domain, the effect of mesh element size on the geyser height can be observed. The coarsest mesh (mesh 4) produces the lowest geyser height. As the mesh element size decreases, the geyser height increases. The geyser height results of mesh 1 and mesh 2 are in good agreement with each other, with an average deviation of 2.6 % between them. Taking the accuracy and computational effort into account, mesh 2 was selected for performing further numerical simulations and the details of mesh 2 are once again highlighted in table 5.7.

Table 5.7: The details of the mesh chosen for the numerical simulations after the mesh sensitivity study.

Mesh ID	Mesh element size	No. of elements
Mesh 2	125 µm	221120

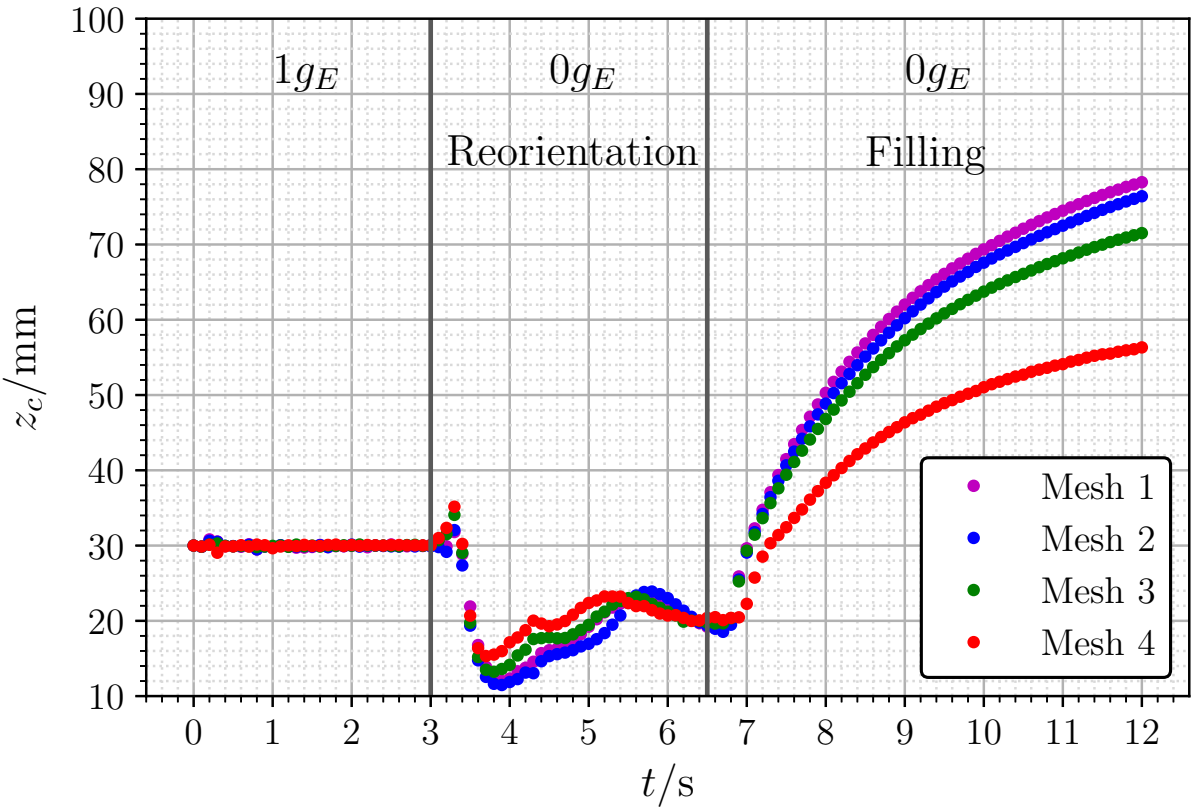

Figure 5.6: Evolution of the centre point of the interface over time for different meshes at $Q_L = 1.30\,\mathrm{mL\,s^{-1}}$ and $H_L = 30\,\mathrm{mm}$.

Chapter 6

Results and Discussion

The results of the ground experiments, drop tower experiments, parabolic flight experiments as well as the 2D numerical simulations are discussed in this chapter. Then, the numerical simulation results are compared with some of the drop tower experiments. Furthermore, a parametric study carried out with different initial liquid fill heights H_L and refined volumetric flow rates Q_L is presented and the results of simulations and drop tower experiment are compared with the existing literature.

The contents in sections 6.2 and 6.8 have been published in Govindan and Dreyer 2023 [40]. Some of the contents in section 6.4 have been published in Govindan and Dreyer 2023 [41]. These contents are reused here with permission.

6.1 Ground experiments

Ground experiments of liquid filling into the experiment tank were performed with the same experimental setup, as described in section 4.1.1. HFE-7500 was used as the test liquid. The ground experiments were performed for different initial liquid fill heights in the range of $9.6\,\mathrm{mm} \leq H_L \leq 45.6\,\mathrm{mm}$. The liquid was filled into the experiment tank for 4.6 s and the interaction of the incoming liquid jet with the liquid interface was observed. The volumetric flow rates were varied between $0.8\,\mathrm{mL\,s^{-1}} \leq Q_L \leq 4.8\,\mathrm{mL\,s^{-1}}$ for every initial liquid fill height H_L. Based on the inlet Reynolds number Re_1 given in table 4.5, the flow remained laminar for all the chosen volumetric flow rates. The experiments were performed under isothermal conditions with an average liquid temperature of $T_L = 23\,^{\circ}\mathrm{C}$.

Under the influence of gravity, the body forces are dominant and as a result, the liquid interface remains flat. The interface shape in normal gravity is defined by the Bond number, which compares the hydrostatic and capillary pressures, as shown in equation 2.31. A higher hydrostatic pressure exists in normal gravity due to the placement of the experiment tank above the pump platform, as shown in figure 4.1. The liquid meniscus has a curved shape at the wall and the contact point of the meniscus rises to a height h at the wall due to capillarity.

For HFE-7500 at 25 °C, the capillary length calculated from equation 2.32 is $L_c = 1.02\,\text{mm}$ and the meniscus rising height in normal gravity determined from equation 2.33 is $h = 1.45\,\text{mm}$.

The filling patterns formed during the filling of liquid into the experiment tank in normal gravity for different H_L and Q_L are shown in figures 6.1 and 6.2. Figure 6.1 corresponds to the filling time of $t = 0.5\,\text{s}$ and figure 6.2 corresponds to the filling time of $t = 4.5\,\text{s}$. The liquid filling in normal gravity was recorded by two cameras with a frame rate of 500 frames per second and a resolution of 512×512 pixels. However, in figures 6.1 and 6.2, the images are cropped to show only the regions of interest. Furthermore, the images corresponding to an initial liquid fill height of $H_L = 45.6\,\text{mm}$ were captured from the camera CAM2, while all the other images were captured from the camera CAM1. A quiescent filling takes place for $Q_L = 0.8\,\text{mL}\,\text{s}^{-1}$ for all the initial liquid fill heights H_L, where the liquid jet momentum is diffused in the bulk liquid and the jet does not perturb the liquid interface, as seen in figures 6.1 and 6.2. A small bulge at the centre of the liquid interface can be observed for $Q_L = 1.8\,\text{mL}\,\text{s}^{-1}$. The momentum of the liquid jet overcomes the body forces to form a tiny bulge on the liquid interface. While the bulge is still developing for all H_L at $t = 0.5\,\text{s}$ for $Q_L = 1.8\,\text{mL}\,\text{s}^{-1}$ in figure 6.1, the height of the bulge decreases as H_L increases at $t = 4.5\,\text{s}$, which can be observed in figure 6.2 (b), (g), (l), (q) and (v). The liquid jet penetrates the interface and a more pronounced bulge can be seen in both figures 6.1 and 6.2 for $Q_L = 2.8\,\text{mL}\,\text{s}^{-1}$ for all H_L. The bulge begins to oscillate.

As the flow rate is increased to $Q_L = 3.8\,\text{mL}\,\text{s}^{-1}$, the liquid jet becomes unstable and forms irregular flow structures, as seen in figures 6.1 and 6.2. Furthermore, the liquid jet creates a depression on the liquid interface, which also triggers the propagation of the surface waves for $Q_L = 3.8\,\text{mL}\,\text{s}^{-1}$ and $Q_L = 4.8\,\text{mL}\,\text{s}^{-1}$. The fragments of the liquid jet that fall back into the interface, set the liquid interface in motion and thereby the interface begins to undergo sloshing. A clear increase in fill levels with time can be noticed from the position of the meniscus between the figures 6.1 and 6.2 for all Q_L and H_L. Within the range of tested flow rates, the interface can be termed stable for $Q_L \leq 2.8\,\text{mL}\,\text{s}^{-1}$ and unstable for $Q_L > 2.8\,\text{mL}\,\text{s}^{-1}$ for all the tested initial liquid fill heights H_L in normal gravity. The critical flow rate at which the interface becomes unstable can be determined more accurately, if the flow rates are refined in the range of $2.8\,\text{mL}\,\text{s}^{-1} < Q_L < 3.8\,\text{mL}\,\text{s}^{-1}$.

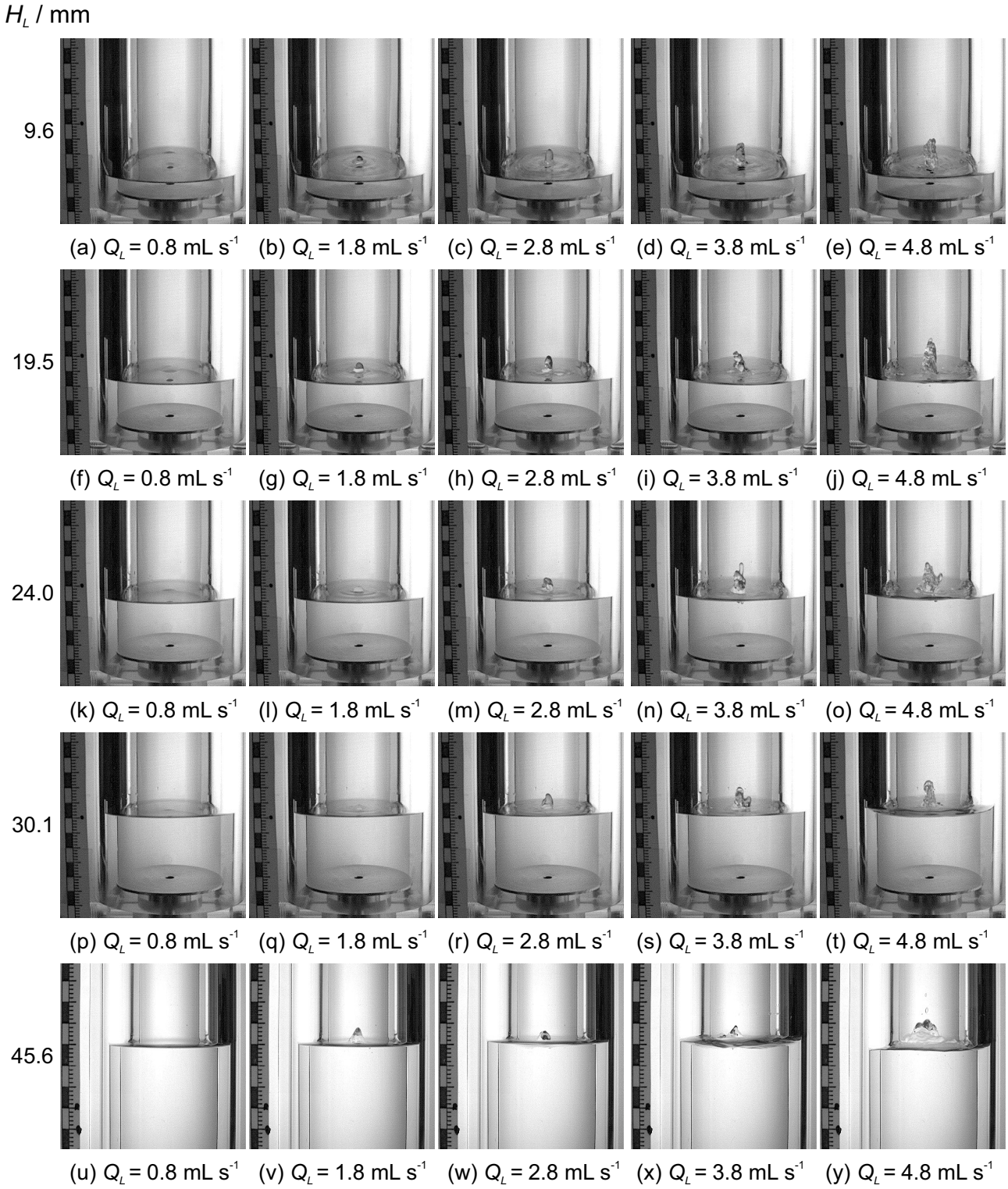

Figure 6.1: Filling patterns observed during the filling of liquid into the experiment tank under normal gravity conditions for different initial liquid fill heights H_L and volumetric flow rates Q_L at $t = 0.5\,\mathrm{s}$.

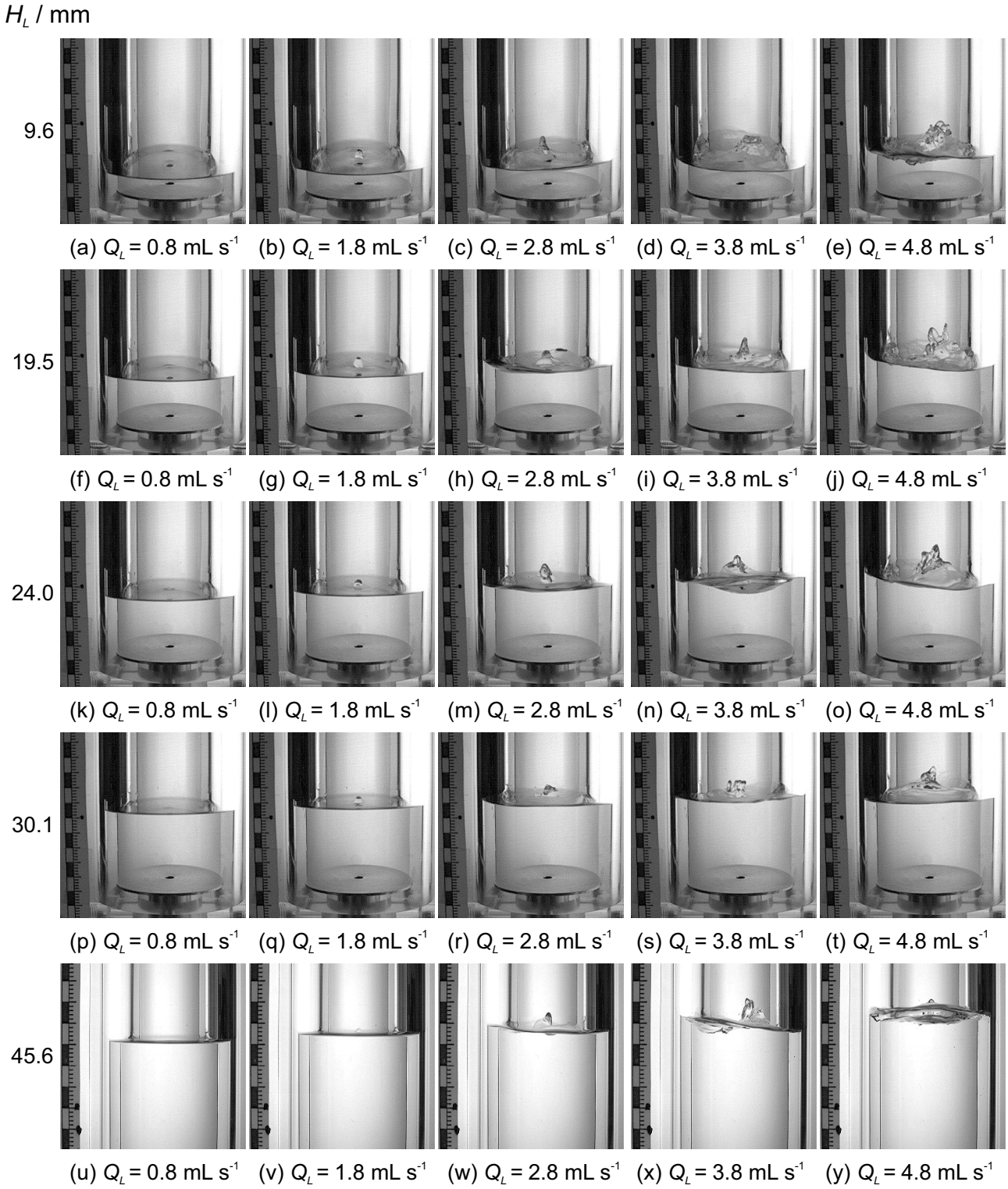

Figure 6.2: Filling patterns observed during the filling of liquid into the experiment tank under normal gravity conditions for different initial liquid fill heights H_L and volumetric flow rates Q_L at $t = 4.5\,\mathrm{s}$.

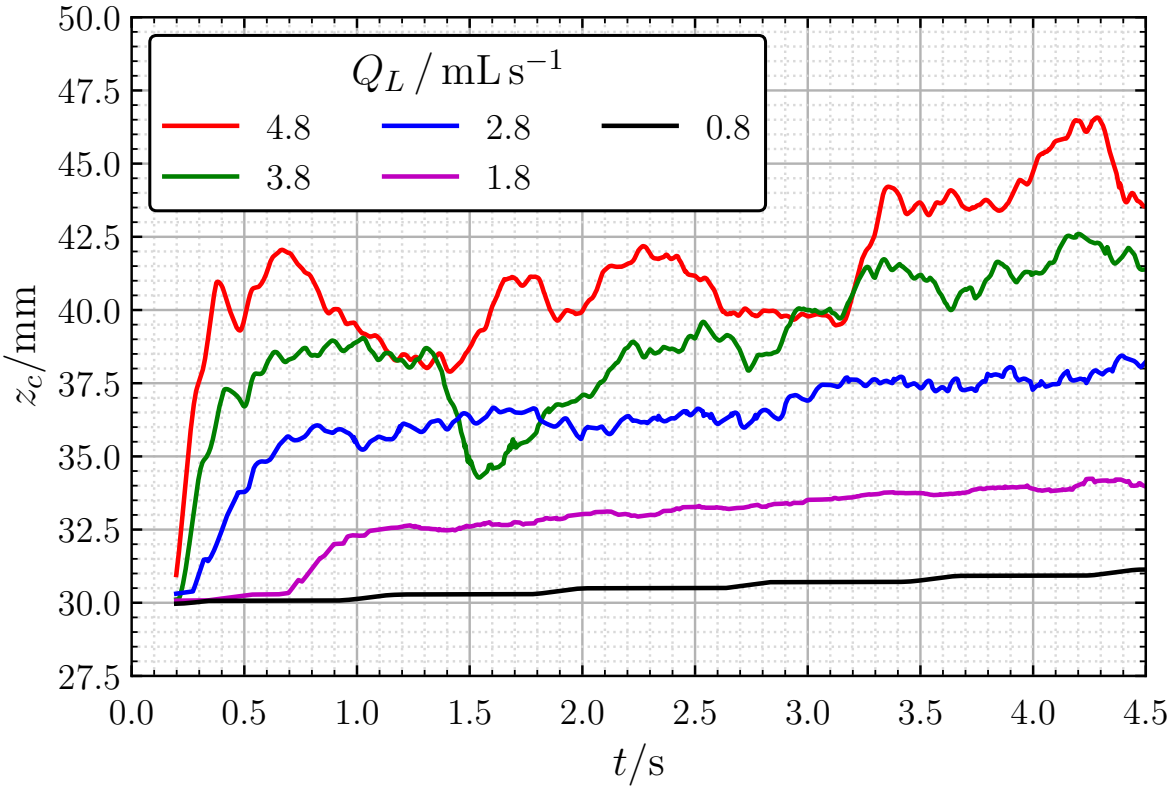

Figure 6.3: Evolution of the centre point position of the interface over time during the liquid filling in normal gravity for $H_L = 30.1\,\text{mm}$ and different Q_L.

The centre point position of the liquid interface (z_c) during the liquid filling in normal gravity is plotted over time for an initial liquid fill height of $H_L = 30.1\,\text{mm}$ for different Q_L in figure 6.3. This can also be called the surface elevation in normal gravity. The recorded images were processed and the centre point of the interface was detected as an edge. A moving average of 100 was performed on the original data, which was sampled at 500 frames per second. A smooth increase in the centre point position can be observed for $Q_L = 0.8\,\text{mL s}^{-1}$ and $1.8\,\text{mL s}^{-1}$, as the interface remains stable. This demonstrates a quiescent and steady filling of the tank. The perturbation of the interface by the liquid jet causes an initial rise in the position of the centre point for $Q_L \geq 1.8\,\text{mL s}^{-1}$. After an initial surge, the centre point of the interface shows a growing trend with fluctuations for $Q_L = 2.8\,\text{mL s}^{-1}$. A clear indication of an unstable interface is shown for higher flow rates of $Q_L = 3.8\,\text{mL s}^{-1}$ and $Q_L = 4.8\,\text{mL s}^{-1}$, where the centre point fluctuations are amplified due to the sloshing motion of the interface and formation of unsteady flow structures.

The ground experiments helped to understand the experimental setup and formulate a procedure for data evaluation and image processing. It was shown from the ground experiments that the interface becomes unstable for $Q_L > 2.8\,\text{mL s}^{-1}$ for all the initial liquid fill heights H_L chosen in the study. The influence of the initial liquid fill height H_L on the critical flow rate Q_L for determining the instability of the interface could not be precisely identified within the selected range in the ground experiments. Furthermore, the dominant body forces restrict the development of an undisturbed liquid jet in the ullage region, which would otherwise occur for lower flow rates in microgravity.

6.2 Drop tower experiments

The data from 15 tests, as listed in table 4.3, are considered for the analysis. The drop tower experiment results are divided into two sections:

1. Liquid reorientation
2. Filling of the tank

6.2.1 Liquid reorientation

In order to observe the reorientation of the liquid interface inside the tank and also to determine the starting time of the liquid filling into the experiment tank under microgravity conditions, three reorientation tests were carried out with a pre-filled tank of $H_L = 30\,\text{mm}$. The filling of tank was not performed during the reorientation tests in microgravity. One test was a drop test with a microgravity time of 4.6 s and the other two tests were catapult tests with a longer microgravity time of 9 s. As soon as the capsule enters microgravity, the liquid meniscus rises along the tank wall, due to the complete wetting behaviour and the contact angle of 0° of the test liquid HFE-7500. There is a capillary wave, that propagates from the tank wall towards the centre axis and the centre point of the liquid interface begins to move downwards. This leads to an axial sloshing of the liquid inside the tank and the interface becomes hemispherical.

The reorientation of liquid under microgravity at different time steps is shown in figure 6.4 for the catapult test F31. The flat interface of the liquid with some vibrations can be observed at $t = 0\,\text{s}$ in figure 6.4(a). The vibrations are caused due to the launch of the catapult system. Then, the interface changes from a gravity-dominated shape to a capillary-dominated shape in microgravity and this leads to a hemispherical shape of the interface, as seen in figure 6.4(b). At $t = 9\,\text{s}$, the interface approaches its equilibrium position in microgravity.

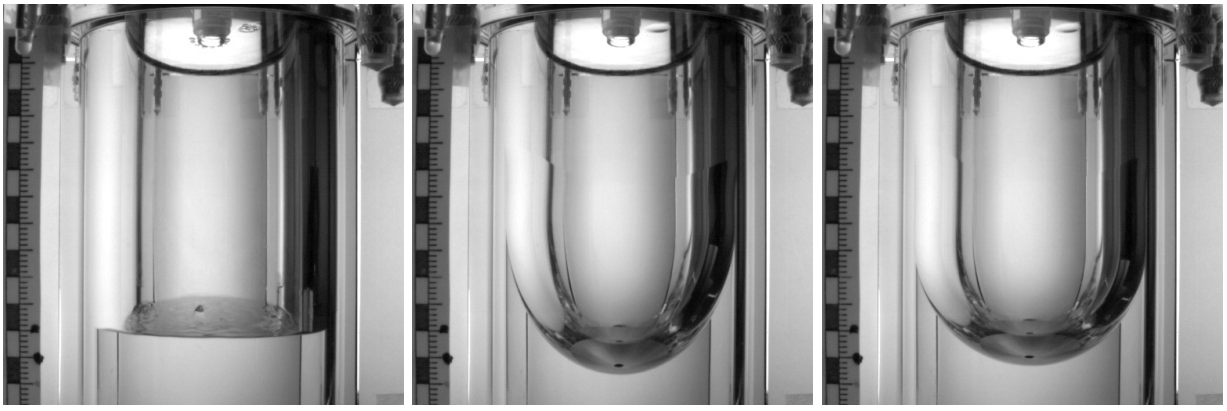

(a) t = 0 s (b) t = 4.5 s (c) t = 9 s

Figure 6.4: Liquid reorientation inside the tank under microgravity for the catapult test F31. The vibrations on the liquid interface at $t = 0\,\text{s}$ are caused due to the launch of the catapult system.

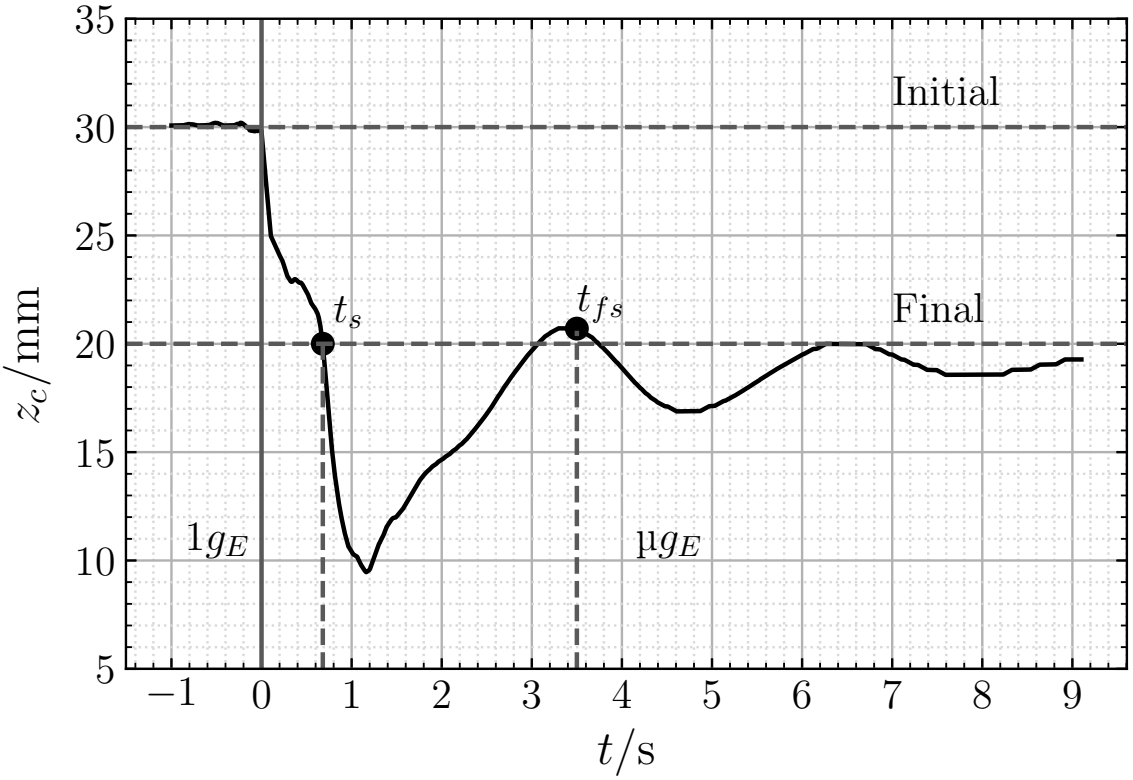

Figure 6.5: The centre point oscillation during the reorientation test F31. The capillary wave hinders the accurate detection of the centre point position for the first few milliseconds in microgravity. The initial fill level in normal gravity and the final equilibrium position in microgravity are marked by the horizontal dashed lines. The solid vertical line indicates the start of microgravity. The first vertical dashed line represents the time t_s, at which the centre point crosses the final equilibrium position for the first time. The second vertical dashed line shows the time t_{fs}, when the liquid filling into the experiment tank was started in the filling experiments.

Based on the procedure explained in appendix section A.3.1, the measured centre point of the interface was corrected. The first correction factor $\triangle z_1$ was calculated using equation A.6 for every time frame and was found to be in the order of 2.3 mm. Then, the first correction factor $\triangle z_1$ was added to the measured centre point of the interface. The position of the centre point of the liquid interface z_c, corrected with the first correction factor $\triangle z_1$, is plotted against time for the test F31 in figure 6.5. It has to be noted that the capillary wave hinders the accurate detection of the centre point position for the first few milliseconds. The plot is created by applying a moving average of 50 to the processed data from the images. The initial and final positions of the centre point are marked with dashed horizontal lines. The solid vertical line represents the start of microgravity at $t = 0$ s. As it can be seen from figure 6.5, in microgravity the centre point undergoes an oscillation that dampens with time. For an initial liquid fill height of $H_L = 30$ mm, the final equilibrium position of the centre point of the liquid interface in microgravity was computed to be $z_{c,0g} = 20$ mm using equation 2.34. After applying the first correction factor $\triangle z_1$ to the detected centre point, the final equilibrium position of the centre point of the interface under microgravity conditions at $t = 9$ s measured for the test F31 was found to be $z_c = 19.3$ mm. The measurement accuracy was in the order of ± 0.3 mm.

The second correction factor was manually calculated as $\triangle z_2 = 0.6\,\text{mm}$ for the final centre point position at $t = 9\,\text{s}$. Due to its complexity, the second correction factor $\triangle z_2$ was only determined for the final centre point position at $t = 9\,\text{s}$ and not for all the time frames. It was assumed that the second correction factor $\triangle z_2$ will have its maximum value at $t = 9\,\text{s}$. Therefore, the corrected final equilibrium position of the centre point of the liquid interface at $t = 9\,\text{s}$ after applying both the correction factors was found to be $z_c = (19.9 \pm 0.3)\,\text{mm}$. This was in good agreement with the theoretically predicted value of $z_{c,0g} = 20\,\text{mm}$ from equation 2.34. The equilibrium time in microgravity was determined as $t_s = 0.68\,\text{s}$ for the test F31, which is marked with a dot in figure 6.5. The experimental value matched well with the predicted value of $t_s = 0.67\,\text{s}$ from equation 2.35. As the centre point of the liquid interface completes its first period of oscillation and is closer to its final equilibrium position at $t = 3.5\,\text{s}$ in microgravity, the liquid inflow was started at $t_{fs} = 3.5\,\text{s}$ in microgravity for all the filling tests.

6.2.2 Filling of the tank

A total of 12 catapult tests were conducted to investigate the stability of the liquid interface perturbed by an incoming liquid jet during the filling of the tank. The liquid jet enters the tank through the primary inlet and momentum exchange takes place with the bulk liquid, as it passes through the bulk liquid. If the momentum of the incoming liquid jet is higher than the capillary pressure of the liquid interface, the jet deforms the liquid interface and a geyser is formed. This geyser then either remains at its position or grows continuously over time. It disintegrates into droplets due to the instability of the liquid column. The geyser flow patterns observed in this thesis work are similar to the patterns I, II and III reported in Aydelott 1979 [3].

The flow regimes can be divided into three categories as subcritical, critical and supercritical regimes. A subcritical flow regime occurs when the incoming liquid jet either does not deform the liquid interface or deforms the interface and forms a geyser, but this geyser does not grow with time. The geyser height is defined as the vertical distance between the origin and the highest point of the liquid interface, as shown in figure 4.5b. If the geyser height increases continuously over time and the geyser starts to disintegrate into droplets, it can be called the critical flow regime. In the supercritical flow regime, the liquid jet completely penetrates the liquid interface and moves rapidly towards the outlet port of the tank.

Due to a longer microgravity time in the catapult tests, the formation and development of geysers could be observed more clearly. The experiments were carried out for volumetric flow rates in the range of $1.00\,\text{mL}\,\text{s}^{-1} \leq Q_L \leq 1.50\,\text{mL}\,\text{s}^{-1}$. Each flow rate was tested twice. The images recorded by camera CAM2 are shown in figure 6.6 for 6 different tests at the microgravity time of $t = 9\,\text{s}$. The incoming liquid jet deforms the interface for $Q_L = 1.00\,\text{mL}\,\text{s}^{-1}$, creating only a small bulge. A small geyser is formed for $Q_L = 1.10\,\text{mL}\,\text{s}^{-1}$, which remains at its height throughout the microgravity time. The geyser height increases, as the flow rate is increased to $Q_L = 1.20\,\text{mL}\,\text{s}^{-1}$. As the geyser grows for $Q_L = 1.20\,\text{mL}\,\text{s}^{-1}$, oscillations are observed. The flow rates in the range of $1.00\,\text{mL}\,\text{s}^{-1} \leq Q_L \leq 1.20\,\text{mL}\,\text{s}^{-1}$ can be classified as subcritical flow rates because the geyser height does not increase with time.

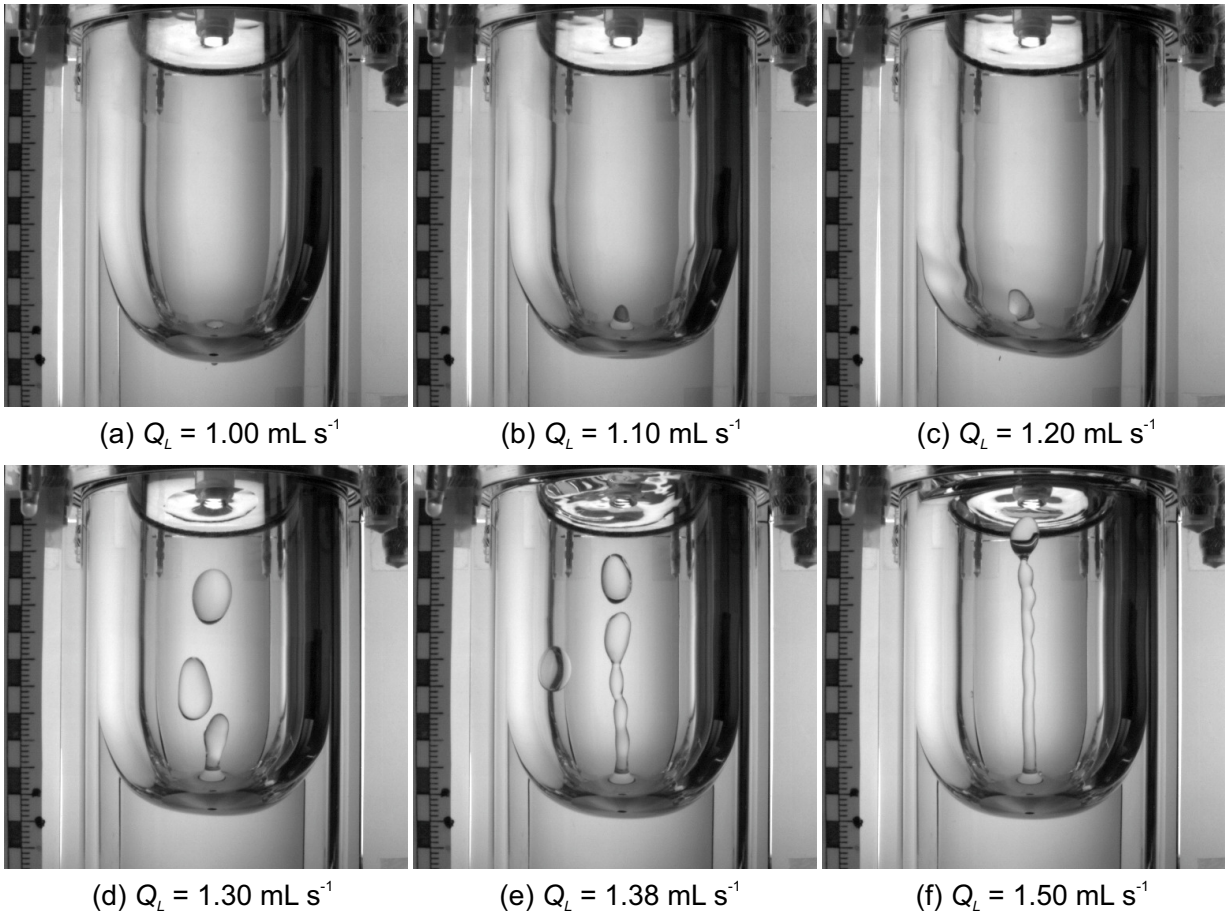

Figure 6.6: Still images from the filling experiments showing the interaction of the incoming liquid jet with the liquid interface under microgravity at $t = 9\,\mathrm{s}$ for different volumetric flow rates Q_L.

The flow rate $Q_L = 1.30\,\mathrm{mL\,s^{-1}}$ is the critical flow rate, where the geyser starts to grow with time and also breaks into droplets, as seen in figure 6.6(d). These droplets reach the outlet port of the tank. The flow rates of $Q_L > 1.30\,\mathrm{mL\,s^{-1}}$ belong to the supercritical flow regime. In this regime, the incoming liquid jet penetrates the interface and directly travels towards the outlet port of the tank, as observed in figures 6.6(e) and 6.6(f). The images from five different tests with flow rates of $Q_L = 1.10\,\mathrm{mL\,s^{-1}}$, $1.20\,\mathrm{mL\,s^{-1}}$, $1.30\,\mathrm{mL\,s^{-1}}$, $1.38\,\mathrm{mL\,s^{-1}}$ and $1.50\,\mathrm{mL\,s^{-1}}$ are presented in figure 6.7. The images are shown at four different time instants in microgravity. The flow rates of $Q_L = 1.10\,\mathrm{mL\,s^{-1}}$ and $Q_L = 1.20\,\mathrm{mL\,s^{-1}}$ can be considered as subcritical flow rates, as the geyser height does not grow with time. The geyser begins to grow for $Q_L = 1.30\,\mathrm{mL\,s^{-1}}$. The geyser disintegrates at $t = 5.5\,\mathrm{s}$ and the detachment of a droplet can be seen in figure 6.7(j). With time, more droplets are generated and they move towards the tank outlet. This is the critical domain, where the geyser pattern is very sensitive to the flow rate. As the flow rate is increased to $Q_L = 1.38\,\mathrm{mL\,s^{-1}}$, the height of the geyser becomes prominent. The instability of the geyser leads to a frequent detachment of droplets. For $Q_L = 1.50\,\mathrm{mL\,s^{-1}}$, a long column of liquid jet is formed, which moves rapidly towards the tank outlet. This can be seen in figures 6.7(q) to 6.7(t). The flow rates of $Q_L = 1.38\,\mathrm{mL\,s^{-1}}$ and $Q_L = 1.50\,\mathrm{mL\,s^{-1}}$ belong to the supercritical flow regime. The instability of the liquid jet is analysed in appendix section A.5.

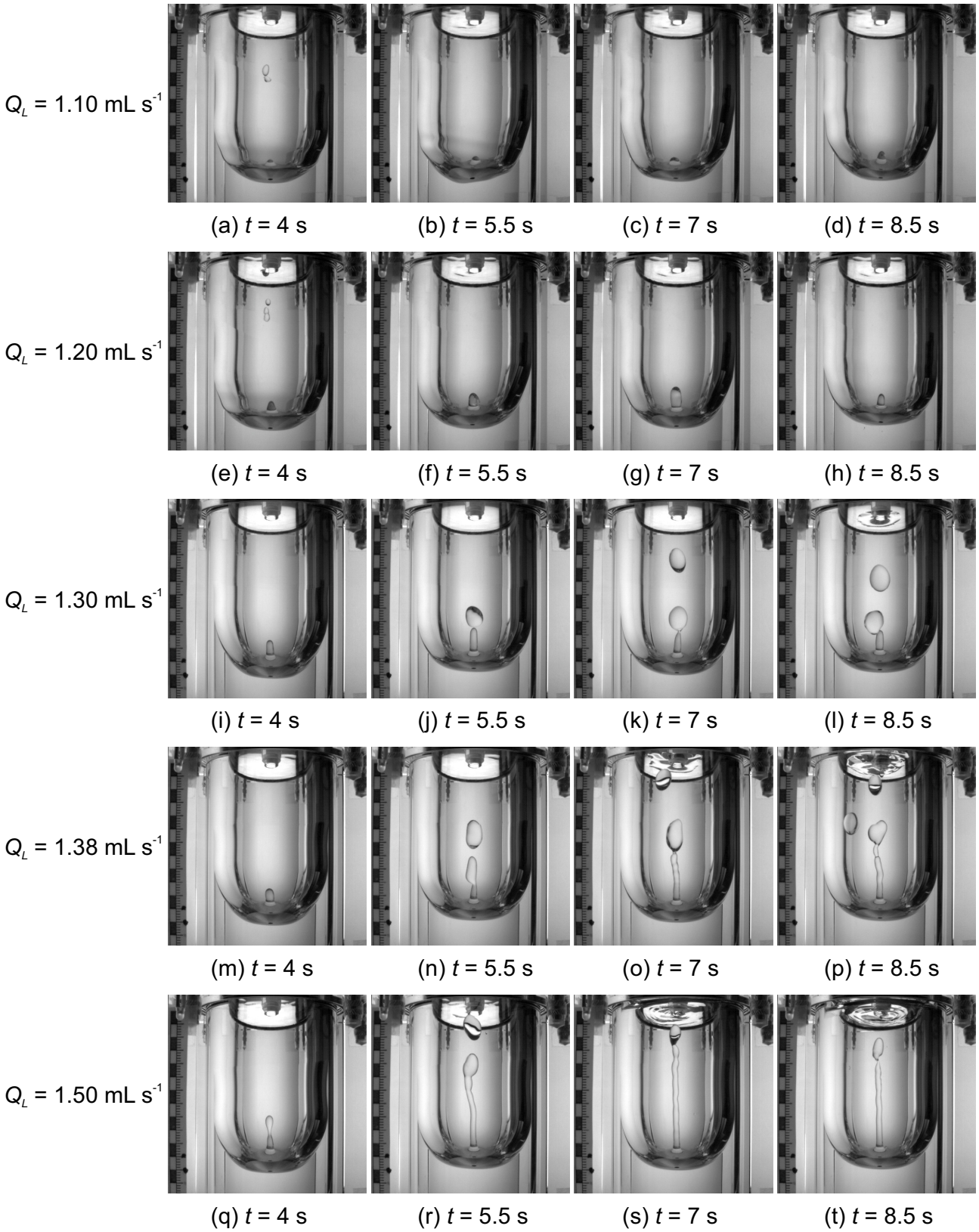

Figure 6.7: Time series of the geyser patterns observed in microgravity. The five rows from top to bottom correspond to $Q_L = 1.10\,\mathrm{mL\,s^{-1}}$, $1.20\,\mathrm{mL\,s^{-1}}$, $1.30\,\mathrm{mL\,s^{-1}}$, $1.38\,\mathrm{mL\,s^{-1}}$ and $1.50\,\mathrm{mL\,s^{-1}}$.

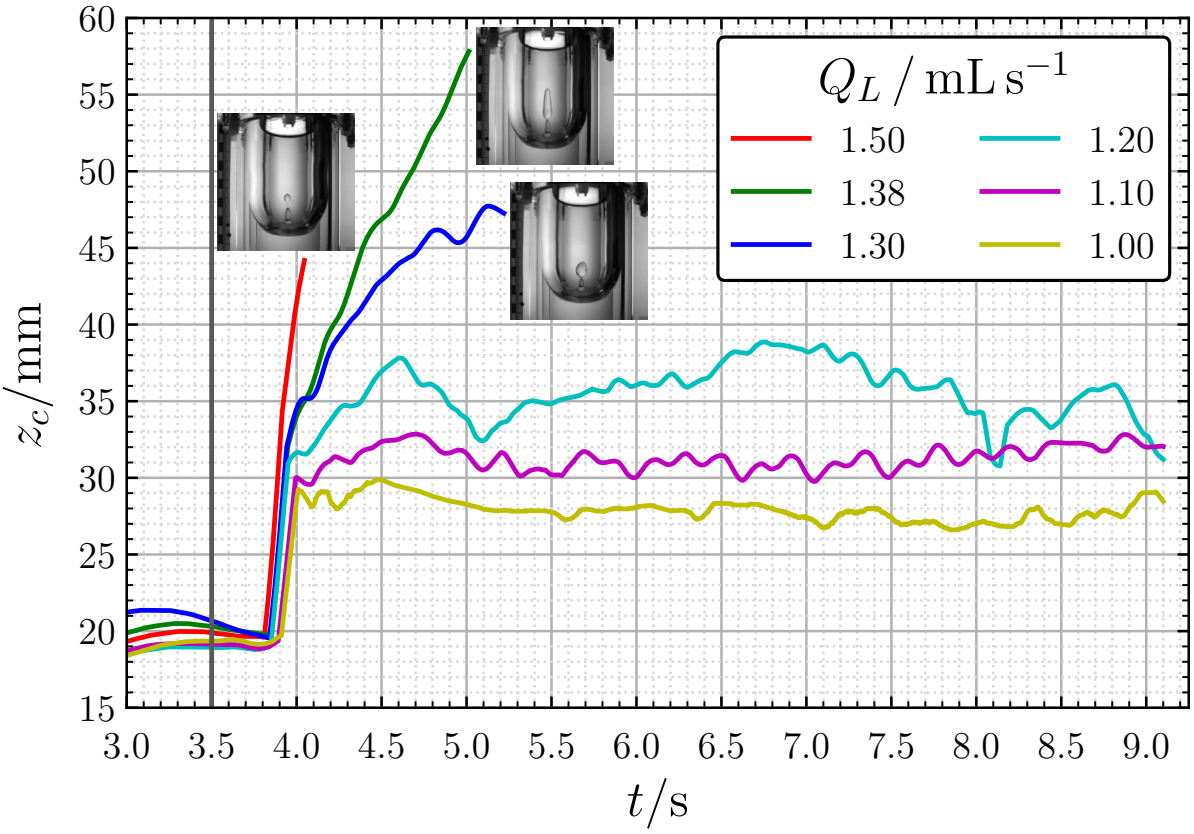

Figure 6.8: Evolution of the centre point of the interface over time during microgravity for different Q_L and $H_L = 30\,\text{mm}$.

The recorded images were processed to measure the height of the geyser versus time. The position of the centre point of the liquid interface, which defines the geyser height, is plotted versus time between $t = 3\,\text{s}$ and $t = 9\,\text{s}$ in figure 6.8 for different volumetric flow rates Q_L. The plot was created after the first correction factor $\triangle z_1$ was taken into account and a moving average of 50 was applied to the data that was recorded at a frequency of 500 frames per second. The second correction factor $\triangle z_2$ was not considered, as it was estimated manually to be in the order of $\triangle z_2 \approx 0.02\,\text{mm}$. The accuracy of the centre point position from the image processing procedure was determined as $\pm 0.2\,\text{mm}$. The method for correcting the centre point of the interface in the filling experiments is described in appendix section A.3.2.

In figure 6.8, the vertical line represents the start of the liquid filling into the tank. For the flow rates in the range of $1.30\,\text{mL s}^{-1} \leq Q_L \leq 1.50\,\text{mL s}^{-1}$, the curves are plotted only until the time when the geyser remains intact and does not disintegrate into droplets. The detachment of droplets is shown in the inset of figure 6.8 for these flow rates. It can be seen that the height of the geyser increases with increasing flow rate. For the subcritical flow rates in the range of $1.00\,\text{mL s}^{-1} \leq Q_L \leq 1.20\,\text{mL s}^{-1}$, the geyser height does not grow continuously with time and fluctuations in the height can be seen. A significant growth could be observed for $Q_L = 1.30\,\text{mL s}^{-1}$. This is the critical flow rate found from the drop tower experiments. The corresponding critical Weber number is $\text{We}_{1cr} = 1.04 \pm 0.03$, calculated from equation 2.57. A sharp increase in the geyser height can be noticed for higher flow rates of $Q_L > 1.30\,\text{mL s}^{-1}$. The higher the flow rate gets, the faster the geyser disintegrates into droplets.

6.3 Parabolic flight experiments

The parabolic flight experiments were carried out to test the procedures of liquid filling and liquid removal under variable acceleration conditions using one experiment tank. In this thesis, only the results from the liquid filling experiments are discussed. The experiment tank was designed in such a way to fulfill the requirements of both liquid filling and liquid removal experiments. Therefore, the interaction of the liquid jet with a well-defined interface during the liquid filling, like in the drop tower experiments, could not be investigated in the parabolic flight experiments. However, the parabolic flight experiments demonstrated the gas-free liquid filling and liquid-free gas venting qualitatively. Due to the violent sloshing of the bulk liquid inside the experiment tank during the reduced gravity phase, it was decided to focus mainly on the liquid filling into an initially empty tank. The liquid inflow from the inlet pipe into an initially empty experiment tank is shown in figure 6.9 for different volumetric flow rates Q_L at different time steps. Because of the strong negative acceleration in the z-axis in the initial part of the reduced gravity phase, the images are shown only from $t = 5\,\mathrm{s}$. The images are cropped such that only the bottom part of the tank surrounding the inlet and the VCP are visible.

For $Q_L = 0.2\,\mathrm{mL\,s^{-1}}$ and $Q_L = 0.3\,\mathrm{mL\,s^{-1}}$, a convex liquid meniscus can be observed pinned to the inlet orifice. The liquid flows out of the orifice and is redirected towards the bottom surface of the tank. As the linear momentum in the liquid is weaker than the cohesive and adhesive forces, the liquid tends to wet the inlet pipe and the tank surfaces. After touching the bottom surface of the tank, the liquid flows radially towards the tank walls on both sides and continues to fill the bottom part of the tank. The accumulation of liquid near the stands of VCP can also be seen in figure 6.9. For the volumetric flow rates in the range of $0.4\,\mathrm{mL\,s^{-1}} \leq Q_L \leq 0.6\,\mathrm{mL\,s^{-1}}$, a slightly bigger curvature of the liquid jet is visible near the inlet orifice. A liquid bridge formed between the stands of the VCP can be noticed. At $t = 15\,\mathrm{s}$ for $Q_L = 0.5\,\mathrm{mL\,s^{-1}}$, the liquid jet touches the VCP surface, which is caused by the sudden disturbance in the axial acceleration. Almost for the whole duration of the reduced gravity phase, the liquid jet remains pinned to the inlet orifice for $Q_L \leq 0.6\,\mathrm{mL\,s^{-1}}$. The thickness of the liquid jet flowing out of the inlet orifice increases and more liquid deposits on the VCP and its stands for $Q_L = 0.7\,\mathrm{mL\,s^{-1}}$. A fluctuating liquid jet with varying shapes can be noticed for $Q_L = 0.8\,\mathrm{mL\,s^{-1}}$. The liquid jet touches the stands of the VCP or the VCP plate, due to the disturbances in the three-axes accelerations at certain time instants. It has to be mentioned that the flow patterns formed from various volumetric flow rates cannot be compared directly because of the different acceleration profiles in every parabola.

The liquid filling into the experiment tank with a volumetric flow rate of $Q_L = 5.0\,\mathrm{mL\,s^{-1}}$ is compared between two tests in figure 6.10 at different time steps. The first row shows the results of the test P26D3, which corresponds to an initially empty tank and the second row shows the results of the test P29D2, which corresponds to a pre-filled tank with an initial liquid fill height of $H_L = 35\,\mathrm{mm}$. The main aim of these tests was to show that gas-free liquid can be filled into a tank at higher fill velocities and the liquid-free gas can be vented through the gas port during the filling. The liquid jet from the inlet pipe hits the VCP and its linear momentum is diffused. The liquid then flows along the surfaces of the VCP and its stands.

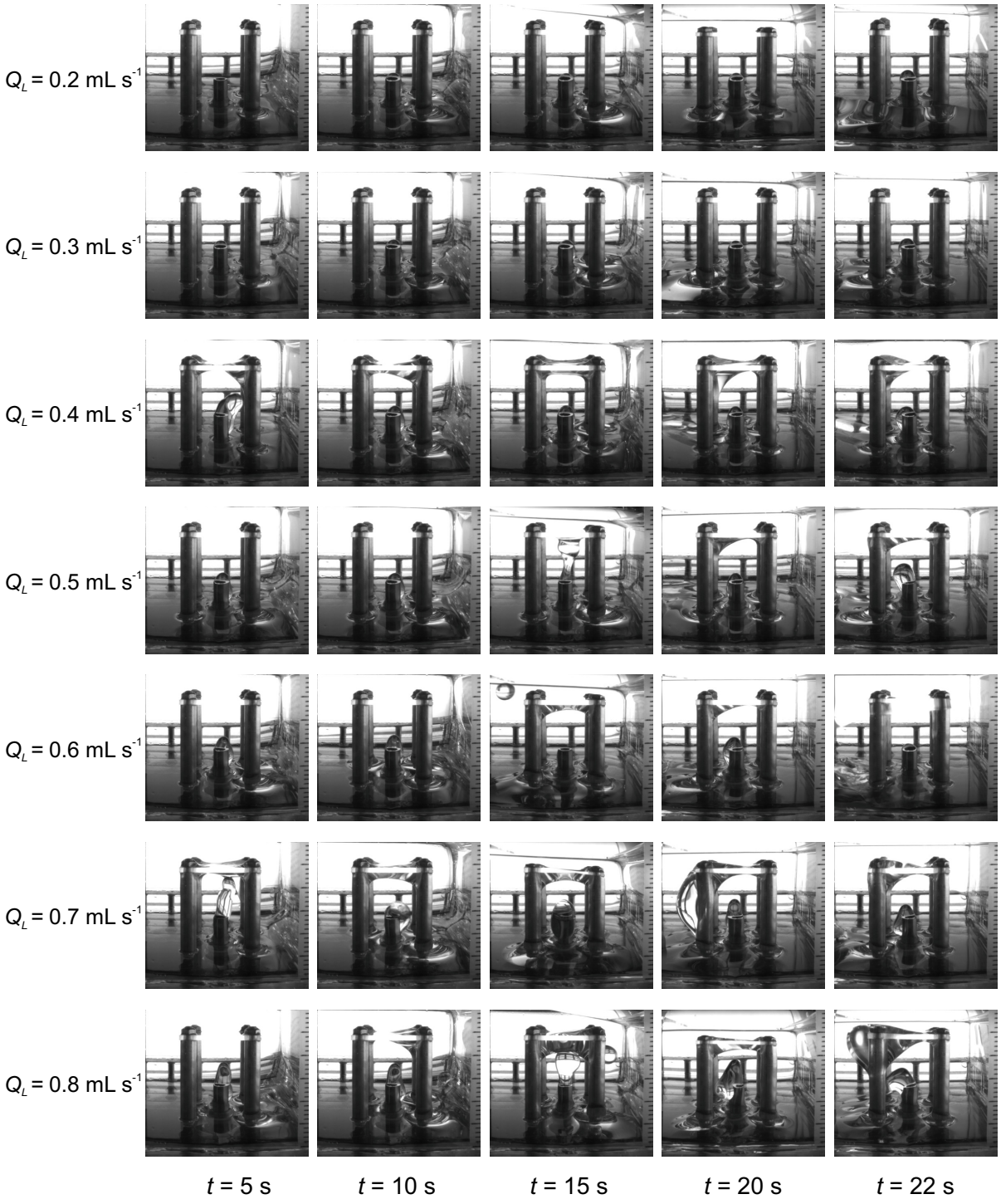

Figure 6.9: Time series of the flow patterns observed during the liquid filling into an initially empty tank in reduced gravity for different Q_L.

For $H_L = 0\,\text{mm}$, the bottom part of the tank is primarily filled. On the other hand, in test P29D2, the bulk liquid undergoes violent sloshing due to the fluctuations in the accelerations. The rapid movement of the liquid distorts the optical observation in the tank for $H_L = 35\,\text{mm}$. Nevertheless, gas-free liquid filling and liquid-free gas venting were demonstrated, despite the violent sloshing of the bulk liquid. It was also shown that faster filling of the tank under reduced gravity can be accomplished by using the VCP.

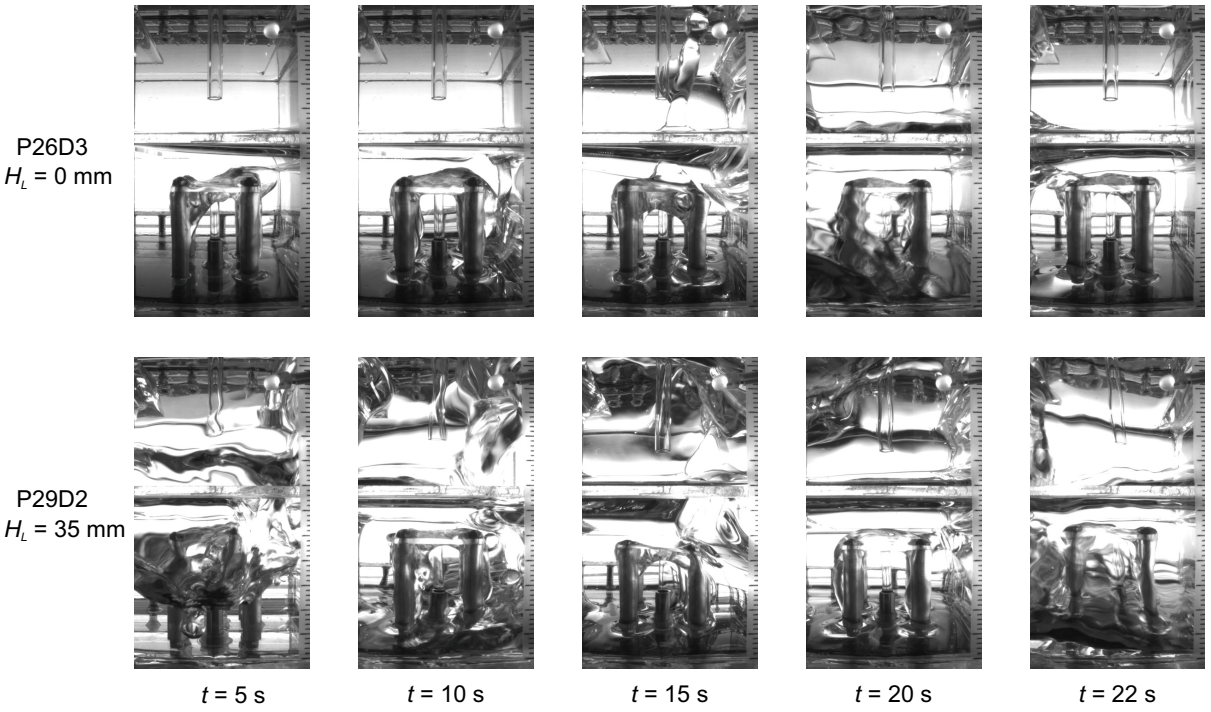

Figure 6.10: Comparison of the flow patterns for an initially empty tank ($H_L = 0\,\text{mm}$) and a pre-filled tank ($H_L = 35\,\text{mm}$) with $Q_L = 5.0\,\text{mL}\,\text{s}^{-1}$.

The time series of the flow patterns observed during the liquid filling into the experiment tank for different Q_L is shown in figure 6.11. All the images correspond to an initial liquid fill height of $H_L = 15\,\text{mm}$. It can be noticed in figure 6.11 that the part of the tank containing the inlet pipe and the VCP looks fairly similar to the images from the filling into an initially empty tank in figure 6.9. This is mainly because of the movement of the bulk liquid already present inside the tank towards the top and sides of the tank, thereby making the bottom part of the tank to contain less liquid. At $t = 5\,\text{s}$, some amount of liquid can be seen collected at the top of the tank, which is caused by the negative acceleration in the z-axis. The upward movement of the liquid towards the top could not be fully restricted, although the ring baffles were mounted inside the tank. However, the liquid jet remained pinned to the inlet orifice for a large extent of time for the tested flow rates, as also observed in the filling tests of an initially empty tank.

A more violent liquid sloshing can be observed inside the tank, when the tank is pre-filled to an initial liquid fill height of $H_L = 25\,\text{mm}$, as shown in figure 6.12 for different Q_L. As a higher volume of liquid is present in the tank, the optical observation is disrupted at certain time instants. Compared to the drop tower experiments, the design constraints and the fluctuations in three-axes accelerations made it complicated to establish a smooth and steady liquid interface in the parabolic flight experiments. Henceforth, the interaction of the liquid jet with the interface could not be studied in the parabolic flight experiments. The parabolic flight experiments only served the purpose of qualitatively demonstrating the concept of gas-free liquid filling and liquid-free gas venting under reduced gravity conditions. Furthermore, the functionality of the hydraulic loop of the parabolic flight experiment was tested under variable acceleration conditions. Therefore, the investigation of interface stability could not be carried out quantitatively.

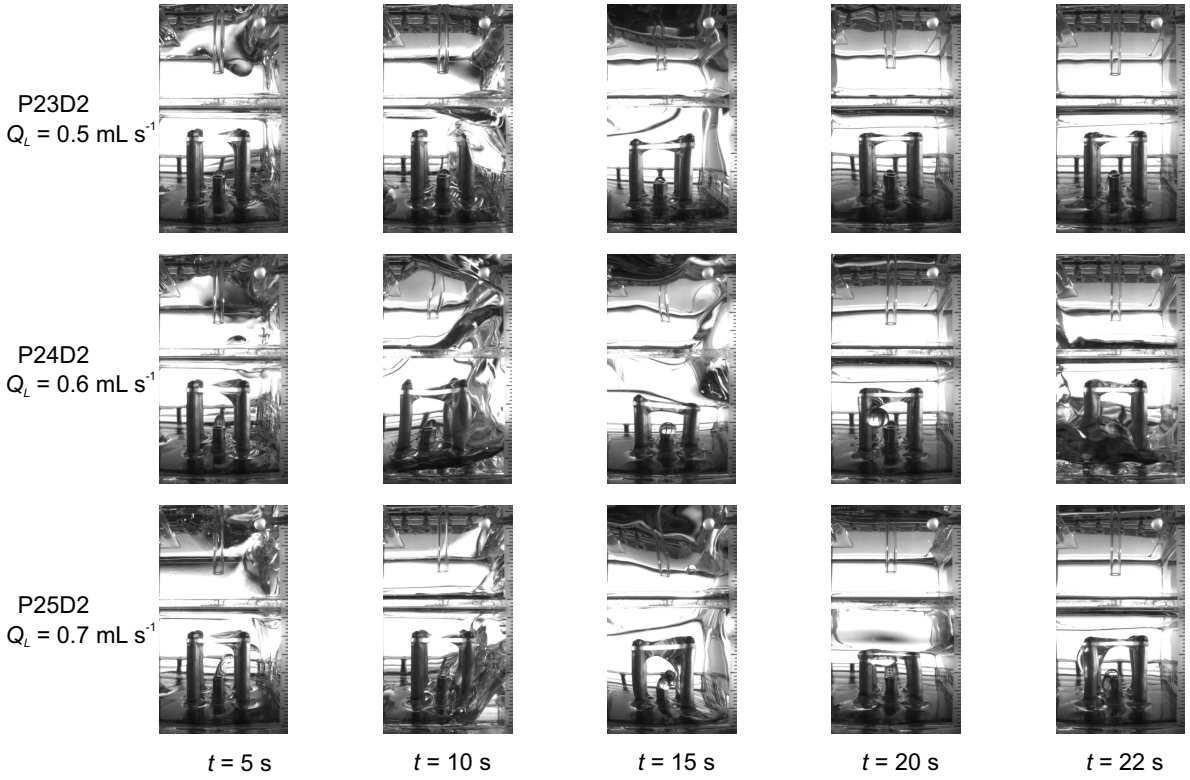

Figure 6.11: Time series of the flow patterns observed during the liquid filling into a pre-filled tank ($H_L = 15\,\mathrm{mm}$) in reduced gravity for different Q_L.

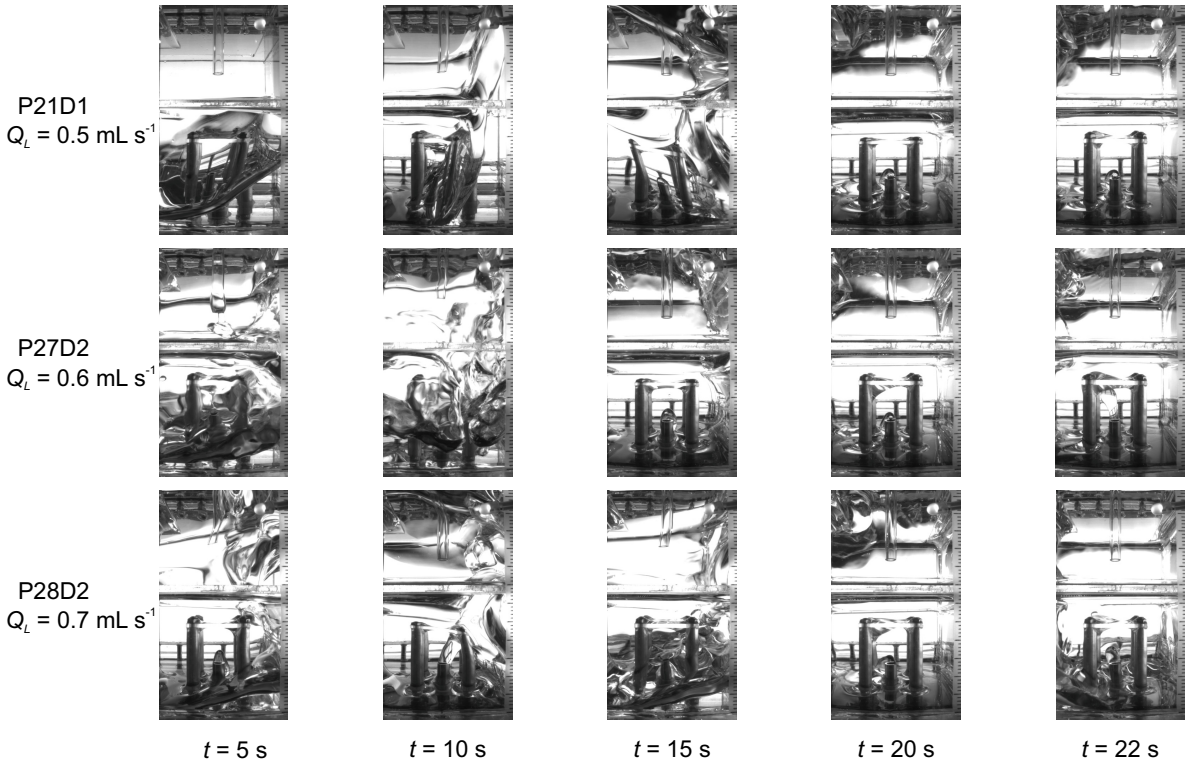

Figure 6.12: Time series of the flow patterns observed during the liquid filling into a pre-filled tank ($H_L = 25\,\mathrm{mm}$) in reduced gravity for different Q_L.

6.4 Numerical simulations

6.4.1 Liquid reorientation

To observe the reorientation of the liquid inside the tank under reduced gravity conditions, a numerical simulation was carried out for a pre-filled tank with an initial liquid fill height of $H_L = 30\,\text{mm}$. In this simulation, all the boundaries were defined as walls with no inflow and outflow. From $t = 0\,\text{s}$ to $t = 3\,\text{s}$, the simulation was run under normal gravity conditions to allow the development of liquid meniscus at the wall. After that, the gravity was turned off and the simulation was run further until $t = 12\,\text{s}$ under reduced gravity conditions. Under reduced gravity conditions, the capillary force becomes dominant and the liquid meniscus starts to rise at the tank wall and a capillary wave travels from the tank wall towards the centre of the tank. Due to this effect, the centre point of the liquid interface moves downwards from its original normal gravity configuration and undergoes an axial sloshing, which dampens with time.

The numerical simulation results of the reorientation of liquid inside the tank under reduced gravity conditions at different time steps are shown in figure 6.13. The volume fraction of the liquid is displayed as the contour in figure 6.13. At $t = 3\,\text{s}$, the interface is at its normal gravity configuration and at $t = 6.5\,\text{s}$, the interface takes the shape of a hemisphere with its centre point closer to the final equilibrium configuration in reduced gravity. At $t = 12\,\text{s}$ the interface approaches its final equilibrium configuration in reduced gravity.

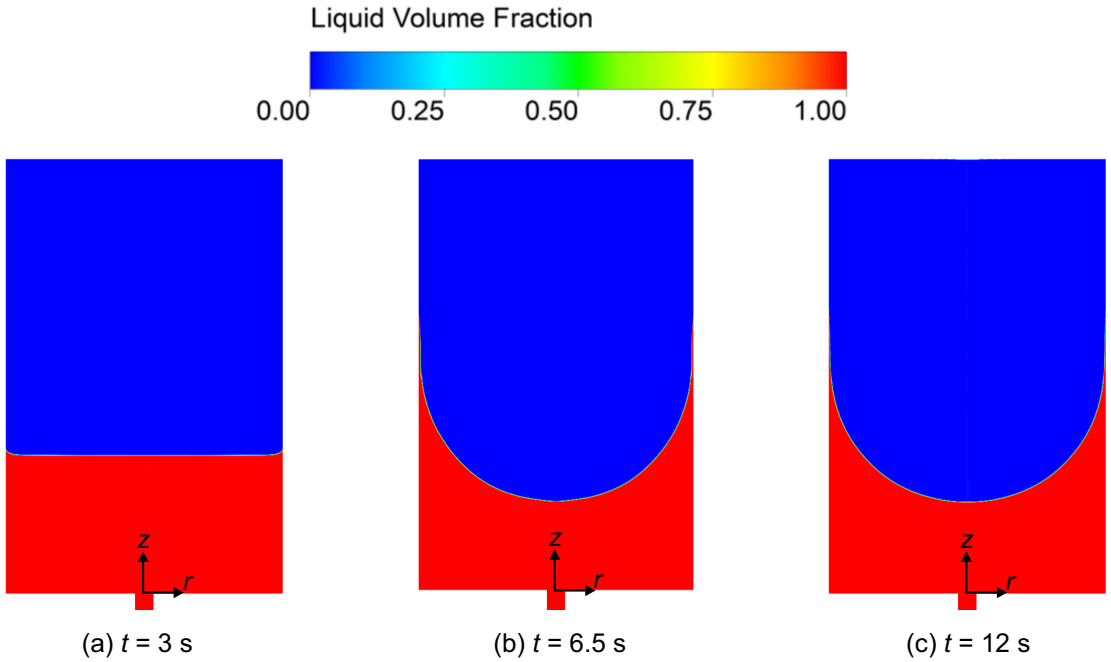

Figure 6.13: Contours of volume fraction showing the liquid reorientation inside the tank under reduced gravity conditions at different time steps. The red colour indicates the liquid HFE-7500 and air is shown in blue colour.

6.4.2 Liquid filling into a pre-filled tank

Further numerical simulations were carried out to study the interface stability in reduced gravity during the filling of a tank with an initial liquid fill height of $H_L = 30\,\mathrm{mm}$. The liquid filling was started at the simulation time of $t = 6.5\,\mathrm{s}$ and continued until $t = 12\,\mathrm{s}$. The time-dependent behaviour of the liquid interface, which is perturbed by the liquid jet, is shown in figure 6.14 for four different volumetric flow rates. The contours of liquid volume fraction and velocity magnitude are shown on the left and right part of each sub-figure respectively.

As the capillary pressure of the liquid interface is stronger than the momentum of the liquid jet for $Q_L = 1.10\,\mathrm{mL\,s^{-1}}$, a small bulge is created and the perturbation of the interface does not grow over time and remains at its position. The liquid spreads radially, as its axial path is hindered. For $Q_L = 1.20\,\mathrm{mL\,s^{-1}}$, the formation and development of the geyser can be seen in figure 6.14(e) to 6.14(h). However, the liquid jet momentum is balanced by the capillary pressure and the growth rate of the geyser declines and settles to a maximum height of about 50 mm. A rapid growth of the geyser over time can be observed in figure 6.14(i) to 6.14(l) for $Q_L = 1.30\,\mathrm{mL\,s^{-1}}$. The momentum of the liquid jet exceeds the capillary pressure of the interface, which makes the liquid jet penetrate the interface completely and leads to a geyser moving towards the tank outlet. However, the duration of the simulation is not long enough to determine whether $Q_L = 1.30\,\mathrm{mL\,s^{-1}}$ can be considered as the critical flow rate. Moreover, in the drop tower experiment, the disintegration of droplets from the geyser was observed for $Q_L = 1.30\,\mathrm{mL\,s^{-1}}$, which could not be seen in the numerical simulations. When the volumetric inflow rate is increased to $Q_L = 1.40\,\mathrm{mL\,s^{-1}}$, the speed of the geyser also increases, which also induces instability and disintegration into liquid droplets, as seen in figure 6.14(o). Based on the criterion defined in section 5.3.4.1, the critical flow rate may lie around $Q_L = 1.40\,\mathrm{mL\,s^{-1}}$ for $H_L = 30\,\mathrm{mm}$, as the breakage of droplets is first observed at this flow rate. These droplets emanating from the geyser touch the tank outlet, as shown in figure 6.14(p).

Assuming the liquid jet to have a radius of 2 mm, the capillary pressure can be calculated from equation 2.29 to be $\triangle p = 16.7\,\mathrm{Pa}$. The liquid jet momentum, which can also be expressed as the stagnation pressure $\rho\, v_I^2$ in the Weber number formulation, is calculated for the flow rates in the range of $1.10\,\mathrm{mL\,s^{-1}} \leq Q_L \leq 1.40\,\mathrm{mL\,s^{-1}}$ and given in table 6.1. It can be seen from table 6.1 that the stagnation pressure is lower than the capillary pressure of $\triangle p = 16.7\,\mathrm{Pa}$ for the flow rates of $Q_L = 1.10\,\mathrm{mL\,s^{-1}}$ and $Q_L = 1.20\,\mathrm{mL\,s^{-1}}$, which restricts the growth of the geyser. The stagnation pressure is marginally higher than the capillary pressure for $Q_L = 1.30\,\mathrm{mL\,s^{-1}}$ and it surpasses the capillary pressure for $Q_L = 1.40\,\mathrm{mL\,s^{-1}}$ making the geyser to grow rapidly in the ullage region.

Table 6.1: Calculation of the stagnation pressure for different Q_L.

No.	$Q_L/\mathrm{mL\,s^{-1}}$	$v_I/10^{-3}\,\mathrm{m\,s^{-1}}$	$\rho\, v_I^2/\mathrm{Pa}$
1	1.10	87.54	12.41
2	1.20	95.49	14.77
3	1.30	103.45	17.34
4	1.40	111.41	20.11

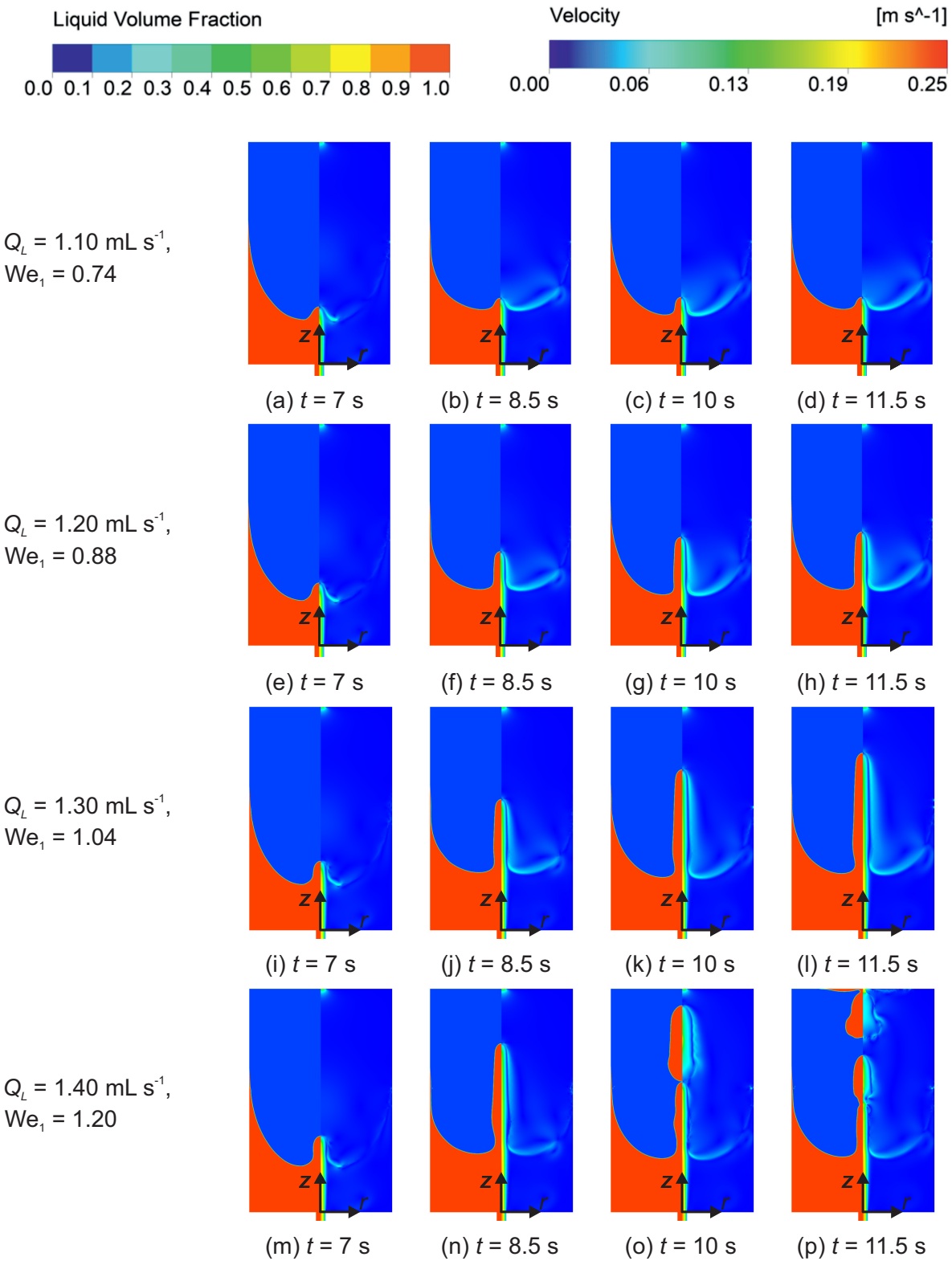

Figure 6.14: Time-dependent behaviour of the liquid interface under reduced gravity for $H_L = 30\,\text{mm}$. The liquid volume fraction is the contour on the left part of the figure and the right part of the figure shows the velocity magnitude.

The critical flow rate from the drop tower experiments was found to be $Q_L = 1.30\,\mathrm{mL\,s^{-1}}$ for $H_L = 30\,\mathrm{mm}$. Therefore, the numerical simulation results of this flow rate have been analysed further. The liquid jet hits the interface at $t = 6.9\,\mathrm{s}$ for $Q_L = 1.30\,\mathrm{mL\,s^{-1}}$. The contour of absolute pressure at $t = 6.9\,\mathrm{s}$ is shown in figure 6.15a. It can be observed that the maximum absolute pressure of 101 337.5 Pa is reached at the centre point of the interface. Because of the absence of a hydrostatic head in reduced gravity, the bulk liquid region does not exhibit significant pressure variations. The low-pressure contours of dark blue colour on the interface indicate a recirculating flow region in figure 6.15a. Above the interface, the ullage region is filled with air, which is at an atmospheric pressure of 101 325 Pa. A pressure difference of $\triangle p = 12.5\,\mathrm{Pa}$ exists across the interface. According to the Young-Laplace equation, the pressure difference across the interface with a constant radius of curvature ($R_1 = R_2 = R_c$) is given in equation 6.1 as

$$\triangle p = \sigma \left(\frac{1}{R_1} + \frac{1}{R_2} \right) = \frac{2\,\sigma}{R_c} \tag{6.1}$$

Substituting the pressure difference ($\triangle p = 12.5\,\mathrm{Pa}$) and the surface tension ($\sigma = 0.0167\,\mathrm{N\,m^{-1}}$) values in equation 6.1, the radius of curvature of the interface R_c for $Q_L = 1.30\,\mathrm{mL\,s^{-1}}$ at $t = 6.9\,\mathrm{s}$ is found to be

$$R_c = \frac{2\,\sigma}{\triangle p} = 2.67 \times 10^{-3}\,\mathrm{m} \tag{6.2}$$

This curvature radius of $R_c = 2.67\,\mathrm{mm}$ was also confirmed from the numerical simulation results by manually detecting the radius during the post-processing.

The variation of absolute pressure along the centreline from the tank inlet ($z = 0\,\mathrm{mm}$) is plotted in figure 6.15b. The absolute pressure remains almost constant until $z = 14\,\mathrm{mm}$. A steep increase in pressure can be noticed in the deformed region of the interface until the centre point of the interface, where the pressure reaches its peak value. Beyond that, the absolute pressure abruptly declines to the atmospheric pressure of air.

The velocity contour with vectors showing the interaction of the liquid jet with the interface is shown in figure 6.16 for different Q_L at $t = 6.9\,\mathrm{s}$ during the filling of liquid into a pre-filled tank with $H_L = 30\,\mathrm{mm}$. The interface is displayed in grey colour in figure 6.16. The deformation of the interface increases, as the velocity of the liquid jet increases. The liquid jet is slowed down, as it begins to spread into the bulk liquid. The liquid jet broadens as it approaches the interface. The direction of velocity vectors depict the entrainment of the bulk liquid into the liquid jet near the interface. The circulating flow patterns in the bulk liquid can be observed near the wall.

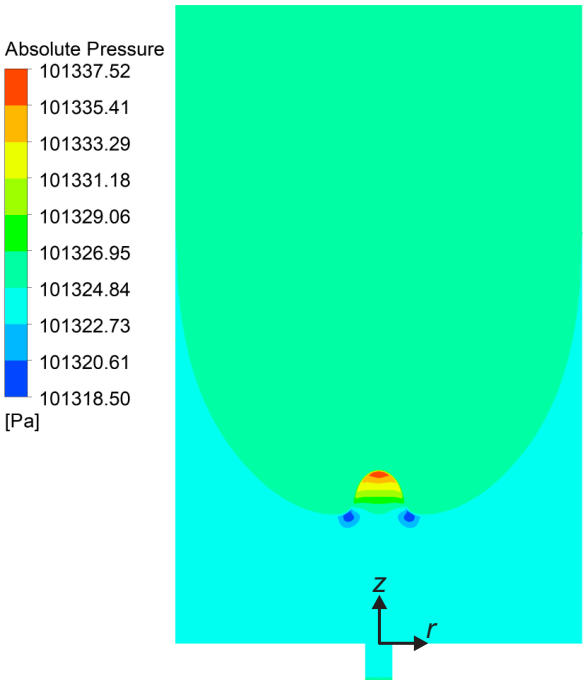

(a) Contour of absolute pressure

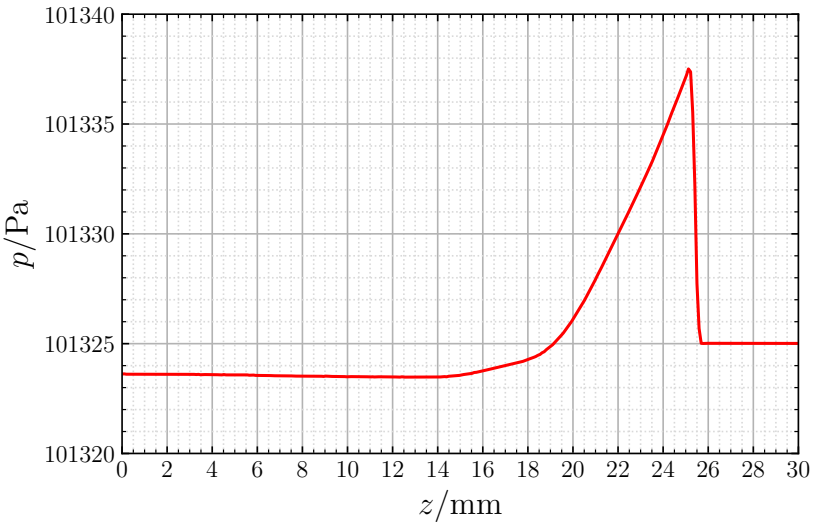

(b) Variation of absolute pressure along the centreline. The absolute pressure reaches its peak value at the interface.

Figure 6.15: Absolute pressure from the 2D numerical simulations of liquid filling into a pre-filled tank with $H_L = 30\,\text{mm}$ for $Q_L = 1.30\,\text{mL}\,\text{s}^{-1}$ at $t = 6.9\,\text{s}$.

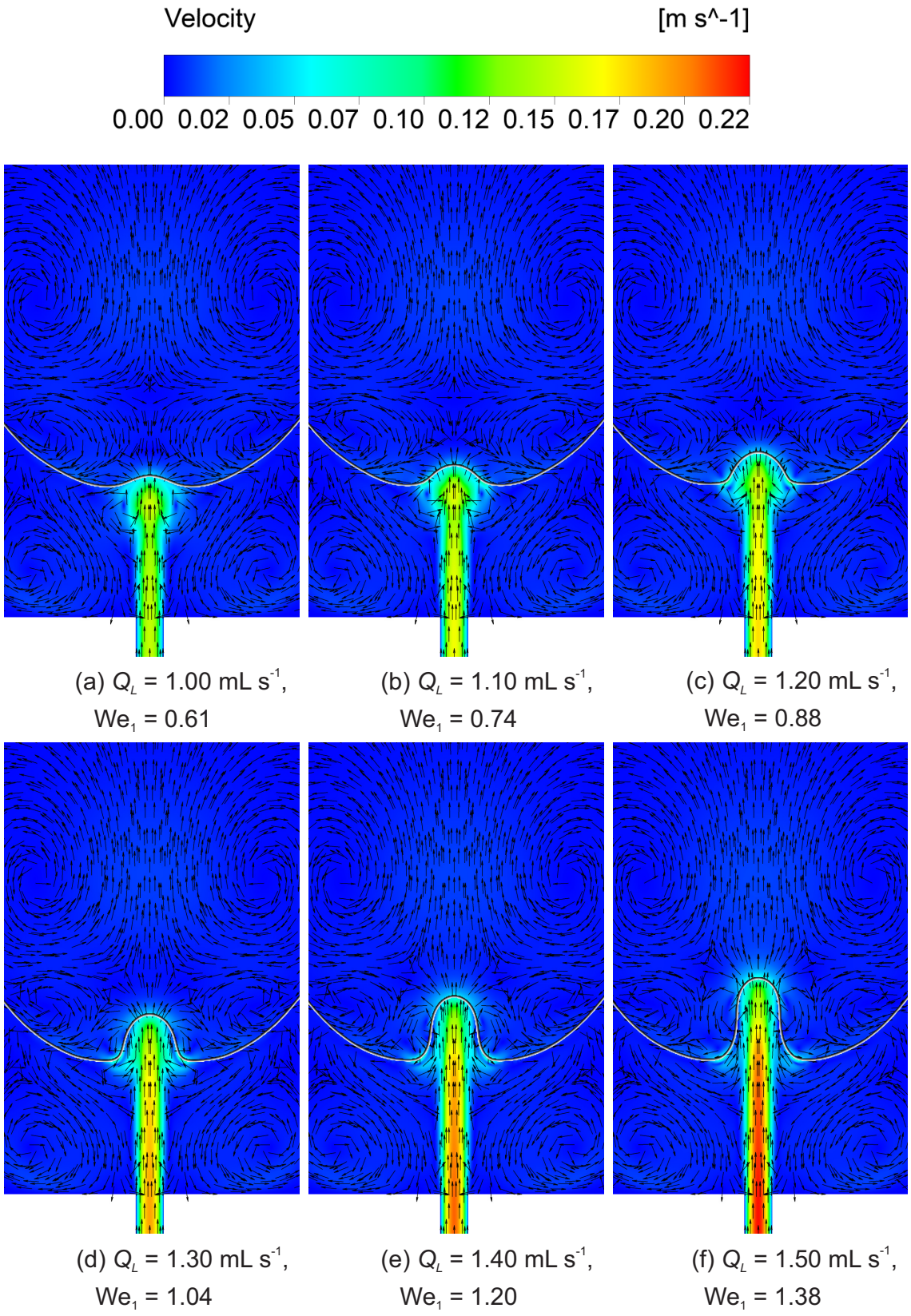

Figure 6.16: Velocity contour with vectors showing the interaction of the liquid jet with the interface for different Q_L with $H_L = 30\,\text{mm}$ at $t = 6.9\,\text{s}$. The interface is shown in grey colour.

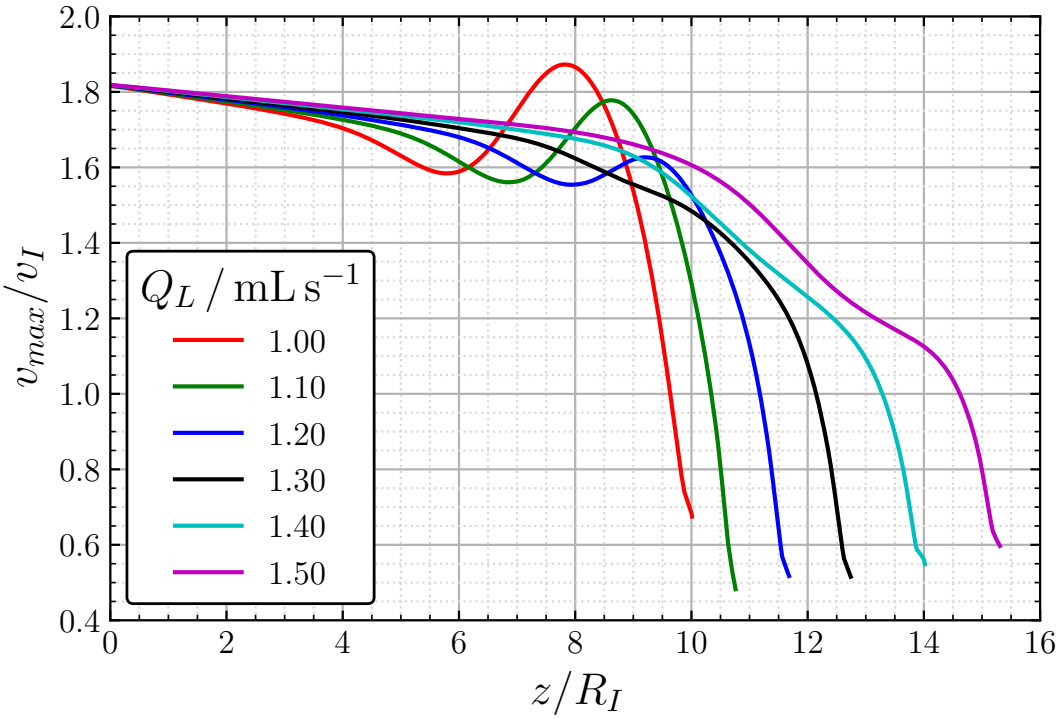

Figure 6.17: Velocity progression along the centreline for different Q_L with $H_L = 30\,\text{mm}$ at $t = 6.9\,\text{s}$.

The velocity progression along the centreline is shown in dimensionless form for different Q_L with $H_L = 30\,\text{mm}$ at $t = 6.9\,\text{s}$ in figure 6.17. The centreline velocity decay is plotted up to the position of the centre point of the interface. Hence, the maximum axial distance (z/R_I) of the curves is different for every flow rate. The centreline velocity begins to decay immediately after the liquid jet enters the tank. The trend of decay is similar for all the flow rates until $z/R_I = 3$, after which the decay rate is slower as the liquid jet velocity increases. The centreline velocity increases between $6 \leq z/R_I \leq 8$ for $Q_L = 1.00\,\text{mL s}^{-1}$ before dropping again. In this domain, the liquid jet broadens up and the flow accelerates locally due to the presence of low-pressure recirculation regions underneath the interface, as seen in figure 6.16(a). A similar behaviour of local acceleration of the flow is also observed for the flow rates of $Q_L = 1.10\,\text{mL s}^{-1}$ and $Q_L = 1.20\,\text{mL s}^{-1}$. The comparison of the absolute pressure contours for different flow rates at $t = 6.9\,\text{s}$ is shown in figure B.1 in the appendix. The absolute pressure contours confirm the presence of low-pressure regions underneath the interface for $Q_L \leq 1.10\,\text{mL s}^{-1}$. As the flow rate is increased, the broadening of the jet near the interface reduces and the interface curvature changes. The low-pressure regions can be seen near the lowermost point of the interface in figure B.1(c), (d), (e) and (f).

For flow rates in the range of $1.30\,\text{mL s}^{-1} \leq Q_L \leq 1.50\,\text{mL s}^{-1}$, the formation of a geyser with a convex shape of the interface is prominently noticeable in figure 6.16(d), (e) and (f). The pressure increases along the centreline below the interface for $Q_L = 1.30\,\text{mL s}^{-1}$, as shown in figure 6.15b, and this results in a continuous decay of the centreline velocity for $Q_L = 1.30\,\text{mL s}^{-1}$ in figure 6.17. A similar trend of centreline velocity decay is observed for the flow rates of $Q_L = 1.40\,\text{mL s}^{-1}$ and $Q_L = 1.50\,\text{mL s}^{-1}$.

The velocity profiles at different locations downstream of the tank inlet are shown in dimensionless form in figure 6.18 for $H_L = 30\,\text{mm}$ and different Q_L. All the plots correspond to the simulation time of $t = 6.9\,\text{s}$, when the liquid jet perturbs the interface. At the tank inlet ($z/R_I = 0$), the velocity profile is not yet fully parabolic, as the ratio of axial velocity v_z and centreline velocity v_{max} is smaller than 1 $\left(v_z/v_{max} < 1\right)$ on the centreline ($r/R_I = 0$). The velocity profile changes downstream from the tank inlet and the deceleration of the liquid jet can be identified from the reduction in the axial velocity further downstream in figure 6.18a. At any given downstream location (z/R_I), the centreline velocity increases with the flow rate. An exception is for $Q_L = 1.00\,\text{mL}\,\text{s}^{-1}$ at $z/R_I = 7.5$, where an enlarged velocity profile illustrates the spreading of the jet. Due to the local acceleration, the axial velocity increases at $z/R_I = 7.5$, as depicted by the black curve for $Q_L = 1.00\,\text{mL}\,\text{s}^{-1}$ in figure 6.18a. A continuous decay in the centreline velocity downstream from the tank inlet can be confirmed for the flow rates of $Q_L = 1.30\,\text{mL}\,\text{s}^{-1}$ and $Q_L = 1.50\,\text{mL}\,\text{s}^{-1}$ in figures 6.18b and 6.18c respectively. The velocity profiles display a similar shape for $z/R_I \leq 7.5$ with higher flow rates of $Q_L = 1.30\,\text{mL}\,\text{s}^{-1}$ and $Q_L = 1.50\,\text{mL}\,\text{s}^{-1}$. The flattening of the velocity profile is evident for $Q_L = 1.50\,\text{mL}\,\text{s}^{-1}$, as the liquid jet diffuses into the bulk liquid. Apart from the velocity profiles that exhibit the jet broadening, all the other velocity profiles coincide with each other at $r/R_I = \pm 0.8$ for all the flow rates having a value of $v_z/v_{max} \approx 0.4$.

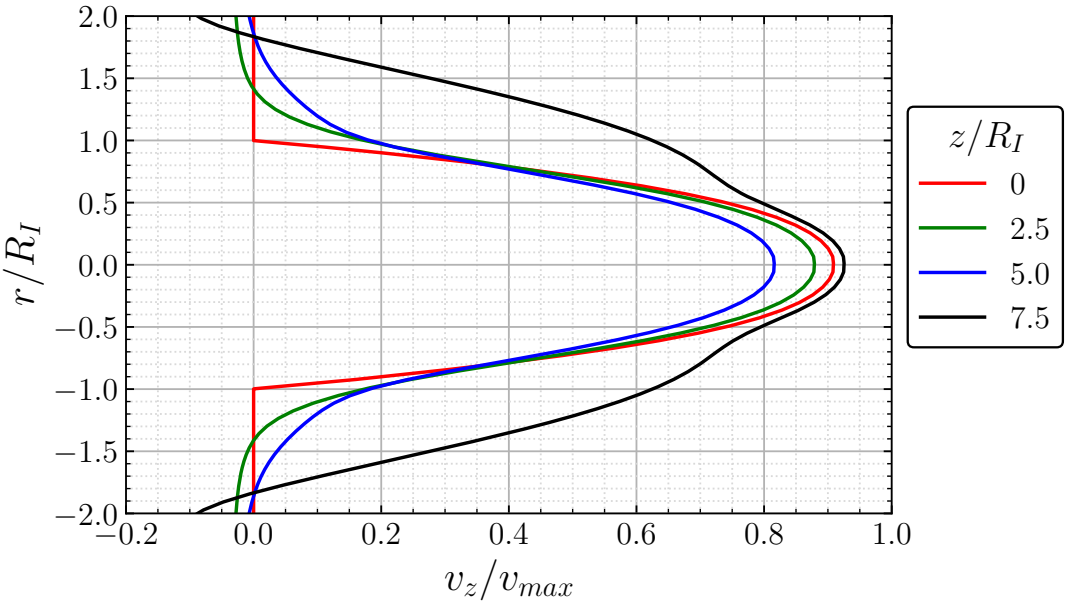

(a) $Q_L = 1.00\,\text{mL}\,\text{s}^{-1}$

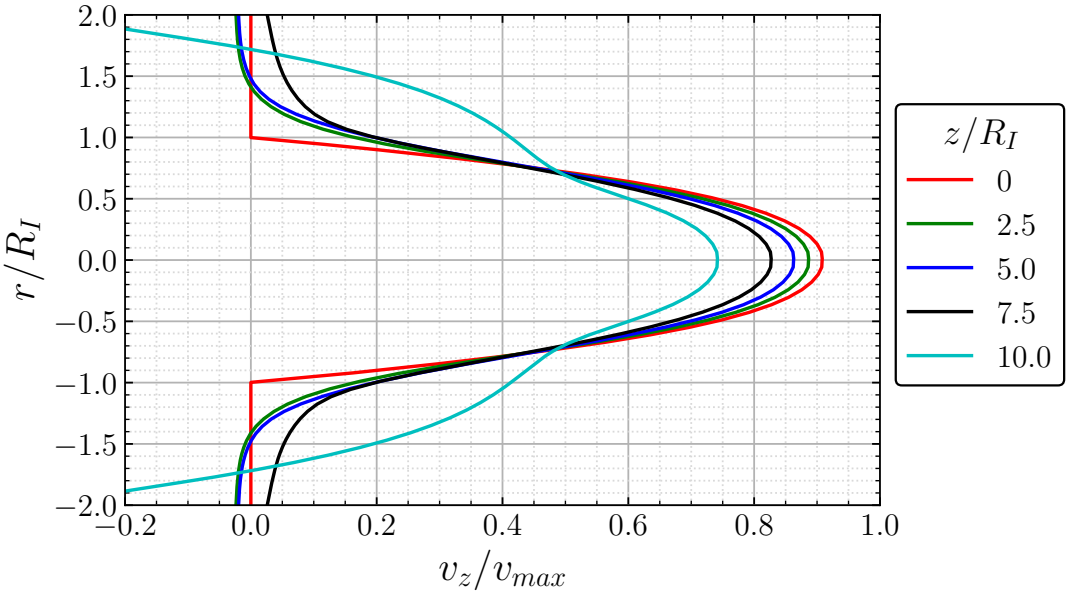

(b) $Q_L = 1.30\,\mathrm{mL\,s^{-1}}$

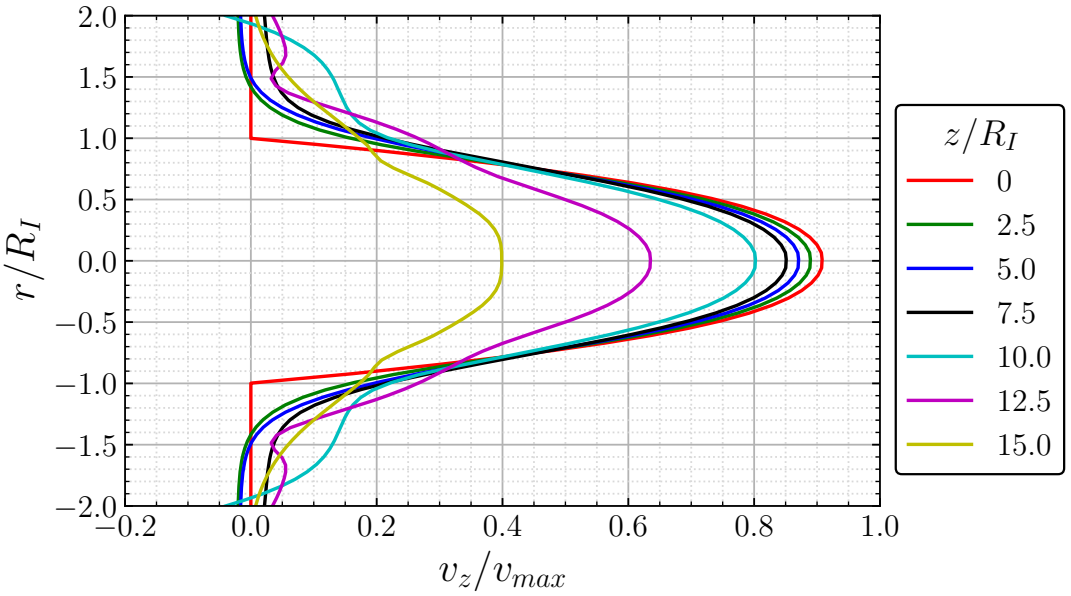

(c) $Q_L = 1.50\,\mathrm{mL\,s^{-1}}$

Figure 6.18: Velocity profiles at different locations downstream of the tank inlet for different Q_L with $H_L = 30\,\mathrm{mm}$ at $t = 6.9\,\mathrm{s}$.

Figure 6.19 shows the velocity contour with vectors depicting the spreading of the liquid jet inside the bulk liquid with $H_L = 30\,\text{mm}$ for different Q_L at $t = 6.9\,\text{s}$. The pink-coloured contour represents the boundary of the liquid jet, where its axial velocity is zero ($v_z = 0\,\text{m}\,\text{s}^{-1}$). The jet boundary is displayed from the tank inlet to the liquid interface. It can be noticed that the liquid jet begins to spread, as soon as it enters the tank. The spreading angle widens as the jet approaches the interface and a bulged shape of the jet boundary can be noticed for $Q_L = 1.30\,\text{mL}\,\text{s}^{-1}$ and $Q_L = 1.50\,\text{mL}\,\text{s}^{-1}$ in figures 6.19(b) and (c) respectively. The velocity vectors depict the entrainment of the bulk liquid into the liquid jet, which causes the jet boundary to bulge.

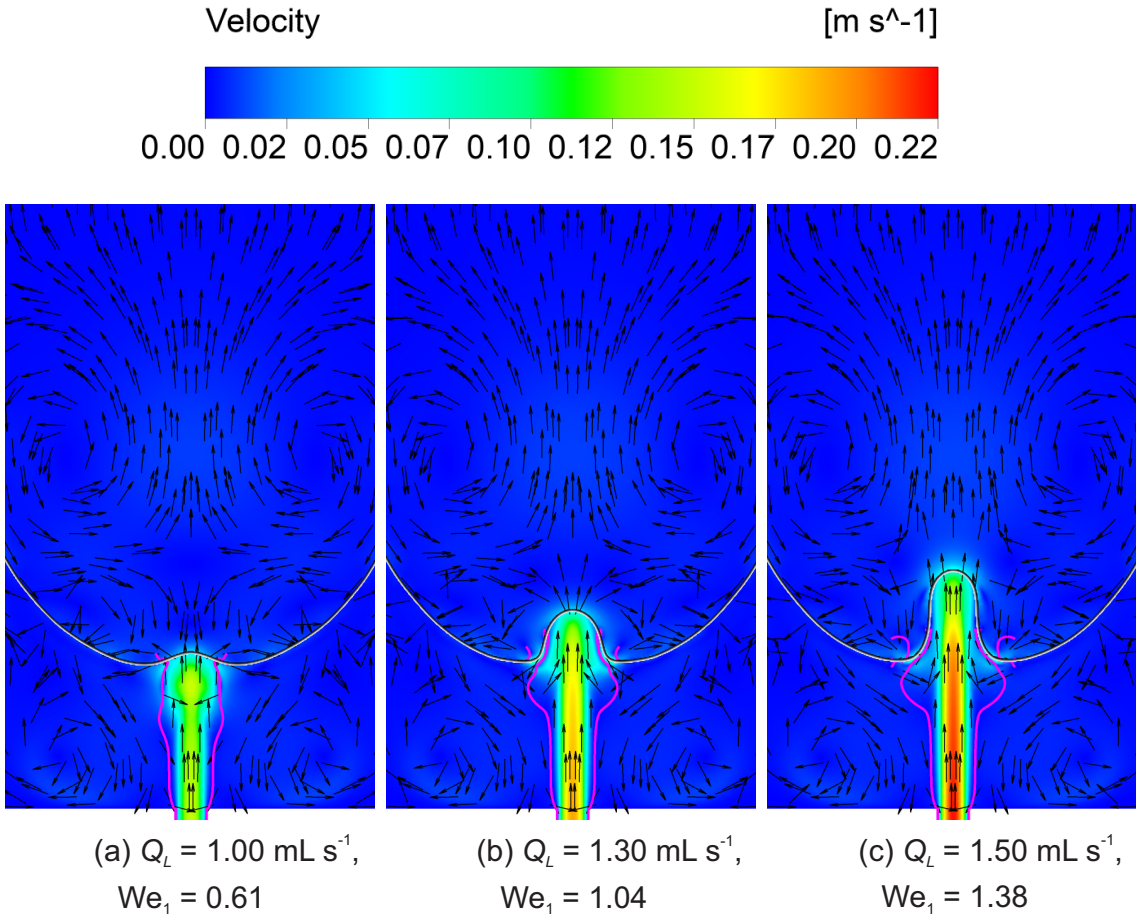

Figure 6.19: Spreading of the liquid jet depicted using velocity contour with vectors for different Q_L with $H_L = 30\,\text{mm}$ at $t = 6.9\,\text{s}$. The pink contour indicates the boundary of the spreading jet.

6.4.3 Liquid filling into an initially empty tank

In some scenarios, the propellant depot tanks or spacecraft tanks that are fully empty have to be refilled in reduced gravity. In order to understand the filling of an initially empty tank by observing the behaviour of an incoming liquid jet, numerical simulations were carried out under reduced gravity conditions for 9 s by initializing the tank completely with air. The simulations were tested for different volumetric flow rates of the liquid HFE-7500 in the range of $1.00\,\mathrm{mL\,s^{-1}} \leq Q_L \leq 1.50\,\mathrm{mL\,s^{-1}}$. The corresponding mass flow rates were defined as the inlet boundary condition. The liquid volume fraction and velocity contours of the filling of an initially empty tank in reduced gravity are shown in figure 6.20 for different volumetric flow rates at $t = 9\,\mathrm{s}$.

For a volumetric flow rate of $Q_L = 1.00\,\mathrm{mL\,s^{-1}}$, the liquid jet forms a small bulge near the tank inlet and flows radially towards the tank wall. The liquid rising at the wall can be observed in figure 6.20(a). The axial flow surpasses the radial flow and the liquid jet forms a geyser for $Q_L = 1.10\,\mathrm{mL\,s^{-1}}$, which grows and stabilizes at a certain height. A continuously growing geyser, that moves towards the tank outlet, is observed for $Q_L = 1.20\,\mathrm{mL\,s^{-1}}$. Beyond this, as the flow rate increases, the growth rate of the geyser also increases followed by the disintegration of the geyser into droplets, as seen in the case of the pre-filled tank with $H_L = 30\,\mathrm{mm}$. The liquid droplets touch the outlet port of the tank and also spread radially on the top wall, as seen in figures 6.20(d), (e) and (f). The critical flow rate is expected to be in the range of $1.20\,\mathrm{mL\,s^{-1}} < Q_L < 1.30\,\mathrm{mL\,s^{-1}}$, as the breakage of droplets occurs for $Q_L = 1.30\,\mathrm{mL\,s^{-1}}$. Furthermore, the flow rates of $Q_L > 1.30\,\mathrm{mL\,s^{-1}}$ can be categorized as supercritical flow rates for the liquid filling into an initially empty tank.

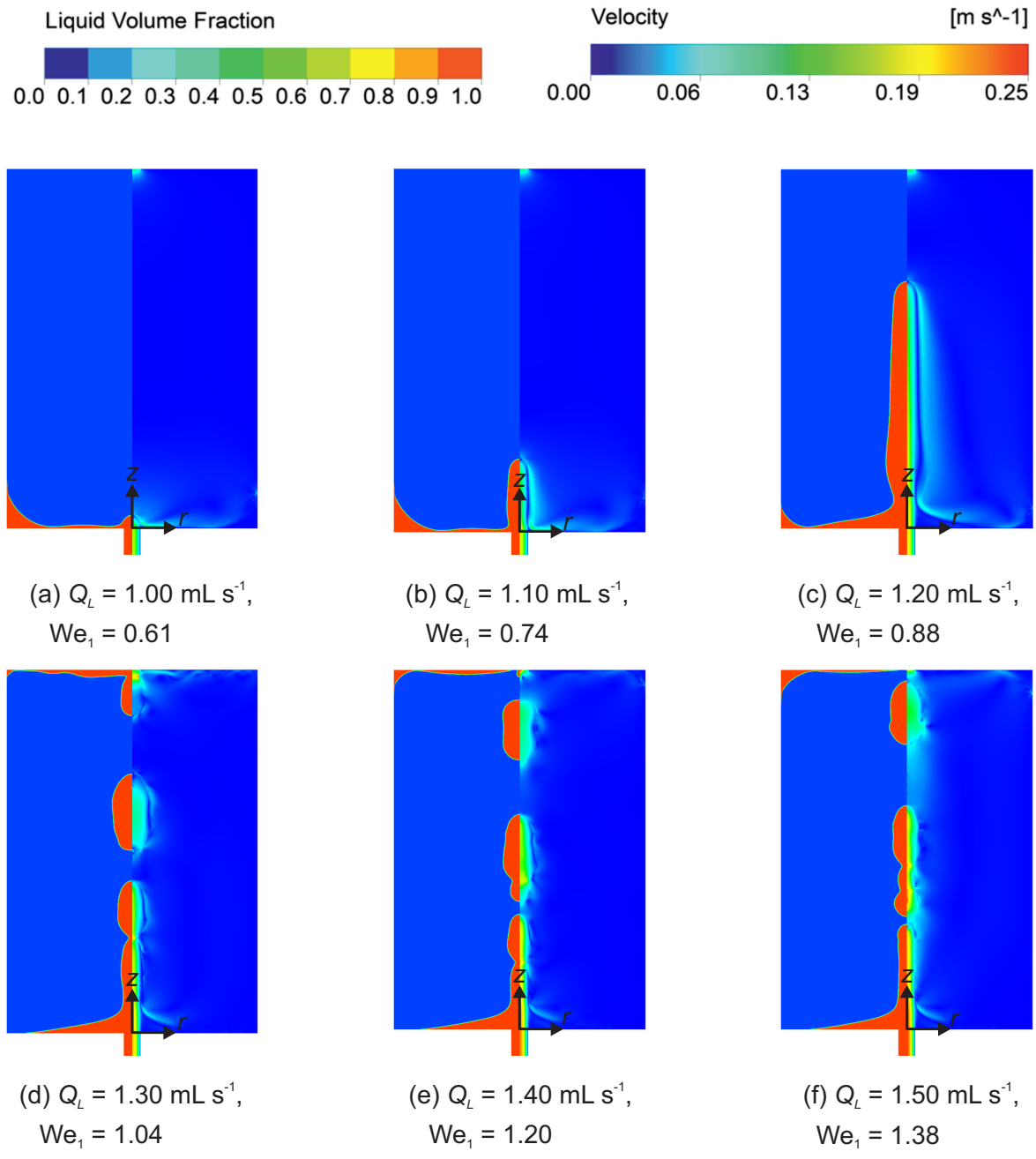

(a) Q_L = 1.00 mL s^{-1}, We_1 = 0.61

(b) Q_L = 1.10 mL s^{-1}, We_1 = 0.74

(c) Q_L = 1.20 mL s^{-1}, We_1 = 0.88

(d) Q_L = 1.30 mL s^{-1}, We_1 = 1.04

(e) Q_L = 1.40 mL s^{-1}, We_1 = 1.20

(f) Q_L = 1.50 mL s^{-1}, We_1 = 1.38

Figure 6.20: Liquid filling into an initially empty tank under reduced gravity. All the figures correspond to the simulation time of $t = 9\,\mathrm{s}$. The liquid volume fraction is the contour in the left part of the figure and the velocity magnitude is the contour in the right part of the figure.

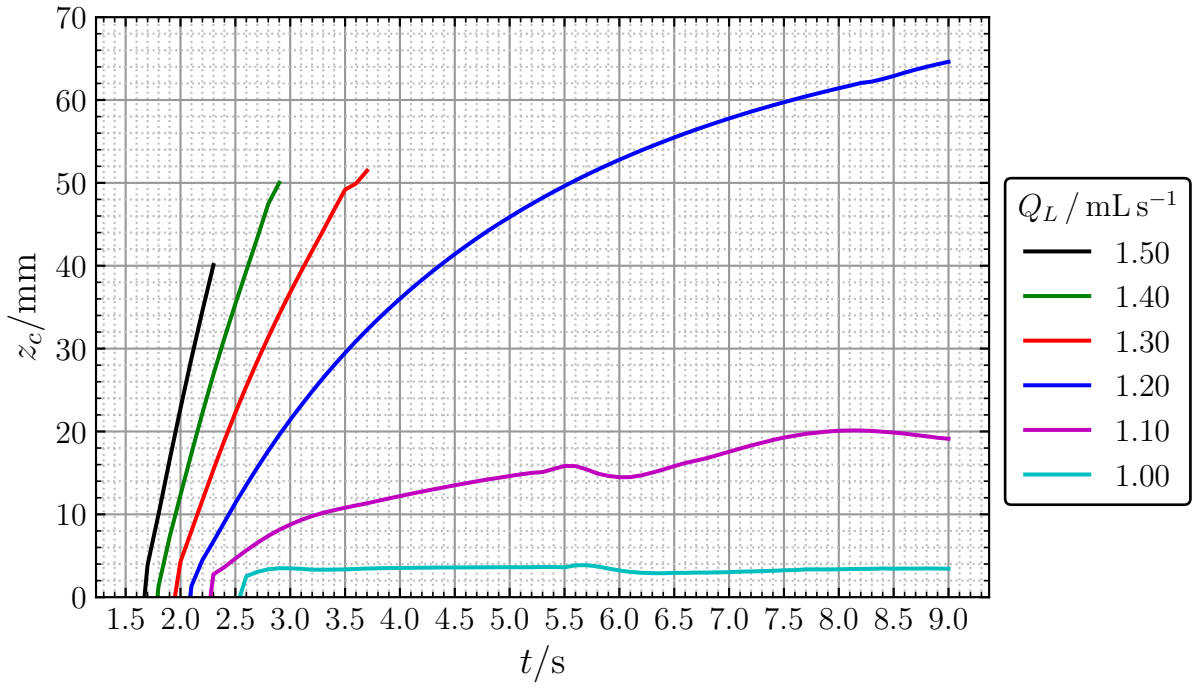

Figure 6.21: Evolution of the centre point of the interface during the filling of an initially empty tank in reduced gravity.

The centre point of the liquid interface during the filling of liquid into an initially empty tank is plotted against time for different volumetric flow rates in figure 6.21. The plots are shown from the time instant the liquid jet exits the inlet pipe and enters the tank. The centre point of the liquid interface remains almost constant over time for $Q_L = 1.00\,\mathrm{mL\,s^{-1}}$. For $Q_L = 1.10\,\mathrm{mL\,s^{-1}}$, the liquid jet forms a geyser, that grows to a maximum height of $z_c = 20.1\,\mathrm{mm}$. A steady increase in geyser height with time is observed for $Q_L = 1.20\,\mathrm{mL\,s^{-1}}$. For higher volumetric flow rates in the range of $1.30\,\mathrm{mL\,s^{-1}} \leq Q_L \leq 1.50\,\mathrm{mL\,s^{-1}}$, the curves in figure 6.21 imply a rapid development of geysers and these curves are plotted until the time when the geyser remains intact and droplets are not formed. For $Q_L = 1.30\,\mathrm{mL\,s^{-1}}$, the geyser becomes unstable and disintegrates into droplets after $t = 3.7\,\mathrm{s}$. For $Q_L > 1.30\,\mathrm{mL\,s^{-1}}$, the detachment of droplets occurs earlier with an increase in flow rate.

6.5 Comparison between the drop tower experiments and numerical simulations

According to Friese et al. 2019 [34], the final equilibrium position of the centre point of the interface in reduced gravity can be found from equation 2.34. Therefore, for a tank radius of $R_T = 30\,\text{mm}$ and an initial liquid fill height of $H_L = 30\,\text{mm}$, the centre point position at its final equilibrium configuration in reduced gravity is 20 mm. The centre point oscillation during the reorientation of liquid under reduced gravity is compared between the drop tower experiment F31 and the numerical simulation for $H_L = 30\,\text{mm}$ in figure 6.22. The centre point position is shown in green colour for the experiment and in red colour for the simulation. The initial and final positions are marked by dashed horizontal lines in figure 6.22. The reduced gravity begins at time $t = 0\,\text{s}$ and ends at $t = 9\,\text{s}$.

Immediately after the reduction of gravity, the centre point moves upwards first and then begins to move downwards. This phenomenon could be observed clearly in the numerical simulation, but not in the experiment. While the capillary wave hinders the detection of the centre point in the experiment for the first few milliseconds in reduced gravity, the centre point steadily moves downwards in the simulation. The first pass of the centre point across the final equilibrium configuration is at $t = 0.5\,\text{s}$ from the numerical simulation, which is lower than the equilibrium time of $t_s = 0.67\,\text{s}$ calculated for the given tank geometry and liquid from the correlation reported by Siegert et al. 1964 [78]. In the experiment, the equilibrium time was found to be $t_s = 0.68\,\text{s}$. A clear offset can be noticed between the simulation and experiment curves. Although the oscillation amplitudes are higher in the simulation than in the experiment, at $t = 3.5\,\text{s}$, the centre point positions from both experiment and simulation lie closer to each other. After $t = 8\,\text{s}$, the oscillations dampen and the centre point can be seen tending towards the final equilibrium configuration in reduced gravity. At $t = 9\,\text{s}$, the centre point position is predicted well by the simulation and is in good agreement with both experiment and theoretical value, as compared in table 6.2. After the centre point crosses the final equilibrium position, the oscillation from the simulation contains three maxima, whereas the experimental curve contains only two maxima before they dampen out. Furthermore, the period of oscillation was calculated to be $T_w = 3\,\text{s}$ in both experiment and simulation. This results in an oscillation frequency of $f = 0.3\,\text{Hz}$ in both experiment and simulation.

Table 6.2: Comparison of the centre point position at its final equilibrium configuration in reduced gravity at $t = 9\,\text{s}$.

No.	Method	$z_{c,0g}/\text{mm}$
1	Theory (Friese et al. 2019 [34])	20.0
2	Experiment - F31 (after correction)	19.9 ± 0.3
3	Numerical simulation	19.9

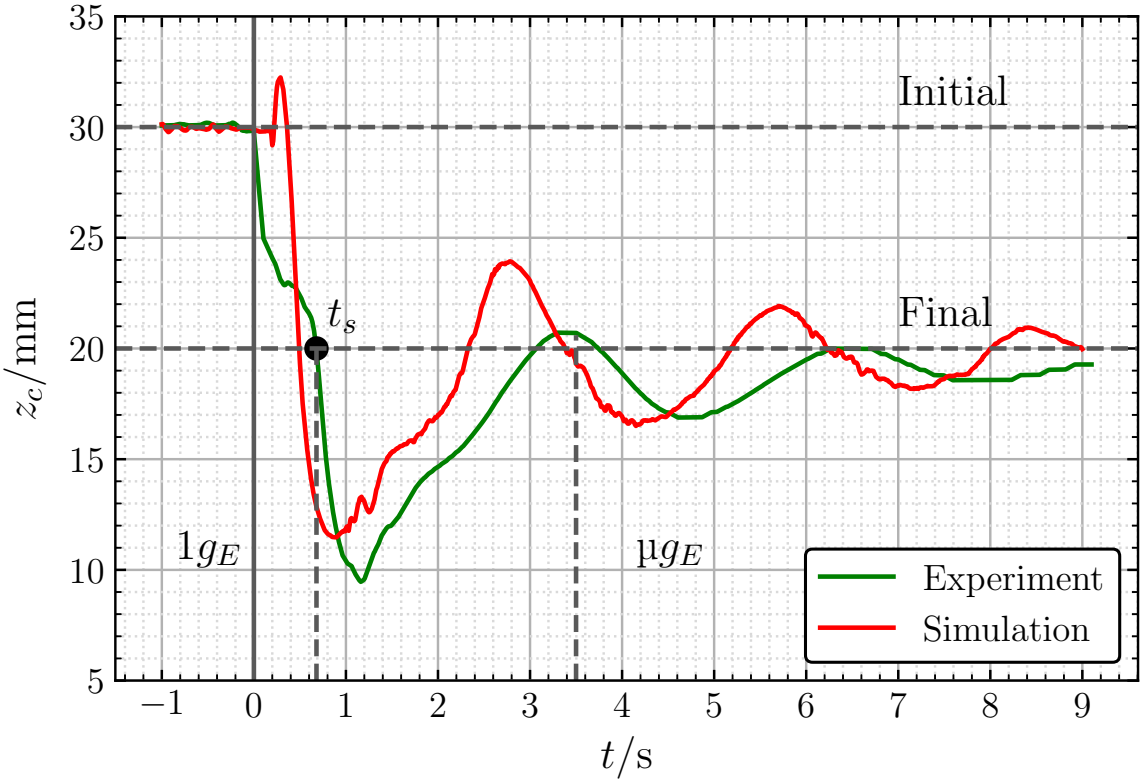

Figure 6.22: Comparison of the centre point oscillation between the drop tower experiment and numerical simulation during the reorientation of liquid inside the experiment tank under reduced gravity for $H_L = 30\,\text{mm}$. The dashed horizontal lines mark the initial and final positions of the centre point. The solid vertical line indicates the start of reduced gravity. The first dashed vertical line from the left corresponds to the equilibrium time t_s in reduced gravity and the second dashed vertical line depicts the start of liquid filling.

The position of the centre point of the geyser is measured from the origin of the tank, as shown in figure 5.4b. This position, which is also called the geyser height, is compared between the drop tower experiments and numerical simulations for $H_L = 30\,\text{mm}$ in figure 6.23. The time frame of the simulations is synchronized with the drop tower experiments, such that the plot can be generated for the reduced gravity time between $t = 3.5\,\text{s}$ and $t = 9\,\text{s}$. The solid curves represent the experiment data and the dotted curves illustrate the simulations in figure 6.23. The plot compares the centre point position of the geyser for four different inlet Weber numbers. The experimental curves for $\text{We}_1 = 1.04$, $\text{We}_1 = 1.38$ and the simulation curve for $\text{We}_1 = 1.38$ are respectively plotted only until the point the geyser does not disintegrate into droplets. The geyser height from the simulation is lower than the experiment for $\text{We}_1 = 0.74$. After $t = 5\,\text{s}$, the numerical simulations over-predict the geyser height than the experiments for $\text{We}_1 = 0.88$ and $\text{We}_1 = 1.04$. The oscillations of the geyser, which were observed in the experiments, could not be reproduced in the 2D simulations. Therefore, in the simulations, the geyser continuously grows without the breakage of droplets for $\text{We}_1 = 1.04$. The trend of the simulation matches with the experiment for $\text{We}_1 = 1.38$. However, the breakage of the first droplet occurs only after $t = 5.2\,\text{s}$ in the simulation, as against $t = 4.1\,\text{s}$ in the experiment. The mean percentage deviation in the geyser height values between the 2D numerical simulations and drop tower experiments for $H_L = 30\,\text{mm}$ was found to be approximately 11.3 %.

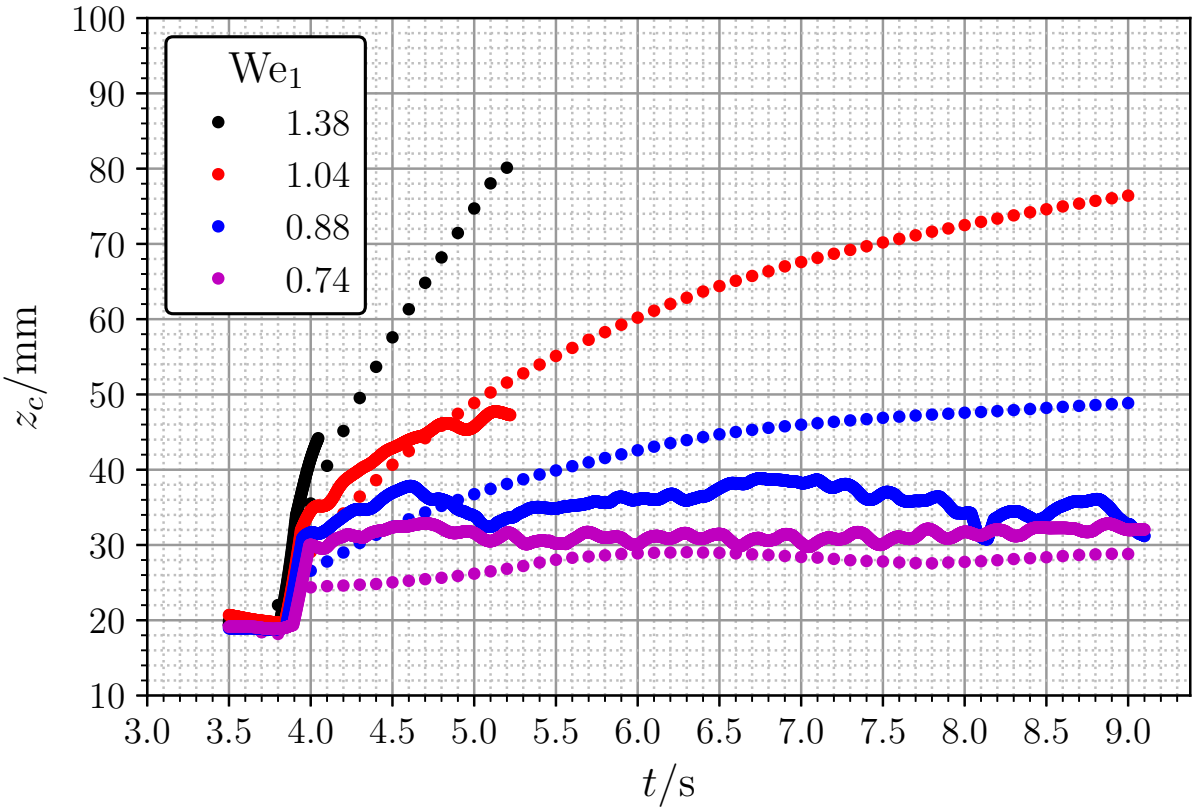

Figure 6.23: Comparison of the geyser height between the drop tower experiments and numerical simulations during the filling of a pre-filled tank with $H_L = 30\,\text{mm}$. The solid curves represent the experiment data and the simulation results are presented as dotted curves.

The flow patterns formed due to the interaction of the liquid jet with the interface are compared between the numerical simulations and drop tower experiments in figure 6.24 for different volumetric flow rates Q_L with an initial liquid fill height of $H_L = 30\,\text{mm}$. The simulation figures correspond to a simulation time of $t = 12\,\text{s}$ in reduced gravity, which is equivalent to $t = 9\,\text{s}$ in the experiments. The flow direction is in the $+z$ direction. The contour plots of the simulations in figure 6.24 are divided into two halves, with the liquid volume fraction as the left contour and the velocity magnitude as the right contour.

The simulation replicates the perturbation of the interface and formation of a small bulge at the centre of the tank for $Q_L = 1.10\,\text{mL}\,\text{s}^{-1}$, as observed in the drop tower experiment. For $Q_L = 1.20\,\text{mL}\,\text{s}^{-1}$, the geyser oscillates and surface waves are formed in the experiment. On the other hand, in the simulations, the oscillation of the geyser is not captured and the geyser reaches a maximum height of 50 mm and remains stable. The simulation results for $Q_L = 1.30\,\text{mL}\,\text{s}^{-1}$ show that the geyser height increases continuously with time and the liquid jet moves towards the outlet of the tank without any disintegration of droplets. However, in the experiment for $Q_L = 1.30\,\text{mL}\,\text{s}^{-1}$, which is considered as the critical flow rate, the liquid jet becomes unstable and breaks into droplets. The instability of the liquid jet and disintegration of droplets are captured in the simulation for the supercritical flow rate of $Q_L = 1.50\,\text{mL}\,\text{s}^{-1}$. However, in the experiment, the breakage of droplets occurs earlier than in the simulation.

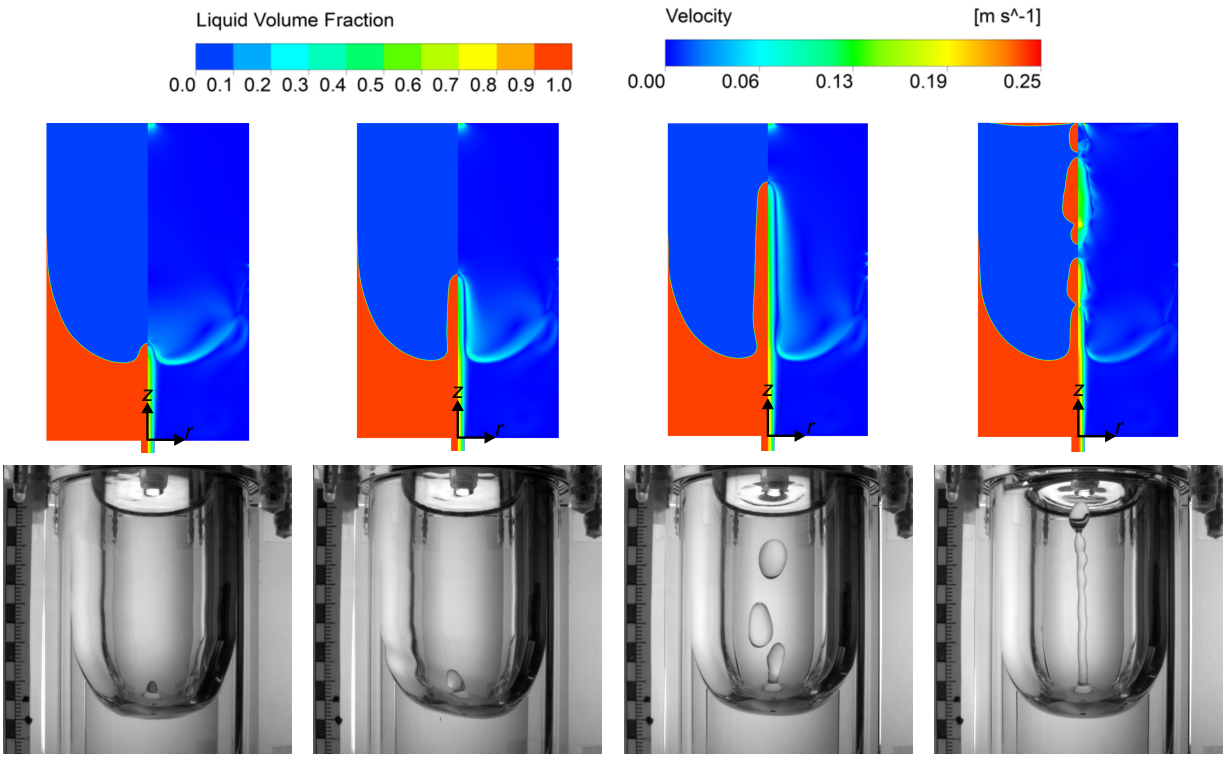

(a) Q_L = 1.10 mL s^{-1}, We$_1$ = 0.74 (b) Q_L = 1.20 mL s^{-1}, We$_1$ = 0.88 (c) Q_L = 1.30 mL s^{-1}, We$_1$ = 1.04 (d) Q_L = 1.50 mL s^{-1}, We$_1$ = 1.38

Figure 6.24: Comparison of the geyser patterns between the numerical simulations (top) and drop tower experiments (bottom) for different Q_L with $H_L = 30\,\text{mm}$. In the simulation results, the contour is liquid volume fraction in the left and velocity magnitude in the right.

It can be summarized that the 2D numerical simulations do not reproduce the geyser shape, geyser oscillations and disintegration of droplets very well. Furthermore, the critical flow rate, at which the interface becomes unstable, is over-predicted in the simulations. It has to be noted that the geyser formation and development are 3D phenomena, as the geyser oscillates and creates surface waves and disintegrates into droplets when it becomes unstable. In order to fully model all the effects, a very high spatial and temporal resolution of the computational domain would be required.

6.6 Parametric study

Despite the deviation between the simulation and experimental results, a parametric study was conducted by varying the initial liquid fill heights H_L. Therefore, the numerical simulations were carried out with different initial liquid fill heights of $H_L = 15\,\text{mm}$, $H_L = 45\,\text{mm}$, $H_L = 60\,\text{mm}$ and with the same volumetric flow rates in the range of $1.00\,\text{mL}\,\text{s}^{-1} \leq Q_L \leq 1.50\,\text{mL}\,\text{s}^{-1}$. The test matrix of the simulations can be referred to in table 5.2. The simulation results of the parametric study are discussed in two parts.

In the first part, the flow patterns formed during the liquid filling into a pre-filled tank with different volumetric flow rates Q_L are shown for initial liquid fill heights of $H_L = 15\,\text{mm}$, $H_L = 45\,\text{mm}$ and $H_L = 60\,\text{mm}$. The contours of liquid volume fraction and velocity magnitude are shown on the left and right part of all the figures respectively. All the figures are shown for the simulation time of $t = 12\,\text{s}$, which in turn corresponds to a reduced gravity time of $9\,\text{s}$. In the second part, the plots of centre point evolution over time are shown for different Q_L and all H_L. The trends of geyser height development are discussed for every H_L with the help of these plots.

Figure 6.25 shows the flow patterns formed during the liquid filling into a pre-filled tank with an initial liquid fill height of $H_L = 15\,\text{mm}$ for different volumetric flow rates Q_L. The volume of bulk liquid present in the tank is smaller and as a result of reorientation, the liquid jet travels a shorter distance in the bulk liquid before it interacts with the interface. The flow rates of $Q_L = 1.00\,\text{mL}\,\text{s}^{-1}$ and $Q_L = 1.10\,\text{mL}\,\text{s}^{-1}$ are subcritical because they do not exhibit a significant growth of geysers along the z-axis. Furthermore, for $Q_L = 1.20\,\text{mL}\,\text{s}^{-1}$, the liquid jet momentum overcomes the capillary pressure of the interface and the geyser growth is very evident, as it moves towards the tank outlet. The geyser remains still intact and does not disintegrate into droplets for $Q_L = 1.20\,\text{mL}\,\text{s}^{-1}$. A clear instability behaviour can be observed in figure 6.25(d) for $Q_L = 1.30\,\text{mL}\,\text{s}^{-1}$, where the liquid jet disintegrates and new droplets are formed. This shows that the critical flow rate may be located around $Q_L = 1.30\,\text{mL}\,\text{s}^{-1}$ for $H_L = 15\,\text{mm}$. For $Q_L = 1.40\,\text{mL}\,\text{s}^{-1}$, the liquid jet with a wavy structure can be noticed in figure 6.25(e). These disturbances in the jet lead to the breakage of droplets, which then touch the outlet of the tank. The shapes of the droplets differ from each other in figure 6.25(f) and the spreading of liquid on the top wall can also be seen for $Q_L = 1.50\,\text{mL}\,\text{s}^{-1}$.

The flow patterns for $H_L = 45\,\text{mm}$ are shown in figure 6.26 for different Q_L. The liquid jet only creates a tiny bulge above the interface for $Q_L = 1.00\,\text{mL}\,\text{s}^{-1}$ and $Q_L = 1.10\,\text{mL}\,\text{s}^{-1}$. The linear momentum of the liquid jet is not strong enough to form a geyser. The liquid meniscus rises primarily along the wall. A geyser is created for $Q_L = 1.20\,\text{mL}\,\text{s}^{-1}$, which only grows to a marginal height and stabilizes at its position. A grown geyser, that is approaching the tank outlet, can be noticed in figure 6.26(d) for $Q_L = 1.30\,\text{mL}\,\text{s}^{-1}$. The liquid jet touches the outlet port for higher flow rates of $Q_L = 1.40\,\text{mL}\,\text{s}^{-1}$ and $Q_L = 1.50\,\text{mL}\,\text{s}^{-1}$. The distance available for the liquid jet to freely move in the ullage region is limited due to the tank height. A perturbed liquid jet can be seen for $Q_L = 1.50\,\text{mL}\,\text{s}^{-1}$ in figure 6.26(f).

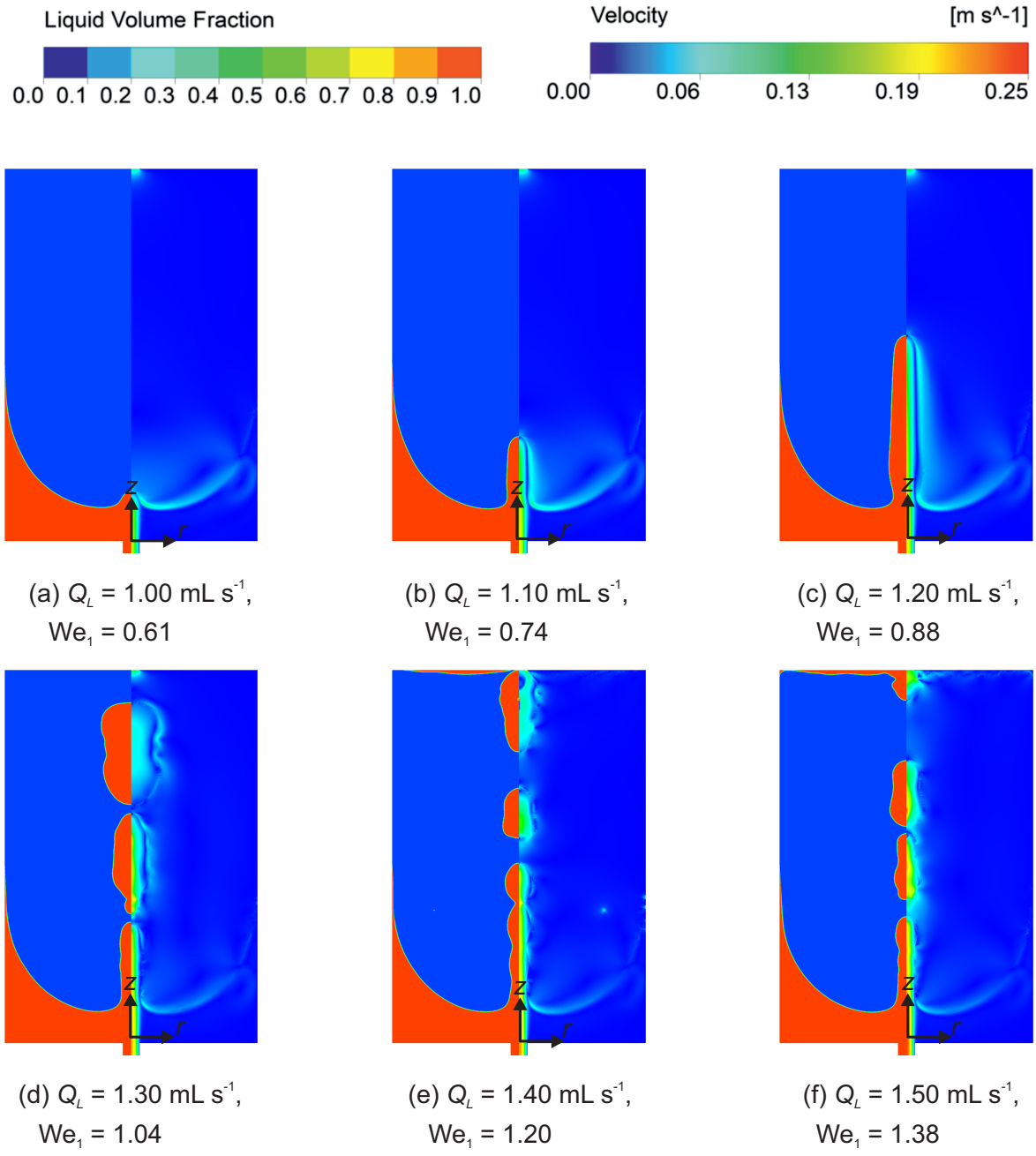

Figure 6.25: Flow patterns formed for different Q_L during the liquid filling into a tank with an initial liquid fill height of $H_L = 15\,\text{mm}$. All the figures correspond to the simulation time of $t = 12\,\text{s}$. The liquid volume fraction is the contour in the left part of the figure and the velocity magnitude is the contour in the right part of the figure.

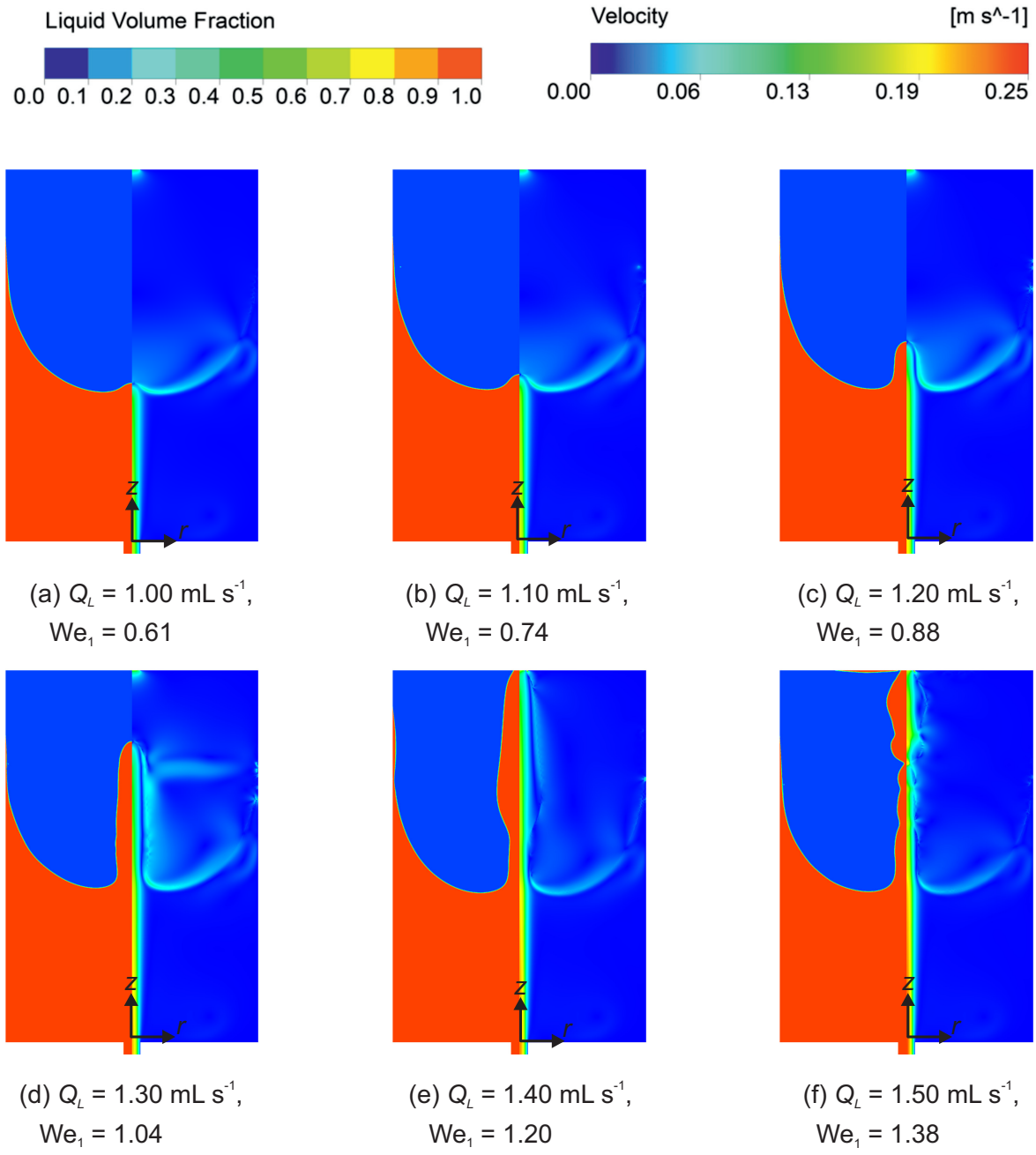

Figure 6.26: Flow patterns formed for different Q_L during the liquid filling into a tank with an initial liquid fill height of $H_L = 45\,\text{mm}$. All the figures correspond to the simulation time of $t = 12\,\text{s}$. The liquid volume fraction is the contour in the left part of the figure and the velocity magnitude is the contour in the right part of the figure.

The flow patterns for $H_L = 60\,\text{mm}$ are shown in figure 6.27 for different Q_L. Due to a higher volume of bulk liquid present inside the tank, the incoming liquid jet has to travel a longer distance before reaching the interface. The spreading of the liquid jet as it travels through the bulk liquid can be noticed in the velocity contours on the right side of figure 6.27. Only a small perturbation of the interface is observed for $Q_L \leq 1.20\,\text{mL}\,\text{s}^{-1}$. A growing geyser is formed for $Q_L = 1.30\,\text{mL}\,\text{s}^{-1}$.

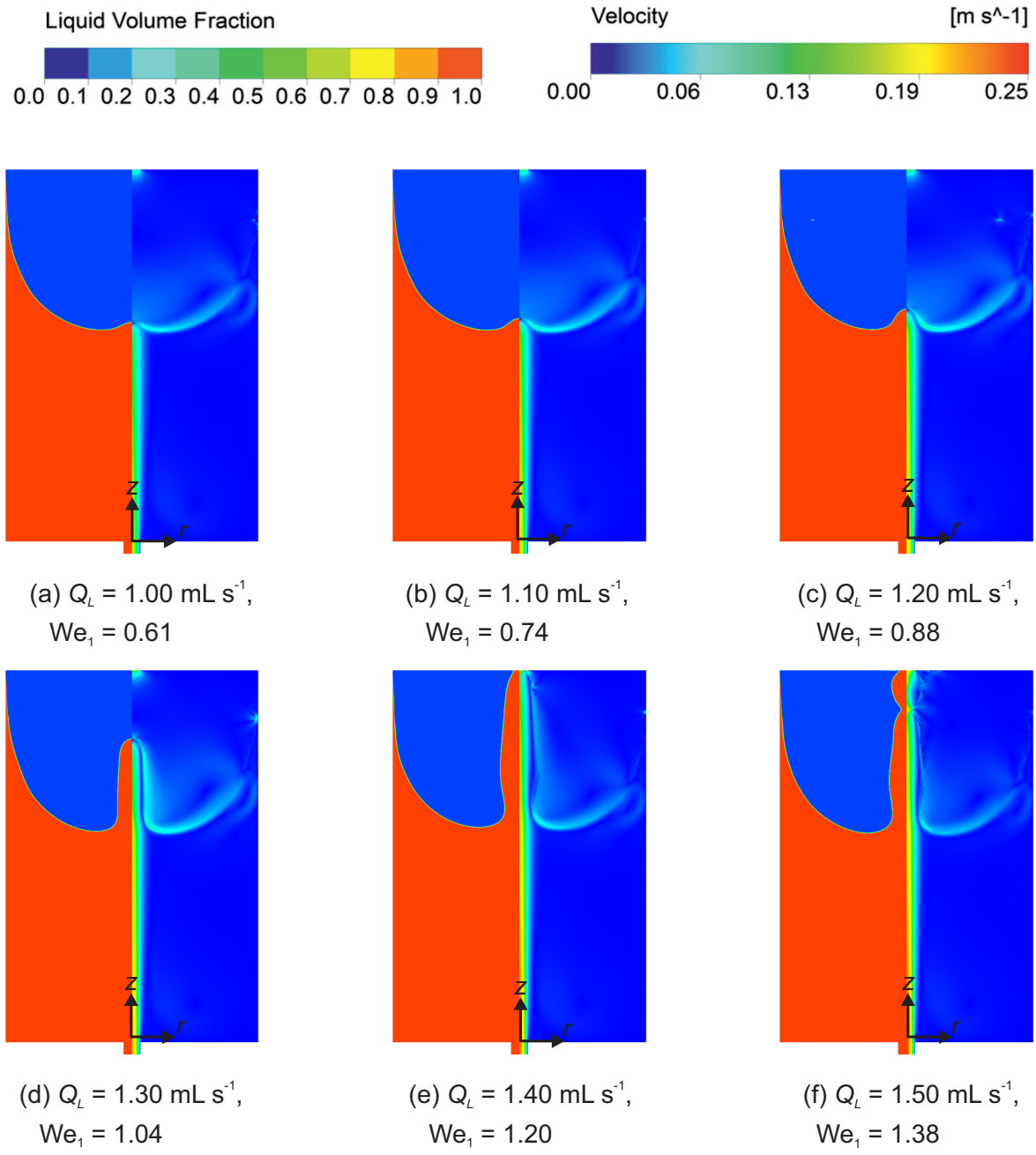

Figure 6.27: Flow patterns formed for different Q_L during the liquid filling into a tank with an initial liquid fill height of $H_L = 60\,\text{mm}$. All the figures correspond to the simulation time of $t = 12\,\text{s}$. The liquid volume fraction is the contour in the left part of the figure and the velocity magnitude is the contour in the right part of the figure.

As the ullage region is smaller for the liquid jet to freely develop after penetrating the interface, the jet touches the tank outlet faster for a higher flow rate of $Q_L = 1.40\,\text{mL}\,\text{s}^{-1}$. A perturbed liquid jet impinging on the tank outlet can be observed for the flow rate of $Q_L = 1.50\,\text{mL}\,\text{s}^{-1}$ in figure 6.27(f). In appendix section B, the interaction of the liquid jet with the interface is shown with the help of velocity contour and vectors in figure B.2 for $H_L = 60\,\text{mm}$. The corresponding centreline velocity progression in dimensionless form is plotted in figure B.3.

The evolution of the centre point of the interface over time is plotted in figure 6.28 for all the initial liquid fill heights H_L and volumetric flow rates Q_L that have been considered for the numerical simulations. The plot 6.28a is shown from $t = 1.5\,\mathrm{s}$ to $t = 9\,\mathrm{s}$ for $H_L = 0\,\mathrm{mm}$. All the other plots are shown from $t = 6.5\,\mathrm{s}$ to $t = 12\,\mathrm{s}$. For some flow rates, the geyser height curves are plotted until the time instant the geyser remains intact and does not disintegrate into droplets or until the time instant the geyser touches the tank outlet. Although the plots for $H_L = 0\,\mathrm{mm}$ and $H_L = 30\,\mathrm{mm}$ were already discussed in previous sections, they are repeated here for comparison purposes.

In figure 6.28a for $H_L = 0\,\mathrm{mm}$, the centre point evolution curves of $Q_L = 1.00\,\mathrm{mL\,s^{-1}}$ and $Q_L = 1.10\,\mathrm{mL\,s^{-1}}$ depict that the centre point positions lie under the height of $z_c = 20\,\mathrm{mm}$. The curve for $Q_L = 1.20\,\mathrm{mL\,s^{-1}}$ shows a continuous growth of the geyser. However, as the simulations were run only until $t = 9\,\mathrm{s}$, it could not be confirmed if the geyser would eventually break into droplets or stabilize at a certain height. For $Q_L = 1.30\,\mathrm{mL\,s^{-1}}$, the geyser disintegrates into droplets after $t = 3.7\,\mathrm{s}$. Hence, the critical flow rate for $H_L = 0\,\mathrm{mm}$ can be predicted to be between $Q_L = 1.20\,\mathrm{mL\,s^{-1}}$ and $Q_L = 1.30\,\mathrm{mL\,s^{-1}}$. A sharp increase in the geyser height can be observed for the flow rates of $Q_L \geq 1.30\,\mathrm{mL\,s^{-1}}$. An increase in flow rate leads to an early disintegration of the droplets from the geyser. In appendix section B, the decay of the centreline velocity is presented in figure B.4 for $H_L = 0\,\mathrm{mm}$.

The characteristics of the geyser height curves can be clearly distinguished in figure 6.28b for $H_L = 15\,\mathrm{mm}$. While the centre point of the interface oscillates around $z_c = 10\,\mathrm{mm}$ for $Q_L = 1.00\,\mathrm{mL\,s^{-1}}$, it only reaches a maximum height of $z_c = 26.4\,\mathrm{mm}$ for $Q_L = 1.10\,\mathrm{mL\,s^{-1}}$. A characteristic curve with a decreasing slope tending towards an equilibrium height is observed for $Q_L = 1.20\,\mathrm{mL\,s^{-1}}$. Similar to $H_L = 0\,\mathrm{mm}$ in figure 6.28a, the breakage of the first droplet from the geyser is observed for the flow rate of $Q_L = 1.30\,\mathrm{mL\,s^{-1}}$, which implies that the critical flow rate for $H_L = 15\,\mathrm{mm}$ lies between $Q_L = 1.20\,\mathrm{mL\,s^{-1}}$ and $Q_L = 1.30\,\mathrm{mL\,s^{-1}}$. In the supercritical regime of $Q_L > 1.30\,\mathrm{mL\,s^{-1}}$, the jet breakup height and time are inversely proportional to the flow rate Q_L.

As can be seen from figure 6.28c for the flow rates of $Q_L = 1.00\,\mathrm{mL\,s^{-1}}$ and $Q_L = 1.10\,\mathrm{mL\,s^{-1}}$, the geyser does not grow beyond the initial liquid fill height of $H_L = 30\,\mathrm{mm}$ and shows a fluctuating behaviour, whereas for $Q_L = 1.20\,\mathrm{mL\,s^{-1}}$, the geyser grows to a maximum height of $z_c = 48.8\,\mathrm{mm}$. A sharp rise in the geyser height without any breakage of droplets can be noticed for $Q_L = 1.30\,\mathrm{mL\,s^{-1}}$. The geyser travels rapidly for $Q_L = 1.40\,\mathrm{mL\,s^{-1}}$ and reaches a maximum height of $z_c = 86\,\mathrm{mm}$, before breaking into droplets. Therefore, it can be said that the critical flow rate is approximately around $Q_L = 1.40\,\mathrm{mL\,s^{-1}}$ for $H_L = 30\,\mathrm{mm}$. An early breakup of the geyser takes place at $t = 8.3\,\mathrm{s}$ for $Q_L = 1.50\,\mathrm{mL\,s^{-1}}$.

Figure 6.28d shows the geyser height curves for $H_L = 45\,\mathrm{mm}$. The geyser climbs to the maximum height of only 5.5 mm above the initial liquid fill height of $H_L = 45\,\mathrm{mm}$ in the subcritical flow regime of $Q_L \leq 1.20\,\mathrm{mL\,s^{-1}}$. For $Q_L = 1.30\,\mathrm{mL\,s^{-1}}$, the geyser shows a significant growth without any formation of droplets. The geyser touches the tank outlet port at $t = 10.3\,\mathrm{s}$ for $Q_L = 1.40\,\mathrm{mL\,s^{-1}}$, as depicted by the green curve in figure 6.28d. Furthermore, the first breakup of the geyser into droplets occurs closer to the tank outlet at $t = 8.6\,\mathrm{s}$ for $Q_L = 1.50\,\mathrm{mL\,s^{-1}}$. Hence, the critical flow rate for $H_L = 45\,\mathrm{mm}$ is predicted to be around $Q_L = 1.50\,\mathrm{mL\,s^{-1}}$.

The centre point evolution curves display a comparable trend for $Q_L \leq 1.20\,\mathrm{mL\,s^{-1}}$ in figure 6.28e for $H_L = 60\,\mathrm{mm}$. A pronounced growth in the geyser height can be noticed for $Q_L = 1.30\,\mathrm{mL\,s^{-1}}$. However, it neither breaks into droplets nor grows beyond the height of about 80 mm until $t = 12\,\mathrm{s}$. Therefore, all the flow rates in the range of $Q_L \leq 1.30\,\mathrm{mL\,s^{-1}}$ can be classified as subcritical flow rates, where the interface remains stable. The geyser touches the tank outlet at $t = 9.9\,\mathrm{s}$ for $Q_L = 1.40\,\mathrm{mL\,s^{-1}}$ and at $t = 8.4\,\mathrm{s}$ for $Q_L = 1.50\,\mathrm{mL\,s^{-1}}$ respectively. As there was no disintegration of droplets from the geyser observed for the tested flow rates, the critical flow rate could not be determined for $H_L = 60\,\mathrm{mm}$ from the numerical simulations.

By comparing the plots of all the initial liquid fill heights H_L, it can be noticed that the geyser development exhibits nearly asymptotic behaviour in the subcritical flow regime. The critical regime is characterized by faster growth, followed by the breakage of droplets. In the supercritical flow regime, the geyser height increases sharply, which leads to an early breakup into droplets.

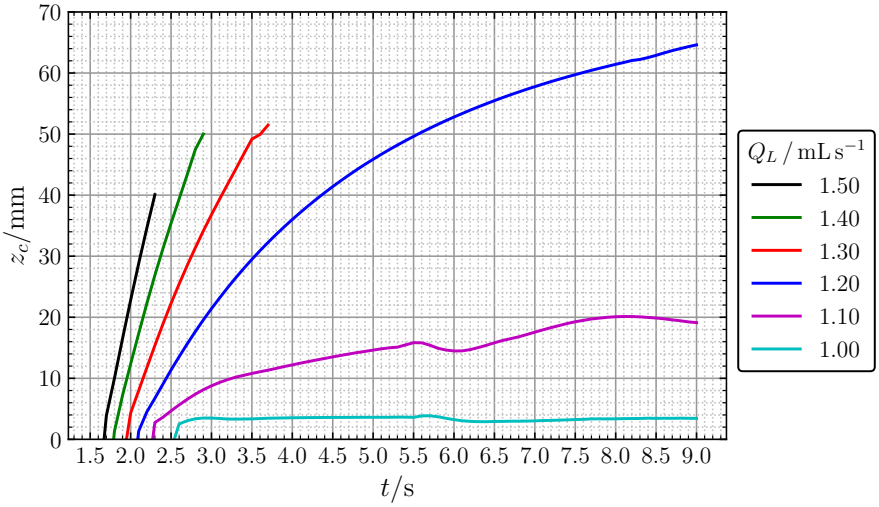

(a) $H_L = 0\,\mathrm{mm}$

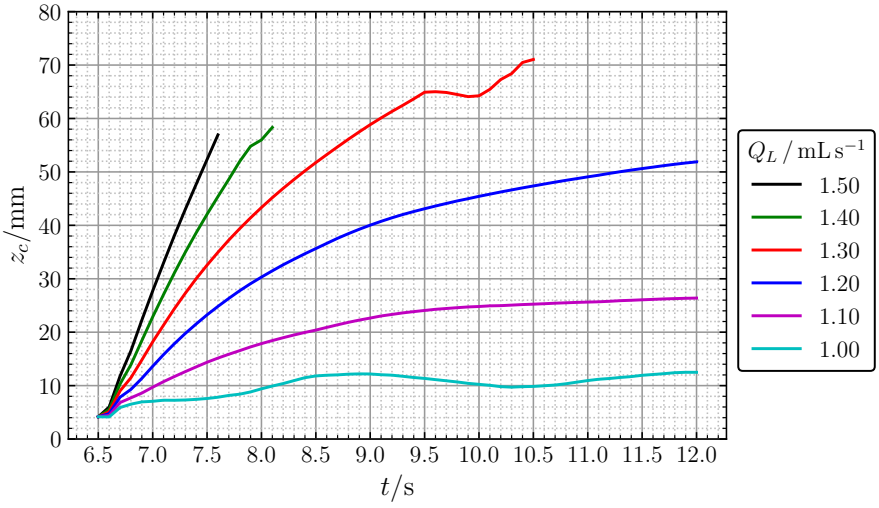

(b) $H_L = 15\,\mathrm{mm}$

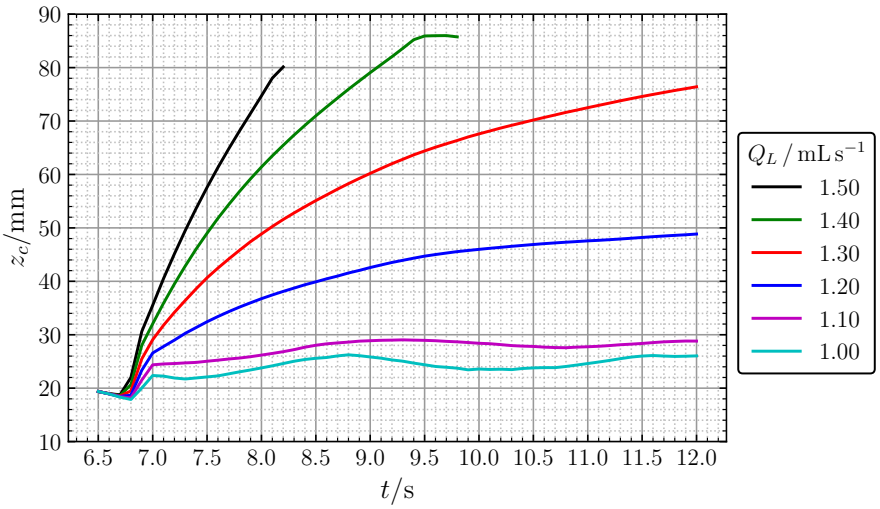

(c) $H_L = 30\,\text{mm}$

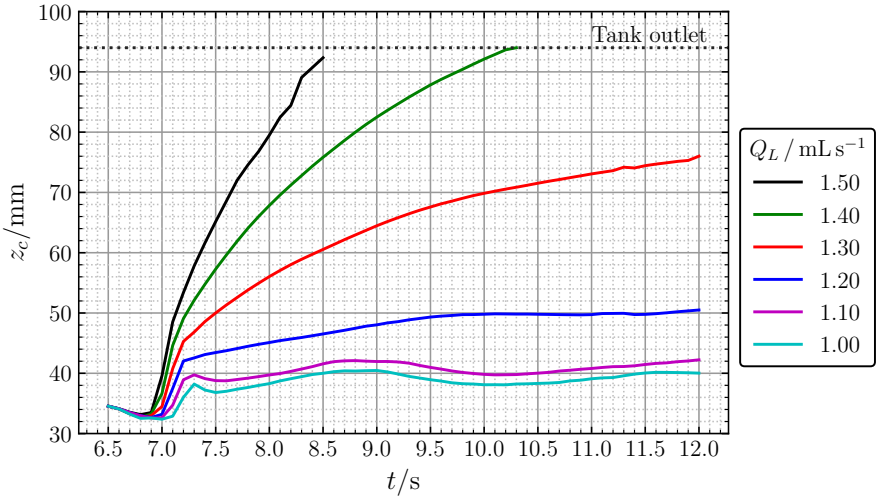

(d) $H_L = 45\,\text{mm}$

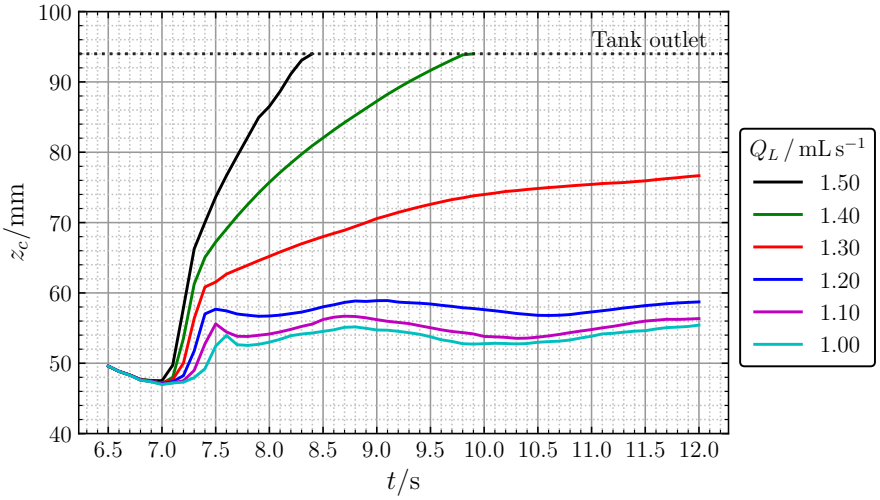

(e) $H_L = 60\,\text{mm}$

Figure 6.28: The numerical simulation results showing the evolution of the centre point of the interface over time for different H_L and Q_L.

6.7 Refinement of the volumetric flow rate Q_L and initial liquid fill height H_L

It can be noticed that a significant variation in the critical flow rates with respect to the initial liquid fill heights H_L could not be determined from the parametric study performed so far, which makes it difficult to observe the effect of initial liquid fill height H_L on the critical Weber number We_{1cr}. Therefore, the step size of the inlet volumetric flow rate Q_L needs to be decreased, in order to identify the critical flow rates more precisely in the numerical simulations. Furthermore, new initial liquid fill heights of $H_L = 7.5\,\text{mm}$, $H_L = 22.5\,\text{mm}$, $H_L = 37.5\,\text{mm}$ and $H_L = 52.5\,\text{mm}$ were taken into account, to find a correlation between the critical Weber number We_{1cr} and the initial liquid fill height H_L. The numerical simulations for the new fill heights of $H_L = 7.5\,\text{mm}$, $H_L = 22.5\,\text{mm}$ and $H_L = 37.5\,\text{mm}$ were carried out with the same volumetric flow rates in the range of $1.00\,\text{mL}\,\text{s}^{-1} \leq Q_L \leq 1.50\,\text{mL}\,\text{s}^{-1}$, as it was done for the other fill heights discussed in section 6.6. For higher initial liquid fill heights of $H_L = 52.5\,\text{mm}$ and $H_L = 60.0\,\text{mm}$, the range was increased to $1.00\,\text{mL}\,\text{s}^{-1} \leq Q_L \leq 1.60\,\text{mL}\,\text{s}^{-1}$, in order to detect the disintegration of droplets.

Then, the volumetric flow rates were refined in the range, where the liquid interface is sensitive to the flow rate and the geyser height curves display a significant change in shape, as seen in figure 6.28. The step size for the refinement of the volumetric flow rate was chosen as $\triangle Q_L = 0.01\,\text{mL}\,\text{s}^{-1}$. Table 6.3 shows the range in which the refinement of the volumetric flow rate was performed for all the initial liquid fill heights.

Table 6.3: The range in which the volumetric flow rates were refined with a step size of $\triangle Q_L = 0.01\,\text{mL}\,\text{s}^{-1}$ for different initial liquid fill heights H_L.

No.	H_L/mm	Refinement range of Q_L/mL s^{-1}
1	0.0	1.10–1.30
2	7.5	1.10–1.30
3	15.0	1.10–1.30
4	22.5	1.20–1.40
5	30.0	1.20–1.40
6	37.5	1.30–1.50
7	45.0	1.30–1.50
8	52.5	1.40–1.60
9	60.0	1.40–1.60

After performing the numerical simulations with refined volumetric flow rates, the plots of the centre point evolution over time are shown in figure 6.29 for the initial liquid fill heights of $H_L = 15\,\text{mm}$, $H_L = 30\,\text{mm}$ and $H_L = 60\,\text{mm}$. The plots are shown for the range of flow rates

that have been refined, as listed in table 6.3. The curves corresponding to the coarse flow rates discussed in the previous section 6.6 are shown as thick lines in figure 6.29. Additionally, the flow rate at which the first breakage of a droplet is observed is also depicted by a thick line.

The growth of the geyser with respect to the flow rate can be identified from the pattern of curves in figure 6.29a for $H_L = 15\,\text{mm}$. The curves show an asymptotic behaviour for flow rates in the range of $1.10\,\text{mL}\,\text{s}^{-1} \leq Q_L \leq 1.20\,\text{mL}\,\text{s}^{-1}$. A smooth increase in the geyser height can be observed for flow rates in the range of $1.20\,\text{mL}\,\text{s}^{-1} \leq Q_L \leq 1.27\,\text{mL}\,\text{s}^{-1}$. The geyser becomes unstable and the first droplet disintegrates from the geyser for $Q_L = 1.28\,\text{mL}\,\text{s}^{-1}$ at $t = 11.2\,\text{s}$, which makes it the critical flow rate for $H_L = 15\,\text{mm}$. The patterns of the geyser height curves for $H_L = 30\,\text{mm}$ look similar to $H_L = 15\,\text{mm}$ in figure 6.29b. The liquid jet touches the tank outlet for $Q_L = 1.36\,\text{mL}\,\text{s}^{-1}$ at $t = 11.7\,\text{s}$. The critical flow rate is found to be $Q_L = 1.37\,\text{mL}\,\text{s}^{-1}$, where the first droplet is detached from the geyser at $t = 10.6\,\text{s}$. As the flow rate increases, the breakup time of the droplet decreases. Figure 6.29c shows that for all the flow rates in the refinement range of $1.40\,\text{mL}\,\text{s}^{-1} \leq Q_L \leq 1.60\,\text{mL}\,\text{s}^{-1}$, the liquid jet touches the tank outlet for $H_L = 60\,\text{mm}$. As the flow rate increases, the time taken by the liquid jet to reach the tank outlet decreases. A steep increase in the geyser height can also be noticed for higher flow rates. However, the critical flow rate could not be determined for $H_L = 60\,\text{mm}$, as no disintegration of droplets was observed for these flow rates. If the tank height is increased, it would be possible to see the instability of the liquid jet and the formation of droplets. In case of a no-vent filling, the liquid jet that impinges on the top surface of the tank would help to cool down the tank walls. The plots for the remaining fill heights can be found in figure B.5 in the appendix section B.1.

The flow patterns formed during the disintegration of the first droplet are shown in figure 6.30 for every initial liquid fill height H_L. The corresponding critical flow rate and the time at which the breakup of a droplet occurs are also given in figure 6.30. The contours of liquid volume fraction and velocity magnitude are shown in the left and right parts of the figures respectively. The higher fill heights of $H_L = 52.5\,\text{mm}$ and $H_L = 60\,\text{mm}$ have been excluded from figure 6.30. Although the first disintegration of a droplet was observed for $H_L = 52.5\,\text{mm}$ at $Q_L = 1.50\,\text{mL}\,\text{s}^{-1}$, it could not be detected for other higher flow rates at $Q_L > 1.50\,\text{mL}\,\text{s}^{-1}$. The behaviour of the liquid jet touching the outlet of the tank without any disintegration of a droplet was noticed in all the flow rates in the refinement range of $1.40\,\text{mL}\,\text{s}^{-1} \leq Q_L \leq 1.60\,\text{mL}\,\text{s}^{-1}$. The corresponding plot of the geyser height over time for $H_L = 52.5\,\text{mm}$ can be referred to in figure B.5f in the appendix section B.1. Furthermore, no breakage of droplets was observed before the liquid jet reaches the tank outlet for $H_L = 60\,\text{mm}$, which can also be interpreted from figure 6.29c. Therefore, the critical flow rate could not be precisely determined from the numerical simulations for $H_L = 52.5\,\text{mm}$ and $H_L = 60\,\text{mm}$.

In figure 6.30, it can be noted that the critical flow rate increases with initial liquid fill height. Furthermore, for pre-filled tanks, the droplet breakup height also increases with fill height. For lower fill heights of $H_L \leq 30\,\text{mm}$, the shape of the droplets appears like a prolate spheroid right after disintegrating from the geyser. For higher fill heights of $H_L \geq 37.5\,\text{mm}$, the droplets already touch the tank outlet when they break up from the geyser. Above the initial liquid fill height of $H_L \geq 15\,\text{mm}$, the droplet breakup time is inversely proportional to the critical flow rate.

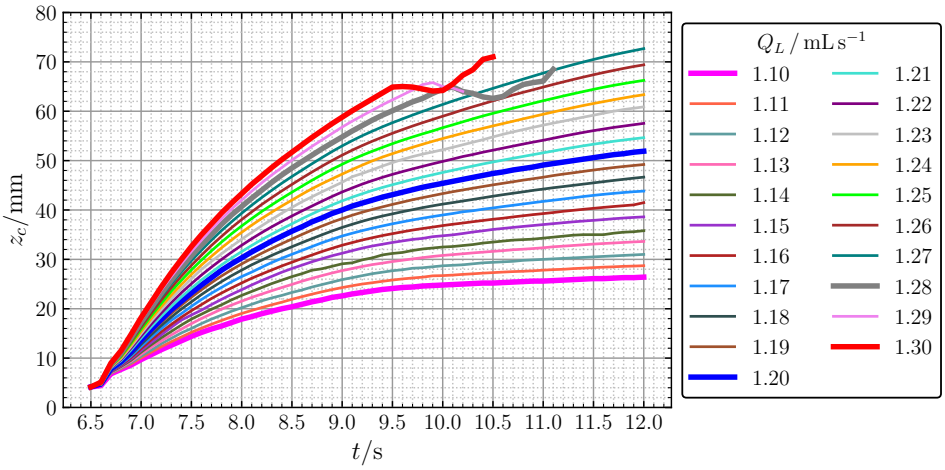

(a) $H_L = 15\,\text{mm}$

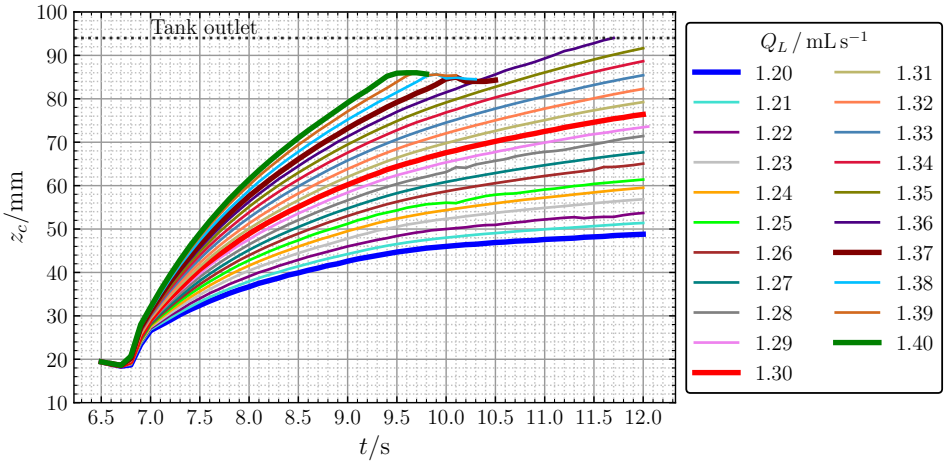

(b) $H_L = 30\,\text{mm}$

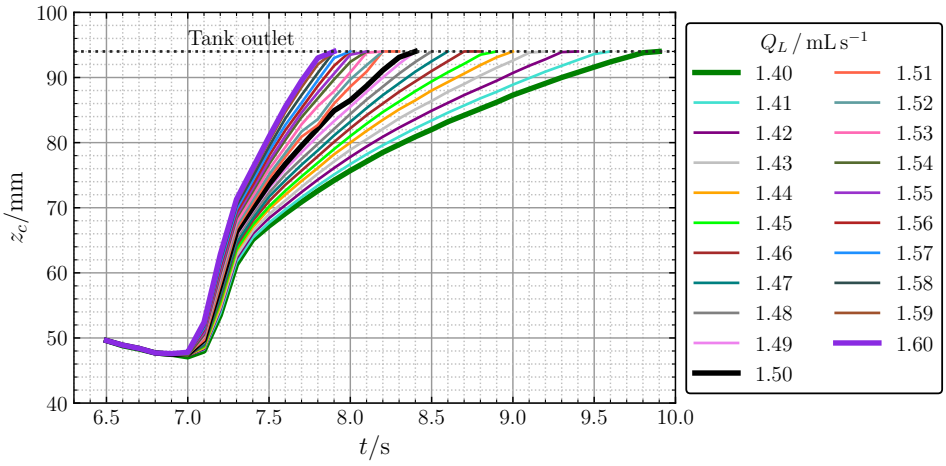

(c) $H_L = 60\,\text{mm}$

Figure 6.29: Evolution of the centre point over time for different H_L with refined Q_L under reduced gravity.

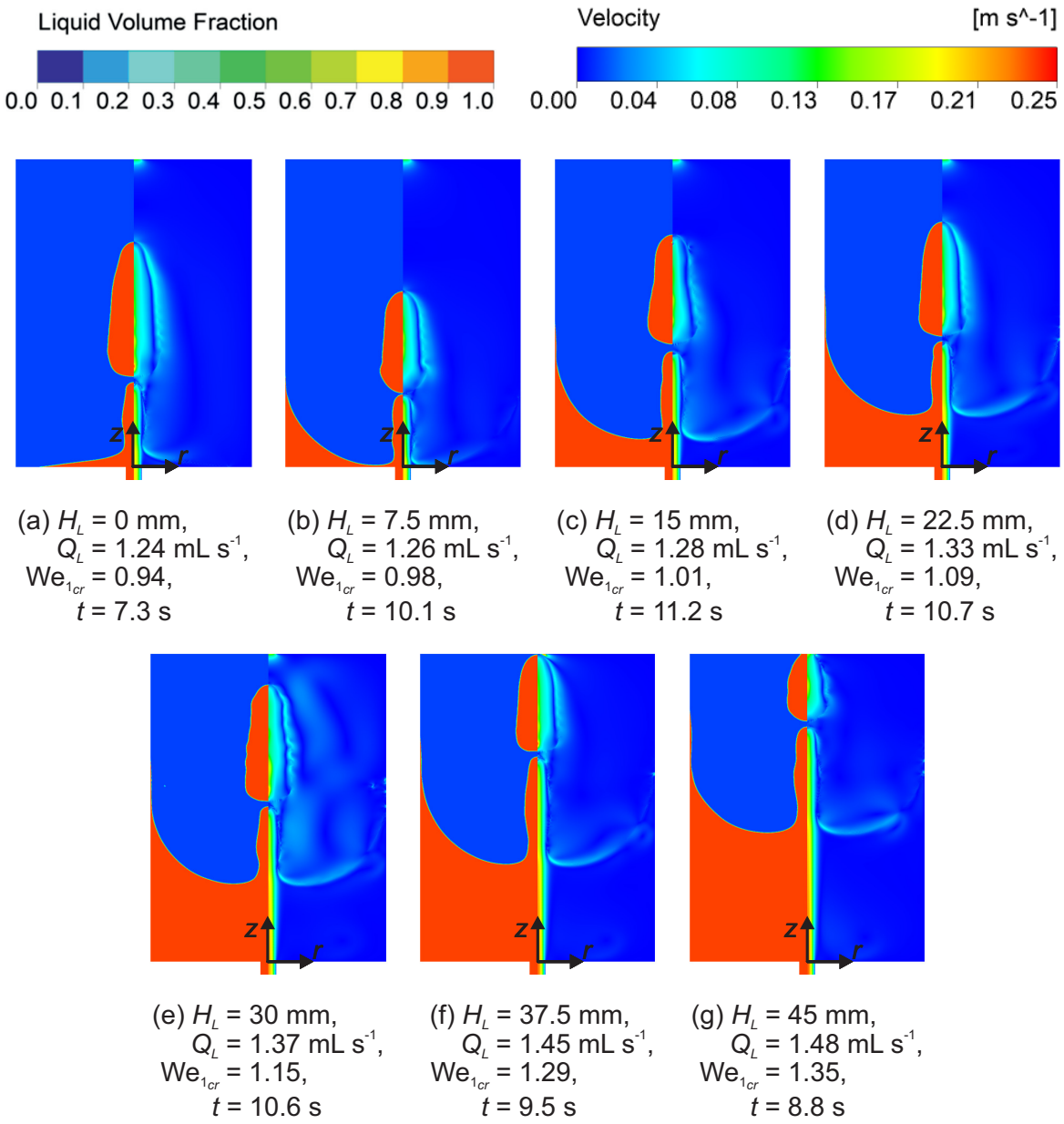

Figure 6.30: The flow patterns formed during the disintegration of the first droplet corresponding to the critical flow rate for every H_L. The liquid volume fraction is the contour in the left part of the figure and the velocity magnitude is the contour in the right part of the figure. The time at which the first droplet disintegrates is also mentioned.

The critical flow rates determined from the refined 2D numerical simulations are summarized in table 6.4 for different initial liquid fill heights H_L. Additionally, the dimensionless numbers corresponding to the critical flow rates are also listed in table 6.4. As the disintegration of droplets could not be detected from the numerical simulations for $H_L = 52.5\,\text{mm}$ and $H_L = 60\,\text{mm}$, the critical flow rates for those fill heights are not included in table 6.4. After performing the refinement of the flow rate and fill height, the direct dependency of the critical Weber number on the initial liquid fill height can be identified from table 6.4.

As the initial liquid fill height H_L increases, the critical flow rate Q_L also increases, which in turn leads to an increase in the critical Weber number and Reynolds number. Furthermore, the time at which the first droplet disintegrates from the geyser is given as t_b in table 6.4, where t_b is calculated as the droplet breakup time after the start of liquid filling in the experiments and simulations under reduced gravity conditions. The maximum height reached by the geyser before it disintegrates into droplets is called the critical geyser height z_{cr} and it is also listed in table 6.4. For comparison, the results of the critical flow rate from the drop tower experiments are included in the last row of table 6.4. For the filling of liquid into an initially empty tank, the droplet detaches from the geyser only at $t_b = 7.3\,\mathrm{s}$, as the liquid jet travels through the inlet pipe and takes about 2 s to enter the tank.

From the numerical simulation results of pre-filled tanks with $H_L > 0\,\mathrm{mm}$, the critical geyser height at which the droplet disintegrates is directly proportional to the initial liquid fill height H_L. With an increase in the critical flow rate, the droplet breakup time reduces for fill heights of $H_L \geq 15\,\mathrm{mm}$. Even though the critical flow rates are different between the drop tower experiment F24 and the numerical simulation for $H_L = 30\,\mathrm{mm}$, it can be noticed that the disintegration of the first droplet is delayed by about 2.4 s in the numerical simulation compared to the drop tower experiment. Moreover, the critical geyser height is almost 1.8 times higher in the simulation than in the drop tower experiment. This again confirms the over-prediction of the 2D numerical simulations in comparison to the drop tower experiments.

Although the disintegration of droplets was chosen as the criterion to determine the critical flow rate in the 2D numerical simulations, it has to be mentioned that the 3D simulations with a higher mesh resolution would predict the droplet breakup height, breakup time and geyser dynamics more precisely. In that regard, the critical flow rates to be found from the 3D simulations may vary from the ones found from the 2D simulations in this thesis.

Table 6.4: Summary of the refined simulation results for different initial liquid fill heights H_L showing the critical flow rates at which the interface becomes unstable. For comparison, the drop tower experiment F24 is included as item 8. The time at which the first droplet disintegrates from the geyser t_b and its corresponding critical geyser height z_{cr} are also listed. NS denotes the numerical simulations and DTE denotes the drop tower experiment.

Method	No.	H_L/mm	Q_L/mL s^{-1}	t_b/s	z_{cr}/mm	We_{1cr}	Re_1
NS	1	0.0	1.24	7.3	69.1	0.94	511.54
	2	7.5	1.26	3.6	53.0	0.98	519.79
	3	15.0	1.28	4.7	68.5	1.01	528.04
	4	22.5	1.33	4.2	75.0	1.09	548.66
	5	30.0	1.37	4.1	84.3	1.15	565.17
	6	37.5	1.45	3.0	93.1	1.29	598.17
	7	45.0	1.48	2.3	93.8	1.35	610.54
DTE	8	30.0	1.30	1.7	47.3	1.04	536.29

6.8 Comparison with the existing literature

The drop tower experiment data (test F24) and the numerical simulation results from table 6.4 are compared for the critical Weber number We_{1cr} with the existing literature from Symons et al. 1968 [86], Symons 1969 [83], Symons 1970 [84] and Symons and Staskus 1971 [87]. Symons 1969 [83] and Symons and Staskus 1971 [87] did not report the initial liquid fill height H_L in normal gravity. Alternatively, the height of the liquid interface H_I at the start of the liquid filling in microgravity was used by them. Therefore, the dimensionless number $\Pi_4 = H_I/R_I$ instead of Π_1 is used for the comparison.

The data points are given in table 6.6 and are sorted in the ascending order of the inlet Weber number Π_0 for each author. All the data points in table 6.6 correspond to an unstable interface. The mean inlet velocity v_I for the critical Weber number is compiled together with the dimensionless numbers $\Pi_0, \Pi_5, \Pi_2, \Pi_3$ and Π_4. The dimensionless number Π_3 has the limits of $1 \leq \Pi_3 \leq 2$. A uniform velocity profile has $\Pi_3 = 1.0$ and a parabolic (fully developed) profile leads to $\Pi_3 = 2.0$. Symons et al. 1968 [86], Symons 1969 [83] and Symons 1970 [84] mentioned partially parabolic profile without a specific definition. Therefore, the value of $\Pi_3 = 1.5$ is assigned to the data of these authors in table 6.6.

Three test liquids are used in the comparison and their properties are listed in table 6.5. The properties of the test liquids ethanol and trichlorotrifluoroethane (TCTFE) are given for the liquid temperature of $T_L = 20\,°C$ and the properties for HFE-7500 correspond to the liquid temperature of $T_L = 25\,°C$.

Table 6.5: Properties of the test liquids used in this study and in the literature.

T_L	Liquid	ρ	μ	σ
°C		$kg\,m^{-3}$	$kg\,m^{-1}\,s^{-1}$	$N\,m^{-1}$
25	HFE-7500	1620	0.00125	0.0167
20	Ethanol	790	0.00120	0.0223
20	TCTFE	1580	0.00070	0.0186

Table 6.6: Comparison of dimensionless numbers between drop tower experiment (DTE) F24, numerical simulations (NS) and literature data. All the data points correspond to an unstable interface. The definitions for the Π-numbers are repeated for convenience: $\Pi_0 = \rho v_I^2 R_I / 2\sigma$, $\Pi_5 = 2\rho v_I R_I / \mu$, $\Pi_2 = R_I / R_T$, $\Pi_3 = v_{max} / v_I$, $\Pi_4 = H_I / R_I$.

No.	Author	Liquid	v_I mm s^{-1}	Π_0	Π_5	Π_2	Π_3	Π_4
1	DTE (F24)	HFE-7500	103.5	1.04	536.29	0.07	2.0	9.8
2	NS	HFE-7500	98.7	0.94	511.54	0.07	2.0	0.0
3			100.3	0.98	519.79	0.07	2.0	0.1
4			101.9	1.01	528.04	0.07	2.0	2.1
5			105.8	1.09	548.66	0.07	2.0	5.9
6			109.0	1.15	565.17	0.07	2.0	9.7
7			115.4	1.29	598.17	0.07	2.0	13.5
8			117.8	1.35	610.54	0.07	2.0	17.3
9	Symons et al. 1968 [86]	Ethanol	129.0	1.18	679.40	0.10	1.5	0.0
10			160.0	1.36	632.0	0.10	1.5	0.0
11			199.0	1.40	524.03	0.05	1.5	0.0
12			141.0	1.41	742.60	0.20	1.5	0.0
13			236.0	1.97	621.47	0.10	1.5	0.0
14			119.0	2.01	1253.47	0.20	1.5	0.0
15	Symons et al. 1968 [86]	TCTFE	89.5	1.36	1616.11	0.10	1.5	0.0
16			139.0	1.64	1254.97	0.10	1.5	0.0
17			81.5	1.69	2207.49	0.20	1.5	0.0
18			70.5	1.69	2546.06	0.20	1.5	0.0
19			117.0	1.74	1584.51	0.10	1.5	0.0
20	Symons 1970 [84]	Ethanol	85.4	0.97	843.42	0.10	1.5	0.0
21			66.5	1.18	1313.97	0.10	1.5	0.0
22	Symons 1970 [84]	TCTFE	62.2	1.23	2105.58	0.10	1.5	0.0
23			57.4	2.10	3883.41	0.10	1.5	0.0
24	Symons 1969 [83]	Ethanol	185.0	1.21	487.17	0.10	1.5	9.2
25			186.4	1.23	490.85	0.10	1.5	12.5
26			192.0	1.31	505.60	0.10	1.5	16.7
27			203.2	1.46	535.09	0.05	1.5	18.1
28			208.4	1.54	548.79	0.05	1.5	21.9
29			219.5	1.71	578.02	0.05	1.5	28.9
30			223.4	1.77	588.29	0.05	1.5	25.5
31	Symons 1969 [83]	TCTFE	132.0	1.48	1191.77	0.10	1.5	9.2

Continued on next page

No.	Author	Liquid	v_I mm s^{-1}	Π_0	Π_5	Π_2	Π_3	Π_4
32	Symons and Staskus 1971 [87]	Ethanol	236.8	1.99	623.57	0.10	1.0	8.0
33			249.0	2.20	655.70	0.10	1.0	16.0
34			259.2	2.38	682.56	0.10	1.0	12.0
35			275.5	2.69	725.48	0.10	1.0	20.0
36	Symons and Staskus 1971 [87]	TCTFE	194.0	3.20	1751.54	0.10	1.0	8.0
37			217.4	4.01	1962.81	0.10	1.0	12.0
38			239.0	4.85	2157.83	0.10	1.0	16.0
39			269.7	6.18	2435.01	0.10	1.0	20.0

In order to observe the influence of the velocity profile of the liquid jet on the interface stability, the inlet Weber number Π_0 is multiplied by the square of the dimensionless number Π_3 to get $\Pi_6 = \Pi_0 \Pi_3^2 = \rho v_{max}^2 R_I/(2\sigma)$. This creates a Weber number related to the centreline velocity of the incoming liquid jet. This Weber number is plotted against the dimensionless liquid height $\Pi_4 = H_I/R_I$ in figure 6.31 for different dimensionless numbers Π_2. The results of test liquids HFE-7500 and ethanol are compared in figure 6.31a. Figure 6.31b shows the results of test liquids HFE-7500 and TCTFE. The literature data is grouped according to the authors and different colours are assigned to each author in figure 6.31. The data points of Symons et al. 1968 [86] are shown in blue colour and the data points of Symons 1969 [83] are indicated in green colour. The data of Symons 1970 [84] are displayed in cyan colour and magenta colour represents the data points of Symons and Staskus 1971 [87]. The results of the drop tower experiment and the 2D numerical simulations performed with HFE-7500 are shown in red colour. The data from the drop tower experiment F24 is marked as a red dot and the data from the numerical simulations are indicated as red triangles in figure 6.31.

It can be noticed in figure 6.31 that the centreline Weber number from the numerical simulation is higher than the drop tower experiment for $\Pi_4 \approx 10$. The numerical simulation over-predicts the critical Weber number by about 10.6 % than the drop tower experiment (F24). Furthermore, the numerical simulation results show a linear increase in the centreline Weber number Π_6 for different dimensionless liquid heights Π_4. A linear trend line has been drawn and the equation of the trend line is also written next to it in figure 6.31. Although the centreline Weber number is over-predicted in the numerical simulations compared to the drop tower experiments, an approximate correlation between the dimensionless numbers Π_4 and Π_6 can be derived from the simulation results for $\Pi_2 = 0.07$ with the test liquid HFE-7500. It can be inferred from figure 6.31a that the centreline Weber number from the numerical simulations with HFE-7500 are higher than the data points with ethanol for pre-filled tanks, because of the difference in velocity profiles of the incoming liquid jet. Compared to a uniform profile or a partially parabolic profile, a fully developed parabolic profile of an incoming liquid jet results in a higher centreline Weber number, as the maximum velocity of a parabolic profile is twice its mean velocity. A uniform velocity profile of the incoming liquid jet leads to lower centreline Weber numbers in Symons and Staskus 1971 [87] than the partially parabolic profile in Symons 1969 [83]. For pre-filled tanks, the dimensionless numbers Π_2 and Π_6 are inversely proportional for the test liquid ethanol, as shown in figure 6.31a.

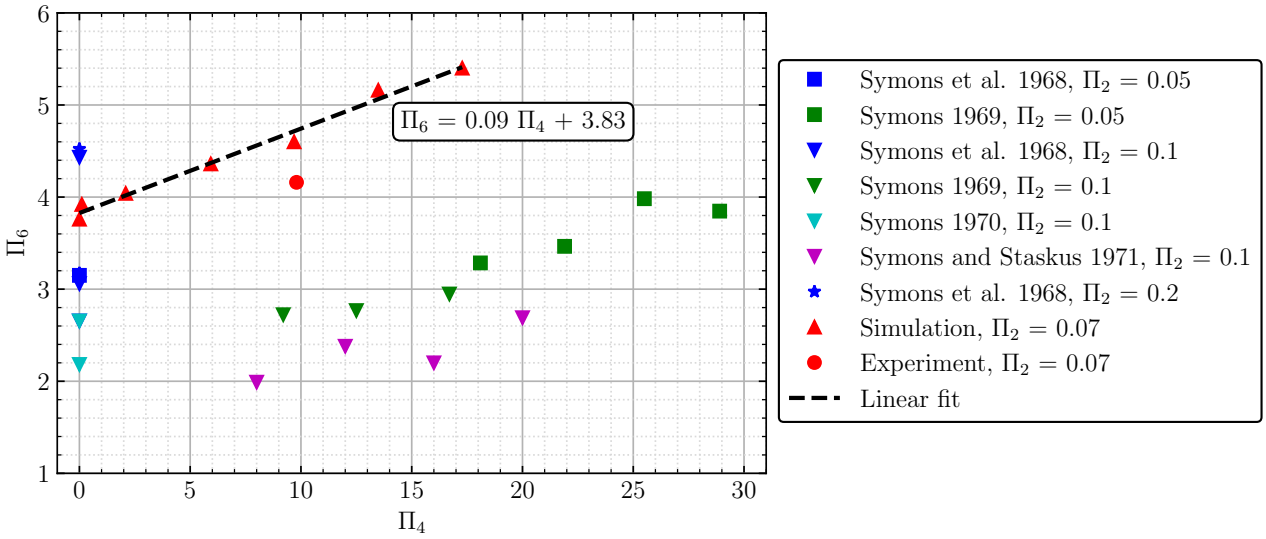

(a) HFE-7500 and ethanol

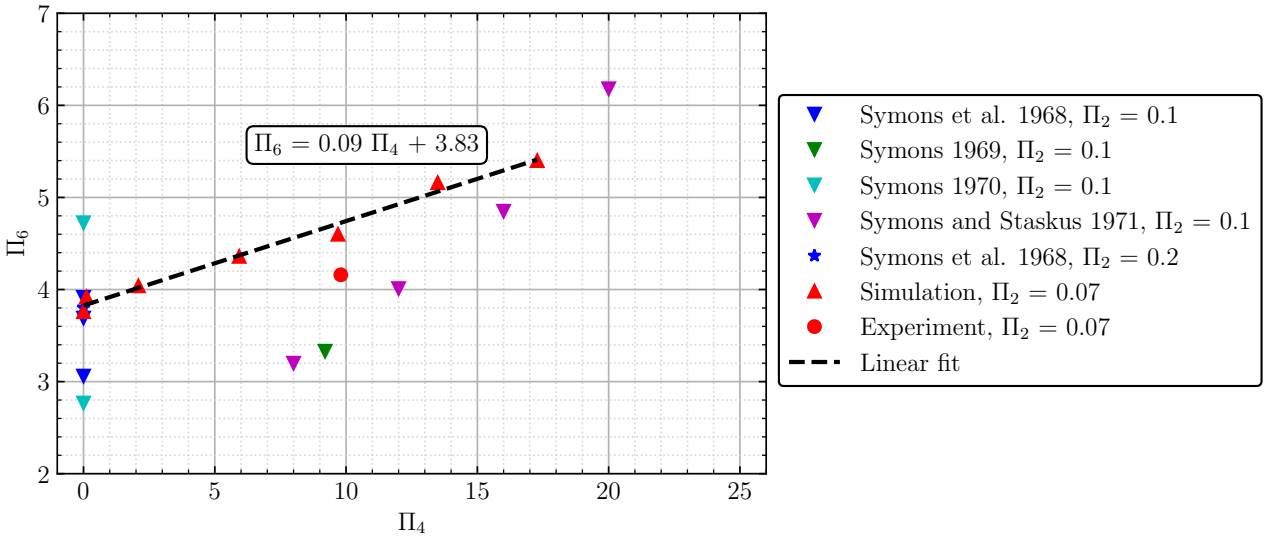

(b) HFE-7500 and TCTFE

Figure 6.31: Comparison of the centreline Weber number $\Pi_6 = \Pi_0\,\Pi_3^2$ against the dimensionless liquid height $\Pi_4 = H_I/R_I$ for different test liquids and different $\Pi_2 = R_I/R_T$. Separate colours are assigned to each author. The red triangles indicate the numerical simulation results and the red dot corresponds to the drop tower experiment (F24) with HFE-7500. The data points correspond to the cases, where the interface becomes unstable.

Compared to HFE-7500, a steep increase in the centreline Weber number can be observed in figure 6.31b for TCTFE with $\Pi_4 \geq 8$ and $\Pi_2 = 0.1$. Some of the data points of Symons et al. 1968 [86] lie closer to the numerical simulation results for an initially empty tank ($\Pi_4 = 0$) in figure 6.31b.

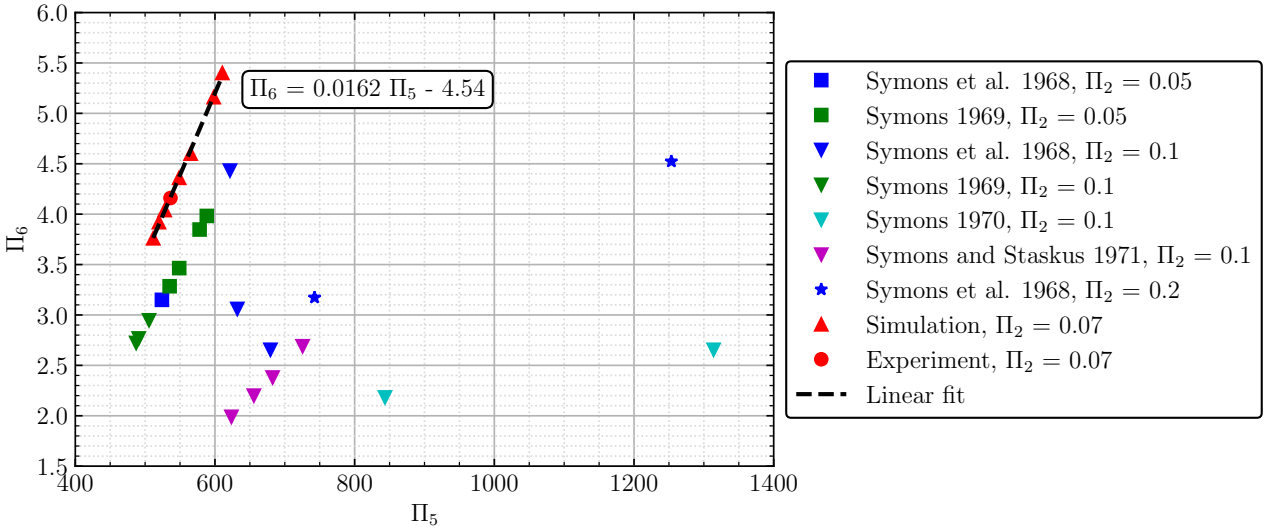

(a) HFE-7500 and ethanol

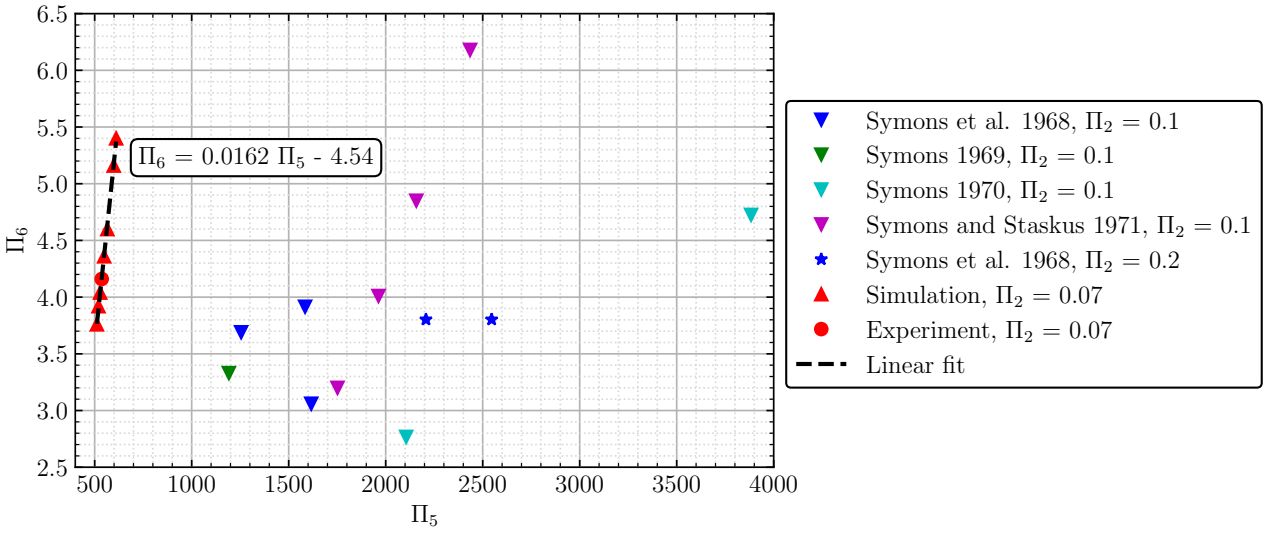

(b) HFE-7500 and TCTFE

Figure 6.32: Comparison of the centreline Weber number $\Pi_6 = \Pi_0\,\Pi_3^2$ against the inlet Reynolds number $\Pi_5 = \mathrm{Re}_1$ for different test liquids and different $\Pi_2 = R_I/R_T$. Separate colours are assigned to each author. The red triangles indicate the numerical simulation results and the red dot corresponds to the drop tower experiment (F24) with HFE-7500. The data points correspond to the cases, where the interface becomes unstable.

The centreline Weber number Π_6 as a function of inlet Reynolds number Π_5 is compared between liquids HFE-7500 and ethanol in figure 6.32a. A sharp rise in the centreline Weber number can be observed for HFE-7500 within the tested range of Reynolds numbers $511 \leq \Pi_5 \leq 611$. A linear curve is fit to the data of HFE-7500 and an equation is displayed in figure 6.32. The significance of the inlet velocity profile is again established, where the data points with the fully developed parabolic profile of HFE-7500 have the highest centreline Weber numbers compared to the partially parabolic or uniform velocity profiles of ethanol.

Figure 6.32b shows the comparison of dimensionless numbers Π_5 and Π_6 for HFE-7500 and TCTFE. All the data points of TCTFE are in a higher Reynolds number regime of $\Pi_5 > 1190$ and therefore not directly comparable with HFE-7500.

The correlations between the dimensionless numbers Π_4, Π_5 and Π_6 derived from the linear curve fitting of the numerical simulation results of HFE-7500 are given in equations 6.3 and 6.4.

$$\Pi_6 = 0.09\,\Pi_4 + 3.83 \tag{6.3}$$

$$\Pi_6 = 0.0162\,\Pi_5 - 4.54 \tag{6.4}$$

The errors in calculating the dimensionless numbers from the numerical simulations and drop tower experiments are estimated in table 6.7.

Table 6.7: Estimation of errors in calculating the dimensionless numbers from numerical simulations and drop tower experiments.

	Π_4	Π_5	Π_6
Experiments	$\pm\,0.15$	$\pm\,8.25$	$\pm\,0.03$
Simulations	$\pm\,0.06$	$\pm\,4.13$	$\pm\,0.02$

Even though a direct comparison of the experiment data (F24) and the numerical simulation data with the literature is not possible, figures 6.31 and 6.32 give an overview of the effect of all the dimensionless numbers on the interface stability. It is evident that a parametric study of Π_2 and Π_3 will be necessary to fully describe the phenomena with HFE-7500. Furthermore, high-resolution 3D numerical simulations would be required to perform further parametric studies in the interest of fully understanding the interface stability. These 3D simulations need to be in any case validated with further experiments.

Chapter 7

Summary

Some of the contents of this chapter have been published in Govindan and Dreyer 2023 [40] and Govindan and Dreyer 2023 [41]. These contents are reused here with permission.

In this thesis, the interface stability during the filling of liquid into a tank under reduced gravity conditions has been investigated. This thesis discusses the liquid filling experiments carried out on the ground, in the Bremen Drop Tower and on the parabolic flight. Furthermore, the liquid filling process modelled using 2D numerical simulations with ANSYS Fluent has also been reported. All the experiments and numerical simulations have been carried out using a multi-species multiphase system of test liquid HFE-7500 and air under isothermal conditions.

An experiment setup was built and assembled in the drop capsule of the Bremen Drop Tower for performing experiments of liquid filling under normal gravity and microgravity conditions. The experiment setup consisted of a fluid loop, in which the liquid flow was driven by a fluid pump. An experiment tank of material polymethyl methacrylate (PMMA) was designed and manufactured in-house. The experiment tank had a cylindrical cross-section with an inner radius of $R_T = 30\,\mathrm{mm}$, a height of $H_T = 94\,\mathrm{mm}$ and inlet and outlet radii of $R_I = R_O = 2\,\mathrm{mm}$. The total empty volume of the experiment tank was 265 mL. An inlet pipe of length $L_I = 220\,\mathrm{mm}$ was connected to the experiment tank, to have a fully developed flow of the incoming liquid at the tank inlet. The liquid filling into the experiment tank was recorded using two high-speed cameras with an image resolution of 512×512 pixels and at the rate of 500 frames per second. The absolute pressure and temperatures were measured using the sensors integrated into the fluid loop.

Liquid filling experiments were conducted under normal gravity conditions with different volumetric flow rates Q_L in the range of $0.8\,\mathrm{mL\,s^{-1}} \leq Q_L \leq 4.8\,\mathrm{mL\,s^{-1}}$ and initial liquid fill heights H_L in the range of $9.6\,\mathrm{mm} \leq H_L \leq 45.6\,\mathrm{mm}$. The test duration of the ground experiments was 4.6 s. The liquid interface remained flat in the ground experiments because of the dominant body force. The incoming liquid jet interacted with the interface and formed different filling patterns for different Q_L and H_L. An unstable liquid interface was observed for flow rates of $Q_L > 2.8\,\mathrm{mL\,s^{-1}}$ for all the initial liquid fill heights H_L. The influence of

the initial liquid fill height H_L on the interface stability could not be studied explicitly for the chosen range of flow rates. However, the experimental setup was intensively tested during the ground experiments and an evaluation procedure was devised for the acquired data and recorded images. This procedure was later used for the evaluation of the drop tower experimental data.

The drop tower experiments of the vented filling of a tank were performed in the Bremen Drop Tower, which offers approximately 9 s of microgravity time. All the tests were carried out with a fixed initial liquid fill height of $H_L = (30 \pm 0.1)$ mm. The tests were divided into two categories: the reorientation of the liquid interface and the liquid filling into the experiment tank through the primary inlet. Three tests were conducted to study the reorientation of the bulk liquid inside the experiment tank under microgravity conditions. An oscillation of the centre point of the liquid interface was observed, which began to damp after $t = 3.5$ s in microgravity. The final equilibrium position of the centre point of the interface was found to be at $z_c = (19.9 \pm 0.3)$ mm for the test F31, which matched well with the theoretical prediction. The reorientation tests helped to define the start time of the liquid filling into the experiment tank in microgravity.

The stability of the liquid interface during the filling of the experiment tank under microgravity was investigated for different volumetric flow rates in the range of $1.00\,\mathrm{mL\,s^{-1}} \leq Q_L \leq 1.50\,\mathrm{mL\,s^{-1}}$. In these tests, the liquid jet entered the experiment tank from the bottom through the primary inlet pipe. The liquid inflow was started at $t = 3.5$ s in microgravity. The longer microgravity time provided in the catapult tests helped to observe the development of different geyser patterns. Three distinct flow regimes were identified based on the formation and growth of the geyser. These regimes were categorized in terms of volumetric flow rates. A stable geyser was formed in the subcritical flow regime of $1.00\,\mathrm{mL\,s^{-1}} \leq Q_L \leq 1.20\,\mathrm{mL\,s^{-1}}$ and in this regime, the geyser did not grow with time. The geyser started to grow in the critical flow regime of $Q_L = 1.30\,\mathrm{mL\,s^{-1}}$ and disintegrated into droplets. In the supercritical flow regime of $Q_L > 1.30\,\mathrm{mL\,s^{-1}}$, a rapid growth of the geyser was observed, which became unstable and resulted in frequent detachment of droplets. These droplets reached the top of the tank. The geyser height was evaluated and plotted over time with the help of image processing tools. This helped to identify the critical volumetric flow rate and its corresponding Weber number, where the liquid interface became unstable. The critical Weber number was found to be $\mathrm{We}_{1cr} = 1.04 \pm 0.03$.

Parabolic flight experiments were conducted during the 39$^{\text{th}}$ DLR parabolic flight campaign on board the Airbus A310 Zero-G aircraft to demonstrate the gas-free liquid filling into a rectangular experiment tank under variable accelerations. Each parabolic maneuver provided a reduced gravity time of 22 s. The experimental setup comprised of hydraulic, electrical and laptop racks. Although the hydraulic loop was designed to perform both liquid removal and liquid filling experiments, in this thesis only the liquid filling experiment results are discussed. The experiment tank with inner dimensions of 100 mm in length, 100 mm in breadth and 130 mm in height was designed and manufactured that included internal components like a screen channel liquid acquisition device (SC-LAD), a velocity control plate (VCP), ring baffles and a gas port (GP). The inlet pipe protruded into the experiment tank to a height of 10 mm from the bottom surface of the experiment tank. The liquid filling into the experiment tank was captured by a camera at a rate of 42 frames per second with an image resolution of 1080×1920 pixels.

The temperatures and pressures were measured in the hydraulic loop using the temperature and pressure sensors. A total of 45 liquid filling tests were conducted, out of which 25 tests were dedicated to study the liquid filling into an initially empty tank. The remaining tests were carried out with different initial liquid fill heights H_L inside the tank. Different flow patterns were detected in the liquid filling tests into an initially empty tank for the volumetric flow rates in the range of $0.2\,\mathrm{mL\,s^{-1}} \leq Q_L \leq 0.8\,\mathrm{mL\,s^{-1}}$. A convex liquid meniscus with intermittent fluctuating movements due to the disturbances in the accelerations was observed pinned to the inlet orifice for $Q_L \leq 0.6\,\mathrm{mL\,s^{-1}}$. As the flow rate was increased, the curvature shape of the liquid jet at the inlet orifice changed and the liquid moved towards the VCP and covered its surfaces. Overall, the liquid was seen wetting the solid surfaces of the inlet pipe, VCP stands and the experiment tank as it filled the bottom part of the tank. In the tests, where the tank was initially pre-filled with liquid, the bulk liquid experienced a violent sloshing due to the accelerations. Although the optical observation of filling was distorted, gas-free liquid filling and liquid-free gas venting were demonstrated in the tests with higher volumetric flow rates Q_L. The provision of VCP enabled a faster filling of the tank, as the linear momentum of the incoming liquid was diffused by the VCP. The stronger negative accelerations in the z-axis forced the liquid to move to the top of the tank, despite the presence of ring baffles. The parabolic flight experiments demonstrated the concepts of gas-free liquid filling and liquid-free gas venting under variable acceleration conditions qualitatively. The study of interface stability could not be carried out in the parabolic flight experiments due to the residual accelerations, which caused violent sloshing of the liquid inside the tank and posed a challenge in establishing a steady liquid interface.

The vented filling of a tank under reduced gravity was modelled in ANSYS Fluent 19.2 using the Multiphase - VOF model. An axisymmetric model of the experiment tank used for the drop tower experiments was created and 2D numerical simulations were carried out to investigate the interface stability for different volumetric flow rates in the range of $1.00\,\mathrm{mL\,s^{-1}} \leq Q_L \leq 1.50\,\mathrm{mL\,s^{-1}}$ and different initial liquid fill heights in the range of $0\,\mathrm{mm} \leq H_L \leq 60\,\mathrm{mm}$. An inlet pipe of radius $R_I = 2\,\mathrm{mm}$ and length of $L_I = 200\,\mathrm{mm}$ was modelled to have a fully developed parabolic velocity profile of the liquid jet. The mass flow rate of liquid was set as the inlet boundary condition and the atmospheric pressure was set as the outlet boundary condition. The transient simulations under reduced gravity conditions were carried out for 9 s, which corresponds approximately to the maximum microgravity time at the Bremen Drop Tower. A mesh sensitivity study with varying mesh element sizes was conducted and it was found that the mesh element size has an influence on depicting the flow behaviour. Therefore, a mesh with an element size of 125 µm was chosen for the simulations.

The numerical simulation of liquid reorientation without any inflow and outflow showed the centre point oscillation and axial sloshing of the interface. Even though the amplitudes of the oscillation between the simulation and experiment were different, the centre point position for the final equilibrium configuration at $t = 9\,\mathrm{s}$ from the numerical simulation ($z_c = 19.9\,\mathrm{mm}$) matched well with both theoretical prediction ($z_c = 20\,\mathrm{mm}$) and the drop tower experiment ($z_c = (19.9 \pm 0.3)\,\mathrm{mm}$). The interface stability during the filling of a tank with an initial fill height of $H_L = 30\,\mathrm{mm}$ was studied for different volumetric flow rates in the range of $1.00\,\mathrm{mL\,s^{-1}} \leq Q_L \leq 1.50\,\mathrm{mL\,s^{-1}}$ using numerical simulations. Similar to the drop tower experiments, the regimes of subcritical, critical and supercritical flow based on the behaviour

of the liquid jet with the interface were observed in the numerical simulations. While the geyser did not grow significantly in the subcritical flow regime, in the supercritical flow regime, the geyser either disintegrated into droplets or touched the outlet port. The lowest flow rate at which the geyser disintegrated into droplets was defined as the criterion for interface instability in the numerical simulations. For the flow rate of $Q_L = 1.30\,\mathrm{mL\,s^{-1}}$, the decay of centreline velocity and the change in velocity profiles downstream from the tank inlet were analysed. Upon comparison with the drop tower experiments, it was found that the numerical simulation over-predicted the geyser height and the oscillations of the geyser could not be reproduced in the 2D simulations. The critical inlet Weber number from the simulations for $H_L = 30\,\mathrm{mm}$ was found to be $\mathrm{We}_{1cr} = 1.15$, which was higher than the drop tower experiments ($\mathrm{We}_{1cr} = 1.04$). Moreover, the simulations showed a delayed breakup of the droplets from the geyser than the drop tower experiment for the supercritical flow rates.

Furthermore, a parametric study of different initial liquid fill heights H_L and a refinement in the volumetric flow rates Q_L was conducted with numerical simulations. The critical Weber number obtained from the drop tower experiments and numerical simulations for different H_L were compared with the existing literature. The dimensionless numbers $\Pi_0 = \rho v_I^2 R_I / 2\sigma$ and $\Pi_3 = v_{max}/v_I$ were combined to form the centreline Weber number $\Pi_6 = \Pi_0\,\Pi_3^2$. The centreline Weber number Π_6 was plotted against the dimensionless liquid height $\Pi_4 = H_I/R_I$ and the inlet Reynolds number $\Pi_5 = 2\rho v_I R_I/\mu$ for different aspect ratios of the inlet radius to the tank radius $\Pi_2 = R_I/R_T$. The simulation results showed a linear increase in the centreline Weber number Π_6, from which correlations of the dimensionless numbers were derived. The comparison revealed that the centreline velocity v_{max}, which is dependent on the velocity profile of the incoming liquid jet, directly affects the stability of the interface. A parabolic velocity profile leads to a higher centreline Weber number Π_6 than a uniform velocity profile, as the maximum velocity of a parabolic profile is twice its mean velocity. It was also shown that for the tested range of Reynolds numbers Π_5, the data of the test liquid HFE-7500 is comparable only with ethanol.

7.1 Outlook

Further drop tower experiments can be carried out in the future with different initial liquid fill heights H_L and the new experimental results can be used to validate the numerical simulations presented in this thesis. In addition to that, other dimensionless numbers Π_2 and Π_3 can be varied to fully understand the liquid filling problem and create a map of different dimensionless numbers that influence the interface stability. Furthermore, high-resolution 3D numerical simulations in ANSYS Fluent are required to fully model the dynamic behaviour of the geyser and the disintegration of droplets during the vented filling of a tank. Moreover, the no-vent filling can also be modelled in 3D and the simulations can be carried out by considering the phase change for predicting the thermodynamic behaviour of the tank during the filling process. In the case of turbulent flows, the LES model can be used for the 3D simulations, although it is computationally time-consuming. According to Kartuzova and Kassemi 2019 [47], the LES model predicts the dynamics of the liquid interface better than the RANS model.

Although the parabolic flight experimental results could not be quantitatively analysed, some of the experiments of liquid filling into an initially empty tank can be modelled in FLOW-3D software and 3D simulations can be performed with real acceleration data. The behaviour of the liquid jet can be studied and these simulations can be used as benchmark cases to validate the FLOW-3D software. In this way, modelling capabilities of the CFD tools like ANSYS Fluent and FLOW-3D can be significantly enhanced and these tools can then be used to design tanks for future space exploration missions.

Based on the experimental and numerical results of liquid filling under isothermal conditions, an ISS experiment is planned for the project ZBOT-FT to demonstrate the removal, transfer and filling of liquid under microgravity conditions. The ZBOT-FT ISS experiment will be carried out under non-isothermal conditions with a single-species system of the test fluid C_5F_{12}. The experimental setup will consist of different modules and be operated in different modes. The fluid flow between the tanks will be driven by pressure and temperature differences, unlike the isothermal experiments that were driven by the volumetric flow rate. The ZBOT-FT ISS experiment will provide valuable data for orbital refuelling and contribute to the technological advancement of propellant depots in space.

Appendix A

Experiments

The contents in sections A.2, A.3 and A.4 have been published in Govindan and Dreyer 2023 [40] and reused here with permission.

A.1 Calibration of the images

The images from both cameras of the drop tower experimental setup were calibrated in the laboratory at ZARM. To determine the centre point of the interface in microgravity, a rectangular ruler with a grid size of 2 mm was used for the calibration of the images. This ruler was placed inside the experiment tank at the centre of the tank ($r = 0\,\text{mm}$) and the tank was filled with the test liquid HFE-7500 until the top. The calibration images of the experiment tank with the ruler inside are shown for both cameras in figure A.1. The centreline of the ruler ($r = 0\,\text{mm}$) was marked with some black dots, such that the centreline can be easily detected in the calibration images and the z-axis pixel values on the centreline can be found.

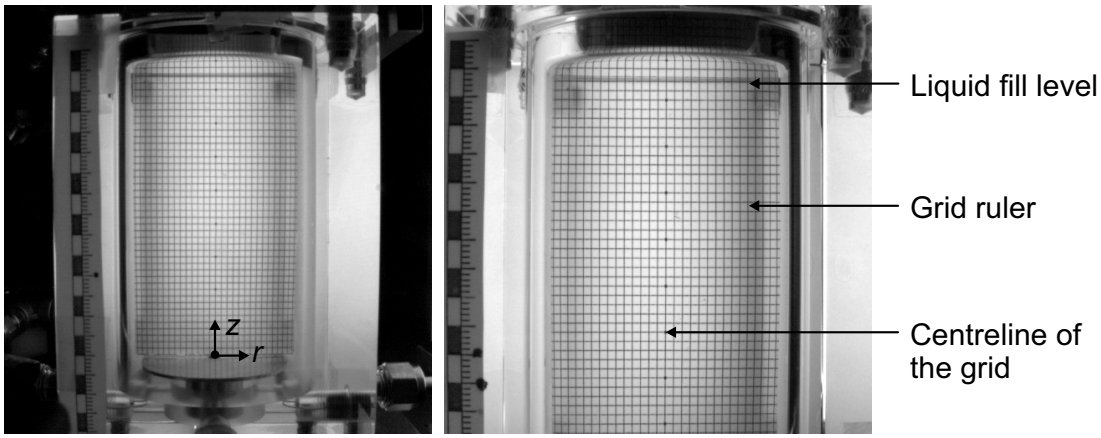

(a) CAM1 (b) CAM2

Figure A.1: Calibration of the images from CAM1 (left) and CAM2 (right) using a grid ruler to determine the centre point of the interface in microgravity.

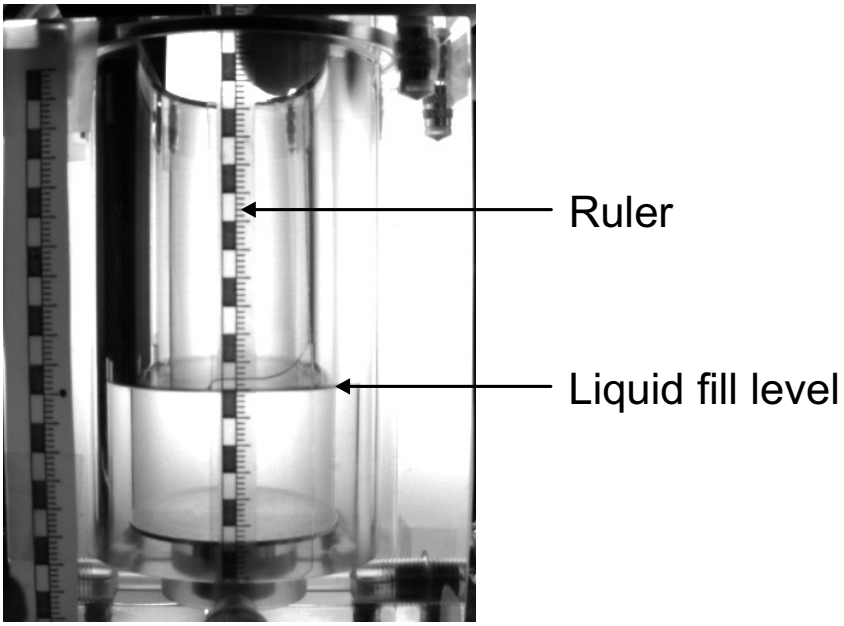

Figure A.2: Calibration of the image from CAM1 using a ruler to determine the initial liquid fill height H_L in normal gravity.

The images from CAM1 were used to determine the initial liquid fill height H_L in normal gravity because CAM1 captured the total view of the experiment tank. A black and white ruler with a unit size of 1 mm was placed inside the experiment tank touching the inner wall of the experiment tank ($r = 30\,\text{mm}$), so that the initial liquid fill height H_L in normal gravity could be measured, as shown in figure A.2. The liquid was filled to a fill height of $H_L = 30\,\text{mm}$ and the pixel values of every line on the ruler were manually determined. This method was followed because the liquid meniscus at the tank wall ($r = R_T = 30\,\text{mm}$) was clearly identified as a thick line in the images under normal gravity conditions, as seen in figure A.2, and this helped to measure the initial liquid fill height H_L in normal gravity.

A.2 Transformation of pixels to millimetres

The transformation functions as second-order polynomials were derived from the calibration of images, in order to convert the detected pixels to millimetres. The transformation functions for CAM1 are given in equations A.1 and A.2. The images recorded by the camera CAM2 were processed for the filling experiments. The transformation function for CAM2 is given in equation A.3. The centre point of the interface was detected as an edge using the Sobel algorithm in MATLAB. The pixel value of the centre point of the interface is denoted as z_{pix} in equations A.1, A.2 and A.3. For the reorientation experiment, equation A.1 was used for transforming the pixels to millimetres. For the filling experiments, the pixels were transformed to millimetres using equation A.3. The initial fill height of the liquid inside the experiment tank in normal gravity was detected at the tank wall ($r = R_T$) from CAM1 and the pixels were converted to millimetres from equation A.2. After the transformation, z_{cu} was the position of the centre point of the interface in millimetre.

$$(z_{cu})_{r=0} = (-2 \times 10^{-5}\, z_{pix}^2) - (0.2423\, z_{pix}) + 104.62 \tag{A.1}$$

$$(z_{cu})_{r=R_T} = (-4 \times 10^{-5}\, z_{pix}^2) - (0.1924\, z_{pix}) + 95.62 \tag{A.2}$$

$$(z_{cu})_{r=0} = (-6 \times 10^{-6}\, z_{pix}^2) - (0.1775\, z_{pix}) + 100.07 \tag{A.3}$$

A.3 Correction of the centre point

A.3.1 Reorientation experiment

The light rays from the LED panels get refracted as they travel through the media of liquid, solid and air to reach the cameras. Due to the bending of light, the detected centre point of the interface has to be corrected. The path of a single light ray is traced from the centre axis of the experiment tank (z-axis) to the lens of the camera CAM1 in figure A.3. The real centre point of the interface is indicated by a black dot on the z-axis in figure A.3. Due to the hemispherical shape of the interface in microgravity, the light ray does not pass through the centre point of the interface. Instead, it passes as a tangent through a point on the hemispherical interface. This point is projected to the z-axis and is called the apparent centre point, which is marked as a black square in figure A.3. The camera perceives the light ray to travel in a straight line without any bending. Therefore, the centre point captured by the camera is marked as a black triangle in figure A.3. This uncorrected centre point z_{cu} has to be corrected using two correction factors $\triangle z_1$ and $\triangle z_2$.

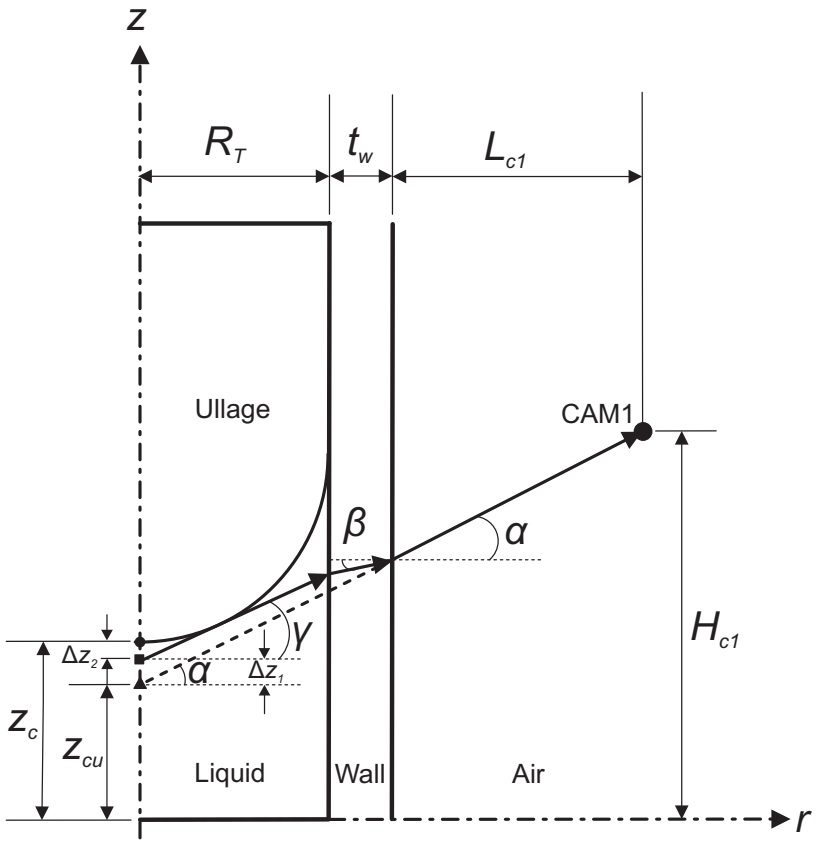

Figure A.3: Generic drawing depicting the ray tracing for the reorientation experiment.

The refractive index of the test liquid HFE-7500 is $n_l = 1.29$, as reported by Tang et al. 2009 [88]. The solid medium is the experiment tank wall, which is made up of PMMA material. The refractive index of PMMA is $n_s = 1.49$, as reported by Beadie et al. 2015 [5] and the refractive index of air is $n_a = 1$. The angle of refraction α in the air was calculated from equation A.4. In equation A.4, H_{c1} denotes the height of the camera lens from the origin of the experiment tank and L_{c1} is the distance of the camera lens from the outer wall of the experiment tank, as shown in figure A.3. The thickness of the experiment tank wall is $t_w = 10\,\text{mm}$. For CAM1, $H_{c1} = 52\,\text{mm}$ and $L_{c1} = 126\,\text{mm}$. The other angles of refraction in solid medium β and liquid medium γ were calculated using Snell's law from equation A.5 by applying the corresponding indices of refraction. Then, the first correction factor $\triangle z_1$ was calculated using equation A.6. The first correction factor for the test F31 was estimated to be in the order of $\triangle z_1 = 2.3\,\text{mm}$.

$$\alpha = \tan^{-1}\left(\frac{H_{c1} - z_{cu}}{R_T + t_w + L_{c1}}\right) \tag{A.4}$$

$$n_a \sin\alpha = n_s \sin\beta = n_l \sin\gamma \tag{A.5}$$

$$\triangle z_1 = (R_T + t_w)\tan\alpha - t_w \tan\beta - R_T \tan\gamma \tag{A.6}$$

The second correction factor $\triangle z_2$ was found manually by geometrically constructing a tangent to the hemispherical interface. The starting point of the tangent is the position of the lens of CAM1. The interface shape was assumed to be hemispherical with its real centre point at $z_c = 20\,\text{mm}$. The tangent was extended to the centre axis (z-axis) and the height difference between the apparent centre point and the real centre point was measured. Because of its complexity, the determination of the second correction factor $\triangle z_2$ was only done for the microgravity time of $t = 9\,\text{s}$. For the reorientation test F31, the second correction factor was estimated as $\triangle z_2 = 0.6\,\text{mm}$. Applying both correction factors, the real position of the centre point of the interface at $t = 9\,\text{s}$ was found using equation A.7. For all the other time instants, the second correction factor was assumed as $\triangle z_2 = 0$ in equation A.7.

$$z_c = z_{cu} + \triangle z_1 + \triangle z_2 \tag{A.7}$$

A.3.2 Filling experiment

The images from CAM2 were processed for the filling experiments F10, F11, F12, F24, F30 and F23. The Sobel algorithm was used to detect the edge of the liquid interface as pixel values. The image frame, in which the liquid jet hits the liquid interface, was identified manually for each experiment. In all the frames before that, the centre point of the liquid interface was detected as the lowermost edge of the liquid interface on the z-axis. After the perturbation of the liquid interface by the liquid jet, the centre point was detected as the uppermost edge of the geyser on the z-axis. The detected edges as pixel values were then transformed to millimetres using equation A.3. In the experiments F24, F30 and F23, the edges were detected only until the image frame, when the first droplet detaches from the geyser.

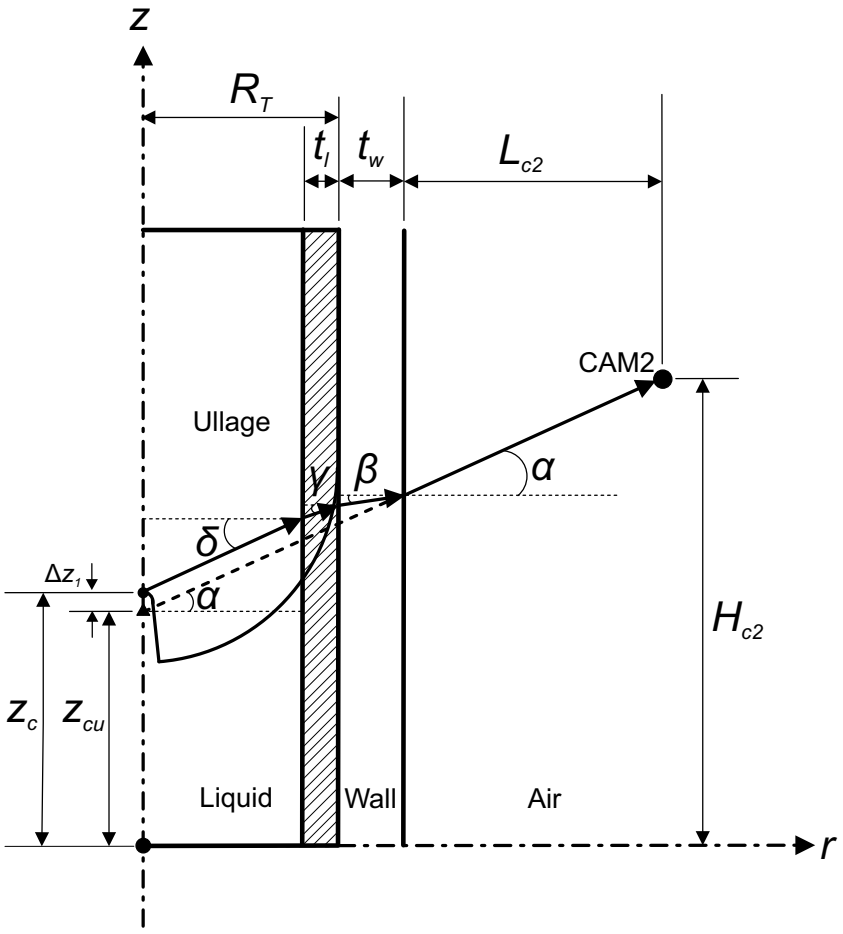

Figure A.4: Generic drawing depicting the ray tracing for the filling experiment. The shaded part is a representation of the liquid layer at the wall.

The first correction factor $\triangle z_1$ was determined following the same method as shown in section A.3.1 for the frames, where the liquid interface was not penetrated by the liquid jet. However, the height of the camera CAM1 H_{c1} was replaced by the height of the camera CAM2 H_{c2} in equation A.4. For CAM2, $H_{c2} = 54.5\,\text{mm}$. The distance of the camera lens of CAM2 from the experiment tank wall is the same as that of camera CAM1. $L_{c1} = L_{c2} = 126\,\text{mm}$.

The thickness of the liquid layer at the experiment tank wall should also be known for the frames, where a geyser is formed. This was required for finding the first correction factor $\triangle z_1$, as the light ray from the geyser travels through four media (ullage, HFE-7500, PMMA and air) before it reaches the camera, as shown in figure A.4. For a given pixel value of the centre point of the geyser, the outermost edge in the radial direction from the tank wall ($r = R_T$) towards the centre axis of the tank (z-axis) was detected as the liquid layer boundary near the wall. The thickness of the liquid layer was found by counting the pixels between the tank wall and the liquid layer boundary. Then, these pixels were converted to millimetres by multiplying them by a factor of 0.25. This factor comes from the calibration images of CAM2, where 1 pixel = 0.25 mm in the radial direction r near the tank wall. Finally, the first correction factor $\triangle z_1$ was determined using equation A.8, where t_l is the thickness of the liquid layer and δ is the angle of refraction of the light ray in the ullage. The refractive index of the ullage is assumed to be the same as the refractive index of air ($n_a = 1$).

In the filling experiments, the first correction factor $\triangle z_1$ was found to be in the range of $0.2\,\text{mm} \leq \triangle z_1 \leq 0.9\,\text{mm}$.

$$\begin{aligned} \triangle z_1 = (R_T + t_w)\tan\alpha - t_w \tan\beta \\ - t_l \tan\gamma - (R_T - t_l)\tan\delta \end{aligned} \tag{A.8}$$

In the filling experiment F30, the first correction factor $\triangle z_1$ was calculated using equation A.9, for the image frames, where the uncorrected centre point of the geyser was above the camera height ($z_{cu} > H_{c2}$). In all the other frames, where a geyser was formed, the first correction factor $\triangle z_1$ was calculated using equation A.8.

$$\begin{aligned} \triangle z_1 = t_w \tan\beta + t_l \tan\gamma + (R_T - t_l)\tan\delta \\ - (R_T + t_w)\tan\alpha \end{aligned} \tag{A.9}$$

The second correction factor $\triangle z_2$ for the filling experiments was manually calculated to be in the order of 0.02 mm. Therefore, only the first correction factor was considered in the correction of the centre point of the geyser, as shown in equation A.10.

$$z_c = z_{cu} + \triangle z_1 \tag{A.10}$$

A.4 Correction of the initial liquid fill height

The initial fill height of the liquid H_L inside the experiment tank in normal gravity was determined by processing the images of the camera CAM1. The liquid meniscus in normal gravity was detected at the experiment tank wall ($r = R_T$) as pixel values. The pixel values were then converted to millimetres using equation A.2. The first correction factor $\triangle z_1$ was calculated by tracing the light ray from the tank wall to the camera lens, as shown in figure A.5. The trigonometry and Snell's law were applied only to two media: PMMA and air. The first correction factor $\triangle z_1$ was found using equation A.11. The order of magnitude of the first correction factor was estimated as $\triangle z_1 = 0.6\,\text{mm}$ in normal gravity. The corrected initial liquid fill height in normal gravity was determined using equation A.12.

$$\triangle z_1 = t_w \tan\alpha - t_w \tan\beta \tag{A.11}$$

$$z_c = (z_{cu})_{r=R_T} + \triangle z_1 \tag{A.12}$$

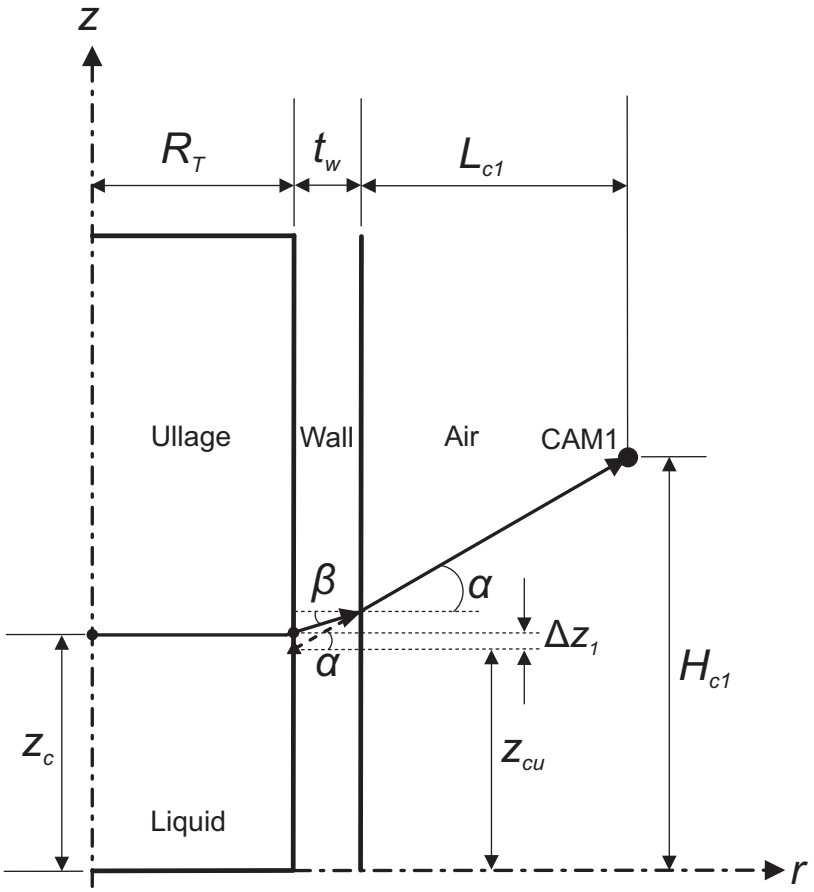

Figure A.5: Generic drawing depicting the ray tracing for measuring the initial liquid fill height in normal gravity.

A.5 Analysis of the liquid jet instability

The liquid jet that penetrates the interface and traverses the ullage region becomes unstable and breaks into droplets due to the Rayleigh-Plateau instability. The sinusoidal perturbations, that exist in the jet, grow with time and lead to the breakup of droplets. An unperturbed stable jet, which looks like a cylindrical liquid column, is shown in figure A.6 with a diameter of D_{ju}. From the image analysis of the drop tower experiments, the diameter of the unperturbed jet was found to be $D_{ju} = (4.0 \pm 0.2)\,\mathrm{mm}$.

Considering a steady unperturbed jet radius of $R_{ju} = 2\,\mathrm{mm}$, the critical length L_{cr} is calculated from equation 2.52 as $L_{cr} = 12.57\,\mathrm{mm}$. The fastest-growing perturbation wave will have a wave number of $k = 0.35\,\mathrm{mm}^{-1}$ and a maximum wavelength of $\lambda_{max} = 18.04\,\mathrm{mm}$. The Ohnesorge number calculated from equation 2.56 is $\mathrm{Oh} = 5.37 \times 10^{-3}$.

The liquid jet with perturbations is shown in figure A.7 for the drop tower experiment F30 ($Q_L = 1.38\,\mathrm{mL\,s^{-1}}$). The liquid jet bulges and contracts alternatively due to the perturbations. Due to the variations in the radius of curvature, pressure gradients are created, which cause the jet to breakup. Furthermore, the droplets are formed as the liquid tries to reach the state of minimum energy because of its surface tension.

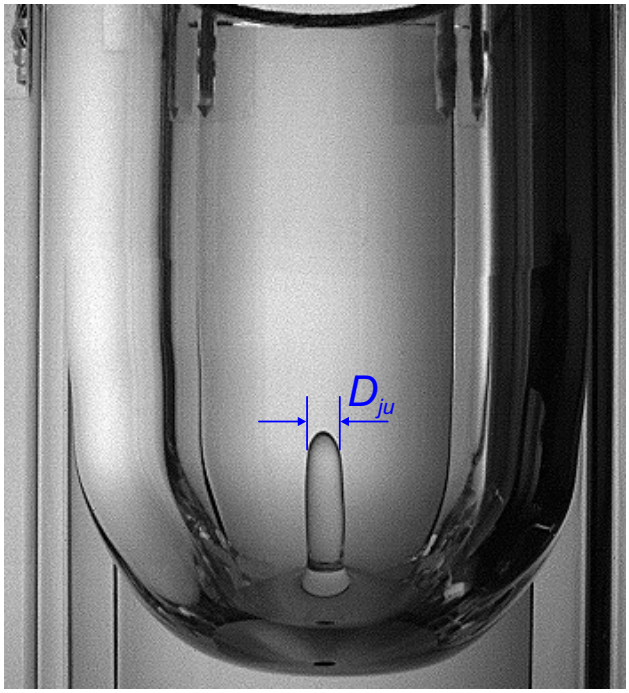

Figure A.6: Image from the drop tower experiment F24 showing the unperturbed stable liquid jet after it penetrates the interface. The diameter of the unperturbed jet is D_{ju}. The original image is cropped to show the regions of interest.

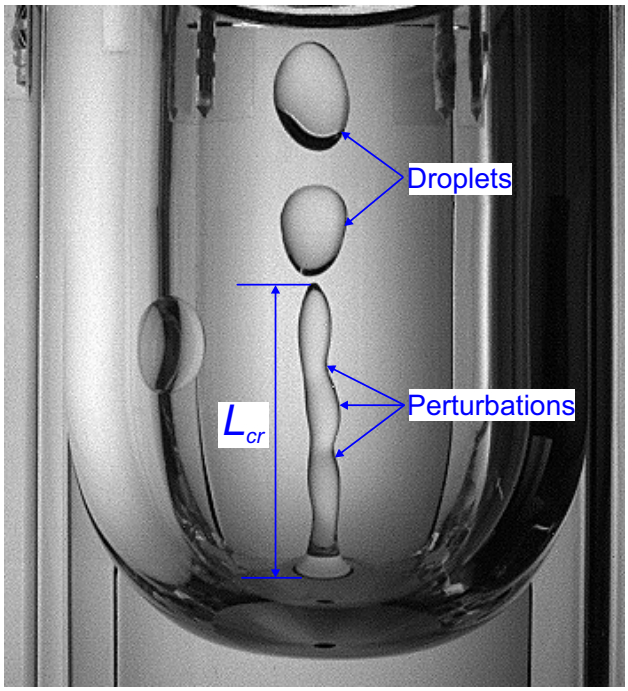

Figure A.7: Image from the drop tower experiment F30 showing the perturbations and formation of droplets after the liquid jet penetrates the interface and becomes unstable. The length above the interface at which the jet breakup occurs is the critical length L_{cr}. The original image is cropped to show the regions of interest.

Table A.1: Mean critical length and critical time of the jet breakup for the critical and supercritical regimes in the drop tower experiments.

No.	Test ID	Q_L/mL s^{-1}	n_d	L_{cr}/mm	t_{cr}/s
1	F24	1.30	3	10.18	1.50
2	F25	1.30	4	15.91	1.29
			Mean	13.04	1.39
3	F19	1.38	8	28.82	0.65
4	F30	1.38	6	23.21	0.88
			Mean	26.01	0.76
5	F22	1.50	6	30.97	0.51
6	F23	1.50	11	46.12	0.43
			Mean	38.54	0.47

The height above the interface at which the jet breaks into droplets is the critical length L_{cr}, as shown in figure A.7. The critical time t_{cr} is calculated as the time at which the droplet is formed after the liquid jet has attained a steady unperturbed state. The critical lengths and critical times for all the droplets were calculated from the images of the drop tower experiments in critical and supercritical regimes and the corresponding mean values are shown in table A.1. Moreover, the number of droplets n_d that were formed from the liquid jet in each experiment is also listed in table A.1. The size of the droplets could not be evaluated from the experimental data, as the size of each droplet varied. The difference in critical length L_{cr}, critical time t_{cr} and the number of droplets n_d can be noticed in table A.1 for the same flow rate Q_L. However, from the mean values, it can be deduced that with an increase in flow rate Q_L, the critical length L_{cr} increases, the critical time t_{cr} decreases and more droplets are formed. The droplet count in test F22 is lower due to the ingestion of gas bubbles that led to the complete breakup of the liquid jet. Although not directly comparable, the mean critical length $L_{cr} = 13.04\,\text{mm}$ calculated corresponding to the critical flow rate ($Q_L = 1.30\,\text{mL s}^{-1}$) from the drop tower experiments is approximately in the same order of magnitude of a steady jet with a radius of $R_{ju} = 2\,\text{mm}$, which has a theoretically predicted critical length of $L_{cr} = 12.57\,\text{mm}$. However, due to an increase in the jet velocity, the critical lengths of other tests are higher than the theoretical value.

It has to be mentioned that these results have been reported from the drop tower experiments and only help to get an overview of the jet instability during the liquid filling into a tank under microgravity conditions.

A.6 Experiment tank of the parabolic flight experiment

The technical drawing of the experiment tank used in the parabolic flight experiment is shown in figure A.8. The origin of the coordinate system is marked by a dot in the middle of the inlet pipe. The experiment tank had inner dimensions of 100 mm in length, 100 mm in breadth and 130 mm in height. The screen channel liquid acquisition device (SC-LAD) is on the right side of the drawing, which was mainly used for the liquid removal experiments.

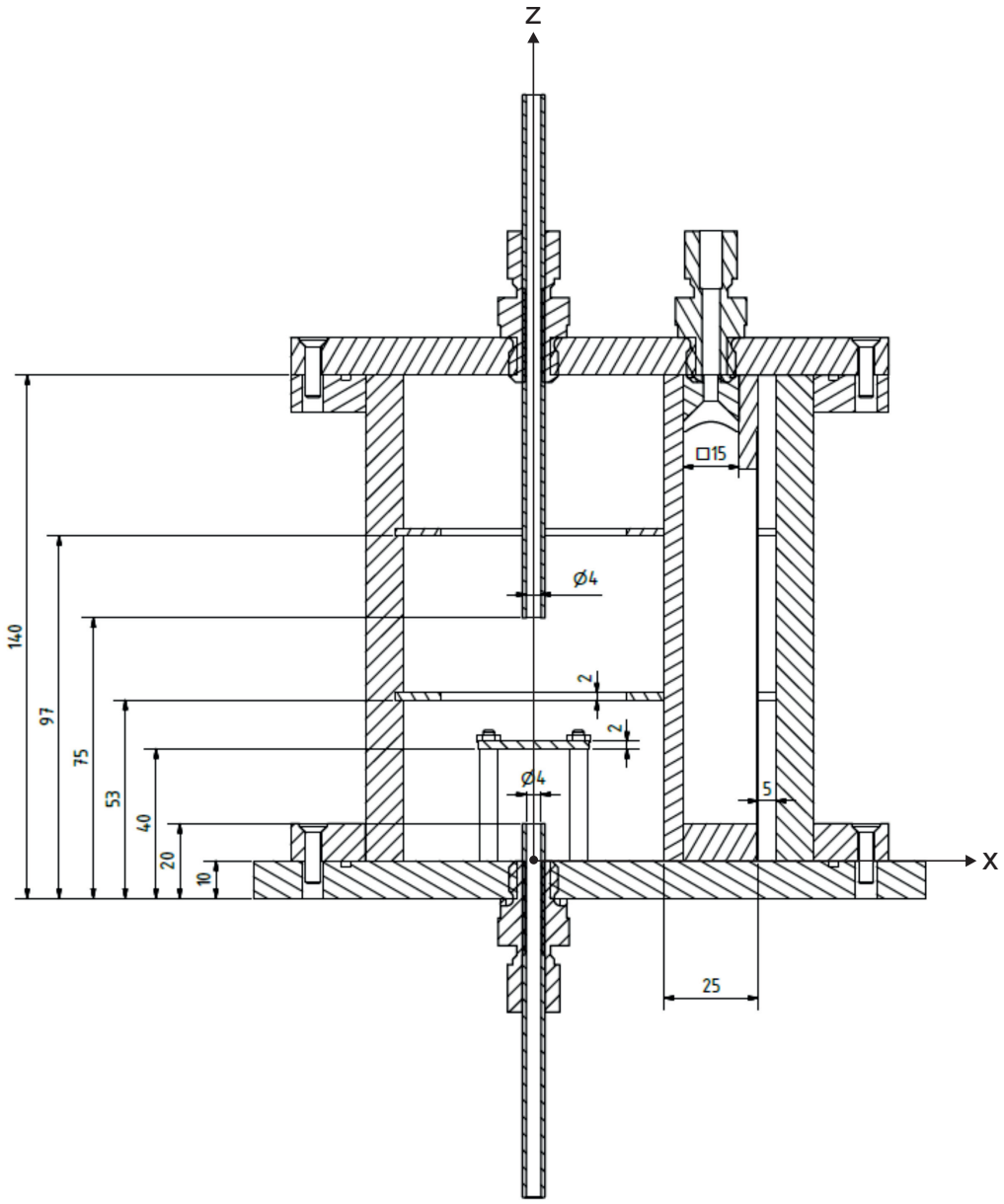

Figure A.8: Technical drawing of the experiment tank used in the parabolic flight experiment. The origin of the coordinate system is marked by a dot in the middle of the inlet pipe. All dimensions are in mm.

Appendix B

Numerical Simulations

Figure B.1 shows the contours of absolute pressure for different Q_L with $H_L = 30\,\text{mm}$ at $t = 6.9\,\text{s}$ during the perturbation of the interface by the liquid jet under reduced gravity. The low-pressure regions are visible underneath the interface for the flow rates $Q_L \leq 1.10\,\text{mL}\,\text{s}^{-1}$ and as the flow rate increases, the interface curvature changes and the low-pressure regions can be seen near the lowermost point of the interface.

Figure B.2 depicts the velocity contour with vectors showing the perturbation of the interface by the liquid jet for $H_L = 60\,\text{mm}$ and different Q_L under reduced gravity. The liquid jet hits the interface at different times depending on the velocity. The interface is depicted in grey colour.

The decay of the centreline velocity in dimensionless form is plotted for $H_L = 60\,\text{mm}$ at $t = 7.3\,\text{s}$ in figure B.3 and for $H_L = 0\,\text{mm}$ at $t = 9\,\text{s}$ in figure B.4 respectively.

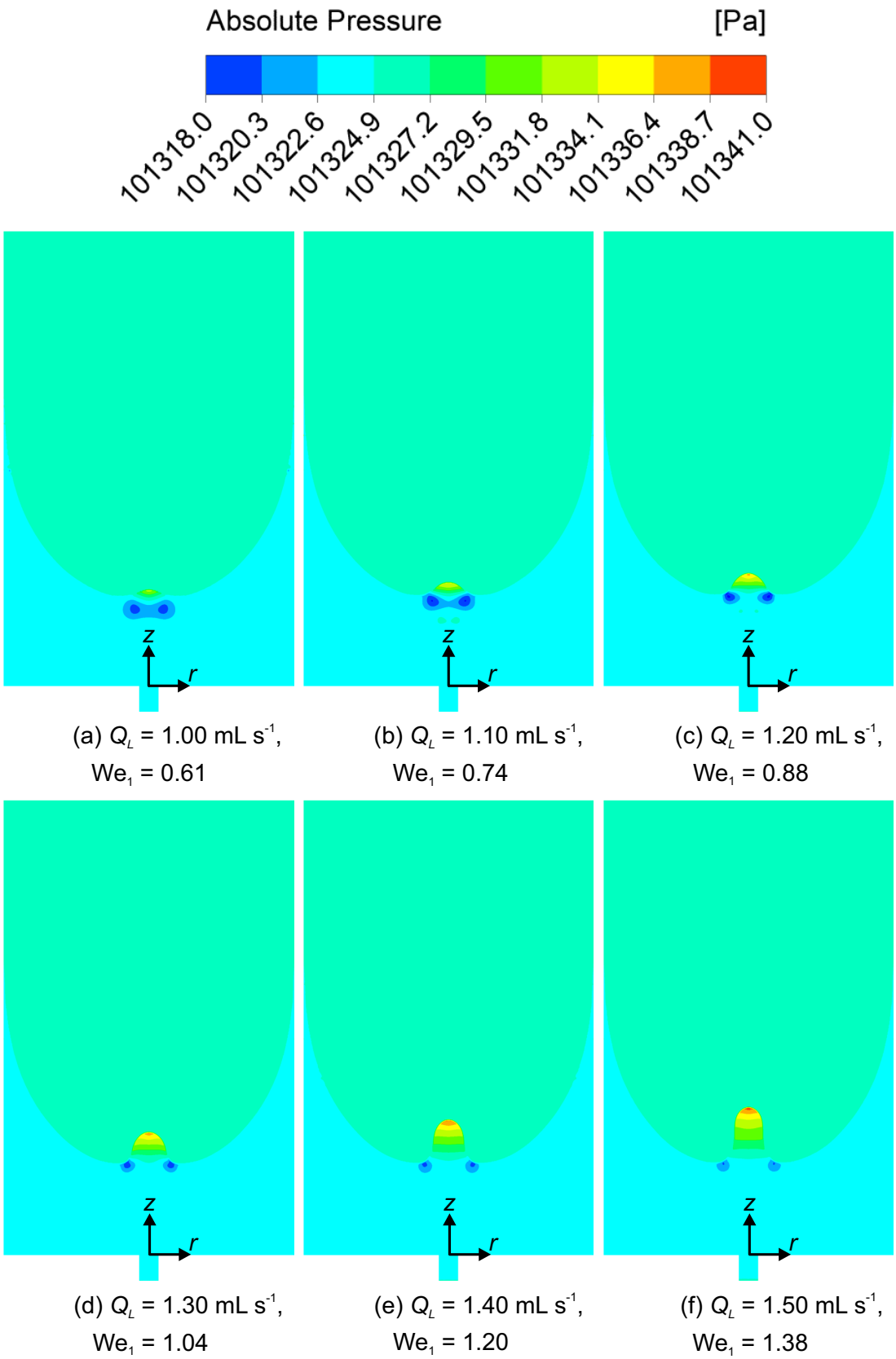

Figure B.1: Contours of absolute pressure showing the perturbation of the interface by the liquid jet for different Q_L with $H_L = 30\,\text{mm}$ at $t = 6.9\,\text{s}$ under reduced gravity.

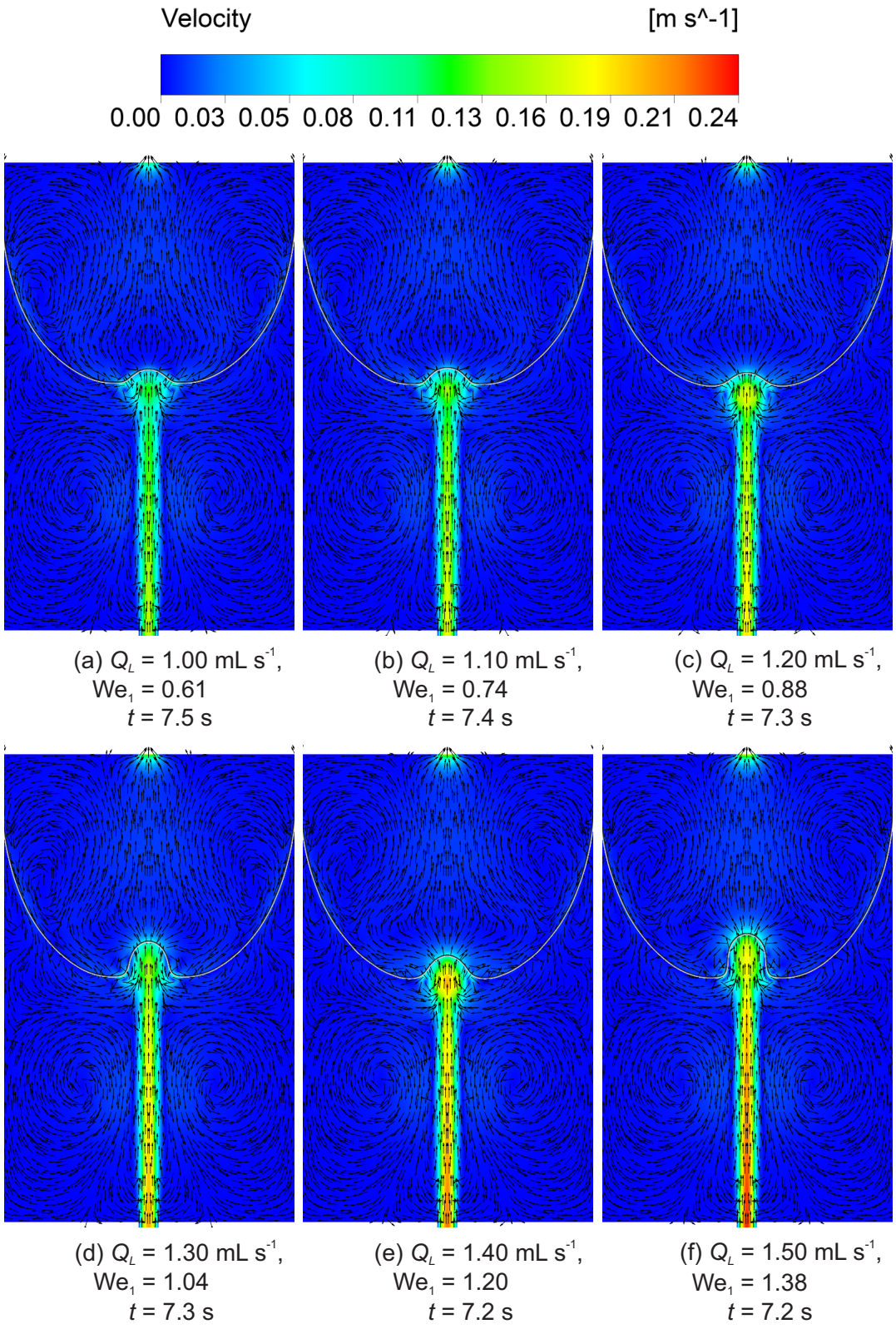

Figure B.2: Velocity contour with vectors showing the perturbation of the interface by the liquid jet for $H_L = 60\,\text{mm}$ and different Q_L under reduced gravity. The liquid jet hits the interface at different times depending on the velocity. The interface is depicted in grey colour.

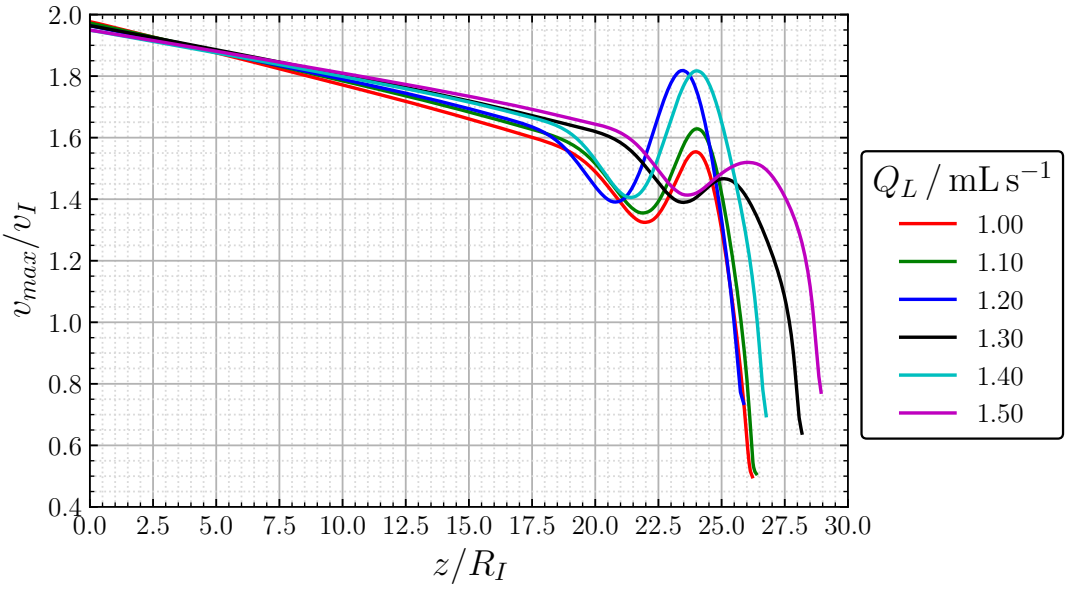

Figure B.3: Decay of the velocity along the centreline for $H_L = 60\,\text{mm}$ in dimensionless form at $t = 7.3\,\text{s}$.

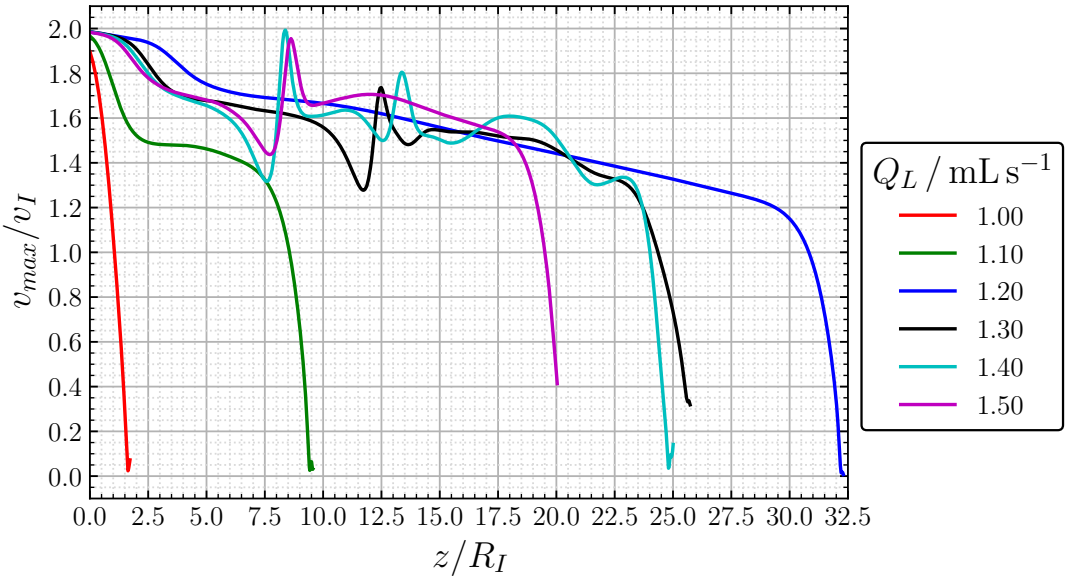

Figure B.4: Decay of the velocity along the centreline for $H_L = 0\,\text{mm}$ in dimensionless form at $t = 9\,\text{s}$.

B.1 Geyser height curves

The curves showing the evolution of the geyser height over time with refined volumetric flow rates under reduced gravity are plotted for the initial liquid fill heights of $H_L = 0\,\text{mm}$, $H_L = 7.5\,\text{mm}$, $H_L = 22.5\,\text{mm}$, $H_L = 37.5\,\text{mm}$, $H_L = 45\,\text{mm}$ and $H_L = 52.5\,\text{mm}$ in figure B.5. The curves corresponding to the simulations with coarse volumetric flow rates and to the critical flow rates, where droplet disintegration occurs, are depicted by thick lines.

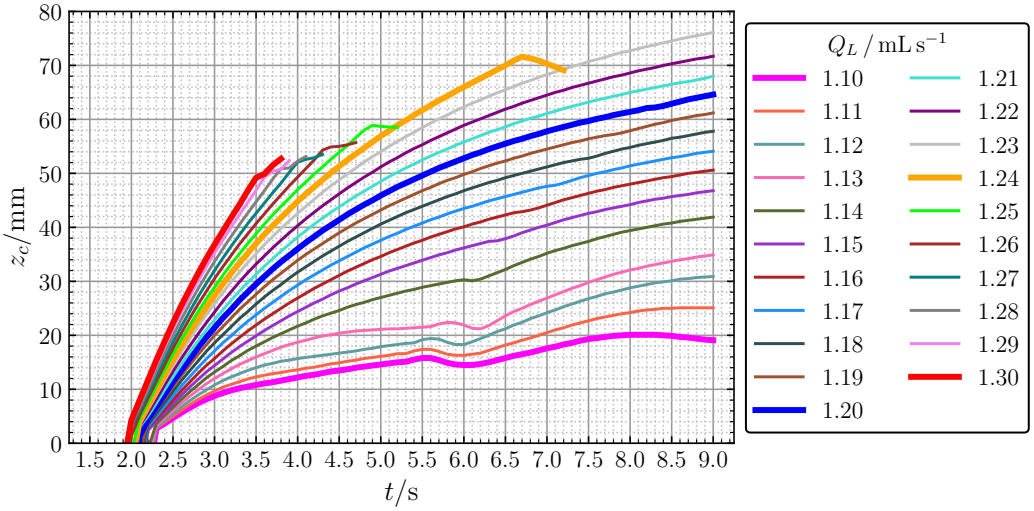

(a) $H_L = 0\,\mathrm{mm}$

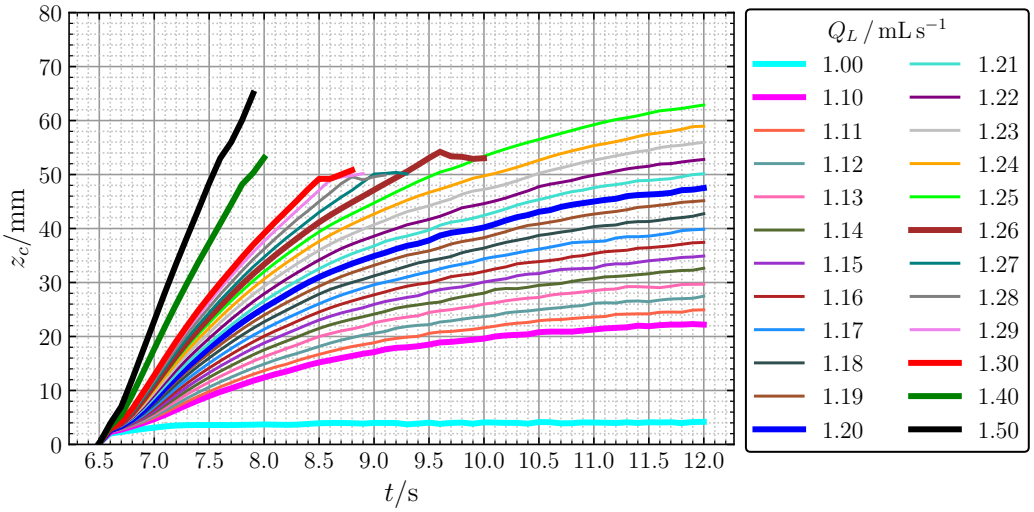

(b) $H_L = 7.5\,\mathrm{mm}$

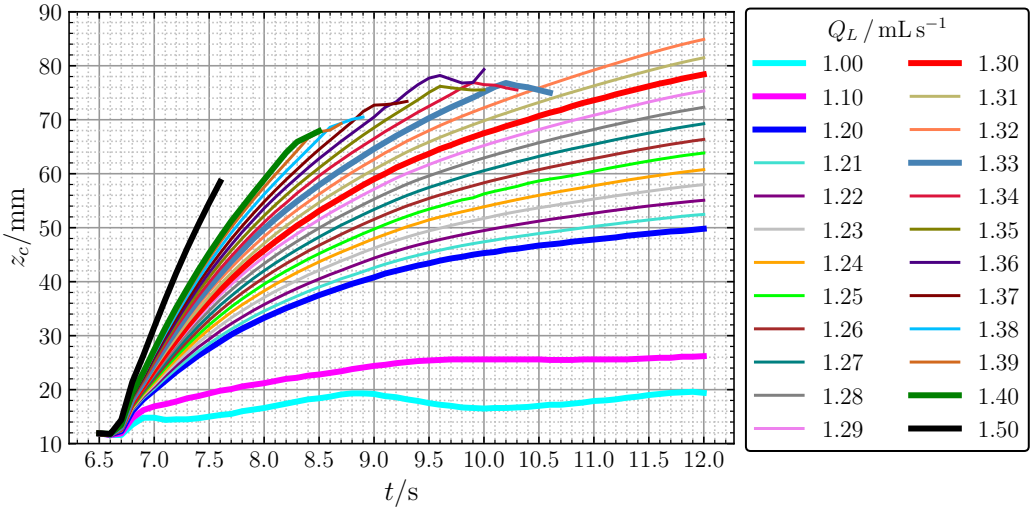

(c) $H_L = 22.5\,\mathrm{mm}$

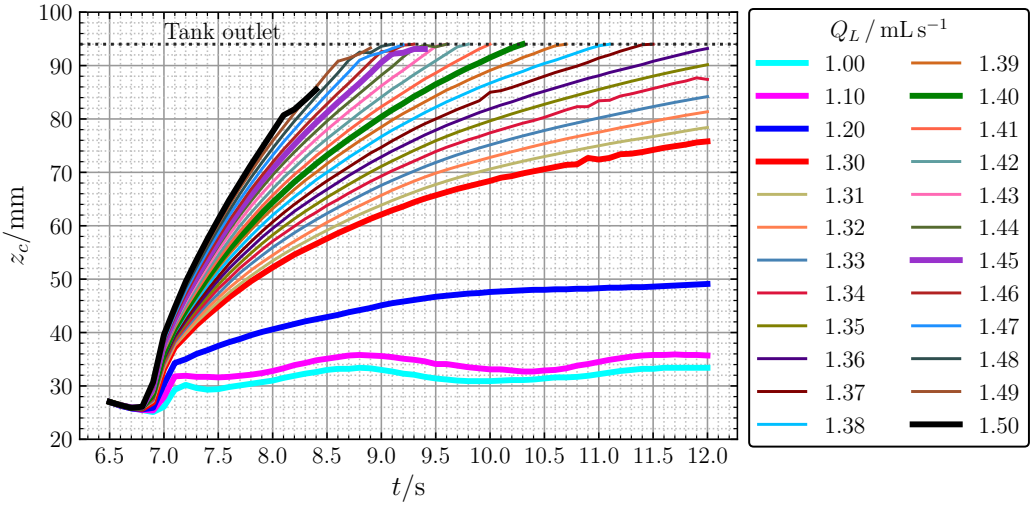

(d) $H_L = 37.5\,\mathrm{mm}$

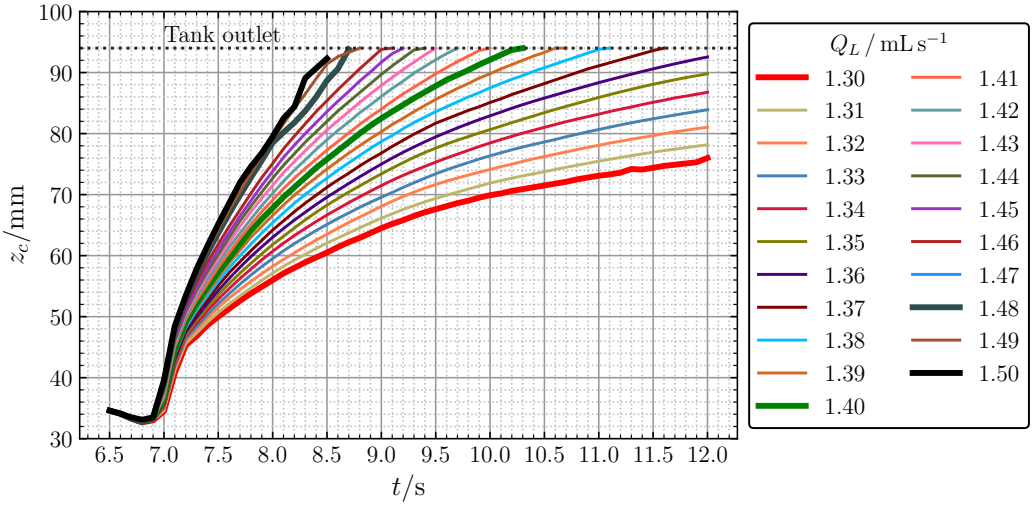

(e) $H_L = 45\,\mathrm{mm}$

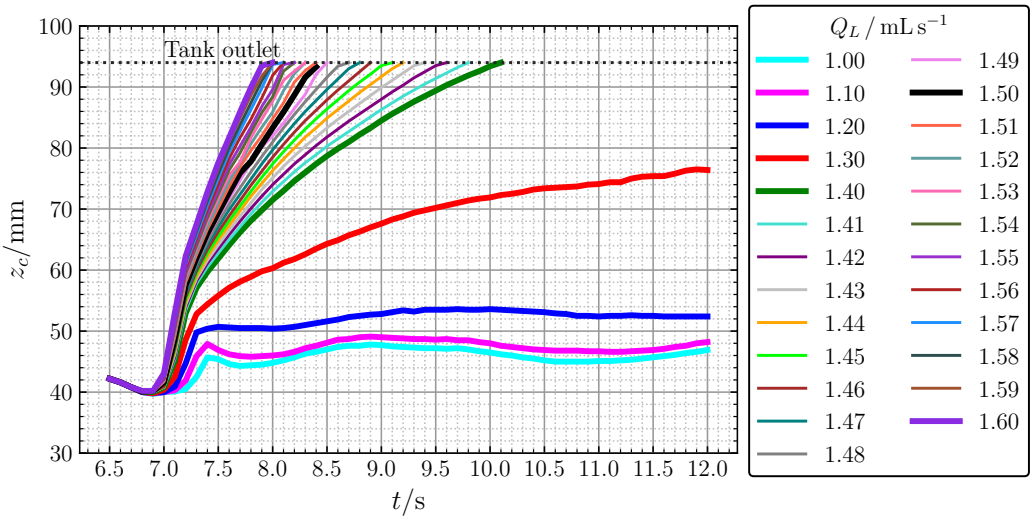

(f) $H_L = 52.5\,\mathrm{mm}$

Figure B.5: Evolution of the geyser height over time for different H_L with refined Q_L under reduced gravity.

Publications

1. Govindan, S. N. C., Dreyer, M. E. Experimental Investigation of Liquid Interface Stability During the Filling of a Tank in Microgravity. *Microgravity Sci. Technol.* 35, 23 (2023). https://doi.org/10.1007/s12217-023-10044-1

2. Govindan, S. N. C., Dreyer, M. E. Numerical investigation of interface stability in reduced gravity for the application of on-orbit refueling of spacecraft tanks. *International Journal of Energetic Materials and Chemical Propulsion* 22, 5, pp. 27-44 (2023). https://doi.org/10.1615/IntJEnergeticMaterialsChemProp.2023048294

Conferences attended

1. Govindan, S. N. C., Dreyer, M. E. Numerical simulation of vented filling of a tank in reduced gravity. 8th Space Propulsion Conference, Estoril, Portugal, 2022.

2. Govindan, S. N. C., Dreyer, M. E. Free surface behaviour during the filling of a tank in microgravity. 1st International Workshop on Challenges in Micro-gravity Fluid Dynamics Modelling, Noordwijk, The Netherlands, 2022.

3. Govindan, S. N. C., Dreyer, M. E. Experimental study of surface stability in microgravity. 44th COSPAR Scientific Assembly, Athens, Greece, 2022.

4. Govindan, S. N. C., Dreyer, M. E. Experimental investigation of interface stability in reduced gravity. 14th European Fluid Mechanics Conference, Athens, Greece, 2022.

5. Govindan, S. N. C., Dreyer, M. E. Analysis of liquid-gas interface stability under reduced gravity. Deutscher Luft- und Raumfahrtkongress 2023, Stuttgart, Germany, 2023.

Bibliography

[1] ANSYS Inc. *ANSYS Fluent Theory Guide*, Release 2019 R3 ed., 2019.

[2] ANSYS Inc. *ANSYS Fluent User's Guide*, Release 2019 R3 ed., 2019.

[3] Aydelott, J. C. Axial jet mixing of ethanol in cylindrical containers during weightlessness. Technical Paper NASA TP-1487, NASA Lewis Research Center, 1979.

[4] Baine, M., Grush, G., and Hurlbert, E. An open exploration architecture using an L-1 space propellant depot. In *SpaceOps 2010 Conference* (2010), no. AIAA 2010-2158.

[5] Beadie, G., Brindza, M., Flynn, R. A., Rosenberg, A., and Shirk, J. S. Refractive index measurements of poly(methyl methacrylate) (PMMA) from 0.4-1.6 μm. *Appl. Opt. 54*, 31 (2015), F139–F143.

[6] Bentz, M. D., Albayyari, J. M., Knoll, R. H., Hasan, M. M., and Lin, C. S. Tank Pressure Control Experiment: Results of three space flights. In *33rd AIAA/ASME/SAE/ASEE Joint Propulsion Conference and Exhibit* (1997), no. AIAA-97-2816.

[7] Bird, R. B., Stewart, W. E., and Lightfoot, E. N. *Transport Phenomena*, second ed. No. ISBN 0-471-41077-2. John Wiley & Sons, Inc., 2002.

[8] Bisht, K. S., and Dreyer, M. E. Phase separation in porous media integrated capillary channels. *Microgravity Sci. Technol. 32* (2020), 1001–1018.

[9] Brackbill, J. U., Kothe, D. B., and Zemach, C. A continuum method for modeling surface tension. *J. Comput. Phys. 100*, 2 (1992), 335–354.

[10] Breisacher, K., and Moder, J. Preliminary simulations of the ullage dynamics in microgravity during the jet mixing portion of tank pressure control experiments. In *51st AIAA/SAE/ASEE Joint Propulsion Conference* (2015), no. AIAA 2015-3853.

[11] Breon, S. R., Boyle, R. F., Francom, M. B., DeLee, C. H., Francis, J. J., Mustafi, S., Barfknecht, P. W., McGuire, J. M., Krenn, A. G., Zimmerli, G. A., and Hauser, D. M. Robotic Refueling Mission-3 - an overview. *IOP Conf. Ser.: Mater. Sci. Eng. 755*, 012002 (2020).

[12] Bruns, T. E., Fischer, A., Scheufler, H., Gerstmann, J., Hansen, H. C., Johnson, W. L., Dux, I. J., and Oleson, S. R. Future-oriented Research platform for Orbital cryogenic Storage Technologies (FROST). In *Aerospace Europe Conference 2020 - AEC* (2020).

[13] Burelbach, J. P., Bankoff, S. G., and Davis, S. H. Nonlinear stability of evaporating/condensing liquid films. *J. Fluid Mech. 195* (1988), 463–494.

[14] Bush, J. W. M. Interfacial Phenomena - Lecture 11 Fluid Jets. Lecture Notes 18.357, Massachusetts Institute of Technology, USA, 2010. `https://ocw.mit.edu/courses/18-357-interfacial-phenomena-fall-2010/resources/mit18_357f10_lecture11/`. Accessed on 16th January 2024.

[15] Chai, P. R., and Wilhite, A. W. Cryogenic thermal system analysis for orbital propellant depot. *Acta Astronaut. 102* (2014), 35–46.

[16] Chandler, F., Bienhoff, D., Cronick, J., and Grayson, G. Propellant depots for earth orbit and lunar exploration. In *AIAA SPACE 2007 Conference & Exposition* (2007), no. AIAA 2007-6081.

[17] Chato, D. J. Thermodynamic modeling of the no-vent fill methodology for transferring cryogens in low gravity. In *AIAA/ASME/SAE/ASEE 24th Joint Propulsion Conference* (1988), no. AIAA-88-3403.

[18] Chato, D. J. Ground testing on the nonvented fill method of orbital propellant transfer: Results of initial test series. In *AIAA/SAE/ASME/ASEE 27th Joint Propulsion Conference* (1991), no. AIAA-91-2326.

[19] Chato, D. J. Ground testing for the no-vent fill of cryogenic tanks: Results of tests for a 71 cubic foot tank. In *29th Joint Propulsion Conference and Exhibit* (1993), no. AIAA-93-1967.

[20] Chato, D. J. Cryogenic fluid transfer for exploration. *Cryogenics 48* (2008), 206–209.

[21] Chato, D. J., and Kassemi, M. The Zero Boil-Off Tank (ZBOT) Experiment Role in Development of Cryogenic Fluid Storage and Transfer Technologies. In *Annual Meeting of the American Society for Gravitational and Space Research* (2012), no. E-664086.

[22] Chato, D. J., and Martin, T. A. Vented Tank Resupply Experiment: Flight test results. *J. Spacecraft Rockets 43*, 5 (2006), 1124–1130.

[23] Committee for the Decadal Survey on Biological and Physical Sciences in Space, Space Studies Board, Aeronautics and Space Engineering Board, Division on Engineering and Physical Sciences. Recapturing a Future for Space Exploration: Life and Physical Sciences Research for a New Era. Tech. rep., National Research Council, Washington DC, USA, 2011.

[24] Conrath, M., and Dreyer, M. E. Gas breakthrough at a porous screen. *Int. J. Multiphas. Flow 42* (2012), 29–41.

[25] DeLee, C. H., Barfknecht, P., Breon, S., Boyle, R., DiPirro, M., Francis, J., Huynh, J., Li, X., McGuire, J., Mustafi, S., Tuttle, J., and Wegel, D. Techniques for on-orbit cryogenic servicing. *Cryogenics 64* (2014), 289–294.

[26] Dodge, F. T. *The new dynamic behavior of liquids in moving containers.* Southwest Research Institute, San Antonio, Texas, 2000.

[27] Dominick, S. M., and Driscoll, S. L. Fluid Acquisition and Resupply Experiment (FARE-I) flight results. In *AIAA/SAE/ASME/ASEE 29th Joint Propulsion Conference and Exhibit* (1993), no. AIAA 93-2424.

[28] Dominick, S. M., and Tegart, J. R. Low-g propellant transfer using capillary devices. In *AIAA/SAE/ASME 17th Joint Propulsion Conference* (1981), no. AIAA-81-1507.

[29] Dominick, S. M., and Tegart, J. R. Fluid dynamics and thermodynamics of a low gravity liquid tank filling method. In *28th Aerospace Sciences Meeting* (1990), no. AIAA-90-0509.

[30] Dominick, S. M., and Tegart, J. R. Orbital test results of a vaned liquid acquisition device. In *30th AIAA/ASME/SAE/ASEE Joint Propulsion Conference* (1994), no. AIAA 94-3027.

[31] Eggers, J., and Villermaux, E. Physics of liquid jets. *Rep. Prog. Phys. 71*, 036601 (2008).

[32] Fikes, J., Howell, J. T., and Henley, M. In-space cryogenic propellant depot (ISCPD) architecture definitions and systems studies. In *57th International Astronautical Congress* (2006), no. IAC-06-D3.3.08.

[33] Flachbart, R. H., Hedayat, A., Holt, K. A., Sims, J., Johnson, E. F., Hastings, L. J., and Lak, T. Large-scale liquid hydrogen tank rapid chill and fill testing for the advanced shuttle upper stage concept. Technical Publication NASA/TP-2013-217482, NASA Marshall Space Flight Center, 2013.

[34] Friese, P. S., Hopfinger, E. J., and Dreyer, M. E. Liquid hydrogen sloshing in superheated vessels under microgravity. *Exp. Therm. Fluid Sci. 106* (2019), 100–118.

[35] Gaebler, J. A., Lugo, R. A., Axdahl, E. L., Chai, P. R., Grimes, M. S., Long, M. R., Rowland, R. A., and Dr. Wilhite, A. Reusable lunar transportation architecture utilizing orbital propellant depots. In *AIAA SPACE 2009 Conference & Exposition* (2009), no. AIAA 2009-6711.

[36] Gerstmann, J., and Dreyer, M. E. Axisymmetric surface oscillations in a cylindrical container with compensated gravity. *Ann. NY Acad. Sci. 1077* (2006), 328–350.

[37] Gille, J. P. Analysis and modeling of fluid transfer in orbit. In *AIAA/ASME/SAE/ASEE 22nd Joint Propulsion Conference* (1986), no. AIAA-86-1718.

[38] Gille, J. P. Analysis and modeling of no-vent transfer of cryogens in orbit. In *AIAA/ASME 4th Joint Thermophysics and Heat Transfer Conference* (1986), no. AIAA-86-1252.

[39] Goff, J. A., Kutter, B. F., Zegler, F., Bienhoff, D., Chandler, F., and Marchetta, J. Realistic near-term propellant depots: Implementation of a critical spacefaring capability. In *AIAA SPACE 2009 Conference & Exposition* (2009), no. AIAA 2009-6756.

[40] Govindan, S. N. C., and Dreyer, M. E. Experimental investigation of liquid interface stability during the filling of a tank in microgravity. *Microgravity Sci. Technol. 35*, 23 (2023).

[41] Govindan, S. N. C., and Dreyer, M. E. Numerical investigation of interface stability in reduced gravity for the application of on-orbit refueling of spacecraft tanks. *International Journal of Energetic Materials and Chemical Propulsion 22*, 5 (2023), 27–44.

[42] Hartwig, J. W. Screen channel liquid acquisition device bubble point tests in liquid nitrogen. *Cryogenics 74* (2016), 95–105.

[43] Hochstein, J. I., Gerhart, P. M., and Aydelott, J. C. Computational modeling of jet induced mixing of cryogenic propellants in low-g. In *AIAA/SAE/ASME 20th Joint Propulsion Conference* (1984), no. AIAA-84-1344.

[44] Hochstein, J. I., Marchetta, J. G., and Thornton, R. J. Microgravity geyser and flowfield prediction. *J. Propul. Power 24*, 1 (2008), 104–110.

[45] Honkonen, S. C., Bennett Jr., F. O., and Hepworth, H. K. An analytic model for low-gravity tank chilldown and no-vent fill: The General Dynamics No-Vent Fill Program (GDNVF). In *AIAA 26th Thermophysics Conference* (1991), no. AIAA 91-1380.

[46] Howell, J. T., Mankins, J. C., and Fikes, J. C. In-space cryogenic propellant depot stepping stone. *Acta Astronaut. 59* (2006), 230–235.

[47] Kartuzova, O., and Kassemi, M. CFD jet mixing model validation against Zero-Boil-Off Tank (ZBOT) microgravity experiment. In *AIAA Propulsion and Energy 2019 Forum* (2019), no. AIAA 2019-4282.

[48] Kassemi, M., Kartuzova, O., and Hylton, S. Results of the microgravity Zero-Boil-Off Tank (ZBOT) experiment. In *69th International Astronautical Congress (IAC)* (2018), no. IAC-18-A2.2.6-43028.

[49] Kneer, R., Haustein, H. D., Ehrenpreis, C., and Rohlfs, W. Flow structures and heat transfer in submerged and free laminar jets. In *15th International Heat Transfer Conference IHTC-15* (2014), no. IHTC15-KN28.

[50] Koenemann, T. *Bremen Drop Tower Payload User's Guide Version 1.2.* ZARM FAB mbH, Bremen, 2022. `https://www.zarm.uni-bremen.de/fileadmin/user_upload/drop_tower/ZARM_BDT_PUG_ver1.2.pdf`. Accessed on 27th June 2022.

[51] Krahl, R., and Gerstmann, J. Non-isothermal reorientation of a liquid surface in an annular gap. In *4th International Berlin Workshop on Transport Phenomena with Moving Boundaries* (2007), pp. 227–241.

[52] Kulev, N. *Behavior of cryogenic liquids under compensated gravity and non-isothermal boundary conditions.* No. ISBN 978-3-7369-7152-3. Cuvillier Verlag Göttingen, 2020.

[53] Kulev, N., and Dreyer, M. E. Drop tower experiments on non-isothermal reorientation of cryogenic liquids. *Microgravity Sci. Technol. 22* (2010), 463–474.

[54] Kutter, B. F., Zegler, F., Lucas, S., Hines, L., Ragab, M., Spradley, I., and Hopkins, J. Atlas centaur extensibility to long-duration in-space applications. In *AIAA Space 2005 Conference* (2005), no. AIAA 2005-6738.

[55] Kutter, B. F., Zegler, F., O'Neil, G., and Pitchford, B. A practical, affordable cryogenic propellant depot based on ULA's flight experience. In *AIAA SPACE 2008 Conference & Exposition* (2008), no. AIAA 2008-7644.

[56] Landau, L. D., and Lifshitz, E. M. *Fluid Mechanics*, second ed. No. ISBN 0-08-033933-6. Pergamon Books Ltd., 1987.

[57] Lei, J., Jia, D., Bai, M., Feng, Y., and Li, X. Research and development of Tianzhou cargo spacecraft. *Space: Science & Technology 3*, 0006 (2023).

[58] Li, J.-C., Lin, H., Li, K., Zhao, J.-F., and Hu, W.-R. Liquid sloshing in partially filled capsule storage tank undergoing gravity reduction to low/micro-gravity condition. *Microgravity Sci. Technol. 32* (2020), 587–596.

[59] Li, J.-C., Lin, H., Zhao, J.-F., Li, K., and Hu, W.-R. Dynamic behaviors of liquid in partially filled tank in short-term microgravity. *Microgravity Sci. Technol. 30* (2018), 849–856.

[60] Li, Z.-G., Zhu, Z.-Q., Liu, Q.-S., Lin, H., and Xie, J.-C. Simulating propellant reorientation of vehicle upper stage in microgravity environment. *Microgravity Sci. Technol. 25* (2013), 237–241.

[61] Ma, Y., Li, Y., Zhu, K., Wang, Y., Wang, L., and Tan, H. Investigation on no-vent filling process of liquid hydrogen tank under microgravity condition. *Int. J. Hydrogen Energ. 42*, 12 (2017), 8264–8277.

[62] Majumdar, A. No vent tank fill and transfer line chilldown analysis by Generalized Fluid System Simulation Program (GFSSP). In *Thermal and Fluids Analysis Workshop (TFAWS)* (2013), no. M13-2805.

[63] Marchetta, J. G., and Benedetti, R. H. Simulation of jet-induced geysers in reduced gravity. *Microgravity Sci. Technol. 22* (2010), 7–16.

[64] McLean, C., Pitchford, B., Mustafi, S., Wollen, M., Walls, L., and Schmidt, J. Simple, robust cryogenic propellant depot for near term applications. In *2011 Aerospace Conference* (2011), no. 1044.

[65] Michaelis, M., Dreyer, M. E., and Rath, H. J. Experimental investigation of the liquid interface reorientation upon step reduction in gravity. *Ann. NY Acad. Sci. 974* (2002), 246–260.

[66] Moran, M. E., and Nyland, T. W. Hydrogen no-vent fill testing in a 5 cubic foot (142 liter) tank using spray nozzle and spray bar liquid injection. In *28th Joint Propulsion Conference and Exhibit* (1992), no. AIAA-92-3063.

[67] Moran, M. E., Nyland, T. W., and Driscoll, S. L. Hydrogen no-vent fill testing in a 1.2 cubic foot (34 liter) tank. Technical Memorandum NASA TM-105273, 1991.

[68] Moran, M. E., Nyland, T. W., and Papell, S. S. Liquid transfer cryogenic test facility - Initial hydrogen and nitrogen no-vent fill data. Technical Memorandum NASA TM-102572, 1990.

[69] Mustafi, S., Johnson, W., Kashani, A., Jurns, J., Kutter, B., Kirk, D., and Shull, J. Subcooling for long duration in-space cryogenic propellant storage. In *AIAA SPACE 2010 Conference & Exposition* (2010), no. AIAA 2010-8869.

[70] Novespace. *A310 ZERO-G User Guide*, 2019. UG-2019-01-EN.

[71] Perrin, T. M., and Casler, J. G. Architecture study for a fuel depot supplied from lunar assets. In *AIAA SPACE 2016 Conference* (2016), no. AIAA 2016-5306.

[72] Rankin, G. W., and Sridhar, K. Developing region of laminar jets with parabolic exit velocity profiles. *J. Fluid. Eng. 103*, 2 (1981), 322–327.

[73] Schmidt, G. R., Carrigan, R. W., Hahs, J. E., Vaughan, D. A., and Foust, D. C. No-vent fill pressurization tests using a cryogen simulant. Technical Memorandum NASA TM-103561, 1991.

[74] Schmitt, S., and Dreyer, M. E. Free surface oscillations of liquid hydrogen in microgravity conditions. *Cryogenics 72*, 1 (2015), 22–35.

[75] Schuster, J. R., Russ, E. J., and Wachter, J. P. Cryogenic on-orbit liquid depot storage, acquisition, and transfer satellite (COLD-SAT). Contractor Report NASA CR-185249, 1990.

[76] Schweickart, R. B. Thermodynamic analysis of a demonstration concept for the long-duration storage and transfer of cryogenic propellants. *Cryogenics 64* (2014), 283–288.

[77] Shankar Subramanian, R. Boundary Conditions in Fluid Mechanics. Lecture Notes CH560: Transport Phenomena, Clarkson University, USA, 2015. `https://web2.clarkson.edu/projects/subramanian/ch560/notes/BoundaryConditionsinFluidMechanics.pdf`. Accessed on 21st April 2023.

[78] Siegert, C. E., Petrash, D. A., and Otto, E. W. Time response of liquid-vapor interface after entering weightlessness. Technical Note NASA TN D-2458, 1964.

[79] Simmons, B. D., Marchetta, J. G., and Hochstein, J. I. Reduced gravity cryogenic propellant tank re-supply simulation and geyser prediction. In *43rd AIAA Aerospace Sciences Meeting and Exhibit* (2005), no. AIAA 2005-1150.

[80] Smitherman, D., and Woodcock, G. Space transportation infrastructure supported by propellant depots. In *AIAA SPACE 2011 Conference & Exposition* (2011), no. AIAA 2011-7160.

[81] Stief, M., Gerstmann, J., and Dreyer, M. E. Reorientation of cryogenic fluids upon step reduction of gravity. In *PAMM* (2005), vol. 5, WILEY-VCH Verlag GmbH & Co. KGaA, pp. 553–554.

[82] Street, D. A scalable orbital propellant depot design. AE8900 MS Special Problems Report, Space Systems Design Lab (SSDL), School of Aerospace Engineering, Georgia Institute of Technology, USA, 2006.

[83] Symons, E. P. Liquid inflow to partially full, hemispherical-ended cylinders during weightlessness. Technical Memorandum NASA TM X-1934, NASA Lewis Research Center, 1969.

[84] Symons, E. P. Interface stability during liquid inflow to initially empty hemispherical ended cylinders in weightlessness. Technical Memorandum NASA TM X-2003, NASA Lewis Research Center, 1970.

[85] Symons, E. P., and Labus, T. L. Experimental investigation of an axisymmetric fully developed laminar free jet. Technical Note NASA TN D-6304, NASA Lewis Research Center, 1971.

[86] Symons, E. P., Nussle, R. C., and Abdalla, K. L. Liquid inflow to initially empty, hemispherical ended cylinders during weightlessness. Technical Note NASA TN D-4628, NASA Lewis Research Center, 1968.

[87] Symons, E. P., and Staskus, J. V. Interface stability during liquid inflow to partially full, hemispherical ended cylinders during weightlessness. Technical Memorandum NASA TM X-2348, NASA Lewis Research Center, 1971.

[88] Tang, S. K. Y., Li, Z., Abate, A. R., Agresti, J. J., Weitz, D. A., Psaltis, D., and Whitesides, G. M. A multi-color fast-switching microfluidic droplet dye laser. *Lab on a Chip 9* (2009), 2767–2771.

[89] Taylor, W. J., and Chato, D. J. Improved thermodynamic modeling of the no-vent fill process and correlation with experimental data. In *26th Thermophysics Conference* (1991), no. AIAA 1991-1379.

[90] Taylor, W. J., and Chato, D. J. Comparing the results of an analytical model of the no-vent fill process with no-vent fill test results for a 4.96 cubic meters (175 cubic feet) tank. In *AIAA/SAE/ASME/ASEE 28th Joint Propulsion Conference and Exhibit* (1992), no. AIAA-92-3078.

[91] Thomas, A. L. Force and mass balances of the incompressible, isothermal, planar laminar jet issuing from a finite source. *Chemical Engineering Science 8*, 3 (1958), 254–264.

[92] Thornton, R. J., and Hochstein, J. I. Microgravity propellant tank geyser analysis and prediction. In *39th AIAA Aerospace Sciences Meeting & Exhibit* (2001), no. AIAA-2001-1132.

[93] Vaughan, D. A., Foust, D. C., and Schmidt, G. R. Enhancement of the no-vent fill process. In *AIAA/SAE/ASME/ASEE 27th Joint Propulsion Conference* (1991), no. AIAA-91-1842.

[94] Vaughan, D. A., and Schmidt, G. R. Analytical modeling of no-vent fill process. *J. Spacecraft Rockets 28*, 5 (1991), 574–579.

[95] Viskanta, R. Heat transfer to impinging isothermal gas and flame jets. *Exp. Therm. Fluid Sci. 6*, 2 (1993), 111–134.

[96] Wang, C., Li, Y., and Wang, R. Performance comparison between no-vent and vented fills in vertical thermal-insulated cryogenic cylinders. *Exp. Therm. Fluid Sci. 35*, 2 (2011), 311–318.

[97] Wang, C., and Wang, R. The effects of vertical and horizontal placement on no-vent fill of cryogenic insulated vessels. *Cryogenics 50*, 8 (2010), 480–485.

[98] Wendl, M. C., Hochstein, J. I., and Sasmal, G. P. Modeling of jet-induced geyser formation in a reduced gravity environment. In *29th Aerospace Sciences Meeting* (1991), no. AIAA-91-0803.

[99] White, F. M. *Fluid Mechanics*, seventh ed. No. ISBN 978-0-07-352934-9. The McGraw-Hill Companies Inc., 2011.

[100] Zegler, F., and Kutter, B. Evolving to a depot-based space transportation architecture. In *AIAA SPACE 2010 Conference & Exposition* (2010), no. AIAA 2010-8638.